Radar and Laser Altimeter measurements over Arctic Sea Ice

Katharine Anne Giles

A thesis submitted to the University of London for the degree of Doctor of Philosophy

Centre for Polar Observation and Modelling
Department of Space and Climate Physics
University College London

March 2005

ProQuest LLC
789 East Eisenhower Parkway
P.O. Box 1346
Ann Arbor, MI 48106-1346

Abstract

To validate sea ice models, basin wide sea ice thickness measurements with an accuracy of ± 0.5 m are required; to analyse trends in sea ice thickness, it is necessary to detect changes in sea ice thickness of 4 cm per year on a basin wide scale. The estimated error on satellite radar altimeter estimates of sea ice thickness is ± 0.45 m and the estimated error on satellite laser altimetry estimates of sea ice thickness is ± 0.78 m. The Laser Radar Altimetry (LaRA) field campaign took place in the Arctic during 2002. It was the first experiment to collect coincident radar and laser altimetry over sea ice. This thesis analyses the data from LaRA to explore the potential of combining radar and laser altimetry to reduce the uncertainties in measurements of sea ice thickness.

Two new methods to analyse the LaRA data are described. The first is the University College London (UCL) Delay/Doppler radar altimeter (D2P) re-tracking algorithm and the second is the UCL D2P power simulator. Each method is calibrated and the associated error is estimated. The UCL D2P power simulator reproduces the D2P returns closely, and is used to estimate the elevation difference between the reflecting surface of the radar and the laser with an accuracy of ± 0.07 m. The laser is shown to consistently reflect from a higher surface than the radar. The offset between the laser and the radar is consistent with observed snow depths and compares well to snow depth distributions from in-situ data. We find that reducing the error in snow depth to 7 cm reduces the radar error in sea ice thickness from ± 0.45 m to ± 0.37 m and the laser error in sea ice thickness from ± 0.78 m to ± 0.55 m.

Acknowledgements

I would like to thank my supervisor, Dr. Seymour Laxon, for his guidance, support and encouragement throughout my time at UCL, and for helping me to turn my work during my PhD. into this thesis. My thanks also extend to other members of CPOM, In particular Dr. David Wallis for our numerous and invaluable conversations about the operation of the D2P radar altimeter, his encouragement and enthusiasm, and for his review of parts of this thesis, and Professor Duncan Wingham for encouraging me to take a rigorous approach to data analysis and for aiding my understanding of the principles of operation of the D2P radar altimeter.

I should acknowledge several outside institutions and individuals who were involved in the LaRA field campaign. ESA, NASA and NOAA who funded the campaign, Dr. Keith Raney and Dr. Carl Leuschen from the Applied Physics Laboratory, Johns Hopkins University, the scientists and flight crew at the Wallops Flight Facility in particular Dr. Bill Krabill and Dr. Serdar Manizade. Serdar and Carl, thank you for answering my numerous questions about the laser and radar altimeters. My thanks also go to Dr. Dave McAdoo at NOAA.

The work presented in chapter four was done in collaboration with Sine Munk Hvidegaard from the National Survey and cadastre (KMS) so thanks are also due to her.

Finally, I would like to thank my parents for all their support throughout my education and my sister and friends for providing lots of welcome breaks from study during the course of my PhD.

In memory of Freddie and Marian Giles

List of contents

List of contents (continued) page

List of contents (continued) page

List of contents (continued) page

List of contents (continued) page

List of contents (continued) page

List of contents (continued) page

List of figures

List of figures (continued) page

List of figures (continued) page

List of figures (continued) page

List of figures (continued) page

List of figures (continued) page

List of tables

1) The climate system and sea ice

1.0) Introduction

The aim of the work described in this thesis is to assess the potential of combining coincident radar and laser altimetry to reduce uncertainties in the measurement of sea ice thickness from both radar and laser altimetry. This thesis analyses data from the LaRA field campaign, the first experiment to collect coincident radar and laser altimetry over sea ice. In addition, this thesis aims to understand how the experiment could be improved in future field campaigns, as the experiment is an important precursor to the airborne validation campaigns for the CryoSat satellite.

The ability to measure sea ice thickness on a basin wide scale at regular intervals provides a valuable resource for climate modelling and therefore for the prediction of climate change. In section 1.1, we describe the global climate system and how it is modelled. In section 1.2 we describe the influence of sea ice on the climate system and in section 1.3 we describe sea ice models and how they are validated. Section 1.4 describes sea ice observations and their findings. Section 1.5 describes a recent advance in the measurement of sea ice thickness from satellite radar altimetry and the uncertainties present in the technique. Section 1.6 describes the measurement of sea ice thickness from satellite laser altimetry and the uncertainties present in the technique. Finally, in section 1.7, we outline the main aims of the work described in this thesis.

1.1) The global climate system

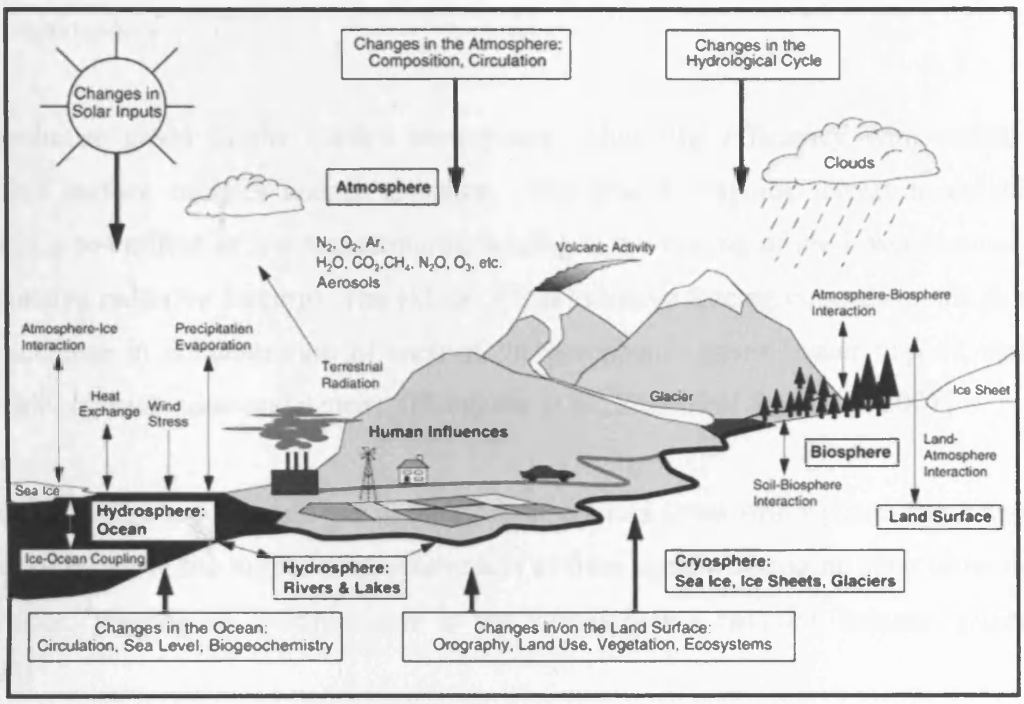

Figure 1.1: The global climate system: components of the system (bold), their processes and interactions (thin arrows) and some aspects that may change (bold arrows) [Houghton et al., *Chapter 1*, 2001]

The climate system is composed of five major components: the atmosphere, hydrosphere, the cryosphere, the land surface and the biosphere. This composite system is subject to various external forcing mechanisms; the most important is the sun.

When radiation from the Sun encounters the Earth it is either reflected, absorbed or transmitted by the atmosphere. The radiation transmitted through the atmosphere is then either absorbed or reflected by the Earths surface The energy reaching the Earth's surface is redistributed by the atmospheric and oceanic currents and radiated back to space at infrared wavelengths. [Houghton et al., *Technical Summary*, 2001]

1.1.1) The components of the climate system

The Atmosphere

Greenhouse gases in the Earth's atmosphere reduce the efficiency with which the Earth's surface radiates energy to space. They absorb outgoing terrestrial radiation, which is re-emitted at low temperatures, leading to a warming of the lower atmosphere (a positive radiative forcing). The extent of this radiative forcing depends on the size of the increase in concentration of each of the greenhouse gases (water vapour, carbon dioxide, nitrous oxide and ozone). [Houghton et al., *Technical Summary*, 2001]

Ozone acts as a green house gas in the troposphere and lower stratosphere. But a natural layer of ozone in the higher stratosphere acts as filter against damaging solar ultra-violet radiation, playing an essential role in the stratosphere's radiative balance. [Ahrens, 1993]

Aerosols suspended in the troposphere, from both natural and anthropogenic sources, have a complex effect upon climate. For example, if the albedo of an aerosol particle is higher than that of the surface it is above, the amount of sunlight reflected back into space is likely to increase causing the air temperature to lower and visa versa. Certain aerosols, although they reflect radiation from the sun back to space, may also absorb outgoing infrared radiation [Ahrens, 1993]. Changes in aerosol concentrations can effect cloud amount and reflectivity. Volcanic eruptions eject large amounts of sulphate gases into the stratosphere that interfere with incoming solar radiation, producing a large, but transitory, cooling effect [McIlveen, 1992].

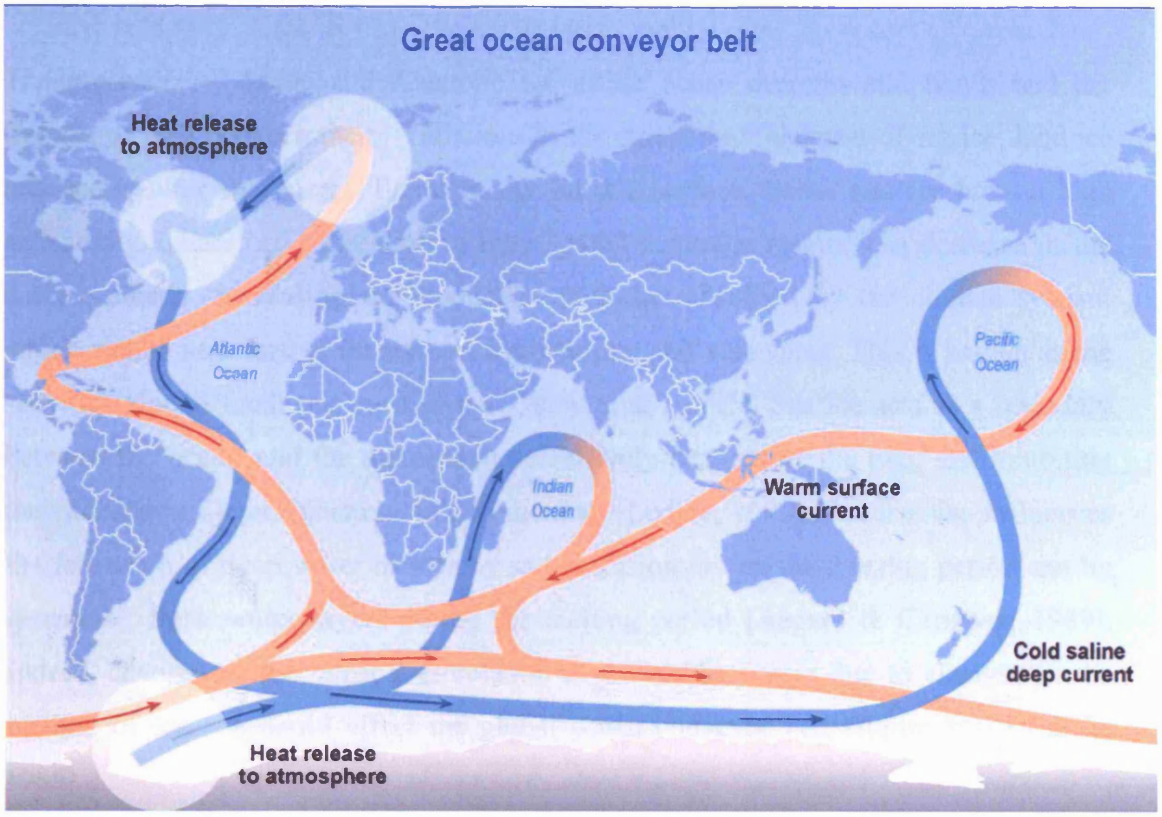

Figure 1.2: The ocean conveyor belt – Warm surface currents (orange) and cold deep currents (blue) are connected in the deepwater formation areas in the high latitudes of the Atlantic and around Antarctica. It is at these points where the major ocean to atmosphere transfer of heat occurs. [Watson, 2001]

The Ocean absorbs more than half the solar radiation reaching the earth's surface, largely in the top 100m. Heat from this layer is then transferred back to the atmosphere by evaporation, moved and mixed downwards, or remains in the surface layer and is transported to other areas of the ocean. Figure 1.2 illustrates the transport of heat around the oceans. For example: The warm surface current crossing the Atlantic Ocean (the Gulf Stream) transports warm water from the East coast of America, towards the NE Atlantic, leading to Britain's relatively mild climate when compared to many other places at the same latitude. [Vaughan & Cracknell, 1994]

The Cryosphere

The presence of Arctic and Antarctic ice affect ocean currents and winds and the transfer of heat between them. Variations in the extent and thickness of sea ice, land ice and snow, alter the energy fluxes at the Earth's surface. Snow and ice have a high reflectivity. Therefore a decrease in their spatial coverage results in a decrease in the surface albedo, increasing the amount of radiation absorbed by the climate system, which results in a further increase in temperature, and visa versa. This is known as the snow/ice albedo feedback mechanism [Curry et al., 1995]. Sea ice acts as a boundary between the ocean and the atmosphere, effectively decoupling the two, and inhibiting the exchange of heat, moisture and momentum [Ledley, 1993]. Sea ice also influences the formation of deep water masses by salt extrusion during the freezing period and by generating fresh water layers during the melting period [Aagard & Carmack, 1989]. Indeed, changes to the vertical circulation in the northern seas due to changes in the melting of sea ice could affect the global ocean conveyor belt (figure 1.2) [Rudels, 1995].

The Land Surface and Biosphere

Topography, vegetation and seasonal snow cover influence airflow, absorption of solar energy and the water cycle. The Biosphere helps to determine the atmospheric concentration of carbon dioxide [Houghton et al., *Chapter 1*, 2001].

Variations in the Climate system

The Sun's energy output varies by 0.1% over an 11 year cycle. A variation of 0.1% amounts to a variation of about 0.24 W m^{-2} at the Earth's surface. This is small compared to the estimated radiative forcing due to anthropogenic increases in CO_2 (2 to 2.5 W m^{-2}). However larger-amplitude solar cycles may exists and the combination of cycles may amplify the variation. [Reid, 2000].

Variations of the Earth's orbit cause changes in the seasonal and latitudinal distribution of solar energy. These changes play a strong role in controlling variations such as glacial and inter-glacial periods.

Human activities, such as the increased production of CO_2 by burning fossil fuels, change the climate. Increases in the concentration of CO_2 change the balance between incoming radiation from the sun and outgoing radiation from the earth, causing a warming in the lower atmosphere [Vaughan & Cracknell, 1994]. Changes in land use, such as changes in agriculture and irrigation, deforestation and urbanisation, alter the physical and biological properties of the land surface and therefore the climate system [Houghton et al., *Chapter 1*, 2001].

Changes in aerosol concentrations, from anthropogenic sources and from volcanic activity, effect the radiative balance, and therefore the climate. Aerosols scatter and absorb radiation and modify the radiative properties of clouds. [Houghton et al., *Technical Summary*, 2001]

Time scales of change

The climate system responds to changes of radiative forcing on different time scales. The large heat capacity of the ocean means that the transient response to a change in forcing may range from days (at the surface) to millennia (at depth). The atmosphere reacts rapidly to changes in forcing on a timescale of hours or days [Vaughan & Cracknell, 1994]. Sea ice has a high interannual variability [Laxon et al., 2003] whereas ice sheets react on timescales of millennia. Land processes react on timescales of days to months, and the biosphere reacts on timescales from hours to centuries [Vaughan & Cracknell, 1994]. As a consequence any change will alter the global hydrological cycle and atmospheric and oceanic circulation affecting weather patterns, regional temperatures and precipitation [Houghton et al., *Technical Summary,* 2001].

1.1.2) Modelling the climate system

To understand the climate and climate change we must study the fundamental physics of the processes involved in the climate system's behaviour. Problematically, analytical solutions of the equations describing the climate system are not feasible due to their non-linear nature and complicated boundary conditions. Therefore numerical techniques

are employed involving the use of simulation modelling. Climate models provide the only means of producing climate predictions.

Coupled (atmosphere-ocean), general-circulation models (CGCM) provide the best means of simulating the climate system, both globally and regionally. Models are designed on a grid, and the atmosphere and ocean sections may have different grid spacing and number of layers. Interaction between the atmosphere and ocean occurs at the sea surface, therefore the sea surface temperature and sea ice cover are key predictands in the model simulation. [Carson, 1999]

In 1988 the World Meteorological Organization (WMO) and the United Nations Environment Programme (UNEP) set up the Intergovernmental Panel on Climate Change (IPCC). The first report of the working group 1 (WG1) Houghton et al.,(1990) established a consensus on what appeared to be common to the results of most of the models. Further investigations have been conducted since then and we summarise the results below.

Based on current models

- Under the IPCC A2[1] scenario, for the end of the 21st century, the mean change in global average surface air temperature is 3.0°C (with a range of 1.3 to 4.5°C), and 2.2°C (with a range of 0.9 to 3.4°C) for the B2[2] scenario. The scenarios also indicate that in winter the warming for all high latitude northern regions exceeds the global mean warming in the model by 40% [Houghton et al., *Technical Summary*, 2001]. Figure 1.3 shows the predicted change in annual average surface air temperature from 1960-1990 to 2070-2100, due to a doubling of the atmospheric concentration of carbon dioxide over the 21st century, from the Hadley Centre's global, coupled, general-circulation model (HadCM3).

[1] Continuously increasing population and gradual economic growth and technological change, rapid CO_2 increase. [Houghton et al., *Technical Summary*, 2001].
[2] Continuously increasing population, focus on environmental protection, intermediate economic growth and slow technological change. Much slower CO_2 increase with values not yet doubled by 2100. [Houghton et al., *Technical Summary*, 2001].

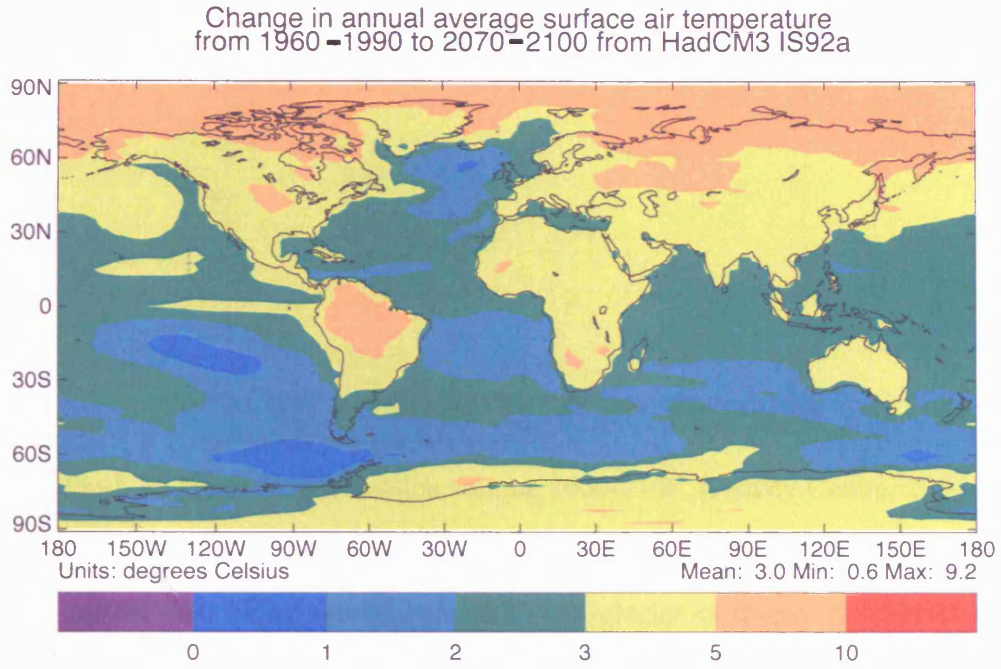

Hadley Centre for Climate Prediction and Research, The Met. Office

Figure 1.3: Change in the annual average surface air temperature between the late 20th Century and the late 21st Century. [Hadley Centre, 2004]

- A2 and B2 scenarios indicate that precipitation will increase in summer and winter over high latitudes. Winter increases are also seen over northern mid latitudes, tropical Africa and Antarctica. Summer increases in southern and eastern Asia. Australia, Central America and southern Africa show decreases in winter rainfall. [Houghton et al., *Technical Summary*, 2001]
- Glaciers and ice caps will continue to retreat along with Northern Hemisphere snow cover and sea ice. The Antarctic ice sheet is likely to increase due to increased precipitation, whereas the Greenland ice sheet is likely to decrease. [Houghton et al., *Technical Summary*, 2001]. Figure 1.4 shows the predicted decrease in sea ice volume between 2000 and 2100, from the Hadley Centre's CGCM, HadCM3 predicts a decrease of 60% in sea ice volume by the end of the 21st century.

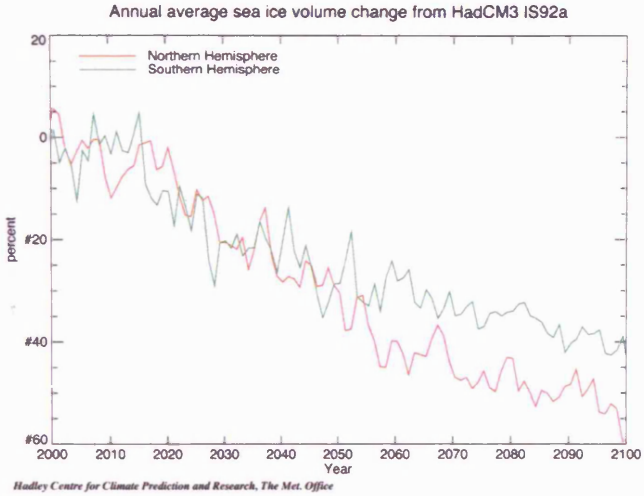

Figure 1.4: Predicted reduction in sea-ice volume 2000-2100. [Hadley Centre, 2004]

- Global average sea level rise from 1990 to 2100 lies in the range 0.11 to 0.77 m, due to: thermal expansion (0.11 to 0.43 m), glacier contribution (0.01 to 0.23 m), Greenland contribution (-0.02 to 0.09 m) and Antarctic contribution (-0.17 to 0.02 m) [Houghton et al., *Technical Summary*, 2001].

The differences between CGCMs and causes for uncertainty within each model, result from:

- The modelling of the physical processes. Uncertainty identifying the size and sign of feedback processes such as those due to changes in snow, ice, clouds and water, results in a climate sensitivity[3] lying in the range 1.3 to 4.5 K. If clouds and ice are kept fixed the range reduces to 2 to 3 K [Carson, 1999].
- The choice of grid spacing. This varies between models and can also effect the representation of variables within a grid cell. For example: The ocean component of the HadCM3 has a horizontal resolution of 1.25° by 1.25° on a latitude-longitude grid, and 20 vertical layers [Carson, 1999]. Sea-ice floes interact with each other, and the atmosphere, at scales smaller than the grid cells. Therefore the behaviour of sea-ice must be approximated or parameterised within the grid cell. Its behaviour cannot be modelled explicitly.
- The boundary conditions and their parameterisation.
- The assumptions made about the future.

[Vaughan & Cracknell, 1994]

[3] Climate sensitivity – the long-term change in globally averaged surface temperature following a doubling of carbon dioxide.

Summary

Climate sensitivity is important as both a model and a climate characteristic [Carson, 1999]. Results from CGCMs show that warming in the polar regions exceeds the global mean warming by 40% [Houghton et al., *Technical Summary*, 2001]. The largest increases in temperature are found over sea ice in winter and the smallest warming over sea ice in summer [Carson, 1999]. Changing the representation of clouds and ice in CGCMs results in a climate sensitivity lying in the range 1.3 to 4.5 K. Keeping them fixed reduces the range to 2 to 3 K. [Carson, 1999]. Knowledge of sea ice, its effect on the global climate and how to parameterise it within models, is therefore critical for the accurate prediction of future climate [Houghton et al., *Chapter 14*, 2001].

1.2) The influence of Arctic sea ice on the global climate

In section 1.1 the influence of the cryosphere on the global climate system was briefly described. In this section we take a detailed look at the influence of Arctic sea ice on the climate system.

1.2.1) Sea ice and the thermohaline circulation

The thermohaline circulation is the vertical, density driven ocean circulation that results from changes in the content of heat and/or salt. Changes in heat are caused by fluxes across the air-sea interface; changes in salinity are caused by the addition or removal of fresh water either through evaporation and precipitation or by the freezing and melting of ice. [Brown et al., 1998]. In the North Atlantic, warm saline water (North Atlantic Drift) is transported poleward due to differential heating between high and low latitudes [Clark et al., 2002]. This water circulates in the Norwegian and Greenland Seas, cools and sinks. The resulting deep water is highly saline due to the high salinity outflow from the Arctic Ocean that is a result of brine expulsion when sea ice is formed. The deep water in the Norwegian and Greenland basins outflows through the Denmark Strait and into the depths of the Atlantic (see figure 1.2). [Brown et al., 1998]. The circulation system can be altered or stopped by variations in the freshwater input from the Arctic Ocean. The largest export of fresh water from the Arctic Ocean is via sea ice leaving the Fram Strait into the Greenland Sea [Aagaard & Carmack, 1989]. Increased sea ice

export could alter or stop the Atlantic thermohaline circulation, therefore it is important to monitor and model the volume of sea ice leaving the Arctic accurately. Changes to the Atlantic thermohaline circulation as a result of changes to the hydrological cycle are thought to have caused abrupt climate changes [Clark et al., 2002]. Consequences of change to the Atlantic thermohaline circulation include a reduction in the heat transported to circum-Atlantic region, as well as altering the distribution of water masses in the world's oceans [Clark et al., 2002].

1.2.2) Sea ice and the radiation balance

Sea ice has an albedo ranging from 0.9 in winter after a snowfall to 0.4-0.55 in summer when melt ponds are present on the surface, whereas water's albedo is about 0.1 [Wadhams, 1996]. A decrease in sea ice area exposes more water, which results in an increase in heat absorption and hence warming. This effect creates a positive feedback loop as the warming causes a further reduction in sea ice area and results in a further warming of the atmosphere.

Heat transfer between the ocean and the atmosphere is affected by changes to sea ice thickness and lead fraction. The heat flux lost to the atmosphere from an open lead is two orders of magnitude larger than the heat flux through thick ice cover [Comiso et al., 2003].

1.2.3) Sea ice and greenhouse gas induced climate change

As shown in figure 1.3, many GCMs show a greater warming in the polar regions as a result of increased levels of CO_2. This response is connected with changes to the sea ice coverage [Lindsay, 2003]. Rind et al. (1995) examine the effects of sea ice on climate sensitivity. The temperature sensitivity of their GCM model without a sea ice response is 35-40% less than with a sea ice response, when running a double CO_2 simulation. Their follow up paper, Rind et al. (1997), shows that the key parameters controlling temperature sensitivity are sea ice coverage in the Southern Hemisphere, and sea ice thickness in the Northern Hemisphere. Model simulations show warming in the high latitude northern regions exceeds the global mean warming by 40% at the end of the 21st century [Houghton et al., *Technical Summary*, 2001]. Yet it is unknown if this

enhanced warming is due to real physical feedback processes or to unrealistic simulation of sea ice in the models [Lemke et al., 1997]. The accurate representation of sea ice within GCMs will reduce the uncertainty in climate sensitivity predictions.

1.3) Sea ice models

1.3.1) A general description

Sea ice models can be generally divided into two categories: Thermodynamic and the more sophisticated dynamic-thermodynamic models. Dynamic-thermodynamic sea ice models seem to be less sensitive to global warming and provide the fresh-water/ salt flux associated with the ice motion [Lemke et al., 1997]. On a regional scale sea ice controls the exchange of heat and moisture between the ocean and atmosphere. Here the coupling between the thermodynamic processes and the dynamic process, which modify the ice cover (i.e. the creation of ridges and leads), are important. On a global scale the ice albedo feedback mechanism, and sea ice extent must be well represented within models. Also on a global scale, changes in the transport of ice (and therefore fresh water) to the Greenland and Norwegian Seas could influence the thermohaline circulation, therefore ice transport should be well represented. These effects can only be analysed by climate models that contain realistic sea ice dynamics. [Lepparanta, 1998]

Dynamic-thermodynamic sea ice models are divided into four components:

- *Momentum balance* to describe sea ice drift. Air and water stresses, Coriolis force, internal ice stress, inertial forces and ocean currents are included in the momentum balance.
- *Ice thickness distribution* to describe the redistribution of ice thickness due to thermodynamic and dynamic effects.
- *Ice rheology* relating the ice stress to the ice deformation and ice thickness.
- *Thermodynamic model* which defines the growth and decay rates for different ice thicknesses. The thermodynamic model must also include ocean and atmosphere boundary layers to take into account heat storage and heat fluxes. [Lepparanta, 1998]

1.3.2) A review of sea ice models

Houghton et al. (*chapter 8*, 2001), examine fifteen sea ice simulations from GCMs as part of their Coupled Model Intercomparison Project (CMIP1). Only three of the models have a dynamics component (sea ice is moved by ocean currents), and only three include ice rheology. All the models have a thermodynamic component. The thermodynamic formulations are mostly based on simplified schemes assuming a linear temperature profile through the ice as opposed to a multi-layer heat transfer scheme. Leads are ignored in about half of the models. Some models also ignore the thermodynamic effects of snow on the ice.

Gregory et al., (2002) compare the HadCM3 Atmosphere Ocean General Circulation Model at the Hadley Centre for Climate Prediction simulated changes in Arctic sea ice to observations (HadCM2 was included in the comparison described above). The decrease in sea ice extent simulated by the model agrees closely with observations. The decline in sea ice thickness is consistent with other model results but does not agree with observations based on submarine data. Compared to the basin wide coverage of the remotely sensed ice extent data, these ice thickness measurements provide a poor understanding of changes in sea ice thickness, and Gregory et al., (2002) anticipate the use of satellite altimetry to estimate sea ice thickness.

Kreyscher et al., (2000), compare four sea ice models with different rheology schemes with each other and with observational data in order to identify the optimal sea ice rheology. Verification data for the model dynamics come from buoy drift data, providing trajectory information and drift speed. Ice concentration data are derived from space borne passive microwave sensors, and limited ice thickness observations from submarine upward-looking sonar (ULS) and from moored ULS. Their results show that a viscous-plastic model achieves the best fit and that the most sensitive sea ice properties, with respect to rheology, are the spatial pattern of ice thickness and ice drift velocity on different timescales, seasons and regions. They note that basin wide observations of sea ice thickness would provide the opportunity for new evaluations of sea ice rheologies.

Rothrock et al., (2003) compare annual mean sea ice thickness estimates from seven sea ice models, between 1951 and 1999 in figure 1.5.

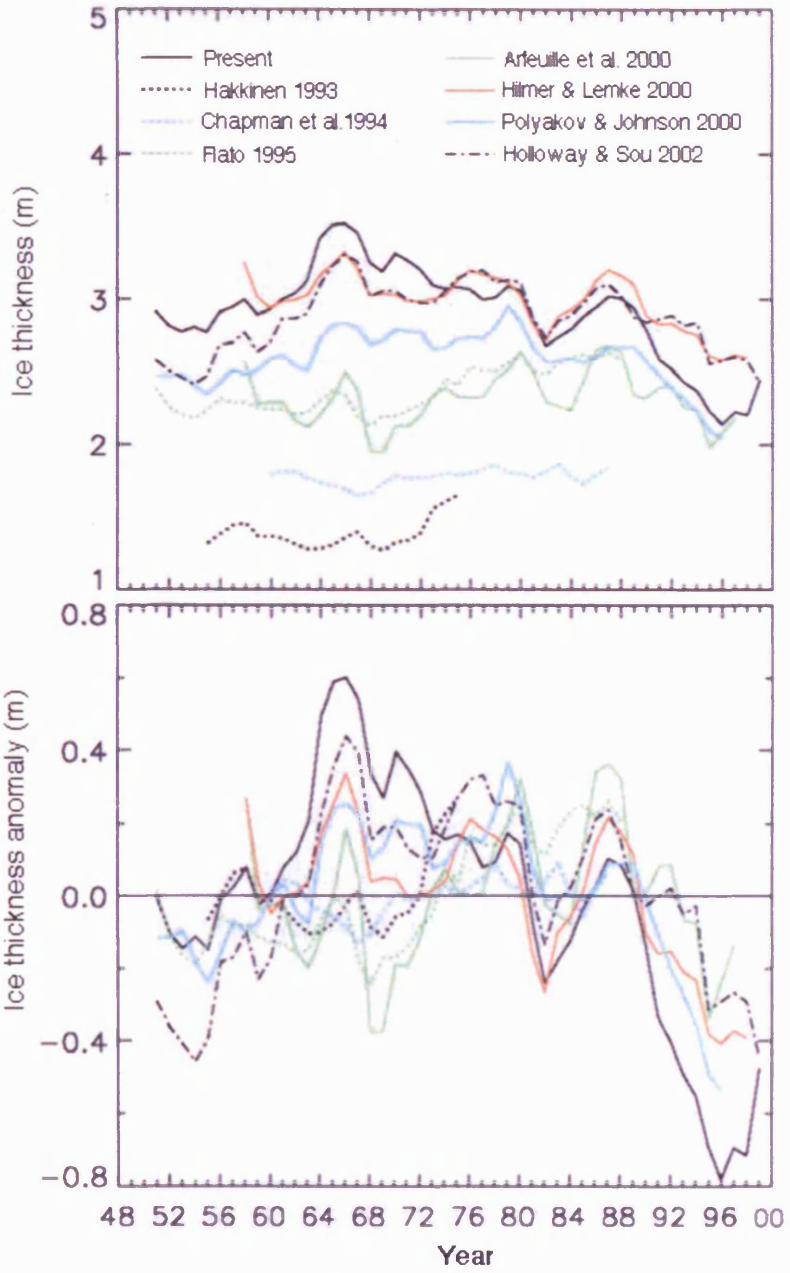

Figure 1.5: (Upper) Annual mean thickness from several ice models during the period 1951 to 1999. (Lower) The thickness anomaly as compared to the mean for each simulation.

Differences between model estimates arise from the way forcing data are incorporated into each model, the model physics, the radiative formulations and the treatment of albedo. [Rothrock et al., 2003]

The results shown by Rothrock et al. (2003) illustrate the need for model intercomparison studies and for the assessment of models by observational data and they advocate satellite altimeter data as a way of updating the sea ice thickness observational record.

Barry et al. (1993) review the Arctic sea-ice climate system with respect to both models and observations. They conclude that model simulations do not adequately address cloud microphysics and sea ice processes; and list the measurement of the surface energy budget and sea ice thickness as two of the most high priority data needs.

1.3.3) Sea ice thickness measurement requirements for model validation

In order to validate the sea ice component in GCMs we require, basin wide, systematic estimates of the average ice thickness at the same horizontal resolution as the GCM in question. The models reviewed in section 1.3.2. have grid cell areas of the order 10^3 km^2. For example; the ocean component of HadCM3 has a 1.25° × 1.25° horizontal resolution [Gordon et al., 2000], which equates to a horizontal resolution of approximately 3000 km^2 in the Arctic. The upper plot in figure 1.5 shows the annual mean ice thickness from eight models. The figure shows up to two metres difference between model predictions. From the figure it is clear that in order to determine which model best represents sea ice thickness, measurements of sea ice thickness need to be accurate to approximately 0.5 metres.

1.4) Observations of sea ice thickness

1.4.1) Sea ice and the Arctic Ocean

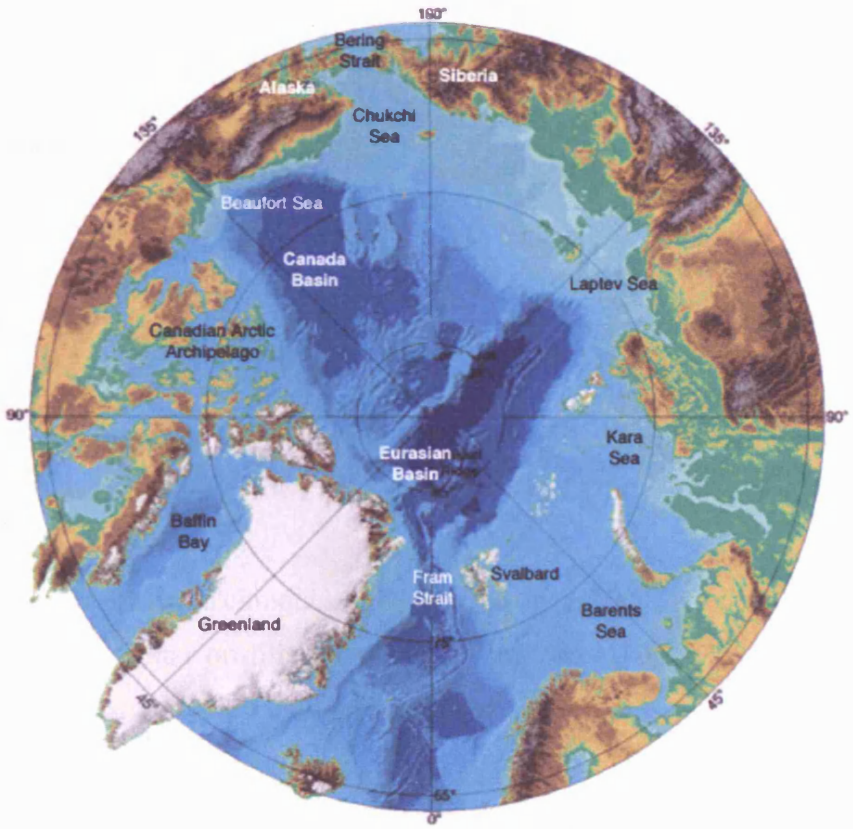

Figure 1.6: The Arctic Ocean. [adapted from Woods Hole Oceanographic Institution, 2004]

The sea ice has an areal coverage extending between 8×10^6 (approximately the area of the United States) and 15×10^6 km, depending on the time of year. Sea ice is divided into categories depending on its age. First Year (FY) ice is ice that has formed over one winter. It can reach thicknesses of 2m, depending on its local climate. Ice that survives the summer melt is known as Multi Year (MY) ice. MY ice continues to increase in thickness during the winter period in subsequent years until it reaches a steady state with a typical thickness of 3.5 to 4.5m. This final thickness may comprise of 10 or more annual layers as ice is ablated away each summer. However, ice thickness is not completely controlled by thermodynamics. The dynamic nature of the ice pack, due to the non-uniform forces exerted by winds and currents, leads to the build up of stresses within the ice. This can result in the formation of leads (open water) within the ice pack.

Leads vary in width from a few meters to several kilometres and in length from a few hundred meters to several hundred kilometres. Ice that is thicker than the steady state MY ice floe expected maximum is also observed. Thicker ice forms by ridging (the closing of leads, which generally results in broken ice piling up and forming pressure ridges). Many small ridges form and occasionally sail and keel heights can reach up to 13 and 47 m respectively. The area between the north coast of Greenland, the Canadian Arctic Islands and the south coast of the Beaufort Sea contains a particularly heavily deformed ice. [Weeks, 2001]

1.4.2) Arctic sea ice thickness observations

In this section we summarise the various in-situ and remote sensing techniques used for sea ice thickness monitoring.

There are five common techniques used for the measurement of sea ice thickness: Drilling, submarine sonar profiling, moored upward sonars, airborne laser profilometry and airborne electromagnetic techniques [Wadhams, 2000].

Drilling provided the first measurements of sea ice thickness in the Arctic. The technique lends itself as a good validation tool for measuring ice thickness in a specific area, but does not give the ice thickness distribution over a region. [Wadhams, 2000]. Measuring sea ice thickness via drilling may also create a bias as it is only possible to drill through ice floes with a certain physical structure [Strass, 1998]. Because of the harsh nature of the Arctic climate it is only practical to drill at certain times of year and in certain locations. Rothrock (1986) examines the error of commission on estimates of mean ice thickness derived from drilling. He concludes that the error of commission is negligible.

In 1958, Nautilus was the first submarine to venture to the North Pole [Wadhams, 2000]. Since then data, collected largely on nuclear submarine cruises for military operations, have been declassified, yielding data on sea-ice characteristics such as ice draught (from which ice thickness can be calculated), concentration data and pressure ridge characteristics. More recently the Scientific Ice Expeditions (SCICEX) programme has provided additional data allowing comparison between the present day

ice cover and some of the historic cruises. Figure 1.7 shows the available submarine draught data over the Arctic Ocean from the National Snow and Ice Data Centre.

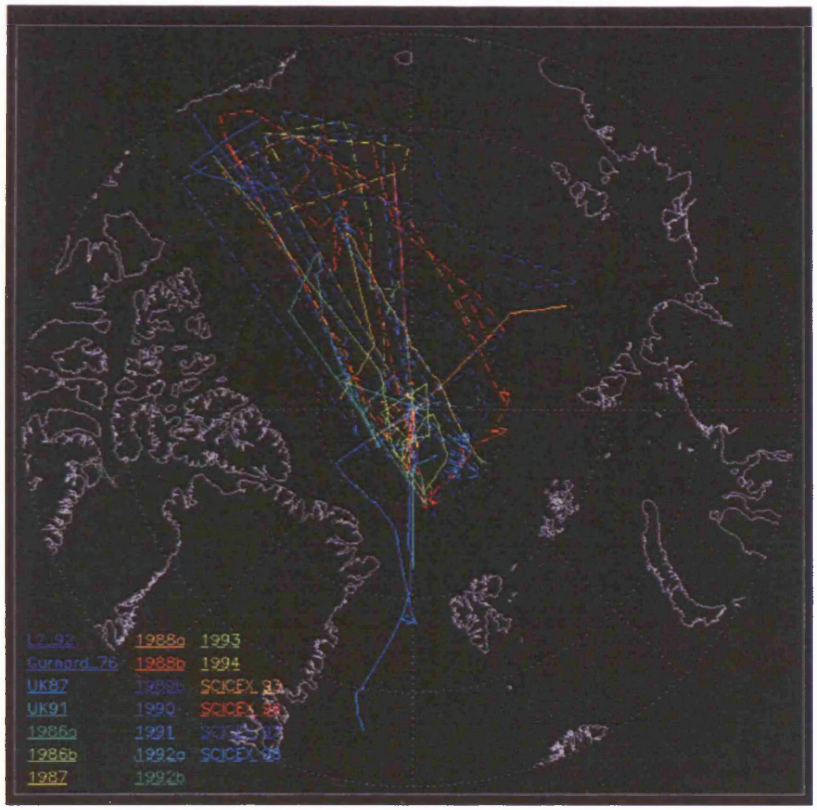

Figure 1.7: Map showing the locations of the submarine cruises available from the National Snow and Ice Data Centre [National Snow and Ice Data Centre, 1998].

Practical considerations prevent submarines surveying sea-ice over the Arctic continental shelves because the water is too shallow [Melling & Riedel, 1995], nor does this technique allow a systematic time series of ice draught at a point in space. Although there have been about 63 submarine cruises under sea ice by the U.S. Navy, many of the resulting data and locations of the tracks are classified [Rothrock et al., 2003]. The statistical reliability of data collected from submarine cruises is affected by two aspects, the first instrumental and the second results from sampling variability. The instrumental problem is caused by the fact that the first sonar echo received does not necessarily come from the point directly above the sonar beam, but from the point illuminated by the cone of the beam. This results in a positive bias in the record [Wadhams, 1997]. Correction is possible only if the beam is narrow in the athwartship direction and has significant beam width only in the fore-and-aft direction [Wadhams, 1981]. Sensor

depth as well as beam orientation determine the bias so it is important to know that the submarine is kept at a constant depth throughout the survey, in some of the older cruises this is not always possible [Wadhams, 1997].The sampling problem arises when computing the mean ice draught over a finite region. The mean is calculated through measuring a finite number of points within the region, which will contain a finite number of leads, ridges and stretches of first and multi-year ice each with a finite spatial size. Re-sampling of the same area along a slightly different track will yield a slightly different value of the mean draught [Wadhams, 1997]. Estimates of the error on measurements of sea ice draught vary between cruises. For example Wadhams *et al.* (1985) estimate the error of commission to be ± 0.15 m. Bourke & McLaren (1992) give two estimates of the total error (commission plus omission), ± 0.06 m ± 0.15 m and Rothrock *et al.* (1999) estimate the total error on ice draught measurements, acquired between 1958 and 1997, to be ± 0.3 m. Bourke and Paquette (1989) show that ice thickness can be estimated from ice draught by multiplying the draught by a conversion constant equal to 1.1 and that the standard deviation of the predicted ice thickness is 0.13 m. Assuming there is no error on their draught measurements (made by drilling), a typical ice draft of 2.8 m, and by propagation of errors, we estimate the conversion constant error to be ± 0.05 m. Therefore, by taking Wadhams *et al.*'s (1985) estimate of the error on ice draught (0.15 m), and assuming a typical ice thickness of 3 m, and by propagation of errors, we estimate an error of ± 0.21 m on ice thickness estimates derived from submarine sonar measurements of ice draught. However, most articles describing submarine data deal with ice draught without out applying a correction for thickness.

Moored Upward Looking Sonars (ULS) provide a time series of the thickness distribution at a fixed location in any water depth [Melling & Riedel, 1995]. ULS operate by transmitting pulses of sound towards the sea surface, measuring the two way travel time and converting this time to distance. The ice thickness calculated from the sonars is a point measurement with a relatively high temporal resolution, approximately every three hours in the polar regions. However, the sonars provide a limited spatial coverage. When calculating ice draught from ULS, variations in the sound speed and the density along the path of the pulse are estimated using an empirical model. Variations in surface air pressure can also affect the draught estimation. Therefore, time

series of air pressure fields are used to correct the data. The echo can be generated by any interface between the ULS and the ice, which can also cause problems when calculating the ice draught. After processing, the residual total error in ice draught can be reduced to 4 cm, compared to an initial error of almost 90 cm [Strass, 1998]. Melling and Riedel (1995) give the accuracy of USL derived ice draft measurements as ± 5 cm. Using Melling and Riedel's (1993) error estimate and Bourke and Paquette's (1989) conversion from ice draught to ice thickness, and propagation of errors, we estimate an error of ± 0.15 m in ice thickness derived from moored ULS measurements of ice draught.

Airborne laser profilometry can provide a detailed picture of the spatial distribution of surface roughness and surface elevation. For the data to be useful the vertical motion of the aircraft must be removed which results in an error of about ±20cm [Comiso et al., 1991]. Comiso et al. (1991) show a quantitative relationship between ice draught, from submarine measurements and ice elevation, from airborne laser measurements. This relationship offers the potential to deduce ice thickness from laser measurements alone.

Hvidegaard and Forsberg (2002), present a method to derive sea ice freeboard heights using a combination of airborne laser altimetry and a precise geoid model. To compute the freeboard they subtract the laser range and the geoid height from the height of the aircraft determined by GPS. They average the data from 50 Hz to 10 Hz to reduce measurement noise. The position of the measurement point is then calculated from 1 Hz GPS data by linear interpolation. They note that the elevation bias in their data is partly due to GPS errors (i.e. errors in locating the measurement points) along with possible laser offsets and misalignments as well as errors in the geoid and dynamic sea surface topography. The bias is removed by assuming that the errors have a relatively long wavelength and assuming that the sea surface corresponds to the lowest elevation values. Freeboard heights are then converted to ice thickness by multiplying by a constant freeboard to thickness ratio that is based on snow depth, ice density and the density of salt water. The estimated accuracy of this technique is ± 15 cm for the freeboard estimation and ± 1 m for the thickness estimation.

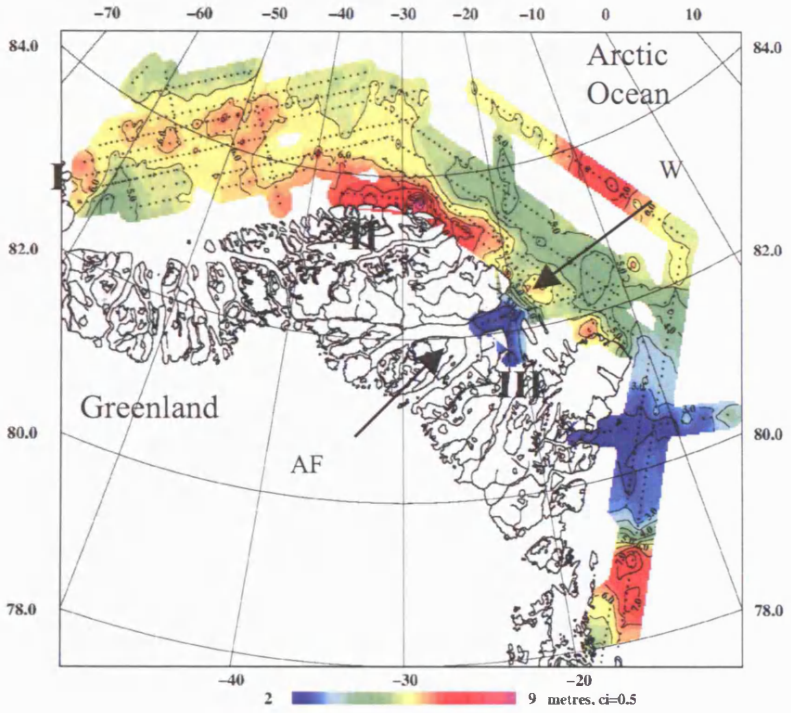

Figure 1.8: Mean ice thickness for mid to late June 1998 [Hvidegaard and Forsberg, 2002].

The use of the term freeboard is somewhat misleading as it implies that the laser measures the elevation of the ice above the water, when it in-truth measures the elevation of the ice and snow layer above the water. Because the snow depth is variable the use of a constant conversion ratio introduces a large amount of uncertainty into the thickness estimation. The high thickness values to the north of Greenland shown in figure 1.8 are likely to be due to high snow depths rather than thick ice [Hvidegaard and Forsberg, 2002].

Airborne electromagnetic techniques were developed from technology used for mineral prospecting during the late 1960s. The methods involves towing a sensor platform, or bird, from which EM fields are transmitted and received, from a helicopter. The EM field transmitted from the bird induces a secondary EM field in the water beneath the ice, which is detected at the receiver allowing the distance between the bird and the water to be estimated [Rossiter & Holladay, 1994]. When combined with a laser profilometer to measure the depth of the snow/ice air interface, the technique can provide the absolute thickness of the ice plus snow in local surveys [Wadhams, 2000]. The footprint of the EM system has a diameter approximately equal to the bird's height

(15 to 30 m), therefore when rapid lateral changes in ice thickness occur (e.g. near ridges) the peak ice thickness tends to be underestimated [Rossiter & Holladay, 1994]. The nature of the apparatus used for this technique, and the low altitude required to achieve a suitably small footprint means that rapid coverage of large areas is unfeasible. The method works over ice greater than one meter thick and less than 12 meters thick, so is only suitable for surveying certain regions [Wadhams, 2000]. Kovacs and Holladay (1990) estimate that airborne electromagnetic techniques are capable of estimating ice thickness to within 10% of a drill hole measured value. Taking the error on the drill hole value of ice thickness to be zero and a typical ice thickness of 3 m, ice thickness measurements from airborne electromagnetic techniques are accurate to ± 0.3 m. Man-portable electromagnetic induction sounding instruments are capable of estimating undeformed sea ice thickness to within about 5% of a drill hole measured thickness [Kovacs et al., 1996]. Eicken et al., (2000), estimate that their ice thickness measurements derived from man-portable EM induction techniques are accurate to ± 5 cm for 2 m thick level ice.

Table 1.1 summarises the various techniques used for sea ice thickness observations and gives estimates of the errors associated with the measurement, where σ_c is the error of commission (i.e. the measurement error) and σ_t is the error in ice thickness which includes some errors in omission due to the uncertainty in the ratio between ice draft and ice thickness.

Technique	Measures	Advantages	Disadvantages	Error estimates
Drilling	• Ice thickness	• Good validation tool • Provides an absolute measure of thickness	• Does not provide thickness distribution • Only drill through certain flows • Limited to certain months	• σ_c=Negligible • σ_t=Negligible

Submarine Profiling	• Ice draught	• Can provide an ice draught profile along large transects • Data is available since the 1950s	• Data access is limited • Cannot survey over the continental shelf • Instrumental bias • Sampling problems	• σ_c=0.15 [Wadhams *et al.*(1985)] • σ_t=0.21 m
ULS	• Ice draught	• High temporal resolution	• Limited spatial coverage	• σ_c=0.05 m • σ_t=0.15 m
Airborne Laser	• Elevation of the ice and the snow above the water	• Provides rapid coverage of large areas • Provides a detailed picture of ice + snow elevation	• Cannot measure through cloud	• σ_c=0.15 m • σ_t=1 m
Electromagnetic Techniques	• Distance between the sensor and the bottom of the ice	• When combined with laser profiling measures the ice + snow thickness	• Cannot provide rapid coverage of large areas • Only suitable for surveying certain regions	• σ_c=10% drill hole • σ_t=0.3 m

Table 1.1: Summary of the advantages and disadvantages of each method of measuring sea ice thickness.

Although the techniques described above provide accurate estimates of sea ice thickness, an additional large omission error is introduced by under-sampling the temporal and spatial variability of ice thickness. Without detailed knowledge of the temporal and spatial covariance scales of sea ice thickness (which does not currently exist) it is impossible to estimate the error of omission of these measurements in providing an estimate of, for example, average sea ice thickness across the whole Arctic.

1.4.3) Knowledge of Arctic sea ice thickness and evidence for change

Basin wide maps of Arctic sea ice draught have been produced by submarine sonar profiling since the early 1970's [Bourke & McLaren, 1992]. More recently Bourke and McLaren (1992) have updated the data set to include contour maps of the mean ice draught, its standard deviation, the mean keel draught and the spatial frequency of ice keels for summer and winter.

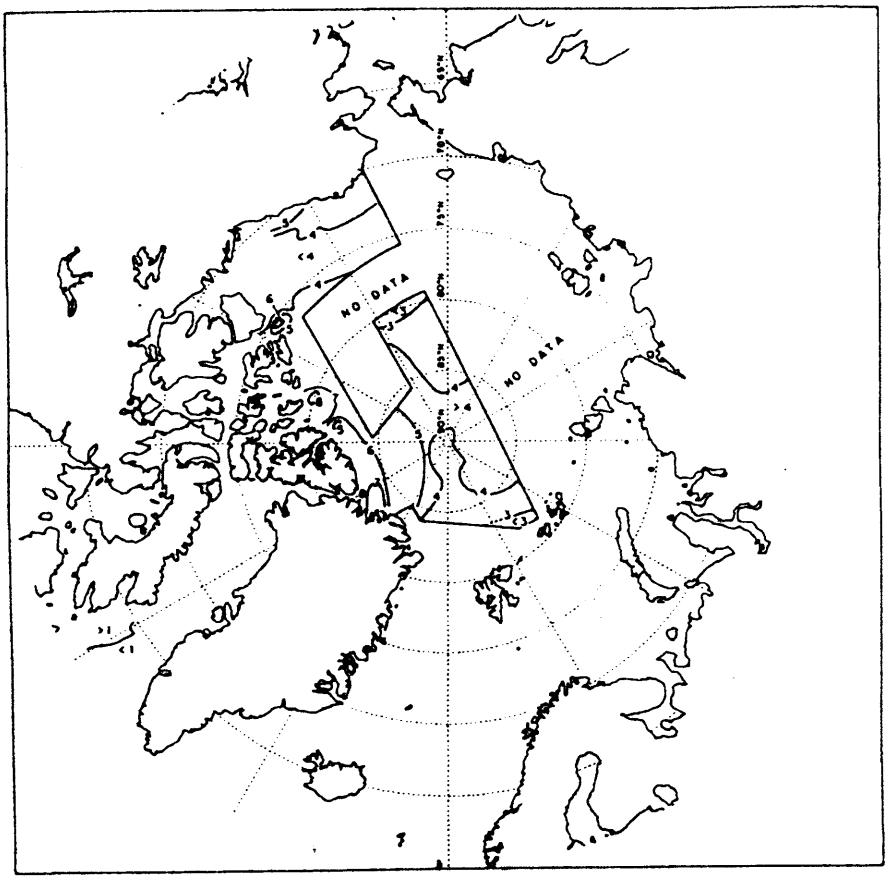

Figure 1.9: Contours of the mean ice draught (meters) for winter [Bourke & McLaren, 1992]

Data were taken from 12 submarine cruises, covering the Alaskan, Canadian and central Arctic regions, recorded between 1958 and 1987. Two estimates of the accuracy of the mean draught averaged over 50 km segments are given, the larger uncertainty is ± 15 cm. Monthly measurements or the quantification of the spatial and temporal variability of the ice draught would improve the contour plots. [Bourke & McLaren, 1992]

Regional studies of ice thickness have been conducted using moored ULS. Vinje et al. (1998) report the findings from a time series of ULS data, between 1990 and 1996, moored in the Fram Strait at 75°N. The modal ice thickness has a maximum of 3.15 m (May) and a minimum of 2.43 m (September). Melling and Riedel (1995) report a mean ice thickness of the order of 3 m, across 348 km of sea ice in the Beaufort Sea.

The majority of evidence for change in sea ice thickness comes from submarine sonar data. McLaren (1989) compares two coincident submarine tracks from August 1958 and August 1970. The tracks run from the Canada Basin, via the North Pole, to the Eurasian Basin. The mean draught in 1958 in the Canada Basin is significantly higher than the mean draught recorded in 1970, with values of 3.08 m and 2.39 m respectively. No major changes in the mean draught were found in the transpolar or Eurasian sections of the track.

Wadhams (1990) compares tracks from two nearly coincident submarine tracks from May 1987 and October 1976. The tracks encompass a triangular region of 3000,000 km^2, between the north of Greenland and the North Pole. The mean draught in 1976 is 5.34 m and is 4.55 m in 1987, a decrease in mean ice draught of 15% over the entire area. The decrease is concentrated between 30° and 50° west and south of 88° north. In the eastern Arctic there are no significant differences in ice thickness between the two years.

McLaren et al. (1992) analyse submarine measurements of sea ice draught around the North Pole from six cruises occurring in late April/early May, between 1997 and 1990. They find that the average ice draught between the late 1970s and the late 1980s decreased by 0.65 m, a thinning of 15%. However, statistical testing of the data set

reveals that there is a 20% probability that the sub sample means will differ by chance by 0.65 m. They conclude that the data set does not provide evidence of a trend in the decrease of sea ice thickness.

Rothrock et al. (1999) compare submarine derived ice draught data between 1993 and 1997, with similar data acquired between 1958 and 1976.

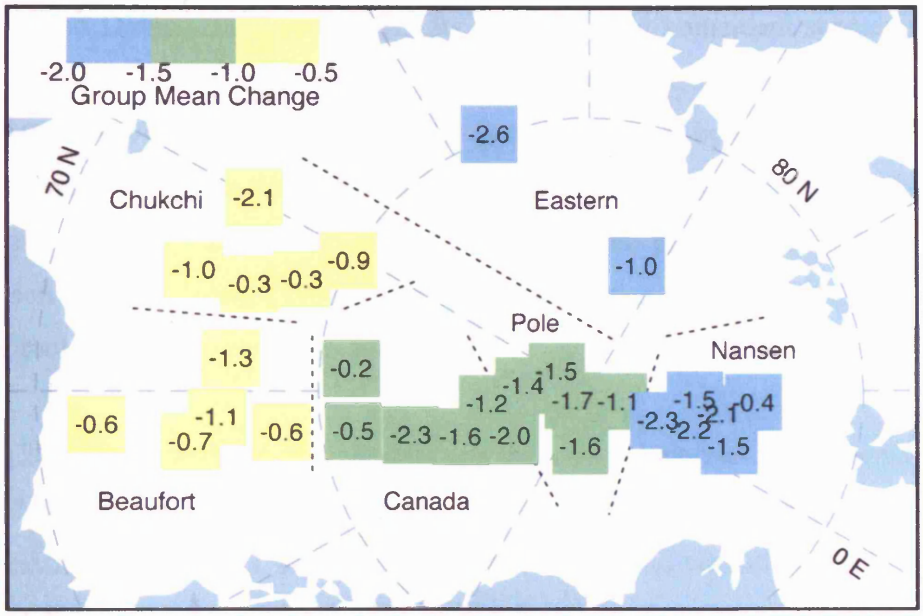

Figure 1.10: Changes in the mean draught from 1958-1976 to the 1990s. The change at each track crossing is shown numerically. The crossings within each regional group are given the same shading, equivalent to their group mean. [Rothrock et al., 1999]

Rothrock and his colleagues compute that the mean draught has decreased by 1.3 m (40%) over the time period. If the decrease in mean draught is constant this is equivalent to a decrease of 15% per decade. Figure 1.10 shows a pattern of regional change with central and eastern areas of the Arctic displaying the greatest decrease in draught. It is important to note that the data used for this investigation were measured in two periods: the first phase between 1958 and 1976, with cruises in different months; USS Nautilus 1958 (August), USS Seadragon 1960 (August), USS Skate 1962 (July), USS Queenfish 1970 (August) and the HMS Sovereign 1976 (October). The second phase occurred between 1993 and 1997 and uses data from the SCICEX cruises which all occurred in September. The USS Nautilus 1958 and the HMS Sovereign 1976 used a

widebeam sonar where as the other submarines used narrowbeam sonars[4], this is corrected by multiplying the draughts by a factor of 0.84. Draught data from the earlier cruises are normalised to September using a model, to allow comparison between the data sets. Therefore the results are only as good as the assumptions inherent in the model.

Wadhams and Davis (2000) present results from two near coincident submarine tracks in the Eurasian Basin. The cruises took place in September-October 1976, and September 1996. A seasonal correction (the same as that used by Rothrock et al. (1999)) is used to standardise the data. Comparisons of the sea ice draught profiles from each year show a decline in sea ice draught of 41% over the 20 year period. Further comparison with Wadhams (1990) leads to the speculation that a substantial part of the thinning took place between 1976 and 1986.

Winsor (2001) compares ice draught data sets from six submarine cruises between 1991 and 1997 (including the SCICEX cruises). His results show no trend towards thinning during the 1990s. The data sets are subjected to a seasonal correction as the SCICEX cruises took place in September 1993, 1996 and 1997 and the other cruises in April or May. A seasonal ice growth of 0.9 m is added to the SCICEX data, based on a coupled ice-ocean model.

[4] Widebeam sonars cannot distinguish between peaks and troughs in the ice and therefore returns an echo that only records the draught at the peaks and hence could overestimate the mean ice draught. Narrowbeam sonars are able to pick out both peaks and troughs.

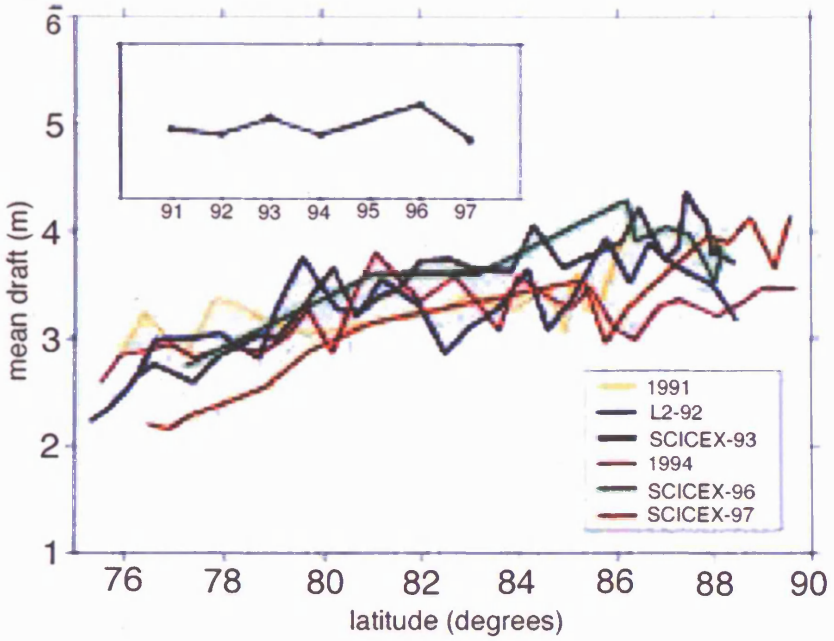

Figure 1.11: Mean ice draught over the central Arctic Basin from the Beaufort Sea to the North Pole. The inserted figure shows the yearly mean draught based on all transects. [Winsor, 2001]

Tucker III et al. (2001) compare submarine ice draught measurements in a narrow band from offshore Alaska to the North Pole. Data from nine cruises between 1976 and 1994, occurring in April (with the exception of one that occurred in May), show that the ice in the western Arctic was significantly thicker in 1976, 1986 and 1987, than in the 1990s. A large fraction of ridged ice (> 3,5 m) is responsible for the large mean draughts in the 1980s. In the 1990s the bulk of the distribution of ice draughts was between 0.3 and 3.5 m, resulting in a lower mean. Data at the North Pole shows no similar trend.

A confused picture emerges from these studies. Table 1.2 summarises the finding of the papers described above. The authors only agree on one area, the Eurasian Basin.

Authors	Year	Western Arctic	Pole	Eurasian Basin	Eastern Arctic
McLaren (1989)	1958 – 1978	Thinning (69 cm)	No Thinning	N/A	N/A
Wadhams (1990)	1976 - 1987	N/A	N/A	Thinning (78.8 cm)	No Thinning
McLaren et al. (1992)	Late 1970s to late 1980s	N/A	Thinning (65 cm) – but dismiss results	N/A	N/A
Rothrock et al. (1999)	1958 - 1997	Thinning (50 – 100 cm)	Thinning (100 – 150 cm)	Thinning (100 – 150 cm)	Thinning (150 – 200 cm)
Wadhams & Davis (2000)	1976 - 1996	N/A	N/A	Thinning (208 cm)	N/A
Winsor (2001)	1991 - 1997	No Thinning	No Thinning	N/A	N/A
Tucker III et al. (2001)	1976 - 1994	Thinning (150 cm)	No Thinning	N/A	N/A

Table 1.2: Summary of findings from investigations into changes in sea ice draught.

The results reported above do not provide a consistent trend in sea ice thickness. Differences in the findings of these papers could be due to some of the corrections made to the data, such as seasonal corrections for ice growth and instrument corrections. However, differences are also due to the differences in spatial and temporal sampling of the data. Before applying any weight to these findings we need to address the question of how the different spatial and temporal samplings effect the results. In order to determine changes in sea ice thickness analysis by season and region, of a systematically collected, basin wide data set, must be performed [McLaren et al., 1990].

1.4.4) Sea ice thickness measurement requirements for trend analysis

The evidence presented above highlights the need for basin wide, systematic measurements of sea ice thickness in order to differentiate between trends in sea ice thickness and trends due to differences in temporal and spatial sampling. In order to detect Rothrock *et al's* (1999) observed decrease in sea ice thickness of 15% per decade, a decrease of approximately four cm per year must be detected (taking the average sea ice thickness to be 2.7 m [Laxon *et al.*, 2003]).

1.5) Sea ice thickness from satellite radar altimetry

1.5.1) Method

Recent developments in the monitoring of sea ice via satellite radar altimetry have been able to provide basin wide, systematically collected, measurements of sea ice thickness. Sea ice thickness is computed by measuring the elevation of the ice and the elevation of the water, then subtracting the first measurement from the second to provide an estimate of the ice freeboard (f_i).

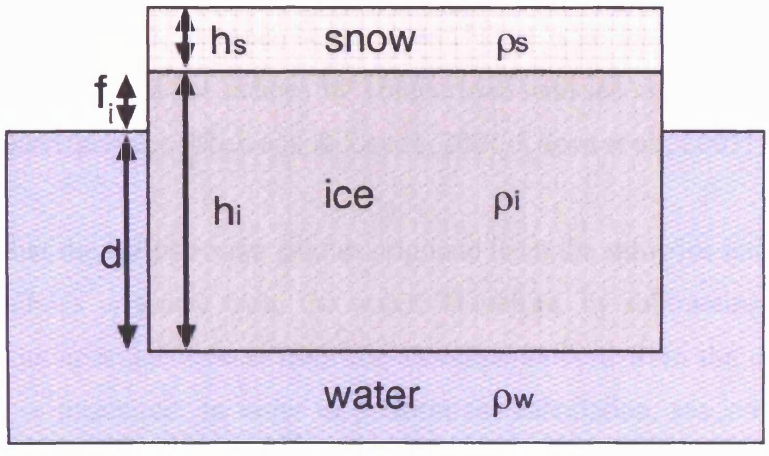

Figure 1.12: The snow/sea ice system. f_i is the ice freeboard, d the ice draught. h_i, ρ_i and h_s, ρ_s are the thickness' and densities of the snow and ice respectively. ρ_w is the density of the water. ρ_i and ρ_w are constants and have values of 915.1 kg m^{-3} and 1023.9 kg m^{-3} repectively [Laxon et al. 2003]. A monthly climatology from Warren et al. (1999) for snow depth and density is used.

f_i is converted to sea ice thickness, assuming hydrostatic equilibrium, using equation 1.1.

$$h_i = f_i \frac{\rho_w}{(\rho_w - \rho_i)} + \frac{h_s \rho_s}{(\rho_w - \rho_i)} \tag{1.1}$$

The radar altimeter data sets used for this analysis were taken from ERS-1 and 2. ERS-1 was launched in July 1991 and has a latitude coverage of ±81.5° and an altitude between 782 and 785 km, ERS-2 was launched in April 1995, into the same orbital plane, its location one day behind that of ERS-1. Both satellites carried a Ku band radar altimeter. Precise satellite radar altimetry measurements of sea ice freeboard and sea surface height are obtained by reprocessing the return echoes [Laxon, 1994] and applying corrections to orbits, tides and atmospheric effects [Cudlip & Milnes, 1994]. Differentiation between open ocean and sea ice is based to the fact that different echoes are received from each type of surface. Diffuse echoes occur over the open ocean caused by disturbance of the water by wind, or from the surface of consolidated ice (first or multi-year) whereas specular echoes occur over relatively smooth surfaces at, or a few cm above, sea level e.g. from leads or thin ice. Areas that contain quantities of both ice and water produce complex echoes, which are subsequently discarded. Diffuse echoes can also occur over the open ocean, even if there is no sea ice present. These can be distinguished from sea ice echoes by comparison with ice concentration data from passive microwave sensors. [Peacock & Laxon, 2004, Laxon et al., 2003]

It is assumed that the diffuse radar echoes originate from the snow/ice interface and that the specular echoes originate from the water. Therefore, by subtracting the elevation derived from the specular echoes from the elevation derived from the diffuse echoes, the quantity f_i is measured. In order to perform the calculation, sea surface elevation measurements are averaged along each ground track over a four year period in order to compute the mean sea surface [Peacock & Laxon, 2004]. The mean sea surface is subtracted from the ice elevations and sea surface elevations, resulting in an ice level anomaly (ILA) and a sea level anomaly (SLA). The local SLA to the ILA is estimated by performing a linear least squares fit to all the SLA estimates within ± 50 km of the ILA measurement. f_i is given by equation 1.2:

$$f_i = h_{ILA} - \bar{h}_{SLA} \tag{1.2}$$

where h_{ILA} is the observed ILA and $\bar{h}_{SLA}$ is the local SLA.

Figure 1.13 shows the average winter Arctic sea ice thickness from October 1993 to March 2001, derived from ERS radar altimetry.

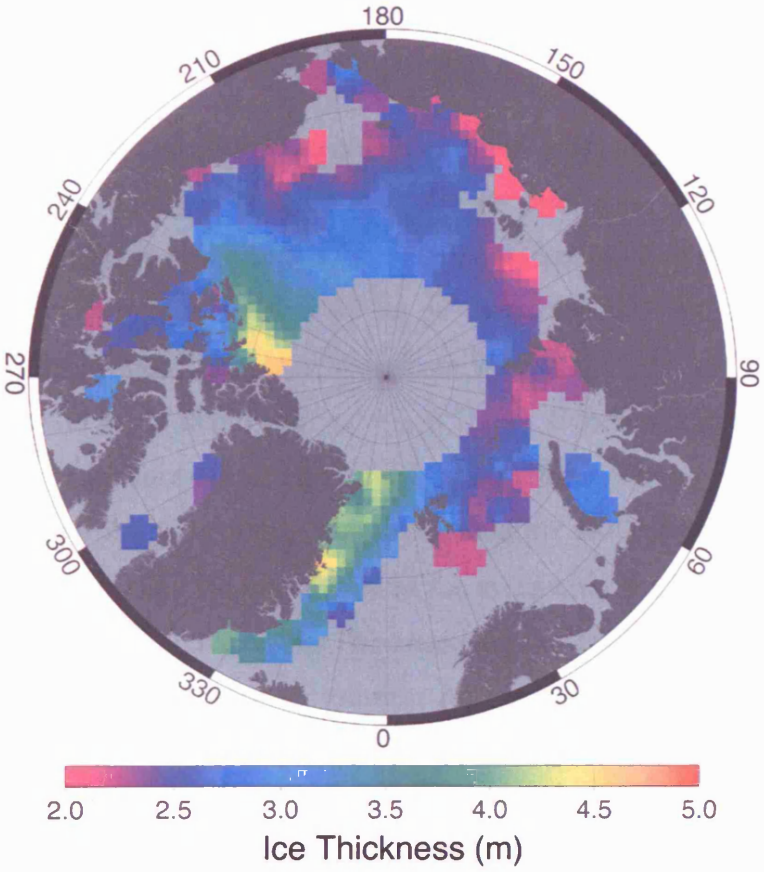

Figure 1.13: Average winter (October to March) Arctic sea ice thickness from October 1993 to March 2001. [Laxon et al., 2003]

1.5.2) Accuracy

To first order, the variance in ice thickness (ε_r^2) is given by equation 1.3:

$$\varepsilon_r^2 = \varepsilon_{fi}^2\left(\frac{\rho_w}{(\rho_w-\rho_i)}\right)^2 + \varepsilon_{hs}^2\left(\frac{\rho_s}{(\rho_w-\rho_i)}\right)^2 + \varepsilon_{\rho s}^2\left(\frac{h_s}{(\rho_w-\rho_i)}\right)^2$$
$$+\varepsilon_{\rho w}^2\left(\frac{f_i}{(\rho_w-\rho_i)} - \frac{f_i\rho_w}{(\rho_w-\rho_i)^2} - \frac{h_s\rho_s}{(\rho_w-\rho_i)^2}\right)^2 + \varepsilon_{\rho i}^2\left(\frac{f_i\rho_w}{(\rho_w-\rho_i)^2} + \frac{h_s\rho_s}{(\rho_w-\rho_i)^2}\right)^2 \quad (1.3)$$

where $\varepsilon_{\rho i}$, $\varepsilon_{\rho w}$, $\varepsilon_{\rho s}$, ε_{hs} and ε_{fi} are the uncertainties in the density of sea ice, sea water and snow, and the uncertainties in the snow height and radar measured freeboard respectively. From Laxon *et al.*, (2003), we take the uncertainties in the densities of sea ice and water to be ± 5 kg m^{-3} and ± 0.5 kg m^{-3} respectively. We take the root mean square (RMS) error in snow height for May[5] from Warren *et al.*, (1999) for our estimate in the uncertainty in snow depth (i.e. ε_{hs} = ± 0.11 m). Combining our estimate of ε_{hs} with the RMS error in snow water equivalent for May from Warren *et al.*, (1999), and by propagation of errors, we estimate that the uncertainty in the density of snow is ± 3 kg m^{-3}. Finally, we estimate the uncertainty in the measurement of ice freeboard ε_{fi} = ± 0.03 m, from equation 4.2 (chapter 4). The uncertainty is calculated assuming that 100 echoes are included in the freeboard estimate (this is typical of a freeboard estimate from ERS [S. Laxon, personal communication]). Using the values given above and assuming that f_i=0.2 m and h_s=0.3 m (an ice thickness of 2.76 m), we estimate that the error (ε_r) in ice thickness, calculated using radar altimetry, is ± 0.45 m.

1.5.3) Uncertainties in the computation of sea ice thickness from radar altimetry

The snow load uncertainty

Monthly values of snow depth and density are taken from the climatology produced by Warren *et al.*, (1999). Measurements were made from 31 drifting stations between 1954 and 1991, and monthly mean values of snow depth and density are computed across the

[5] The data discussed in this thesis were collected during May.

Arctic ocean. The spatial and temporal variation of the snow depth and density is not well known. On an Arctic scale the departure of the snow loading from the climatology appear quite small, however its effect at shorter scales is potentially quite large [Wingham et al., *chapter 4*, 2001].

The density uncertainty

Uncertainty in the density of sea water and sea ice introduce an error into the ice thickness estimation. The variation in the density of sea water is relatively small and therefore has little effect on the thickness measurement. The density of sea ice varies according to season, and at the end of the melt season variability in sea ice density can introduce a variability of 40 cm into the ice thickness estimate. [Wingham et al., *chapter 4*, 2001]

The retrieval error

The ice surface is not smooth. How this affects the estimation of ice elevation depends on the scale of the roughness. If there are many corrugations within the radar footprint the echo will be sensitive to their average properties. However, if there is a large scale structure within the footprint, such as a ridge, the effect on the echo will be complicated and result in a biased elevation estimate. [Wingham et al., *chapter 4*, 2001]

As stated in section 1.5.1, it is assumed that the diffuse radar echo originates from the snow/ice interface. This assumption is based on laboratory measurements by Beaven et al. (1995) and Lytle et al. (1993) and on the large scale comparison with submarine sonar measurements shown in figure 1.14. However there are no direct observations to confirm this assumption [Wingham et al., *chapter 4*, 2001]. If the radar return does not originate from the snow/ice interface then equation 1.1 is incorrect and ice thickness estimates will be too large.

Effect of finite radar bandwidth

The freeboard measurement is made by subtracting the elevation of the sea surface from the elevation of the ice surface. As described in section 1.5.1, the shape of the return

from each of these surfaces is very different therefore the effect of the limited resolution of the system (finite radar bandwidth) on the echoes will be different. This will result in a bias in the elevation difference. [Wingham et al., *chapter 4*, 2001]

Propagation and tidal errors

The importance of propagation and tidal errors depends on how the calculation of f_i is performed. Wingham et al. (2001) provide details of the different calculation methods and their associated errors.

The launch of Envisat in 2002, which carries an improved radar altimeter to those flown on board the ERS satellites and has been launched into the same orbital plane, will allow comparisons of data over the Arctic from the 1990s to the present. Therefore it is vital that the uncertainties in the computation of sea ice thickness are addressed in order to use these data sets to their full potential. CryoSat, due to be launched in 2005, carries an enhanced Ku band radar altimeter and will provide a latitudinal coverage of up to 88°. Its objective, in terms of sea ice, is to measure the temporal trends in sea ice thickness and mass. The CryoSat Calibration and Validation Concept [Wingham, et al. 2001], describes the sources of error in the determination of sea ice thickness and the importance of resolving them in order to use the measurements from the CryoSat radar altimeter to estimate sea ice thickness.

1.6) Sea ice thickness from satellite laser altimetry

1.6.1) Method

The opertunity to measure sea ice thickness via satellite laser altimetry became available in 2003 with the launch of ICESat [see Zwally *et al.*, 2002, for details of the mission]. As with satellite radar observations over arctic sea ice, ICESat offered the opportunity to provide basin wide, systematically collected, measurements of sea ice. At the time of writing, only the results of an initial look at deriving sea ice thickness from ICESat data have been published [see Kwok *et al.*, 2004]. The method used by Kwok *et al.*, (2004) is similar to sea ice thickness estimation from radar altimetry (section 1.5), with the exception that the laser altimeter ranges to the air/snow interface. To determine

the elevation of the ice plus snow above the sea surface they first identified areas of open water or thin ice in leads. These areas correspond to local elevation minima and relatively flat areas along the ICESat ground track. RADARSAT imagery were used to estimate the age of the ice in the leads. From this, ice thickness in leads could be estimated. Finally the lead elevation was subtracted from the ice plus snow elevation to give a snow freeboard estimate. Snow depth was calculated from the climatology given by Warren *et al.*, (1999). The density of ice and snow were assumed to be constant and taken to be 928 kg m^{-3} and 300 kg m^{-3} respectively (water density used in the calculation was not given). As the snow freeboard (f_s) measured by ICESat is the elevation of the ice freeboard plus the snow layer, the equation for ice thickness becomes:

$$h_i = \frac{h_s\rho_s + f_s\rho_w - h_s\rho_w}{(\rho_w - \rho_i)} \qquad (1.4)$$

Figure 1.14 from Kwok *et al.*, (2004) shows two ice thickness profiles.

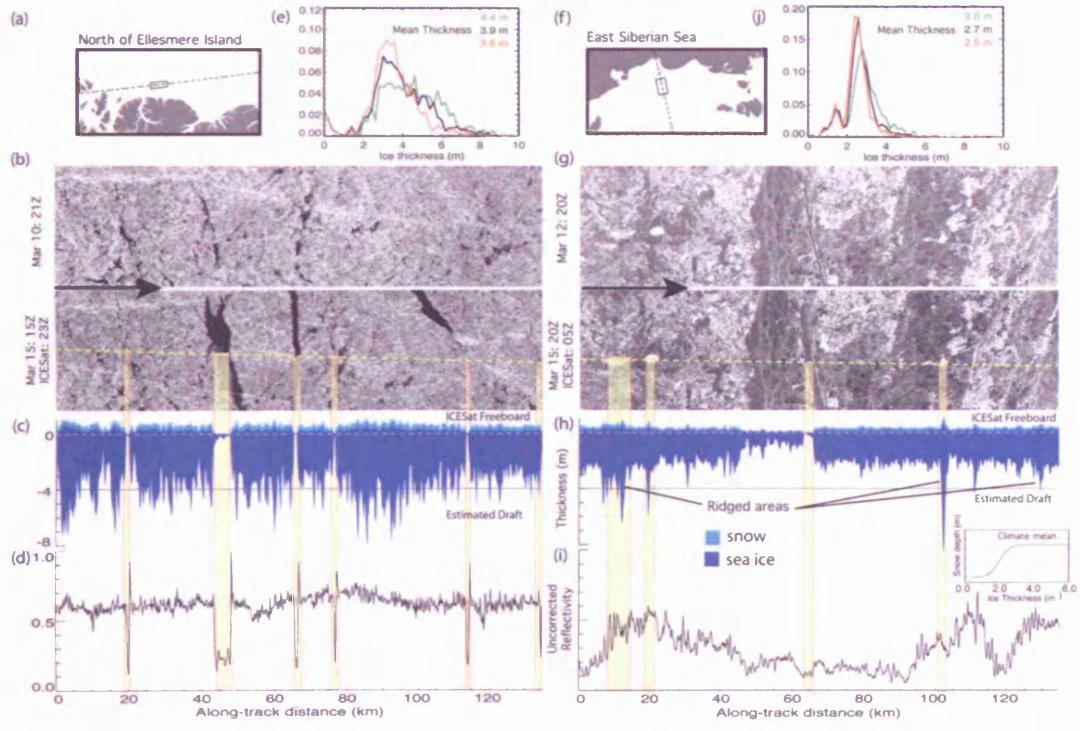

Figure 1.14: Figure 2 from Kwok *et al.*, (2004). Showing two ICESat derived ice thickness profiles. (a, f) Geographic location of data. (b, g) ICESat track (dashed yellow line) and new leads in the RADARSAT images. (c, h) ICESat freeboard profile and estimated ice draught (snow: light blue; ice: dark blue). (d, i) reflectivity along the track. (e, j) the thickness distribution.

1.6.2) Accuracy

Kwok *et al.*, (2004) do not provide a comprehensive analysis of the accuracy of calculating sea ice thickness from ICESat. They estimate that calculating the thickness of ice in thin leads will introduce an uncertainty of 0 – 2.5 cm in the freeboard estimation for the data collected North of Ellesmere Island and of less than 1.5 cm in the East Siberian Sea. They also acknowledge that unknown snow depth is their largest source of error in their conversion of ice plus snow freeboard to ice thickness, and that it could introduce uncertainties in ice thickness of over a metre. From comparison of equation 1.1 and 1.4, we would expect that error in snow depth would result in a larger uncertainty in ice thickness when using laser altimetry as the snow depth term appears twice in equation 1.4 and only once in equation 1.1. Errors in the density values used are not estimated.

From equation 1.4 the variance in the ice thickness calculated from laser measurements of snow freeboard (ε_l^2), to the first order, is given by equation 1.5:

$$\varepsilon_l^2 = \varepsilon_{fs}^2\left(\frac{\rho_w}{(\rho_w-\rho_i)}\right)^2 + \varepsilon_{hs}^2\left(\frac{\rho_s}{(\rho_w-\rho_i)} - \frac{\rho_w}{(\rho_w-\rho_i)}\right)^2 + \varepsilon_{\rho s}^2\left(\frac{h_s}{(\rho_w-\rho_i)}\right)^2$$
$$+\varepsilon_{\rho w}^2\left(\frac{f_s}{(\rho_w-\rho_i)} - \frac{h_s}{(\rho_w-\rho_i)} - \frac{f_s\rho_w}{(\rho_w-\rho_i)^2} - \frac{h_s\rho_s}{(\rho_w-\rho_i)^2} + \frac{h_s\rho_w}{(\rho_w-\rho_i)^2}\right)^2$$
$$+\varepsilon_{\rho i}^2\left(\frac{f_s\rho_w}{(\rho_w-\rho_i)^2} + \frac{h_s\rho_s}{(\rho_w-\rho_i)^2} - \frac{h_s\rho_w}{(\rho_w-\rho_i)^2}\right)^2 \qquad (1.5)$$

where ε_{fs} is the uncertainty in the laser measured snow freeboard. Using the error values given in section 1.5.2 (we assume the same values as for the radar case) and assuming that f_s=0.5 m and h_s=0.3 m (an ice thickness of 2.76 m), we estimate that the error (ε_l) in ice thickness calculated using laser altimetry is ± 0.78 m

1.6.3) Uncertainties in the computation of sea ice thickness from laser altimetry

The snow load uncertainty and density uncertainty described in section 1.5.3 both apply to the computation of sea ice thickness from laser altimetry.

The retrieval error

As with returns from a satellite radar altimeter, the scale of the roughness with in the laser footprint will affect the elevation estimate. However, we expect that elevation estimates from IceSat will be less sensitive to this factor as IceSat's footprint is smaller than that of ERS, EnviSat and CryoSat (for example, the diameter of the ERS pulse limited footprint is 1.7 Km where the diameter of an ICESat footprint is 60 m [Zwally *et al.,* 2002]).

Sea surface estimation

Kwok *et al.* (2004), estimate the sea surface elevation by locating flat areas and local minima along the ground track and by looking at the reflectivity values over theses areas (they associate a low reflectivity value with thin ice or open water). Although this relationship between the reflectivity and the presence of open water is clear in some instances (see, for example, the left hand side of figure 1.14) the relationship is not clear in others (e.g. the plots on the right hand side of figure 1.14). There is no clear distinguishing characteristic between the IceSat returns over open water and ice [S. Farrell, personal communication], unlike the case for the radar, where diffuse echoes are apparent over ice and specular echoes over leads. Kwok *et al.*, (2004), acknowledge that, although their method can be used on a local scale, it cannot be used on a basin wide scale without accurate (to the centi-metre level) estimates of the sea surface topography.

1.7) Main aims of the work described in this thesis

It is clear that the combination of both radar and laser altimetry has the potential to reduce the uncertainties associated with the measurements of sea ice thickness from both instruments. This thesis analyses data from the first experiment to collect coincident radar and laser altimetry data, the LaRA 2002 field campaign. The aim of the work presented here is to evaluate whether the combination of laser and radar altimetry can tell us about the reflecting surface of the radar in the snow/ice system and whether we can use radar and laser altimetry to estimate snow depth. In addition, in the future it may prove possible to combine data from ICESat and CryoSat. However, since exact coincidence cannot be achieved by these satellites it may prove very difficult to distinguish sampling errors from those in the separate instruments. Coincident radar and laser data on an airborne platform can provide valuable insights into how laser and radar altimetry data may be combined.

1.8) Summary

- Modelling the climate system is the only way of predicting climate change. Changes to the parameterisation of ice (and clouds) cause the largest amount of variability in the climate sensitivity. Therefore, in order to obtain an accurate estimate of climate sensitivity, ice must be correctly parameterised. Sea ice plays an important role in the climate system as it acts as a boundary between the ocean and atmosphere, and can effect the thermohaline circulation. It also reacts relatively quickly to changes in forcing and could therefore be an early indicator of changes to the climate system, especially as future warming at the poles is predicted to be 40% greater than the global mean.

- Sea ice models are continually improving but lack basin wide, regularly acquired, data sets on sea ice thickness for validation.

- Current sea ice thickness observations are temporally and spatially limited, and provide contradicting views on recent changes in sea ice thickness.

- Advances in the analysis of data from ERS1 & 2 have produced a method of monitoring sea ice thickness at regular intervals on a basin wide scale. However, some uncertainties exist and it is important that these are resolved in order for this data set, and future data sets, to be used with confidence.

- The equation for calculating sea ice thickness from satellite radar altimetry assumes that the radar return originates from the snow/ice interface. This fundamental assumption is based on limited laboratory evidence and large scale comparison. In order for the sea ice thickness data set to be usable this assumption must be investigated in greater depth.

- Combining satellite radar and laser altimetry has the potential to solve uncertainties associated with estimates of sea ice thickness from both instruments. For both the radar and the laser, the uncertainty in the snow load contributes an error to the estimate of sea ice thickness. If the radar indeed penetrates to the snow/ice surface then the elevation difference between the laser and the radar will give us an estimate of snow depth, provided that we can combine the measurements from two different sensors to the required degree of accuracy.

- The data presented in this thesis provides the first opportunity to quantitatively compare coincident airborne radar and laser data over sea ice.

- The experiment described in this thesis is an important pre-cursor to the airborne validation campaigns for the CryoSat satellite.

2) The electromagnetic properties of sea ice and radar interaction with the snow/ice system

2.0) Introduction

In chapter 1 we described the uncertainties associated with calculating sea ice thickness from radar altimetry. A fundamental assumption in this calculation is that radar returns originate from the snow/ice interface. In this chapter we examine the electromagnetic (EM) properties of sea ice at radar frequencies to see if they can determine the radar interaction with the snow/ice system. In section 2.1 we describe what governs the EM properties. In section 2.2 we describe the radar equation and explain that the backscattering cross section (σ_{bs}) is dependant on the specific target, and that σ_{bs} depends, in part, on the dielectric properties of that target. In section 2.3 we give a qualitative description of radar backscatter from snow covered sea ice. In section 2.4 we describe which dielectric properties are needed to calculate the radar interaction with a target. In sections 2.5 and 2.6 we look at the dielectric properties of sea ice and snow relating to section 2.4. In section 2.6, we then calculate the penetration depth into dry snow for a Ku band radar as a function of temperature. The Ku band is chosen as all radar altimeters discussed in this thesis operate at this frequency. In section 2.7 we discuss the use of theoretical models to describe radar backscatter from snow covered ice and the difficulty in validating them. In section 2.8 we discuss variations of σ_{bs} with angle of incidence. Finally, in section 2.9, we discuss the laboratory evidence for a Ku band radar return originating from the snow/ice interface.

2.1) Determinants of the EM properties of sea ice

Sea ice roughness, texture, chemical composition (including salinity and brine volume) and temperature gradient, combine to determine its EM signature. The winds, currents, air and water temperatures and snow fall, among other variables, influence these properties. The properties of sea ice listed above tend to be inhomogeneous, even over short length scales (tens of meters horizontally and tens of centimetres vertically). Therefore, EM data, collected by remote instruments, tend to rely on empirical

relationships between an EM property (i.e. emissivity) and a geophysical property of the ice (i.e. ice type and concentration). [Jezek et al., 1998]

2.2) The radar equation

The starting point for our discussion on the sea ice properties that affect the power returned to an active microwave remote sensing instrument, is the radar equation. The radar equation gives the relationship between the received signal and the characteristics of the radar and the target. [Ulaby et al., 1982]

$$P_r = \frac{P_t G^2 \lambda^2 \sigma_{bs}}{(4\pi)^3 R^4 L} \tag{2.1}$$

where P_r is the power received by the radar, P_t is the power transmitted by the radar, G is the antenna gain, λ is the wave length, σ_{bs} is the backscattering cross section, R is the range to the target and L is a loss factor, including losses due to atmospheric attenuation.

The backscattering cross section varies for different targets and is a function of the directions of the incident wave and the wave towards the receiver as well as the scatterer shape and its dielectric properties [Ulaby et al., 1982]. σ_{bs} is usually represented by equation 2.2:

$$\sigma_{bs} = \sigma^0 A_\sigma \tag{2.2}$$

where σ^0 is the normalised scattering coefficient of the terrain and A_σ is the area of the footprint.

2.3) Qualitative description of backscatter from sea ice

In section 2.2 we stated that the backscattering cross section is a function of the direction of the incident wave. For radar altimetry the angle of incidence of the wave at the target is 0°, so ideally in this section we would describe backscatter from sea ice at 0° incidence. However, very little research has been performed at this incidence angle

so we give a general description of backscatter from sea ice. Figure 2.1 is a schematic representation of the ice types discussed in this section.

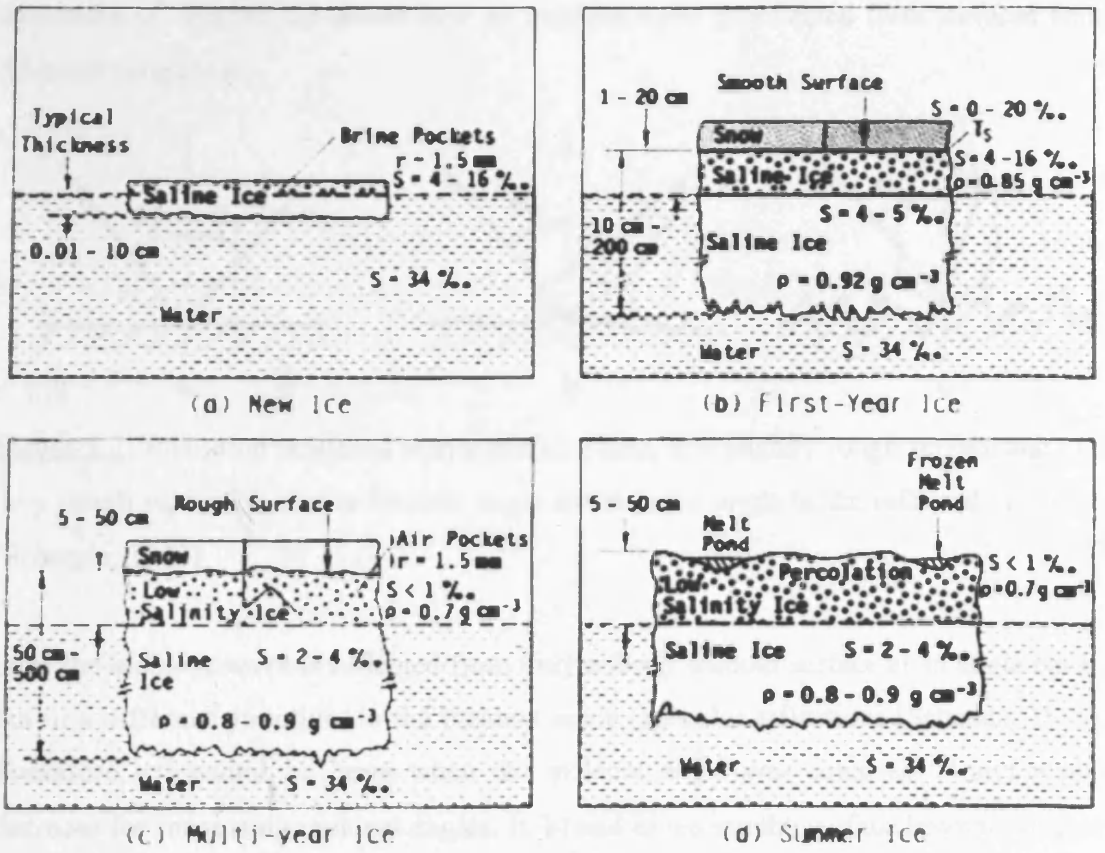

Figure 2.1: Schematic representation of some principal ice types. [Zwally et al., 1983, in Ulaby et al., 1986]

It is convenient to divide sea ice into three ice types (new ice, first year ice and multi year ice) in order to describe its backscatter characteristics.

2.3.1) Winter

New ice

New ice has a typical thickness of 0.01 to 10 cm, it is highly saline and has many brine pockets. The ice is usually quite smooth[1] to microwavelengths after it is a few

[1] For a surface to be smooth to electromagnetic radiation it must forfil the Rayleigh criteria $\sigma_s < \frac{\lambda}{8\cos\theta}$, where σ_s is the standard deviation of surface roughness, λ is the wavelength and θ is the angle of incidence. [Schanda, 1986]

centimetres thick (it may or may not be smooth when it first forms). [Ulaby et al., 1986]. The smoothness of the ice and the angle of incidence of the radiation will determine σ^0. Figure 2.2 shows how an incident wave is reflected from surfaces with different roughness.

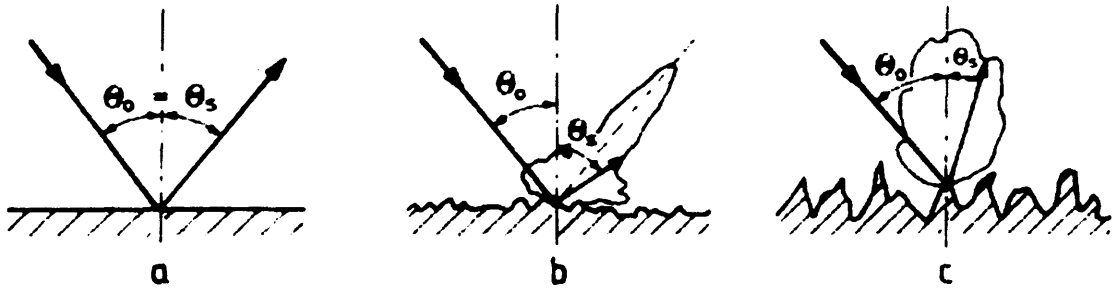

Figure 2.2: Radiation scattered at a) a perfect plane, b) a slightly rough surface and c) a very rough surface. θ_0 is the incident angle and θ_s is the angle of the reflected radiation. [Schanda, 1986]

In a) the incident wave is reflected from the perfectly smooth surface at an angle equal, but in a different direction, to the incident angle (specular reflection) [Schanda, 1986]. Therefore, σ^0 would be large when the incident angle was equal to 0° and would decrease for increasing incident angles. In b) and c) we see the surface become rougher and the incident radiation more and more diffusely scattered (i.e. power is scattered in all directions) [Schanda, 1986]. Therefore σ^0 becomes less for an incident angle of 0° and greater for larger incident angles.

First year ice (FY)

FY ice has a typical thickness of 10 to 200 cm. As the thickness increases, σ^0 tends to increase as well. The high salinity of the ice means that the penetration into the ice is small and the return originates from the surface. [Ulaby et al., 1986]

Multi year ice (MY)

The structure of MY ice is different to FY ice in that it has a lower salinity and contains many air pockets in its upper layer. This results in signal penetration into the upper

layer and volume scattering. The effect is enhanced at higher frequencies and is greater than the effect of surface scattering. σ^0 is higher than for FY ice. [Ulaby et al., 1986]

Snow

The snow cover present on FY and MY ice contributes to some volume scattering, but the affect is minimal while the snow is dry, and the low attenuation of the snow does not effect the signal received from the ice surface. [Ulaby et al., 1986]

2.3.2) Melt season and summer

As the layer of snow begins to melt, σ^0 increases slightly over FY ice due to backscattering from the snow. However the main effect of the melting snow is to roughen the surface of the FY ice by the introduction of superimposed ice. At this point σ^0 decreases slightly over MY ice due to attenuation from the snow. [Ulaby et al., 1986]

By mid summer the snow has disappeared on the FY ice, exposing the roughened surface. The surface of the MY ice, at this time, is wet enough for significant penetration into the volume scattering region. Therefore, σ^0 is greater for FY ice than for MY ice at this point. [Ulaby et al., 1986]

As melting continues, the superimposed ice on the FY ice melts and σ^0 decreases. On MY ice the melt water runs off exposing most of the ice surface, this results in an increase in σ^0 over MY ice. [Ulaby et al. 1986]

In summer the wet snow can mask the return from the ice and contribute a return of its own. [Ulaby et al., 1986]

2.4) Equations describing radar interaction with sea ice

The backscattering cross section of a media depends on the way in which the radiation interacts with a media when it meets that media. It is a function of directions of the incident wave and the reflected wave towards the receiver as well as the scatterer shape

and its dielectric properties [Ulaby et al., 1982]. In section 2.4.1, we describe qualitatively how a radar wave interacts at a boundary between two medium. In section 2.4.2 we describe the dielectric properties that must be known to predict what happens to the energy of a radar wave when it meets a certain media.

2.4.1) Radar scattering

When a radar wave meets a boundary between two media, a portion of the incident energy is scattered back, while the rest is transmitted forward into the lower medium. If the lower medium is homogenous then only surface scattering is important. However, if the lower medium is inhomogeneous, or its constituents have different dielectric properties, then both surface and volume scattering must be considered. During volume scattering energy from the transmitted wave is redistributed in other directions, resulting in a loss of energy. Figure 2.3 illustrates this concept.

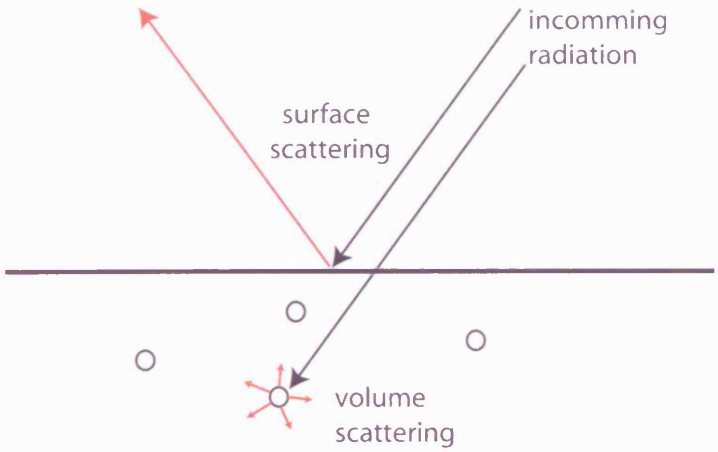

Figure 2.3: Schematic representation of surface and volume scattering.

Energy can also be lost via absorption i.e. the energy is transformed into other types of energy such as heat. The total loss is referred to as extinction and is measured by the extinction coefficient, which is the extinction per unit length. The region within the medium important for volume scattering is calculated by the penetration depth, which is the inverse of the extinction coefficient. [Ulaby et al., 1982]

Therefore to understand where in a medium a return originates from, we must examine the penetration depth in that medium.

The discussion in section 2.4.2 is based on Hallikainen & Winebrenner (1992).

2.4.2) Penetration depth

The penetration depth is defined as the depth δ_p at which the echo power has dropped to $1/e$ of the power just beneath the surface:

$$\frac{P(\delta_p)}{P(0+)} = \frac{1}{e} \tag{2.3}$$

where P(0+) is the power just beneath the surface and $P(\delta_p)$ is the transmitted power at δ_p. The penetration depth can be calculated provided certain dielectric properties of the media are known. These properties are the complex dielectric constant and the extinction, absorption and scattering coefficients.

Complex dielectric constant

The complex dielectric constant (ε) is given by equation 2.4:

$$\varepsilon = \varepsilon' - i\varepsilon'' \tag{2.4}$$

The real part, ε' (permittivity) gives a measure of how easily the energy of an electromagnetic wave passes across a dielectric interface. The imaginary part ε'' (dielectric loss factor), gives the electromagnetic loss of the material. If the contrast in ε' between two media is large then large surface scattering occurs. If the contrast is small then energy is transmitted across the interface and can be scattered and absorbed in the lower media.

The amount of electromagnetic energy lost when an electromagnetic wave passes through a medium, is commonly represented by the loss tangent (tan δ):

$$\tan\delta = \frac{\varepsilon''}{\varepsilon'} \tag{2.5}$$

Extinction, absorption and scattering coefficients

The total electromagnetic loss in a scattering medium is the sum of the absorption loss (κ_a) and scattering loss (κ_s). Scattering loss is caused by particles of different ε embedded in a host medium. The extinction coefficient (total loss) is:

$$\kappa_e = \kappa_a + \kappa_s \tag{2.6}$$

If scattering in the medium is ignored, $\kappa_e \equiv \kappa_a$ and if additionally, κ_a does not depend on depth then the penetration depth is given by:

$$\delta_p = \frac{1}{\kappa_a} = \frac{\sqrt{\varepsilon'}}{k_0 \varepsilon''} \qquad \varepsilon'' << \varepsilon' \tag{2.7}$$

where k_0 is the wave number and is equal to $2\pi/\lambda$, where λ is the wavelength. The penetration depth indicates the maximum depth of the medium that contributes to the backscattering coefficient.

2.5) The dielectric properties of sea ice

Sea ice is a mixture of pure ice and brine. Therefore its complex dielectric constant (equation 2.4) of sea ice (ε_{si}), and the penetration depth into sea ice, depend on the following parameters:

1) The complex dielectric constant of pure ice (ε_i);
2) The complex dielectric constant of the brine pockets (ε_b);
3) The fraction of brine volume (v_b);
4) The shape and orientation of the brine pockets relative to the direction of the electric field of the wave.

Because of its dependence on parameters 1 to 3, ε_{si} is a function of temperature, salinity and frequency. In sections 2.5.1 to 2.5.4 we describe ε_i, ε_b, ν_b and the effect of the shape and orientation of the brine pockets.

2.5.1) Pure ice

Ulaby et al., (1986) give ε_i' a constant value of 3.15, based on experimental results. However, Hallikainen and Winebrenner (1992) give a value of 3.17 and Table 2.1, taken from Ulaby et al.(1986), shows a range of measured values of ε_i' taken at different frequencies and temperatures. Since the variation in ε_i' is small between 9 and 24 GHz, we follow Ulaby et al., (1986) and take ε_i' to be a constant (3.15).

Frequency (GHz)	Temperature Range (°C)	ε_i'	Reference
0.15 to 2.5	-1 to –60	2.90 to 2.95	Westphal (in Evans, 1965)
9.375	0 to –18	3.15	Cumming (1952)
10	-12	3.17	Von Hippel (1954)
10	0 to –35	3.14	Vant et al. (1974)
10	-1 to –49	3.17	Lamb (1946)
24	0 to –185	3.18	Lamb and Turney (1949)
26.4 to 40.0	0 to –35	2.92	Vant et al. (1974)
94.5	-28	3.08	Perry and Straiton (1973)
1000	-173	3.20	Bertie et al. (1969)

Table 2.1: Measured values of the real part of the dielectric constant of pure- or fresh-water ice [Ulaby et al., 1986]

Whilst ε_i' is very stable between 9 to 24 GHz and can be taken to be independent of frequency and temperature, ε_i'' shows strong variations with both parameters. Table 2.2 shows a range or measured values of ε_i''.

Frequency (GHz)	Temperature (°C)	ε_i''	tan δ_i	Reference
2.7	-5	0.0012 ± 0.00002 glacier ice		Westphal (in Koh 1996)
2.4	-5	0.0004 ± 0.0002 bubble free ice		Matzler & Wegmuller (1988)
1.8	-2.5	0.003		Koh (1996)
9.375	-12	0.0025 (from ε_i=3.15)*[2]	7.8×10^{-4}	Cumming (1952)
9.375	0 to -18	0.0082 to 0.0022 0025 (from ε_i=3.15 as above)	$\approx26\times10^{-4}$ to 7×10^{-4} (non-linear relationship)	Cumming (1952)

Table 2.2: Measured values of the imaginary part of the dielectric constant. No measurements were available for the Ku band but from the findings above we would expect ε_i'' to be dependent on both frequency and temperature for Ku band frequencies.

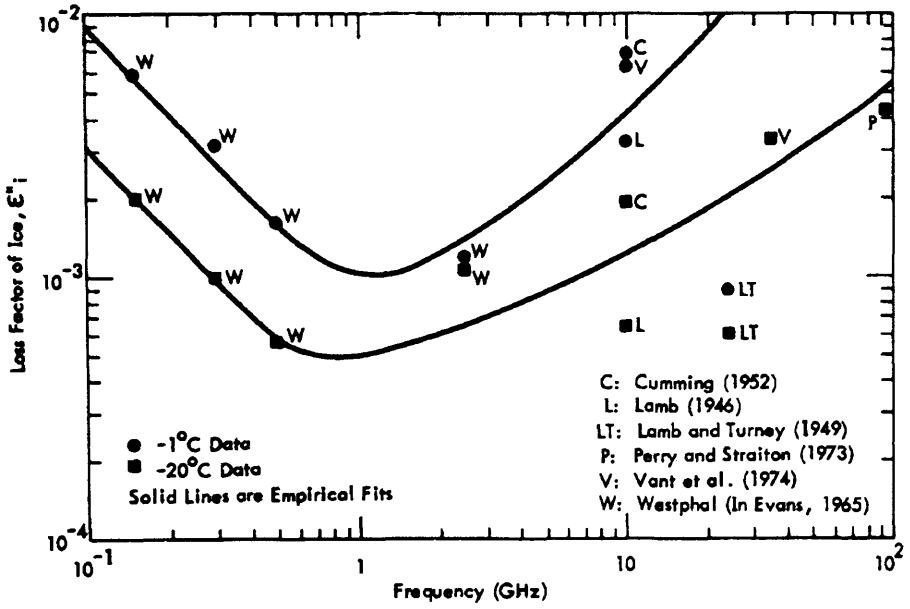

Figure 2.4: Variation of ε_i'' with frequency. [Ulaby, et al., 1986]

[2] '*' indicates that the value displayed was not given in the literature referred to, but has been calculated using equation 2.5.

Experimental evidence (with temperature held constant) suggests that ε_i'' decreases with increasing frequency then changes slope at around 1 GHz and increases with increasing frequency (figure 2.4). The data (shown in figure 2.4) exhibits a large amount of variability, which is partly attributed to the difficulty in accurately measuring ε_i''. [Ulaby, et al., 1982, 1986].

2.5.2) Brine

Brine is a mixture of salt and water. In sea ice, its salinity depends on its temperature. This is because brine exists in pockets within the ice, and a fall in ice temperature causes more water to freeze thereby increasing the brine salt concentration. The brine salinity is calculated by empirical expressions relating the salinity to temperature [see Ulaby et al., 1986]. These relationships mean that ε_b is a function of frequency and temperature only.

Numerical expressions are developed by Ulaby et al. (1986) to estimate ε_b from equations used to calculate the dielectric constant of saline water from Stogryn (1971). Figure 2.5 shows the real and imaginary parts of the complex dielectric constant calculated using these expressions. Comparison of figure 2.5 with figure 2.4 shows that the complex dielectric constant of brine is high compared to that of pure ice.

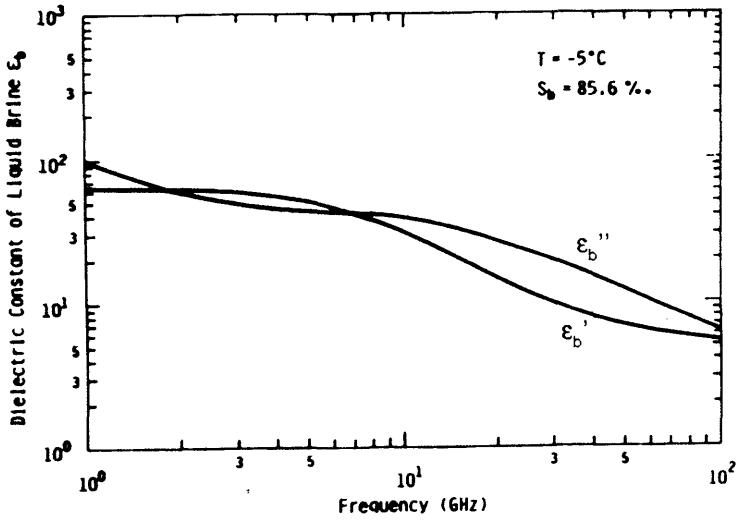

Figure 2.5: The real and imaginary parts of the complex dielectric constant for brine as a function of frequency. [Ulaby et al., 1986].

2.5.3) Brine volume fraction

The brine volume fraction (ν_b) is given by:

$$\upsilon_b = \frac{S_i}{S_b}\frac{\rho_i}{\rho_b} \tag{2.8}$$

where S_i and S_b are the salinities of the sea ice and the brine, and ρ_i and ρ_b are the densities of pure ice and brine, respectively. Ulaby et al. (1986) formulate empirical expressions relating ν_b to S_i and temperature, with a high (0.99) correlation coefficient between the experimental data and their expressions.

2.5.4) The shape and orientation of the brine pockets

Because of brine's high complex dielectric constant compared to that of ice (section 2.5.2), the shape and orientation of the brine pockets is very important when modelling, and measuring, EM radiation's interaction with sea ice [Vant et al., 1978]. Perovich and Gow (1996) analyse thin sections of various sea ice types and measure their brine volumes and brine pocket shapes and sizes. Brine pocket volume ranges from 10^{-4} to a few mm^3 and they are shaped as elongated ellipsoids. Perovich and Gow (1996) also highlight the great degree of variability in ice properties between spatially coincident first year and multi year ice. First year ice contains brine pockets whereas multiyear hummocked ice contains air pockets as the brine has drained from the ice [Tucker et al., 1987]. The orientation of the brine pockets is not described by Perovich and Gow (1996). However, Vant et al., (1974) describe the orientation as the elongated sides of the ellipsoid as being parallel to the growth direction of the ice in first year ice. Although the brine pockets tend to be orientated vertically they can be tilted away from the vertical [Golden et al., 1998], differences in orientation of the brine pockets will affect the dielectric constant. Hallikainen (1992) describes evidence for ε_{si}'', for horizontally orientated brine pockets, increasing by 300% compared to ε_{si}'' for vertically orientated brine pockets, in the 26-40 GHz range.

2.5.5) Penetration depth into sea ice

Sections 2.5.1 to 2.5.3 show that it is possible to estimate ε_i, ε_b and υ_b, if the temperature and the salinity of the ice, and the frequency of the radiation, are known. These parameters can then be used to estimate ε_{si} if the shape and orientation of the brine pockets are known [see Ulaby et al., 1986]. However, ice properties vary on short spatial scales (see sections 2.1 and 2.5.4). Therefore to gain a basic understanding of the complex dielectric constant of sea ice (ε_{si}), it is simpler to used measured values of ε_{si}' and ε_{si}'' over different types of ice rather than predict ε_{si} from ε_i, ε_b and υ_b and the shape and orientation of the brine pockets.

Over the frequency range 1 – 40 GHz most measured values of the real part of the dielectric constant on sea ice fall between $2.5 \leq \varepsilon_{si}' \leq 8$ [Ulaby et al., 1986]. Figure 2.6 shows the variation of ε_{si}' with temperature at a constant frequency of 10 GHz (the authors do not expect a different result at different frequencies), and illustrates that ε_{si}' is dependant on temperature and salinity [Vant et al., 1974].

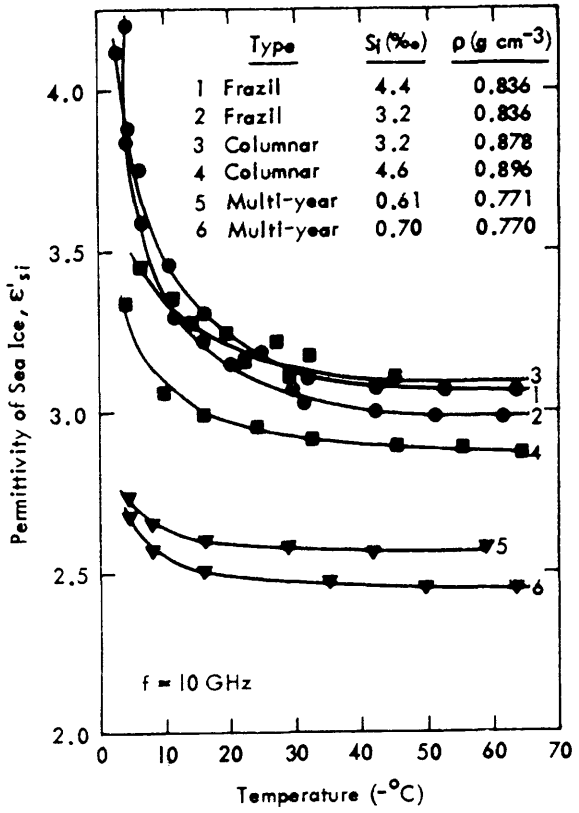

Figure 2.6: Temperature variation of the permittivity of sea ice at 10 GHz [Vant et al., 1974, in Ulaby et al., 1986]

Figure 2.7 shows the variation of ε_{si}'' with temperature at a constant frequency of 10 GHz. The value of ε_{si}'' depends on ice type and brine volume. The fact that frazil ice has a higher ε_{si}'' could be due to the orientation of its brine pockets with respect to the electric field. [Vant et al., 1974]

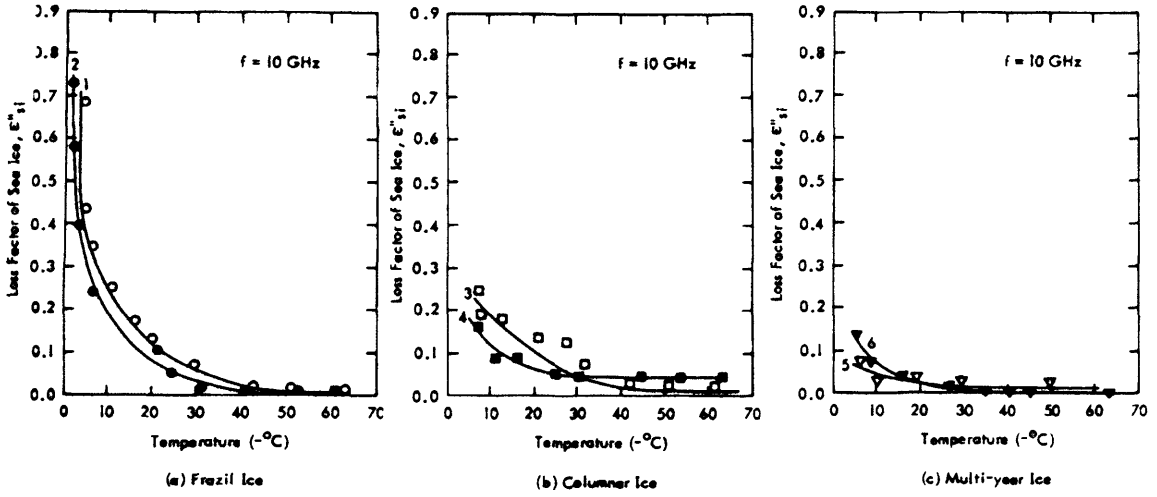

Figure 2.7: Temperature variation of the loss factor for three types of sea ice at 10 GHz. Salinities and densities of the ice samples are given in the inset in figure 2.6. [Vant et al., 1974, in Ulaby et al., 1986]

Unlike ε_{si}', ε_{si}'' varies with frequency (Vant et al., (1974) only show results at 10 GHz). Figure 2.8 shows ε_{si}'' as a function of frequency. ε_{si}'' decreases with increasing frequency then changes slope at about 5 GHz where ε_{si}'' begins to increase with increasing frequency (ε_i'' changes slope at 1 GHz, see figure 2.4). From this figure we would expect ε_{si}'' to be very slightly higher at Ku band frequencies than at 10 GHz.

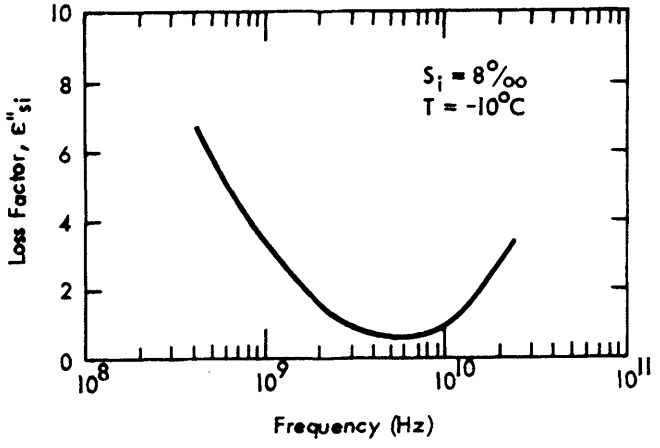

Figure 2.8: ε_{si}'' as a function of frequency. [Hoekstra & Cappillino, 1971, in Ulaby et al., (1986).

Ulaby et al. (1986) calculate the penetration depth in pure ice and FY and MY sea ice, based on the findings in sections 2.5.1 and 2.5.5. Their results are shown in figure 2.9.

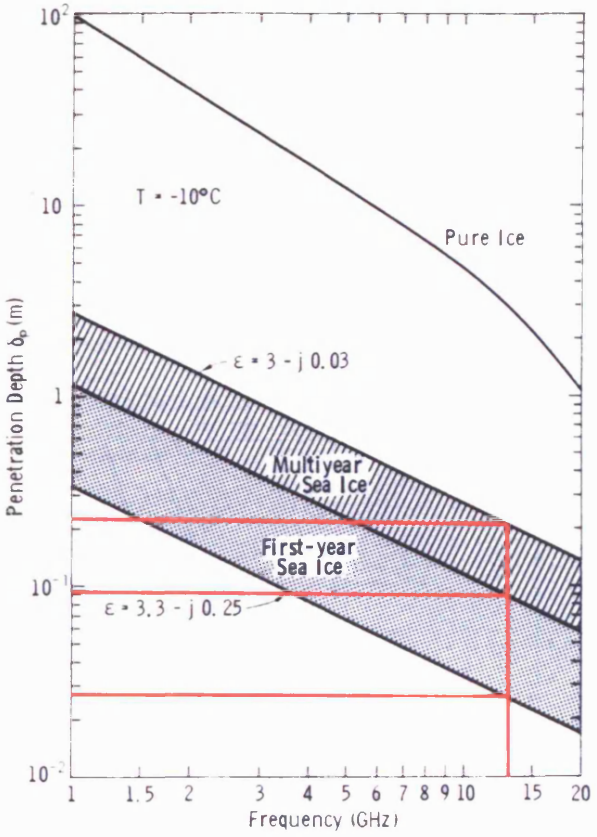

Figure 2.9: Penetration depth into sea ice with variations frequency [Ulaby et al., 1986]. The super-imposed red lines point to values at a frequency of 13.8 GHz (Ku band).

	ε'	ε''
Pure ice	3.15 (section 2.5.1)	Taken from figure 2.4, by interpolating between the –1° and –20° C curves, to find the value at -10°C
FY ice (lower boundary)	3.3 (figure 2.7)	0.25 (figure 2.7 b, chosen to give a high loss example)
FY ice (upper boundary)	3.0 (figure 2.7)	0.07 (figure 2.7 b & c)
MY ice	3.0 (figure 2.7)	0.03 (figure 2.7 c)

Table 2.3: Sources of values used to create figure 2.9. ε_{si} is assumed to be frequency independent.

Examining the temperature sensitivity of the real and imaginary loss factors reveals that the penetration depth increases with increasing negative temperature. Using figure 2.9 as a reference, the penetration depth at 0°C would be two to three times smaller. [Ulaby et al., 1986]

Measurement of simulated sea ice (made from frozen sea water) and/or frozen sodium chloride (NaCl) solution to deduce ε_{si}' and ε_{si}'', as a function of temperature for a range of frequency bands, have produced mixed results. Hallikainen and Winebrenner (1992) summarise a number of experiments, and give the penetration depth (in sea ice) in the 1- to 10 GHz range as between 5 and 100 cm for first year ice and 30 to 500 cm for multiyear ice. Sensors operating at X-band (8 to 12 GHz) provide information on sea ice mainly from the top most 5 to 80 cm, depending on ice type, salinity, and temperature. The corresponding numbers for L-band (1 to 2 GHz) sensors are 40 to 500 cm.

2.6) The dielectric properties of snow

As shown in figure 2.1, a layer of snow sometimes covers FY and MY ice. Therefore, in order to understand where a microwave return originates from in the snow/ice system, the dielectric properties of the snow layer must also be considered. In section 2.6.1 we describe the composition of snow and give values of the complex dielectric constant for snow and discuss it's variation with snow density, temperature and frequency. In section 2.6.2 we investigate the radar penetration depth into dry snow, using the information we have presented in previous sections. Section 2.6.3 discusses the dielectric properties of wet snow.

2.6.1) Dry snow

Dry snow is a mixture of ice crystals and air voids, therefore its complex dielectric constant (equation 2.4) is controlled by:

1) The complex dielectric constant of pure ice (ε_i);
2) The snow density (ρ_s);

A constant value for ε_i' was given in section 2.5.1, and was shown to be independent of temperature and frequency. Therefore, the real part of equation 2.4, for dry snow (ε_{ds}'), is only a function of density. [Hallikainen & Winebrenner, 1992]

The following equations provide good agreement with experimental data:

$$\varepsilon_{ds}' = 1.0 + 1.9\rho_s \qquad \text{for } \rho_s \leq 0.5 \text{ g cm}^{-3} \qquad (2.9)$$

$$\varepsilon_{ds}' = 0.51 + 2.88\rho_s \qquad \text{for } \rho_s \geq 0.5 \text{ g cm}^{-3} \qquad (2.10)$$

where ρ_s is the snow density. Because the real parts of the dielectric constants of air and ice are independent of temperature and frequency in the microwave region, the above equations are expected to be valid throughout the microwave region [Ulaby et al., 1986]. Figure 2.10 shows ε_{ds}' calculated from the two equations compared with measured values of ε_{ds}', as a function of density.

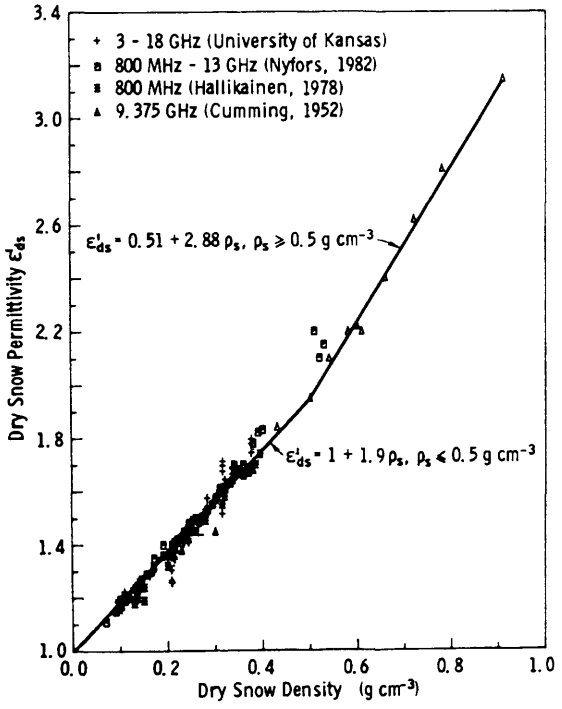

Figure 2.10: Measured ε_{ds}' and its variation with snow density. [Ulaby et al., 1986]

Several formulas exist to relate ε_{ds}'' to ε_i and the ice volume fraction. Their predictions for ε_{ds}'' (plotted as $\varepsilon_{ds}''/\varepsilon_i''$), along with measured values, from Cumming (1952), are shown in figure 2.11.

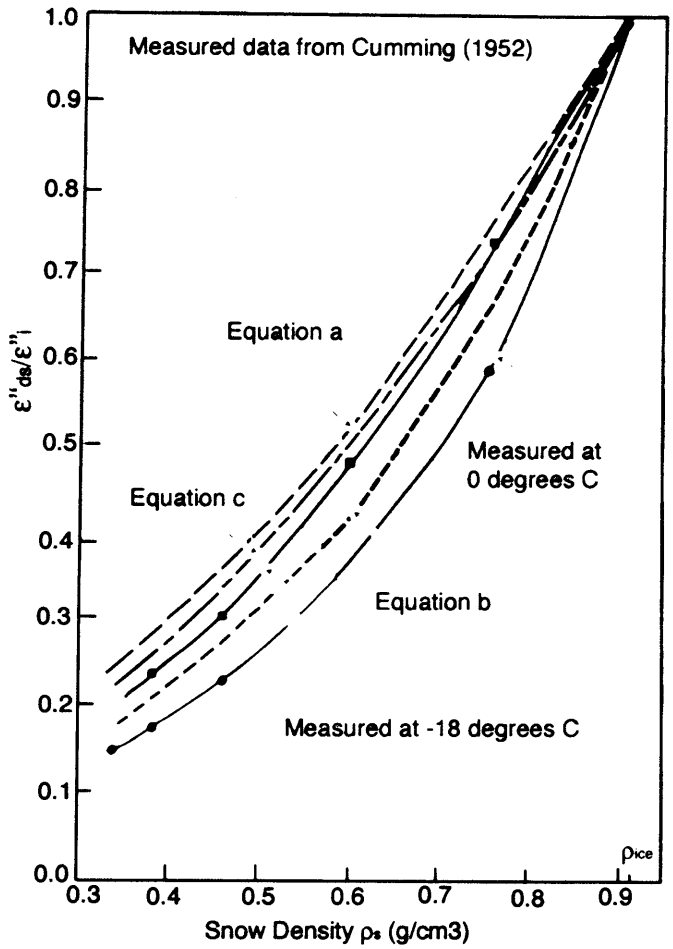

Figure 2.11: Comparisons of model predictions (equations a to c) of $\varepsilon_{ds}''/\varepsilon_i''$ with measured data. [Ulaby et al., 1986].

Figure 2.11 shows that although different models can give reasonable predictions of $\varepsilon_{ds}''/\varepsilon_i''$ there is not a unique solution.

As ε_{ds}' is independent of temperature and frequency examining the loss tangent (equation 2.5) will tell us if ε_{ds}'' is dependent on temperature and frequency as well as density (figure 2.11). Figure 2.12 a) shows that the loss tangent for dry snow is dependent on temperature. Cumming (1952) (figure 2.12 b) also shows similar results. Therefore ε_{ds}'' must be dependent on temperature.

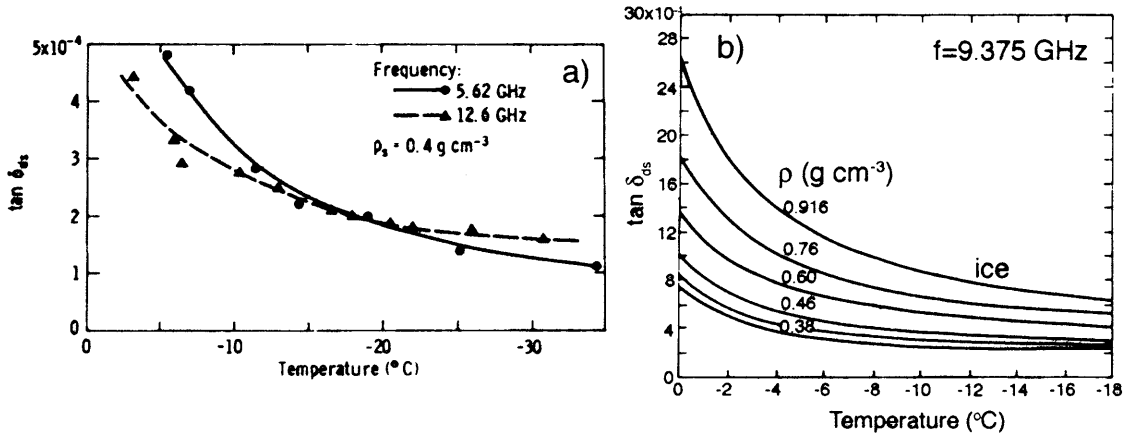

Figure 2.12: a) Measurements of the loss tangent of dry snow as a function of temperature. [Nyfors, 1982 in Ulaby et al., 1986]. b) Measurements of the loss tangent of dry snow as a function of temperature at a frequency of 9.375 GHz. [Cumming, 1952 in Ulaby et al., 1986]

Figure 2.13 shows the loss tangent for dry snow is dependent on frequency. Therefore ε_{ds}'' must be dependent on frequency.

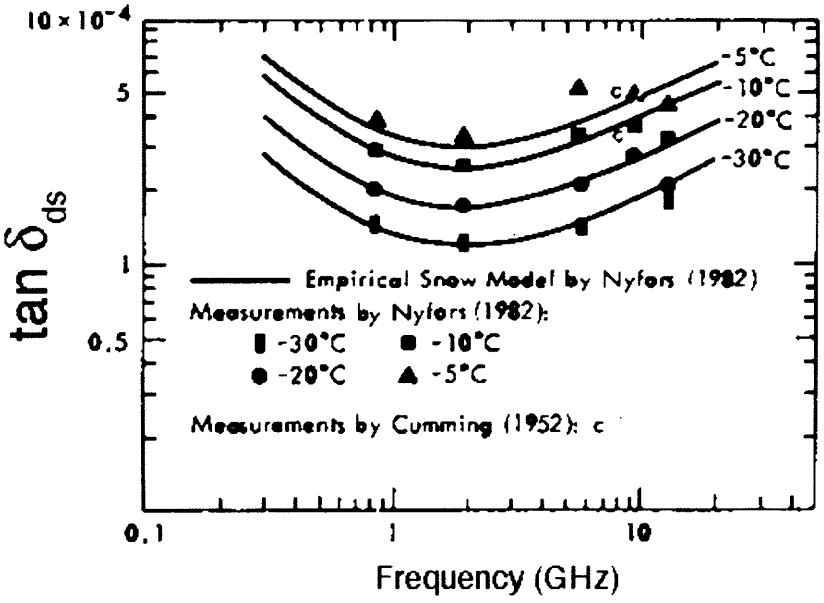

Figure 2.13: The loss tangent of dry snow as a function of frequency with temperature as a parameter. ρ_s is 0.45 g cm^{-3}. [Nyfors, 1982 in Ulaby et al., 1986]

2.6.2) Investigation into the penetration depth for dry snow

Using the data described in section 2.6.1, we calculate the penetration depth into dry snow, for a 13.8[3] GHz radar, in three steps:

Step 1: Penetration depth at 9.375 GHz

We used data inferred from Cumming (1952), figure 2.10 b), to obtain values of the loss tangent for dry snow at different densities; equations 2.9, 2.10 to find values for ε_{ds}'; equation 2.5 to find values for ε_{ds}''; and equation 2.7 to calculate the penetration depth. Figure 2.14 shows how the penetration depth at 9.375 GHz changes with temperature, for different densities of snow.

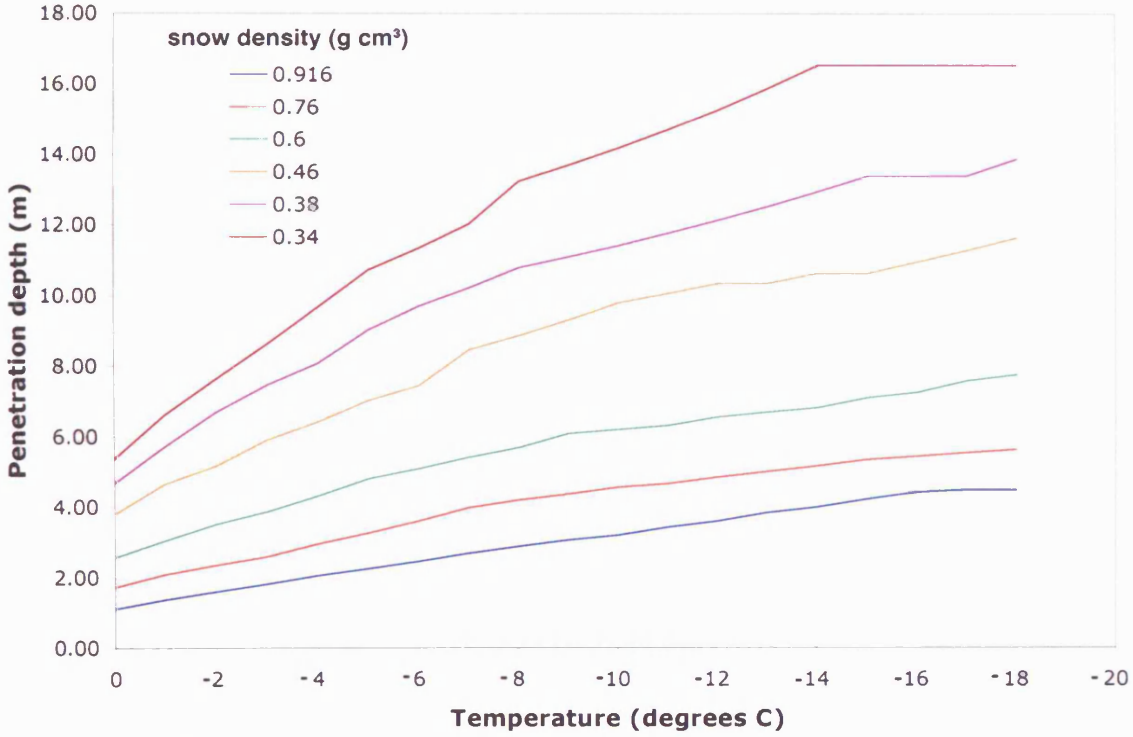

Figure 2.14: Penetration depth into dry snow at 9.375 GHz with respect to temperature and snow density.

Figure 2.14 shows that snow depths would have to be greater than 1 m (for high density snow) for a 9.375 GHz wave not to reach the ice surface.

[3] The frequency of the radar altimeters onboard ERS1/2

Step 2: Variation of the loss tangent with frequency

Figure 2.12 a) shows that the loss tangent of dry snow varies with frequency and temperature. Figure 2.12 a) shows this variation for frequencies of 5.62 GHz and 12.6 GHz. This plot was used to estimate the loss tangent for 13.8 GHz by assuming a linear relationship between frequencies. Figure 2.15 shows the loss tangent for dry snow at 9.62 and 12.6 GHz from Nyfors (1982) in Ulaby et al. (1986), and the calculated loss tangent for 13.8 GHz.

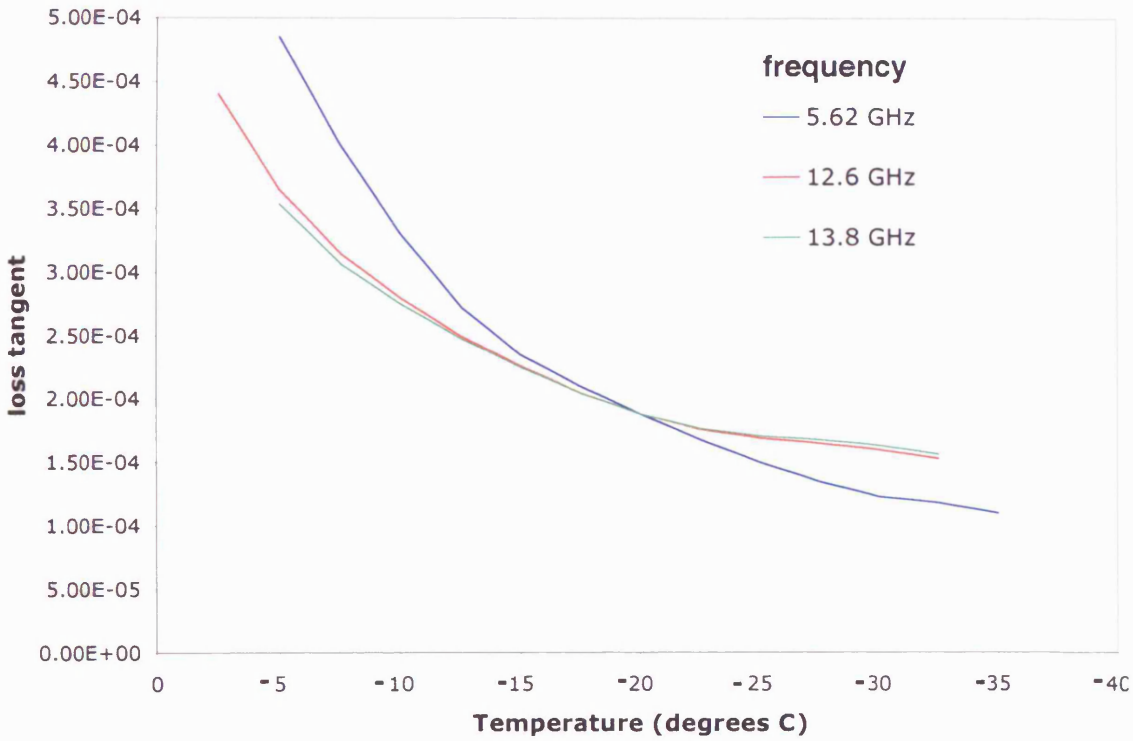

Figure 2.15: Measurements of the loss tangent of dry snow, at 9.62 and 12.6 GHz, as a function of temperature, at constant density of 0.4 g cm^{-3}. Calculated value of the loss tangent of dry snow at 13.8 GHz, as a function of temperature.

Step 3: The penetration depth for 13.8 GHz

Figure 2.16 shows the calculated penetration depth for 13.8 GHz in dry snow, for similar snow densities, as a function of temperature. The blue line shows the penetration depth calculated from the corrected loss tangent (figure 2.15), the red line shows the penetration depth calculated using the assumption the loss tangent does not vary at different frequencies. The data from 2.12 b), where the frequency is 9.375 GHz, is used

to calculate this line. The blue line only extends to –5° C, as the values for the corrected loss tangent in figure 2.15 only extend to around -5° C. The red line extends to zero as the data in 2.12 b) extends to zero. As in step 1: equations 2.9, 2.10 are used to find values for ε_{ds}'; equation 2.5 to find values for ε_{ds}''; and equation 2.7 to calculate the penetration depth. As figures 2.12 a) & b) and 2.13 all show the loss tangent increasing with increasing temperature for frequencies ranging from 0.1 GHz to 14 GHz we would expect that the penetration depth for 13.8 GHz would continue to decrease as the temperature increased (as shown by the dashed line in figure 2.16).

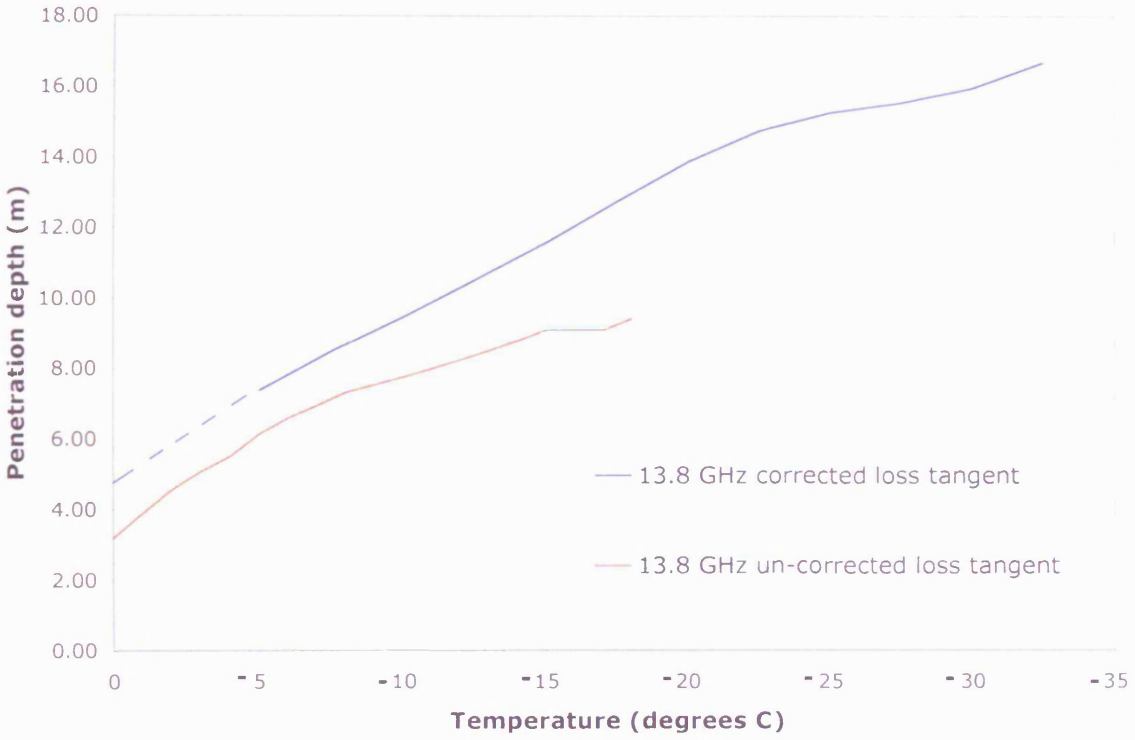

Figure 2.16: Calculated penetration depth for 13.8 GHz in dry snow, for similar snow densities, as a function of temperature. The dashed line shows the expected penetration depth as the temperature approaches zero degrees. Note that these theoretical results do not account for the presence of liquid water that may occur when the temperature fluctuates above 0°C i.e. diurnal temperature variations.

The evidence presented here implies that a radar altimeter with a frequency of 13.8 GHz should penetrate through any reasonable snow depth[4] when the temperature is below 0 °C.

[4] Monthly average snow depths on Arctic sea ice have a maximum of 34 cm [Warren et al., 1999].

2.6.3) Wet snow

The presence of liquid water within the snow layer strongly affects its dielectric properties as water has a high dielectric constant compared to ice and air. The amount of water in the snow is either expressed as the volume fraction of liquid water in the snow (m_v), or as a percentage of liquid water by weight (w_w). The complex dielectric constant (equation 2.4), for wet snow, is controlled by:

1) The complex dielectric constant of ice;
2) The dielectric properties of water;
3) The liquid water volume fraction;
4) The shape of the ice particles and water inclusions.

Hallikainen et al. (1986) compare dielectric measurements of wet snow made at frequencies between 3 and 18 GHz, with 6 dielectric models. Their Debye-like semi-empirical model best describes the behaviour of wet snow as a function of the dry snow density and m_v, and the radar frequency. The model contains a number of constants, which are determined by fitting the model to the measured data. Figure 2.17 shows measured and modelled values of the real and imaginary parts of the dielectric constant for wet snow as a function of water content for 6 GHz frequency.

However, to be able to use the Debye-like model [Hallikainen et al., 1986] to predict the dielectric properties of wet snow at 13.8 GHz over a large area (and hence the scattering characteristics), the liquid water content of the snow would have to be know across the area, and whether or not the empirically derived constants held across a large area would have to be determined. Stiles & Ulaby (1980) examine microwave response to snow wetness and conclude that because m_v and the temperature of the snow are not uniform with depth, it is not possible to formulate a direct relationship between σ^0 or ε, and m_v.

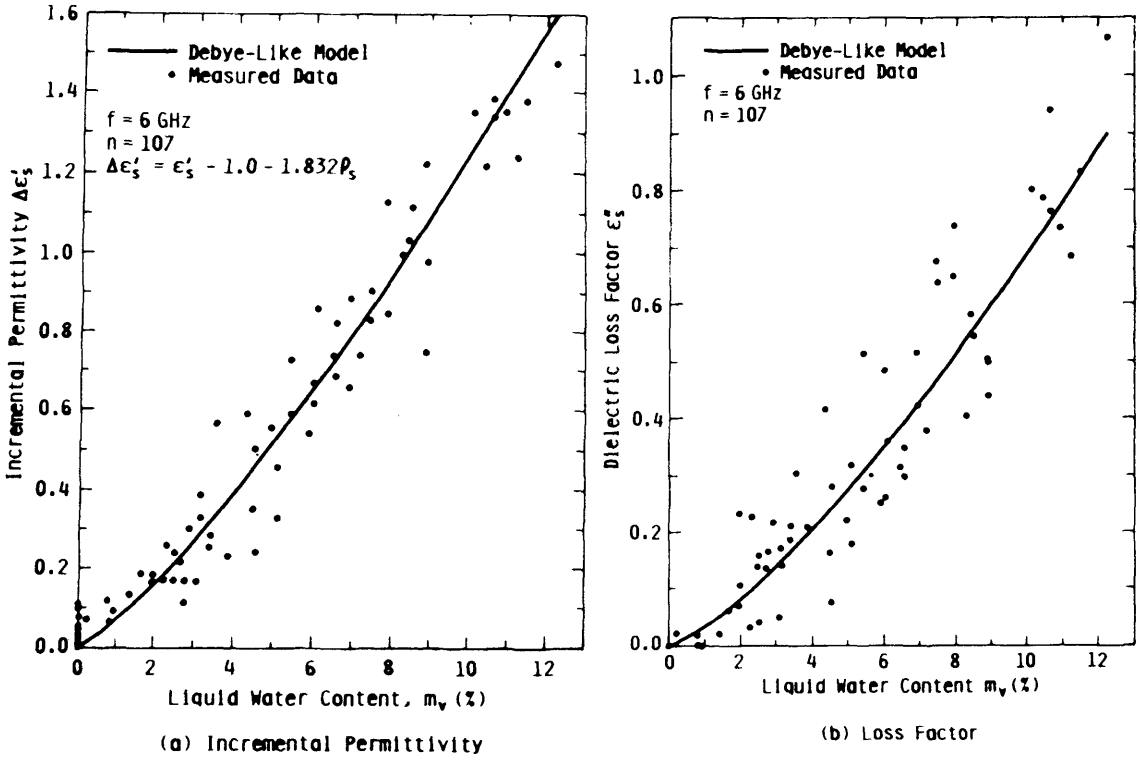

Figure 2.17: a) The real part of the dielectric constant of snow as a function of liquid water content. b) The imaginary part of the dielectric constant of snow as a function of liquid water content. [Hallikainen et al., 1986]

Hallikainen's (1992) review of the dielectric properties of sea ice and snow states that complex dielectric constant (equation 2.4) for wet snow is dominated by its liquid water content [also see Evans, 1965 & Cumming, 1952], and that even with a small volumetric water content (2%) the evidence indicates that radar measurements of the snow ice system will only provide information on the snow layer on top of the ice.

2.7) Modelling radar backscatter from snow covered sea ice

Sections 2.5 and 2.6 describe the physical properties of the ice and snow that affect the radar interaction with the snow/ice system and consider their values at different radar frequencies. These parameters control how far the radiation penetrates into the snow/ice system and depend on a large number of snow and ice conditions (e.g. ice type, salinity

Temperature, brine volume and brine pocket orientation, snow wetness) and on the frequency of the radar. The application of theoretical models to describe the backscatter characteristics is difficult, as it requires detailed data on the statistical properties of the ice and snow conditions [Drinkwater & Crocker, 1988]. The properties of sea ice tend to be inhomogeneous over short distances (section 2.1), and vary in time, which makes in-situ observations expensive and time consuming. Therefore it is not possible to validate the existing models for every snow and ice regime, at different radar frequencies. However, as shown by figures 2.10, 2.11 and 2.17, it is possible to test models while changing only one of the influencing parameters, and to compare the results to observations. These types of tests provide valuable insights into the dielectric properties of snow covered sea ice.

2.8) Variations in the backscatter coefficient with angle of incidence

Before we look at measurements of radar backscatter from snow covered ice surfaces, at Ku band frequencies, we examine the effect of the angle of incidence of the radiation with the ice surface.

A number of studies (see Ulaby et al. 1986) have been conducted to investigate the variation of σ^0 with angle of incidence. Two examples of measurements from Ku band radar, over sea ice, are described below.

Gray et al. (1982) show the change in σ^0 with angle of incidence in both summer and winter conditions. As the angle of incidence increases, σ^0 decreases in both seasons. In the case of MY ice the value of σ^0 during the summer is lower than during the winter.

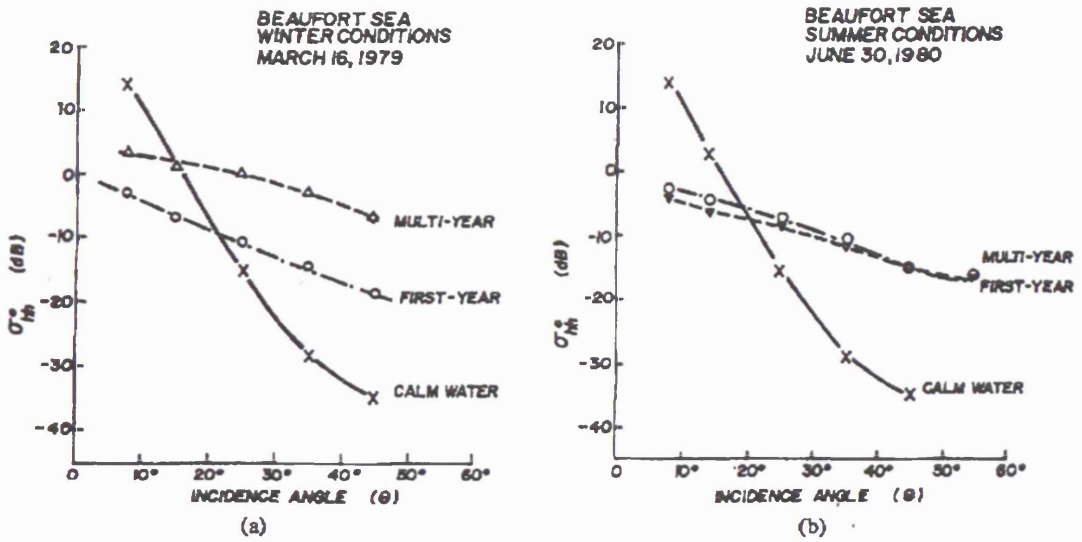

Figure 2.18: Comparison of Ku band backscatter coefficients between winter and summer conditions, at varying angles of incidence. [Gray et al., 1982]

Parashar et al. (1974) show the change σ^0 for angles of incidence from 0° to 60° over different water and ice surfaces in April 1970. As with the data from Gray et al. (1982), σ^0 decreases as the angle of incidence increases. Parashar et al. (1974) also show that rate of decrease with angle of incidence is greater at angles closer to nadir.

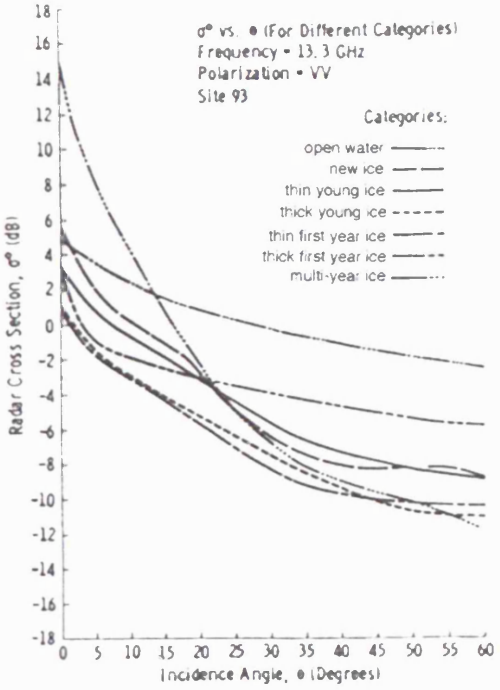

Figure 2.19: Comparison of Ku band backscatter coefficients for different ice categories, at varying angles of incidence. [Parashar et al., 1974]

2.9) Measurements of radar backscatter from snow covered ice sheets, at Ku frequencies, at normal incidence

The evidence presented above shows that the backscattered power from snow covered sea ice is dependent on a number of different parameters including frequency and angle of incidence. The satellite radar altimeters on board ERS1/2, Envisat and CryoSat all operate in the Ku band, and measurements from these satellites are taken at normal incidence. In order to understand the backscatter characteristics of the radiation received by these instruments, specific experiments and models over snow covered sea ice at Ku band frequencies, at normal incidence and in appropriate conditions (i.e. over different ice types, temperatures, salinities for the case of the sea ice and different snow densities and water volume for the snow), must be analysed. Logistically this is very difficult [Carsey et al., 1992] and very few studies incorporating even a few of the above criteria have been made.

Lytle et al. (1993) use laboratory grown, snow covered, thin (0 to 9 cm) urea ice[5], to study radar backscatter data at 13.9 GHz, collected at normal incidence to 55°. They found that the dominant scattering mechanism was from surface scattering at the snow/ice interface. Beaven et al. (1995) use laboratory grown, snow covered, thin (0.5 to 12 cm) saline ice, to study radar backscatter data at 13.4 GHz, collected at normal incidence to 55°. By placing a metal plate on top of the snow and measuring the radar return from this plate they provide a 'range marker' to the snow surface. The metal plate was then removed and the return from the snow covered saline ice sheet recorded. Their result is shown in figure 2.20. The peak of the return from the snow covered ice appears 20 cm further in range, corresponding to the snow/ice interface.

[5] Urea ice has a similar structure to sea ice but does not corrode the equipment like salt water does.

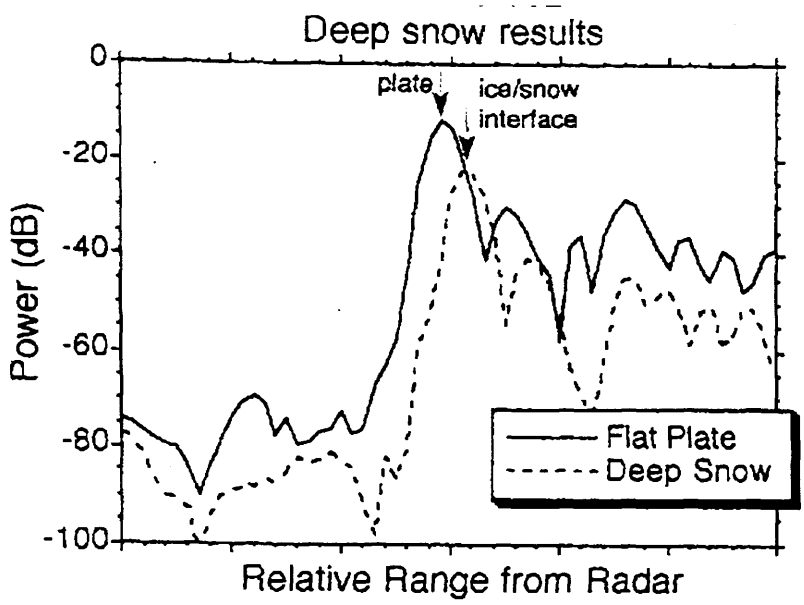

Figure 2.20: Comparison of Ku band radar returns at 0° incidence angle from a 21 cm snow pile over laying 12 cm of saline ice and a metal plate on top of the snow pile. This demonstrates that the return from the snow-covered saline ice is dominated by scattering from the snow/ice interface. [Beaven et al., 1995]

2.10) Summary

- The electromagnetic properties of sea ice depend on the electromagnetic properties of ice and brine, the volume of brine and the shape and orientation of the brine inclusions. Changes in frequency, angle of incidence, temperature, salinity and ice type (i.e. FY or MY), can all alter the electromagnetic properties of sea ice.

- The electromagnetic properties of snow depend on the electromagnetic properties of ice and water, the snow density, the ice particle shape and the water volume. Changes in frequency and temperature can alter the electromagnetic properties of snow.

- We have shown that radiation from a radar altimeter with a frequency of 13.8 GHz should penetrate through any reasonable dry snow depth, provided that the temperature is constantly below 0°C.

- Laboratory evidence suggests that the dominant scattering mechanism in snow covered sea ice is surface scattering from the snow/ice interface. However, these experiments were performed on a small section of saline ice or urea ice. The evidence presented above indicates that electromagnetic properties of snow covered sea ice change with a large number of parameters, which were not varied in the experiments by Lytle et al. (1993) and Beaven et al. (1995).

- Models of the radar interaction with the snow/sea ice system do exist. However, they are difficult to validate without detailed data on the statistical properties of the ice and snow conditions. In-situ observations to collect such a data set would be expensive and time consuming. Therefore other methods to investigate the radar interaction with the snow/ice system must be considered.

- The alternative to collecting vast amount of in situ data on the ice and snow conditions, and using it to validate models, is to conduct an airborne field campaign. Taking simultaneous measurements from radar and laser altimeters over snow covered sea ice will allow us to gain further insight into the scattering problem.

3) Principles of radar and laser altimetry and the Laser Radar Altimetry (LaRA) field campaign

3.0) Introduction

In this chapter we describe the principles of radar and laser altimetry, give examples of their uses, and advantages and disadvantages (sections 3.1 and 3.2). In section 3.3 we introduce the Laser Radar Altimetry (LaRA) field campaign, which involved simultaneous measurements, over sea-ice, from airborne laser and radar altimeters. Section 3.3.1 describes the LaRA payload. Sections 3.3.2 to 3.3.6 give detailed descriptions of each of the instruments carried during LaRA. Section 3.3.7 describes the layout of the instruments on board the aircraft and section 3.3.8 describes their footprint geometry. Sections 3.3.9 to 3.3.11 describe the flights that took place as part of LaRA. Section 3.3.12 describes the georeferencing of the measurements. Sections 3.3.14 to 3.3.17 describe the data processing performed outside of UCL and the data format for each of the instruments. We end the chapter with sections (3.4. and 3.5) describing the Applied Physics Laboratory (APL), at John Hopkins University, calibration of the radar data and their initial comparison of radar data and laser data.

3.1) Radar altimetry principles

3.1.1) Elevation measurement

Radar altimeters measure the two way travel time of a radar pulse to the surface below. The height of the altimeter above the surface is given by:

$$h = \frac{t_r c}{2} \tag{3.1}$$

where h is the height, t_r is the round trip travel time and c is the speed of light. The accuracy of the height estimation is determined by the altimeters range resolution which is given by equation 3.2:

$$\Delta h = \frac{c\tau}{2} = \frac{c}{2\Delta F} \tag{3.2}$$

where τ is the compressed pulse length, and ΔF is the instrument bandwidth. The signal to noise ratio of the measurement is improved by averaging the data. [Raney, 1999, Mantripp, 1996]

There are two modes of operation for a radar altimeter. Pulse limited or beam limited.

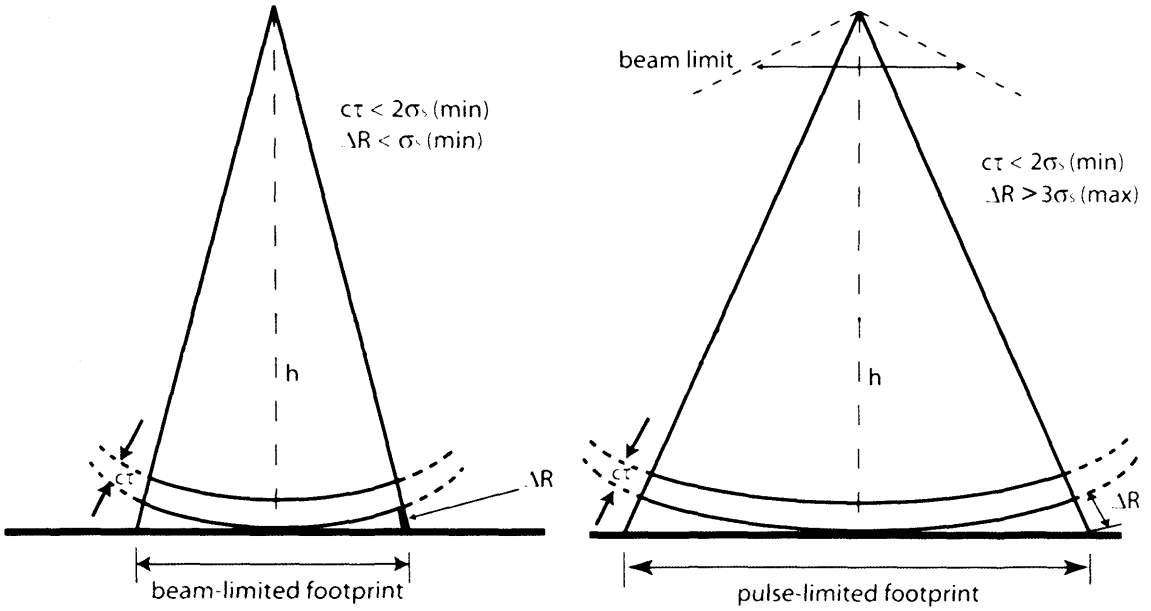

Figure 3.1: Beam limited and pulse limited altimeter operating modes. c is the speed of light, τ is the compressed pulse length, h is the height of the altimeter above the surface, σ_s is the surface roughness and ΔR is the curvature of the beam. [redrawn from Mantripp, 1996]

Although beam limited altimeters are conceptually simpler, pulse limited altimeters are used for spaceborne earth observation due to the following. To meet the constraints shown in figure 3.1, a beam limited satellite altimeter, at the same altitude as ERS, would need an antenna of diameter greater or equal to 9.7 m, and would also require a pointing accuracy of less than or equal to 0.016°, resulting in a very large and expensive instrument. Pulse limited altimeters are therefore used in spaceborne missions, as they require a much smaller antenna (1.2 m for ERS) and less severe pointing requirements.

3.1.2) Pulse limited geometry

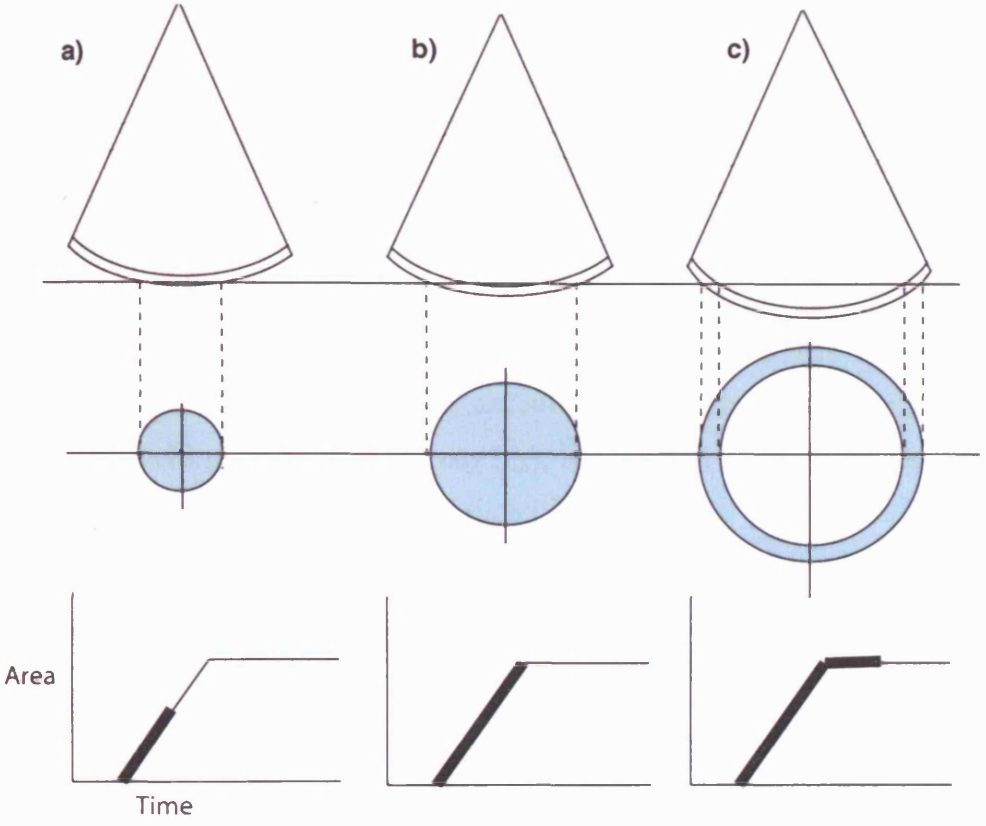

Figure 3.2: Pulse limited geometry. [redrawn from Mantripp, 1996]

Figure 3.2 shows the geometry for a pulse limited operation. The pulse of energy moves away from the antenna as an expanding spherical shell whose thickness is the pulse length. As the pulse intersects the surface, the disk illuminated increases with time (figure 3.2: a). This continues until the rear of the pulse intersects the surface at which point the illuminated area is equal to the pulse limited footprint (PLF) (figure 3.2: b). The pulse now expands as an annulus with area equal to the pulse limited footprint (figure 3.2: c). The size of the PLF increases with surface roughness.

3.1.3) Pulse transmission and reception

As shown by equation 3.2, the range resolution is dependant on the pulse length. Therefore it is desirable to have as short a duration pulse as possible. However, a radar altimeter must be able to receive a signal over the receiver noise. This requires a large initial signal power. In order to achieve the short pulse, high power requirements, pulse

compression techniques are used. This allows a long-duration low power, but high energy, pulse to be transmitted that, after compression, behaves like a short duration, high power pulse with the same energy [Mantripp, 1996]. The frequency of the transmitted pulse is increased at a constant rate over the uncompressed pulse length (τ'). The frequency change over the pulse is ΔF (the bandwidth) and the centre frequency is F_0. This process is known as a linear chirp or ramp. When the signal arrives back at the radar it is passed through an amplifier and mixed with a locally generated signal. The end result is an intermediate frequency (IF) signal whose frequency is equal to the difference between the received and locally generated signal. A deramping chirp, identical to the transmitted chirp, except that its centre frequency differs from the transmitted chirp by the IF frequency (f_{IF}), is generated at a time lag that corresponds to the time (t_d) when the transmitted signal is expected to be received from the surface. [Chelton et al., 1989]. Figure 3.3 illustrates this concept.

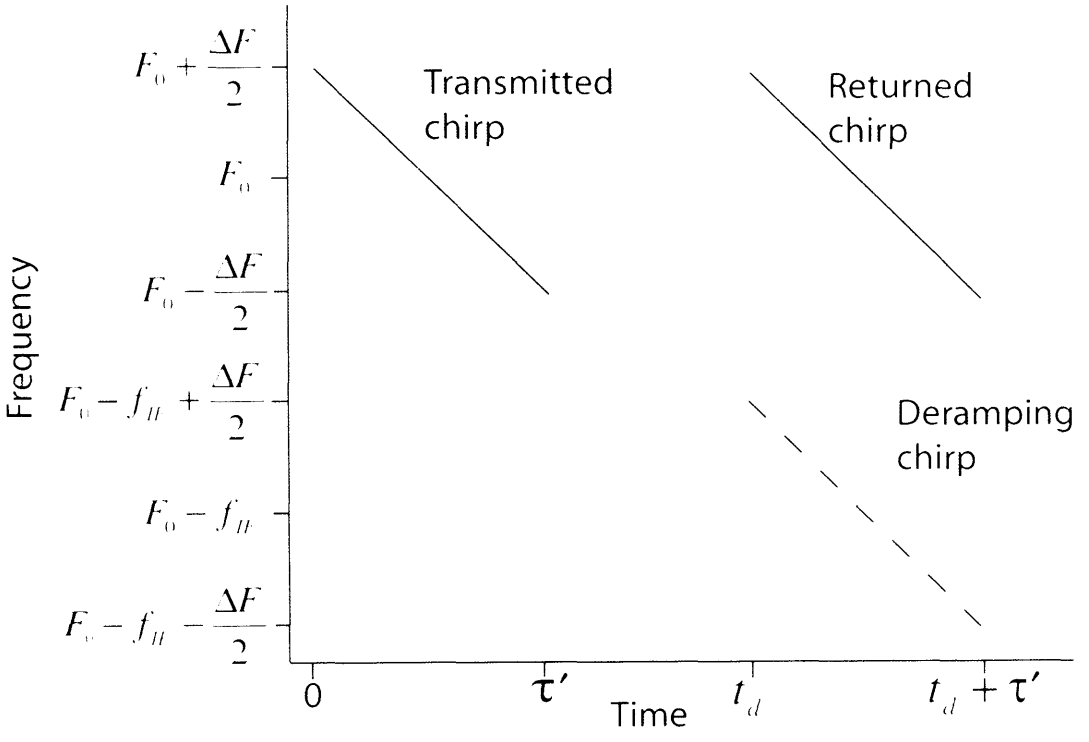

Figure 3.3: Schematic representation of a chirp transmitted by a radar altimeter at time zero. The chirp frequency, centred on F_0, decreases linearly by ΔF over the uncompressed pulse length τ'. A deramping chirp is generated by the altimeter at time t_d, which is the expected arrival time of the returned pulse from the surface. The deramping chirp is identical to the transmitted chirp except that its frequency is lower by an amount f_{IF}. [redrawn from Chelton et al., 1989]

If t_d is timed exactly to match the two-way travel time to the surface then the frequency of the deramped signal will be equal to f_{IF}. However, if the deramping chirp is generated at a time Δt_d earlier (later) than the time the signal is returned (t_1), then the frequency of the deramped signal will be higher (lower) than f_{IF} by an amount:

$$\Delta f' = Q_c \Delta t_d \tag{3.3}$$

where $Q_c = \Delta F / \tau'$ and $\Delta t_d = t_1 - t_d$ [Chelton et al., 1989]. Figure 3.4 illustrates this concept.

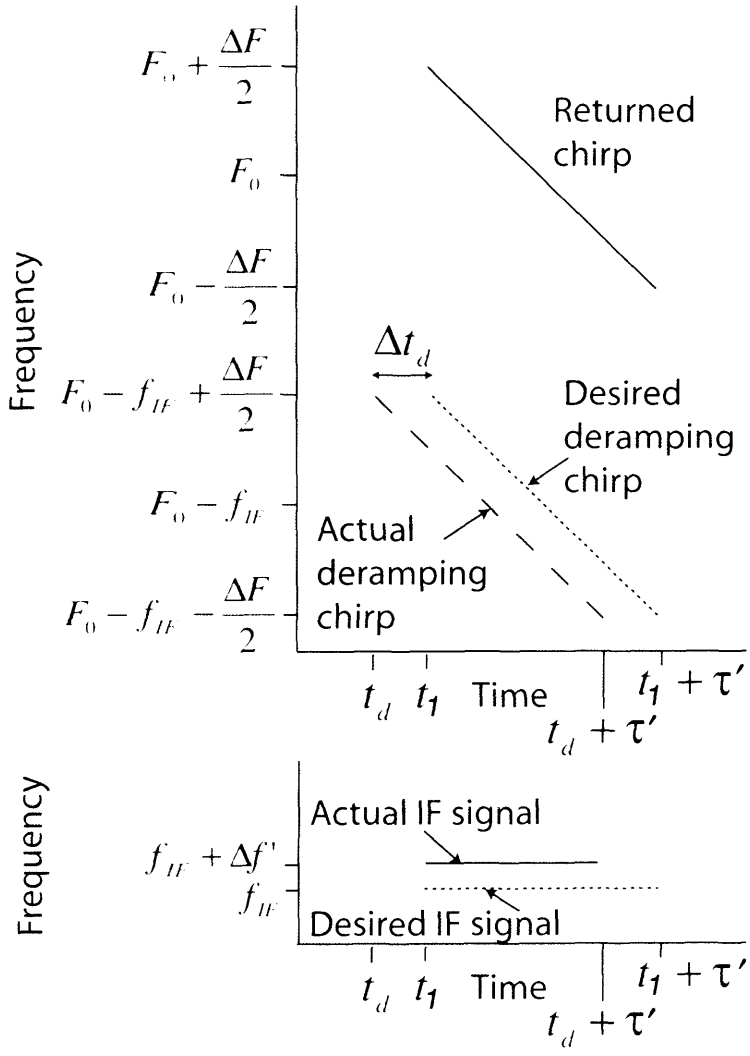

Figure 3.4: Top plot: Schematic representation of a chirp returned from a surface at time t_1. Ideally the deramping chirp would also start at t_1 but it starts at t_d. Bottom plot: Shows the desired IF signal i.e. the signal that would have been produced if the deramping chirp had begun at t_1. The actual IF signal is shown by the solid line. It lies above the IF frequency by $\Delta f'$. [redrawn from Chelton et al., 1989]

In this section we have imagined a single signal returned from a point on the surface. In reality the radar receives many signals from scatterers on the surface. The total returned signal is the sum of the returned chirps from all the scattering elements on the surface. We now describe the total signal (waveform) received from a surface, using the open ocean as an example.

3.1.4) Waveform convolution

When a signal is returned from a surface, its resulting shape ($P_t(t)$) is a convolution of the functions describing the radars point target response ($S_r(t)$) and the average surface impulse response ($P_I(t)$):

$$P_r(t) = S_r(t) \otimes P_I(t) \tag{3.4}$$

$P_I(t)$ is given by the convolution of the height probability density function of the specula points on the surface ($q(z)$) with a term ($P_{FS}(t)$) dependant on the antenna gain, σ^0, which varies with angle, and the range from the radar to the surface.

$$P_I(t) = q(z) \otimes P_{FS}(t) \tag{3.5}$$

[Brown, 1977]

Figure 3.5 shows the form of these three functions over the open ocean and the result of their convolution. $S_r(t)$ and $q(z)$ are assumed to have Gaussian forms, $P_{FS}(t)$ rises to a maximum power when a pulse of infinitesimal width would reach the surface, and the trailing edge has an exponential decay to account for the antenna response pattern.

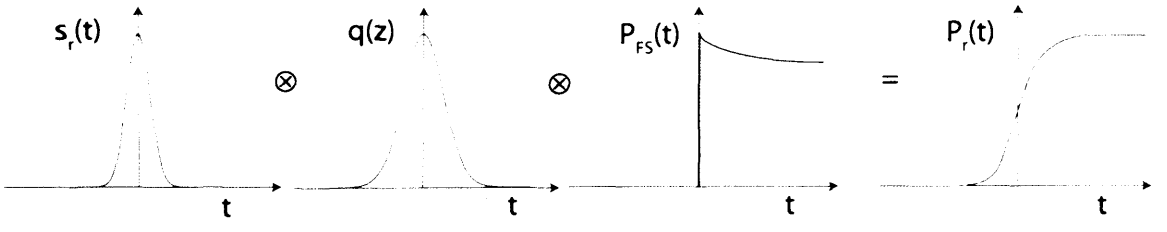

Figure 3.5: A typical return echo over the open ocean.

As figure 3.5 illustrates, it is the half-power point, which gives the range to the mean sea level. In fact, this is true for any surface with a Gaussian height distribution.

3.1.5) Waveform averaging

Individual echoes exhibit large power fluctuations. A return from a rough surface consists of returns from many small specular facets, each return will have a slightly different phase depending on its range from the altimeter. Waveforms are therefore averaged to reduce the fluctuations. However, each waveform must be a statistically independent sample. The maximum pulse repetition frequency (*prf*), to ensure statistical independence, depends on the surface roughness and the orbital velocity.

$$prf_{\max} = \frac{4V_s}{\lambda}\sqrt{\frac{c\tau}{h}} \tag{3.6}$$

where V_s is the orbital velocity, and λ is the wavelength. The number of echoes used for each average must be sufficient to reduce fluctuations enough to provide a good estimate of height and backscatter, but not so many that the along track spatial resolution is degraded beyond an acceptable limit.

3.1.6) Waveform sampling

From equation 3.3 there is an equivalence between two-way travel time (and therefore range) and frequency. To use this relationship to determine the range, the returned waveform must be spectrally analysed. The waveform is sampled in the time domain and undergoes a Fourier transform to covert it to the frequency domain. The effective two-way travel time resolution is equal to $1/\Delta F$. [Chelton et al., 1989]

3.1.7) Advantages and disadvantages of pulse limited radar altimetry

Radar altimeters have been used for earth observation as the pulse attenuation at microwave frequencies, due to the atmosphere, is small. They also have an all weather capability. However, there are two main disadvantages of pulse limited operation:

Firstly, the PLF diameter is less than the full antenna pattern. This means that a large proportion of the radiated power falls outside of the PLF, and cannot be used for height estimation; Secondly, over rough or sloping terrain, performance is degraded. For example, over rough terrain the footprint is enlarged, leading to a less optimal estimate of surface height. [Raney, 1998]. Over an undulating surface, the footprint tends to hop from one elevated region to another, rather than follow the true profile of the surface, resulting in a bias in the elevation estimate. The effect of a sloping surface is illustrated in figure 3.6.

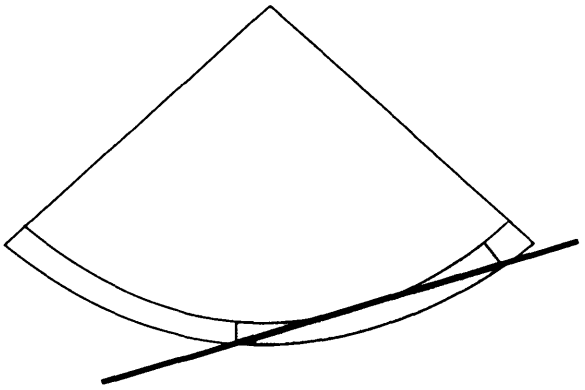

Figure 3.6: The effect of a sloping surface to a pulse limited altimeter. The measurement area moves from nadir. [redrawn from Jensen, 1999]

The sloping surface moves the measurement area away from nadir because the measurement area always is centred around the point on the surface nearest to the altimeter. For example: a satellite with an altitude of 800 km and a surface slope of 0.1°, the distance to the nearest point on the surface is 1.2 m less than the distance to the nadir point. [Jensen, 1999] This is not a problem over sea ice or the ocean as their surfaces are relatively flat, but it is an issue over land ice.

3.1.8) Pulse limited radar altimetry missions

The first ocean monitoring radar altimeter was flown on board NASAs Skylab in 1973. Skylab had a resolution of 15 m and could identify coarse features of the marine geoid such as major ocean trenches. Skylab was followed by GEOS-3 in 1976, which had improved performance and greater global coverage than Skylab, but could only resolve the largest oceanographic features. [ESA, 2005]. Seasat, launched in 1978, was the first dedicated oceanographic satellite. Seasat was launched into a near circular polar orbit

with measurements extending to ±72° latitude. However, only 99 days of data were collected during the mission as it failed due to a short circuit in the satellite electrical system. Nevertheless, during the short time Seasat was operational it provided decimetre-accurate range measurements over the ocean [JPL, 1998]. GEOSAT, launched in 1985, also measured up to ±72° latitude and provided information on the motion of large-scale ocean currents, such as the Gulf Stream. However, it could not resolve smaller surface height variations such as those caused by El Niño. [Vazquez, 2002]. ERS-1, launched in 1991, and its followon mission ERS-2, launched in 1995, have provided estimates of surface wave height and wind speed with an accuracy of a few centimetres, providing information on small scale changes in sea level during events such as El Niño [ESA, 2003]. The ERS altimeters were the first high latitude spaceborne altimeters, with measurements extending up to ±81.5° latitude. TOPEX/Poseidon, launched in 1992, was the first altimetric satellite dedicated to mapping ocean topography. It provided maps of sea level changes as small as 2 cm [Vazquez, 2002]. Envisat, launched in 2002, into the same orbit as the ERS satellites, carries an improved radar altimeter (RA-2) to those on board the ERS satellites. CryoSat, due to be launched in 2005, will carry an enhanced radar altimeter with synthetic aperture processing in the along track direction and two antennas to measure the surface slope, which will further improve measurement precision. The satellite will have the furthest latitudinal extent of any of the altimeters discussed here, with measurements between ±88° latitude The satellite is designed to measure variations in thickness of the continental ice sheets and sea ice cover [Wingham, 1999].

3.2) Laser altimetry principles

3.2.1) Elevation measurement

Laser altimeters operate on the same principle as radar altimeters. They transmit a laser pulse to a surface, and measure the two way travel time, and then convert the time to a distance. The travel time is measured when the return pulse triggers a threshold detector based on intensity. The accuracy with which the travel time can be determined depends on the signal to noise ratio, which depends on: the reflectivity of the surface; the range;

the transmitted power; the amount of incident sunlight, the weather and atmospheric attenuation. [Rees, 2001]

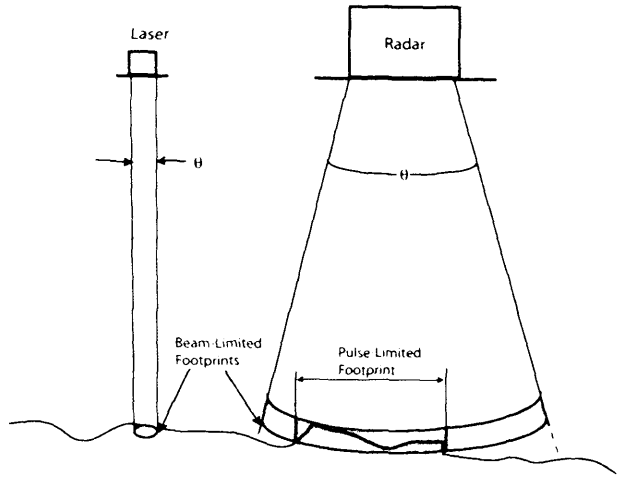

Figure 3.7: Comparison of laser and radar altimetry [Bufton, 1989]

Figure 3.7 compares the footprints from laser and radar altimeters. The laser footprint on the target surface is small compared to the radar footprint. For example, the diameter of the ERS PLF is 1.7 km where the diameter of an ICESat footprint is 60 m [Zwally et al., 2002]. The small footprint is due to the sub-milliradian diffraction of the optical beam from the antenna [Bufton, 1989]. In laser altimetry the pulse- and beam-limited footprints are identical as the beam width is of the order of milliradians. A typical radar altimeter has a beamwidth of degrees, for example the ERS 3dB beam width is 1.3° .[Bufton, 1989]

Horizontal resolution depends on two factors: the footprint size and the spacing between them. Beam divergence and the altitude of the altimeter determine the footprint size; pulse repetition rate and altimeter velocity determine the spacing between footprints. [Bufton, 1989]

3.2.2) Advantages and disadvantages of laser altimetry

Laser altimeters overcome the problems of radar altimeters described in section 3.1.7. As the laser footprint is small in comparison with a pulse limited radar footprint it provides a high accuracy measurement over sloping surfaces [Ishizu, 2002], and all of the radiated power falls within the laser footprint [Raney, 1999]. However, atmospheric scattering and the effect of clouds in the path of the laser pulse, result in a potentially

large error source for the precision of the altitude measurement. Using altimetry measurements made only under cloud free or optically thin cloud conditions reduces the altitude bias [Mahesh et al., 2002], but result in areas with no surface measurements.

3.2.3) Laser altimetry missions

Spaceborne laser altimetry has been used for mapping planetary surfaces over the past 10 years. Clementine, launched in 1994, provided a large scale topographic map of the moon, with a vertical resolution of 40 m and a horizontal resolution of 100 m [Williams, 2002]. In 1996, the NEAR mission's laser altimeter provided a topographic map of the asteroid 433 Eros, with meter-level accuracy [Luthcke et al., 2002]. Also in 1996, NASA launched the Mars Global Surveyor, which carried the Mars Orbiter Laser Altimeter 2 (MOLA-2). MOLA-2 provided geoid, topographic, surface roughness and surface change maps of Mars, and observed clouds, snow and geographical features such as volcanoes. The accuracy of the height data was limited to 5 m. [Ishizu, 2002 & Luthcke et al., 2002]

Earth observation using laser altimeters has been limited. In the 1980s and early 1990s only low resolution instruments were flown on Earth orbiting platforms [Luthcke et al., 2002]. In 1996 and 1997, the Laser Altimeters 1 and 2 (SLA-01, SLA-02) were carried onboard the Space Shuttles launched by NASA. These laser altimeters measured land and ocean elevation, cloud-top height and vegetation. [Ishizu, 2002]. With the launch of the Ice, Cloud and Land Elevation Satellite (ICESat) mission in January 2003, Earth observing laser altimetry has entered a new phase. ICESat has the potential to produce a time series of elevation changes of the ice sheets, measure cloud heights and the vertical structure of clouds and aerosols, land topography, vegetation canopy heights and various sea ice parameters. The predicted accuracy of the surface elevation measurements is 15 cm. [Zwally et al., 2002, Kwok et al., 2004]

3.2.4) Summary of radar and laser altimetry

In general, laser and radar altimeters overcome the disadvantages associated with the other instrument. While laser measurements may only be made in cloud free conditions, radar has an all weather capability. Where the radar accuracy degrades over sloping

surfaces the laser can provide a high accuracy measurement due to its smaller footprint. The smaller footprint of the laser has a second advantage in that, over sea ice, the radar's large footprint results in a higher percentage of mixed water and ice returns within the footprint while the laser's smaller footprint can provide a better resolution between water and ice.

Clearly the potential of combining measurements from laser and radar altimeters is desirable. In chapter 1, sections 1.5 and 1.6, we described the uncertainties associated with the estimate of sea ice thickness from both radar and laser altimeters. To recap: Firstly, the equation for calculating sea ice thickness from radar altimetry is based on the assumption that the radar return originates from the snow/ice interface, but the degree to which this assumption holds is not well known. Secondly, the uncertainty in the snow load contributes an error to the estimate of sea ice thickness from both radar and laser altimetry. In laser derived estimates of sea ice thickness the snow load is the largest uncertainty. Many studies using laser altimetry over sea ice are based on the assumption that the laser reflects from the air/snow interface over snow covered ice (see chapter 4, section 4.3). Therefore analysing coincident radar and laser measurements will allow us to investigate the relative penetration characteristics of the radar, and the potential of estimating snow depth from combined radar and laser altimetry data over snow covered sea ice.

The LaRA field campaign offered the unique opportunity to investigate coincident (in space and time) data from a laser and a radar altimeter.

3.3) Laser Radar Altimetry (LaRA) field campaign

LaRA took place in May 2002 and was funded by ESA, NASA and NOAA. It was an add on to two NASA missions; Arctic Ice Mapping (AIM) 2002 and ICESat Cal/Val. We begin with a description of the LaRA payload.

3.3.1) LaRA payload

Figure 3.8: The LaRA team and the P-3 on the runway at Svalbard, May 2002.

Flights took place onboard the NASA P-3 aircraft, which carried: the John Hopkins University, Applied Physics Laboratory (JHU/APL) Delay/Doppler Phase-monopulse (D2P) Radar Altimeter; two NASA laser altimeters, the Airborne Topographic Mappers (ATM2 and ATM3, ATM 2 operated in profiling mode while ATM3 operated in scanning mode); two digital cameras mounted on the fuselage, taking images of the ice below. The P-3 was also equipped with a Global Positioning System (GPS) receiver and an Internal Navigation System (INS). Sections 3.3.2 to 3.3.6 describe the payload in detail.

3.3.2) The Delay/Doppler Radar Altimeter

The Delay/Doppler Radar Altimeter (D2P) was designed and built at the Johns Hopkins University Applied Physics Laboratory (JHU/APL). The D2P resolves some of the problems that occur with conventional pulse limited altimetry (section 3.1.7). The entire beam limited footprint in the along track direction is used to obtain height estimations as opposed to just using the PLF and the use of a synthetic aperture in the along track direction reduces the width of the post processing along track footprint. This minimises the terrain dependency of the footprint size and position. Figure 3.9 illustrates the difference between pulse limited radar altimetry and the D2P radar altimeter. [Raney, 1998]

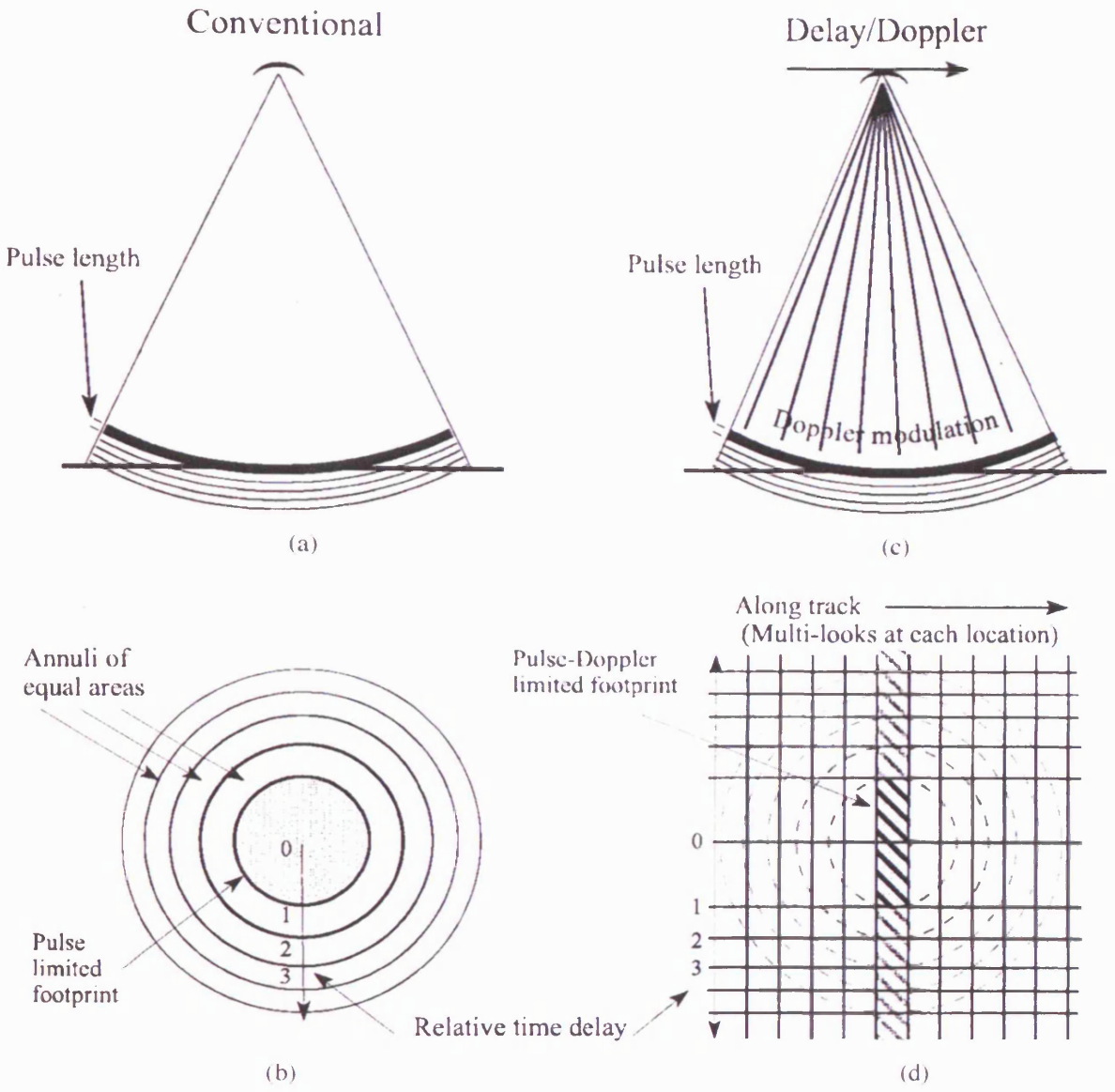

Figure 3.9: Comparison of a conventional pulse limited radar altimeters (a) illumination geometry side view and (b) footprint plan view and a D2P (c) illumination geometry side view and (d) footprint plan view. [Raney, 1998]

The second advantage of the D2P over conventional pulse limited radar altimetry is that it has two antennas which both record the phase of the return. The difference in the phase between to two antennas at the re-track point indicates the angle to the point of first reflection from the scattering surface. [Jensen, 1999]

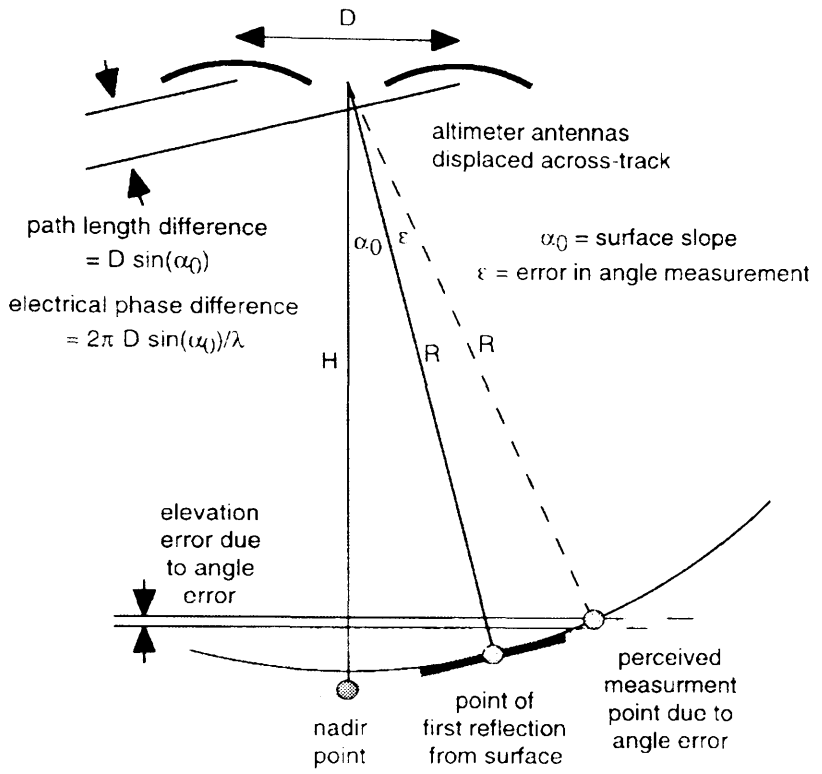

Figure 3.10: Angle measurement for the D2P. Without an angle measurement, the range is taken to be the distance to the nadir point. However, with two receiving antennas, the phase difference can determine the horizontal and vertical position of the measurement point. [Jensen, 1999]

The radar altimeter on board CryoSat also employs synthetic aperture processing in the along track direction and has two antennas to measure surface slope. The along track synthetic processing generates a footprint size of ~ 300 m by 1 km (as compared with ~ 10 km of the pulse limited systems and 60 m of the laser systems) [Wingham[2] et al., 2004].

We now describe the synthetic aperture processing in detail:

The D2P transmits a burst of 16 coherent pulses that form a synthetic aperture in the along track direction. The received signals from each burst are stored and an along track Fourier transform is applied to these data. The result of the Fourier transform is that the along track location of each scatterer is known relative to the D2P nadir. The method relies of Fourier shift theorem, which states that a translation in position in the spatial domain introduces a linear phase shift in the frequency domain [Steward, 1987].

Expanding the discussion in Raney (1998), let the along track signal history for each scatterer be *a(x)* . Let x_0 be the D2P nadir and x_n be the along track position of the nth scatterer. Fourier transform theory gives us the Fourier transform pair:

$$f(x) = \int_{-\infty}^{+\infty} F(u) e^{2\pi i u x} du$$

$$F(u) = \int_{-\infty}^{+\infty} f(x) e^{-2\pi i u x} dx \qquad (3.7)$$

[Steward, 1987]

Let $f(x) = a(x - x_n + x_0)$ and u become f (frequency in the along track direction) and therefore *F(u)=A(f)*. By substituting into equation 3.7:

$$F[a(x - x_n + x_0)] = \int_{-\infty}^{+\infty} a(x - x_n + x_0) e^{-i 2\pi f x} dx$$

$$F[a(x - x_n + x_0)] = \int_{-\infty}^{+\infty} a(x - x_n + x_0) e^{-i 2\pi f x} dx dx$$

$$= \int_{-\infty}^{+\infty} a(x) e^{-i 2\pi f (x + x_n - x_0)} dx \, e^{-i 2\pi f x} dx$$

$$= e^{-i 2\pi f (x_n - x_0)} A(f) \qquad (3.8)$$

The exponential term carries the phase change (Doppler frequency) corresponding to the shift in position. Once the Fourier transform has been applied to all received signals in a burst, the result is a set of measurements whose along track position, relative to the D2P nadir (zero Doppler), is known in terms of a phase change. The Doppler frequency is equivalent to the (along track) angular offset from the nadir position. As the angular offset of a scatterer is known, the extra range delay for a scatterer away from nadir can be calculated. The result is that the range delay for scatterer away from nadir is the same as the range delay as if the scatterer were at nadir. Hence the height of scatterer (h_n) away from nadir is computed. Figure 3.11 illustrates this concept

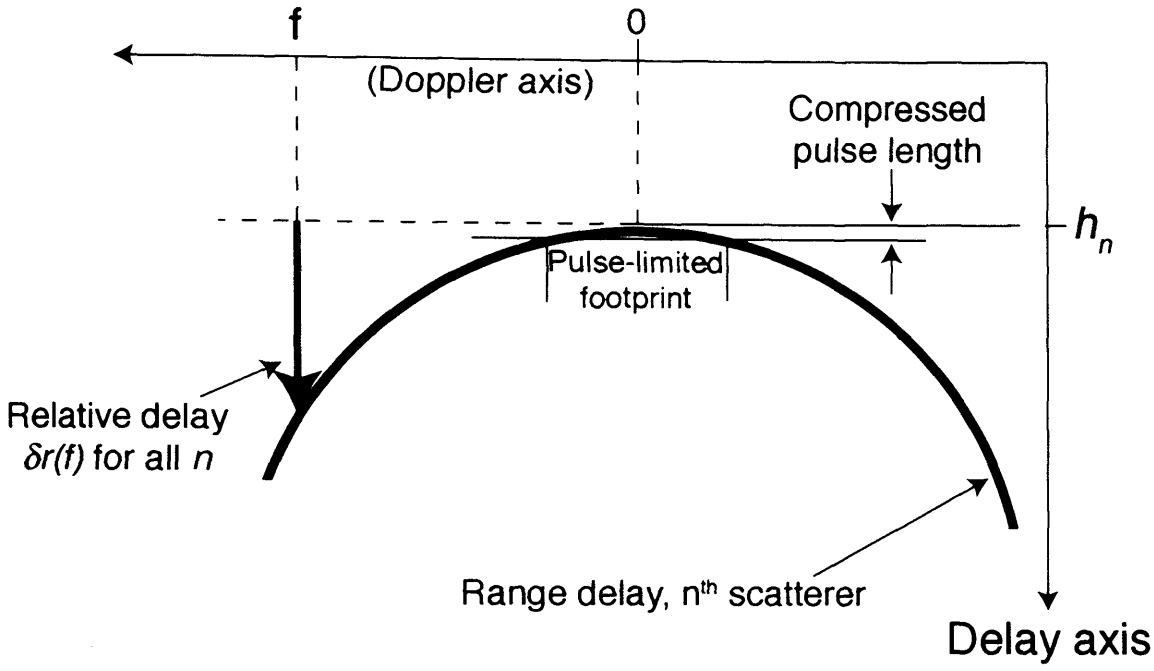

Figure 3.11: The extra delay ($\delta r(f)$) at a scatterer, due to the curvature of the transmitted pulse can be calculated as it is a known function of Doppler frequency (f). h_n is the height at nadir of the nth scatterer. [Redrawn from Raney, 1998].

As subsequent bursts overlap, each scatterer is multilooked a number of times (depending on the aircraft velocity and the pulse repetition rate). The looks are summed to produce the return waveform, reducing the signal to noise ratio.

As a consequence of the processing described above, the D2P's flat surface response has a different shape to that of a conventional pulse limited altimeter. Recall figure 3.2, a conventional pulse limited flat surface response is a step function because return from scatterers outside the pulse limited footprint arrive at the receiver later in time than those within the pulse limited footprint, therefore they contribute to the trailing edge of the return rather than to the leading edge where the range measurement is made. In contrast, the D2P flat surface response is an impulse like return, as shown in figure 3.12.

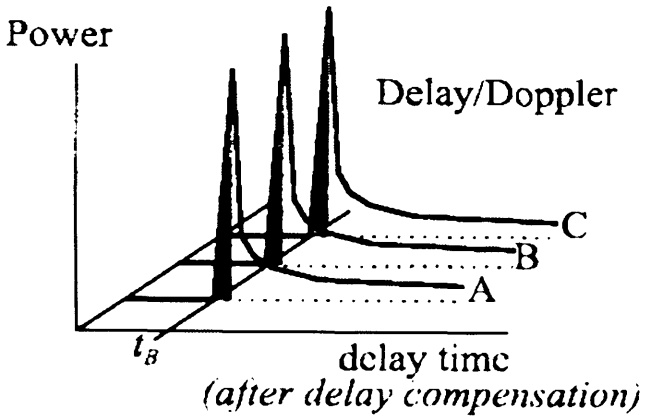

Figure 3.12: Flat surface impulse response for the D2P [Raney, 1998]

As described above, returns from scatterers away from nadir can be corrected for the extra delay time taken by the pulse (due to its curvature) to reach the scatterer. Therefore scatterers away from nadir contribute to the leading edge of the return rather than the trailing edge and can be use in the range measurement.

In sections 3.1.3 to 3.1.6 we described the operation of a conventional pulse limited altimeter. We now use these sections as a basis to describe how the D2P operates. Information on the D2P can also be found in Raney and Jensen, (2001) and Raney, (2002).

Pulse transmission

The D2P transmits a linearly frequency modulated pulse. The chirp generator has a fixed start frequency of 197.5 MHz and stop frequency of 152.5 MHz. The ramp rate depends on the pulse length. The output of the chirp generator is a 175 ± 22.5 MHz signal. This signal is doubled to a 350 ± 45 MHz for use by the frequency generator where it is mixed with a 3125 MHz waveform to produce a 3475 ± 45 MHz waveform. The transmitter then multiplies the waveform by four to the final Ku-band frequency of 13900 ± 180 MHz (i.e. F_0 = 13.9 GHz and ΔF = 360 MHz).

Pulse sampling

The received signal is always sampled at 166.67 MHz (or 6 nseconds). As an example: for the longest pulse length (3.072 μseconds) the signal is sampled 512 times (512 × 1/166.67 MHz = 3.072 μs).

Pulse reception

The receivers deramp the received pulse in three stages.

1) The received signals are mixed with a chirped waveform that is identical to the transmitted chirp other than having a centre frequency 750 MHz lower than the transmitted chirp (i.e. f_{IF} = 750 MHz). The chirp rate is changed for each pulse length to obtain the 360 MHz bandwidth.
2) An 1000 MHz signal is used to convert the 750 MHz signals to a 250 MHz signal
3) A 291.667 MHz signal is used to convert the 250 MHz signal to a 41.667 MHz signal.

This down conversion is modelled after the TOPEX frequency plan [Carl Leuschen, personal communication].

D2P specific operations

In every coherent burst of pulses the range word of the first pulse is used as a reference. The range word describes the delay between the transmitted pulse and the deramping chirp (t_d). If a pulse within the burst has a different range word then a frequency shift is applied to the pulse so that its range word is the same as the reference.

The effect of the vertical velocity of the aircraft must be removed otherwise the shift in phase, caused by the vertical velocity, will affect determination of the location of the scattering area in the along-track direction. The vertical velocity is assumed to be constant within a burst of pulses, and a phase shift is added to the waveforms to counteract this effect.

Figure 3.13 shows a schematic representation of a burst of pulses. Each pulse within the burst illuminates a narrow strip on the ground, known as a Doppler bin.

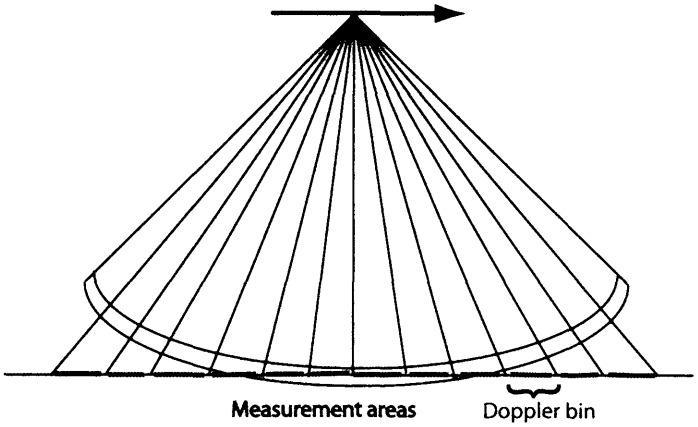

Figure 3.13: Schematic representation of a burst of pulses [redrawn from Raney & Jensen, 2001]

As the aircraft moves, the next burst of pulses will overlap the Doppler bins from the previous burst. However, the aircraft only moves a fraction of the Doppler bin width and therefore the centre of the Doppler bins from the consecutive bursts will not line up. In order to sum the measurements from consecutive bursts over each Doppler bin the bins must be shifted so that they overlap. This is achieved by applying a phase shift to each consecutive burst, and is known as beam steering.

The processing steps, after the deramp, are as follows:

A burst of pulses is read in and corrected for changes in the range word and the vertical velocity of the aircraft, and the burst is beam steered so that its Doppler bins coincide with adjacent bursts Doppler bins. The burst then undergoes an FFT in the along-track direction that relates the along-track position of all scatterers, relative to the radar nadir, to a phase shift (as described above). As the position of the scatterers in the along-track direction is now known the extra range delay due the curvature to the transmitted pulse can be calculated. The signals are zero-padded by a factor of 2 and undergo a range FFT (as in conventional pulse limited altimetry). This process is repeated for the next burst and the resulting signals are summed in each Doppler bin.

3.3.3) D2P Characteristics

Table 3.1 lists the various D2P radar characteristics:

Parameter	Value
Frequency (GHz)	13.9
Pulse Lengths (Microseconds)	3.072, 1.536, 0.768, 0.384
Pulse Band Width (MHz)	360
Peak Transmit Power (W)	5
Pulse Repetition Frequency (Hz)	1750
Antenna Size (cm)	Cross-track 15 Along-track 30
Antenna Gain (dBi[1])	27
Across-track 3dB Beamwidth (deg)	8
Along-track 3dB Beamwidth (deg)	4

Table 3.1: D2P radar characteristics [Raney & Leuschen, 2003, Raney, 2002].

3.3.4) The ATM laser altimeters

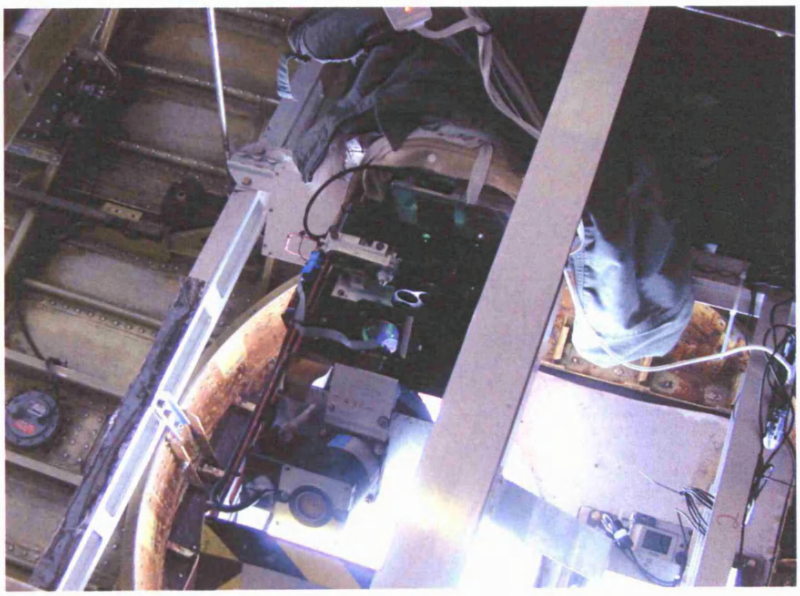

Figure 3.14: ATM mounted in the P-3.

[1] The gain a given antenna has with respect to a theoretical isotropic (point source) antenna.

The ATM system consists of a pulsed laser operating in the visible part of the spectrum (532 nm). The laser beam is directed along an oval shaped pattern by a nutating mirror, with adjustable off nadir settings. The shape of the scanned patterns on the ground depends on the position of the mirror, the topography and the speed and attitude of the aircraft. [Csathó et al., 1996]

During the LaRA campaign two ATM systems were carried, ATM2 and ATM3. They share the characteristics listed in table 3.3, but have different off nadir scanning angles. ATM2 scanned at 15.2° during the calibration flights, and operated in a profiling mode, where the beam was locked in position and directed aft of the P-3, during the sea ice flights. ATM3 scanned at 22.1° during both the calibration and sea ice flights. [S. Manizade, personal communication]

3.3.5) ATM characteristics

Table 3.2 lists the various ATM laser characteristics:

Parameter	Value
Pulse Frequency (Hz)	5000
Pulse Energy (mJ)	0.1
Beam Width (mRad)	~1
Beam Divergence (mRad)	2.0
Pulse Width (nsecs)	1
Wavelength (nm)	532
Scanner Rotation Rate (Hz)	20

Table 3.2: ATM laser characteristics [Raney, 2002 and S. Manizade, personal communication].

3.3.6) Global Positioning System (GPS)

The GPS determines the aircraft's location with sub-decimetre accuracy [Raney, 2002]. A differential phase technique is used to determine the aircraft location (see Krabill and Martin (1987)). Before and after each flight, GPS carrier phase data are recorded on the aircraft and at a near-by ground station. Many systematic errors have nearly the same

effects on measurements made at receivers close to one another. Therefore the data collected is used to solve ambiguities in the carrier phase between the two receivers (i.e. ambiguities caused by propagation of the signal through the atmosphere). When the satellite ephemeris data become available they are used to determine the flight trajectory. The ground station location is determined by at least 24 hours of GPS data. The aircraft position can then be determined relative to the ground station. This technique removes fluctuations in the GPS signal caused by the atmosphere as the signal passes through it, resulting in a more accurate location estimate than that obtained by standard techniques. [Serdar Manizade, personal communication]

A ring laser gyro INS is use to compute the P-3's attitude [Csathó et al., 1996].

3.3.7) The P-3 layout

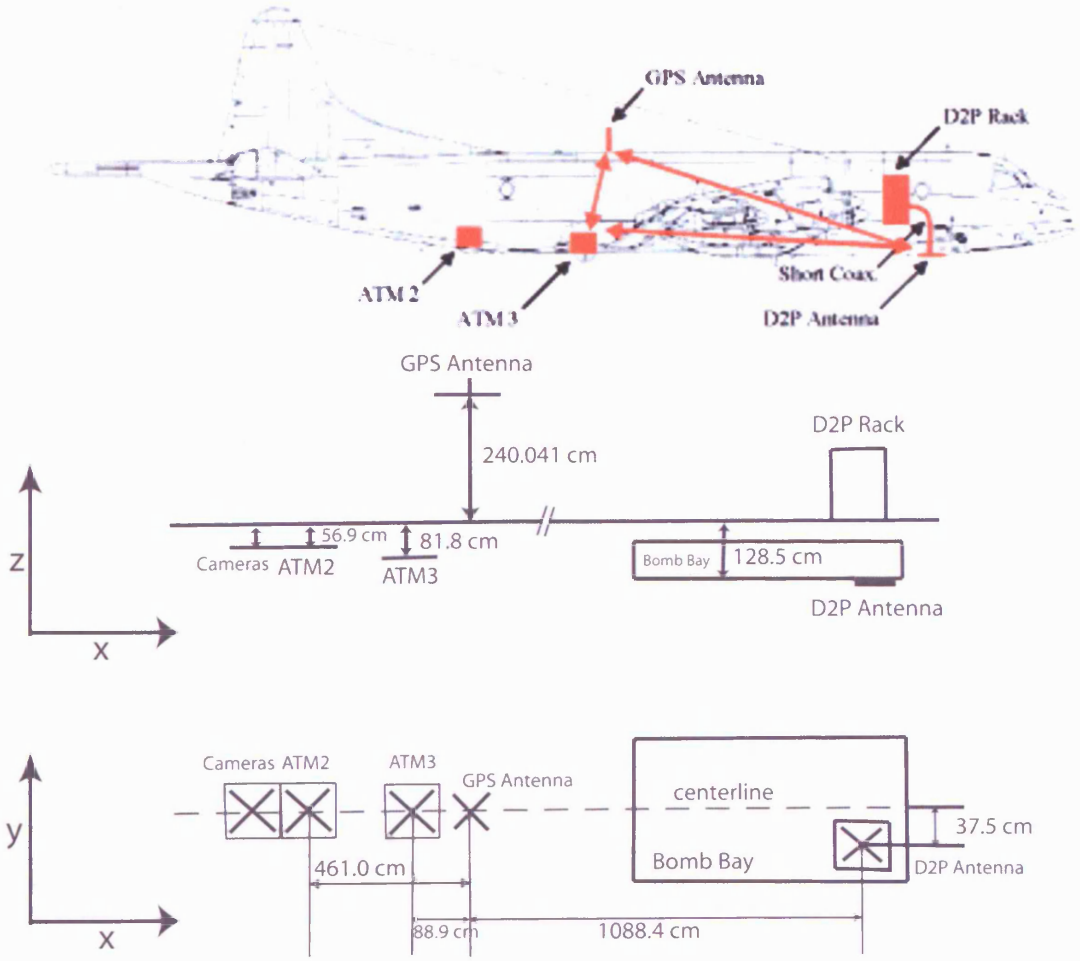

Figure 3.15: Sensor layout in the P-3 aircraft, adapted from Raney and Leuschen (2003).

Figure 3.15 illustrates the instrument layout in the P-3. When georeferencing the measurements it is important to know the exact location of the instruments with respect to the GPS antenna.

3.3.8) Footprint geometry

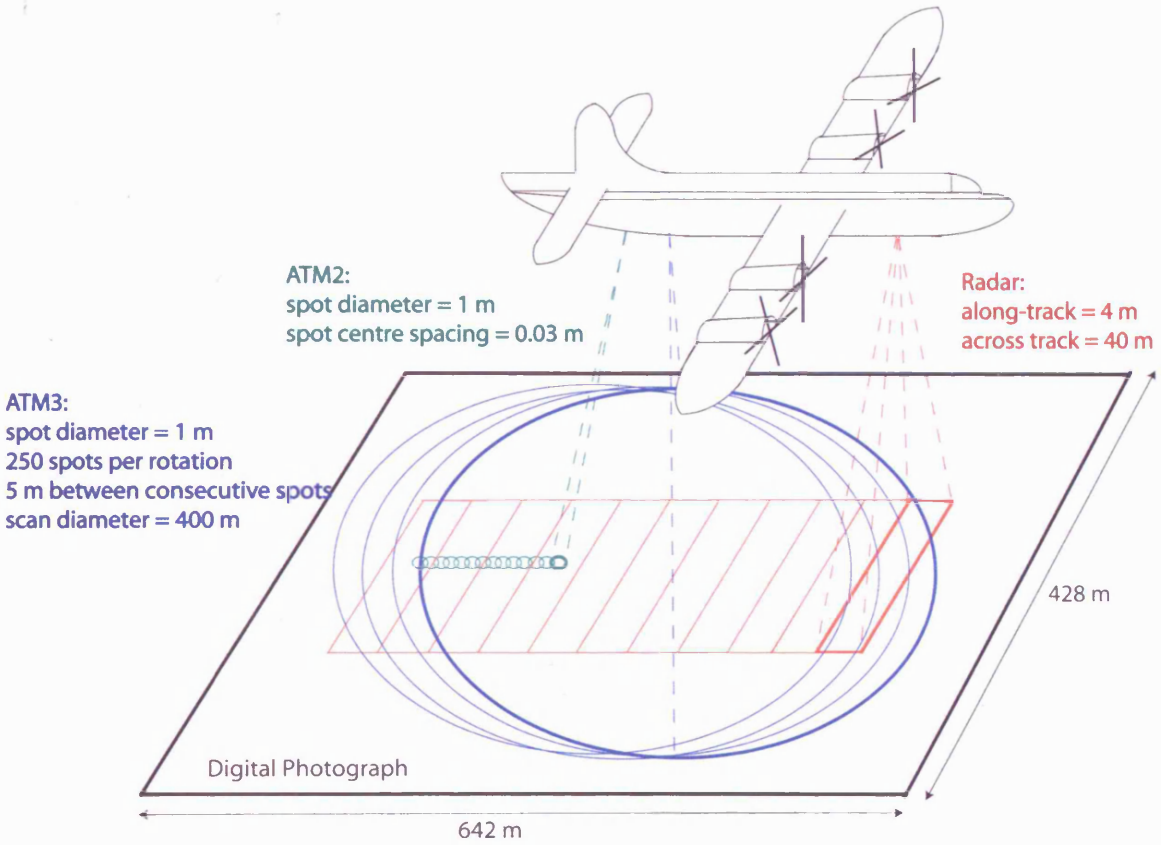

Figure 3.16: LaRA footprint geometry for the P-3 at an altitude of 500 m and velocity 150 ms^{-1}, N.B. the figure is not drawn to scale.

Figure 3.16 shows the footprint geometry of the ATMs and D2P. At a nominal altitude of 500 m, and velocity of 150 ms^{-1}, the radar footprint is 4 m in the along-track direction and 40 m in the across-track direction. Equation 3.9 gives the dimension of the along-track footprint (in meters), which depends on the Doppler processing.

$$\Delta x_{D2P} = \frac{h \times prf \times c}{2 \times N \times \upsilon \times fc} \tag{3.9}$$

[Carl Leuschen, personal communication]

where h is the altitude (500 m), prf is the pulse repetition frequency (1750 Hz), c is the speed of light (3×10^8 m/s), N is the number of pulses per burst (16), υ is the aircraft velocity (150 m/s) and fc is the radar frequency (13.9 GHz). Equation 3.10 calculates the pulse-limited, across-track footprint (in meters).

$$\Delta y_{D2P} = 2\sqrt{hc\tau} \qquad (3.10)$$

[Mantripp, 1996]

The ATM2 (profiling laser) has a circular footprint with a diameter of 1 m and passes through the radar footprint. Individual laser spots from ATM3 also have a diameter of 1 m but sweep out an elliptical scan pattern with a diameter of 400 m, enveloping the ATM2 and D2P footprints.

3.3.9) Flight history for AIM and LaRA

In this section we list the flights from calibration to the end of the LaRA field campaign. The flights conducted between the calibration flights and the LaRA flights were part of AIM and the ICESat Cal/Val missions.

3rd May 2002 Calibration flight at Wallops Flight Facility (WFF)
6th May 2002 Calibration flight at WFF/WFF beach mapping
Transit from WFF to Thule (Greenland),
15th May 2002 Thule transit to Svalbard aborted
17th May 2002 Thule transit aborted
18th May 2002 Thule transit to Svalbard
20th May 2002 Svalbard flight 1
22nd May 2002 Svalbard flight 2 (flights over land ice on Svalbard)
23rd May 2002 Svalbard flight 3
24th May 2002 Svalbard transit to Thule

3.3.10) Calibration flights

Calibration data for this study were collected on the 3rd and 6th May 2002. On the 3rd,

the P-3 made two passes over the Wallops runway, one at 300 m and one at 600 m. The D2P recorded data during both passes. ATM3 collected data during the 600 m pass, no ATM2 data were collected on the 3rd due to an alignment problem [S. Manizade, personal reference]. A second calibration flight took place on the 6th May. Only ATM data were collected during this flight. Both ATMs were operational and three passes, at different altitudes, were made. Both ATMs operated in scanning mode.

A GPS truck survey of the runway was also conducted on the 3rd May. A GPS antenna was attached to the roof of a truck, which was driven across the runway in a grid pattern while data was logged on the receiver in the truck and at a stationary base station. The antenna position over the runway was then calculated and the height of the antenna above the ground subtracted to give the ground elevation above the reference ellipsoid. The error on the survey was less than 2 cm. [S. Manizade, personal reference]

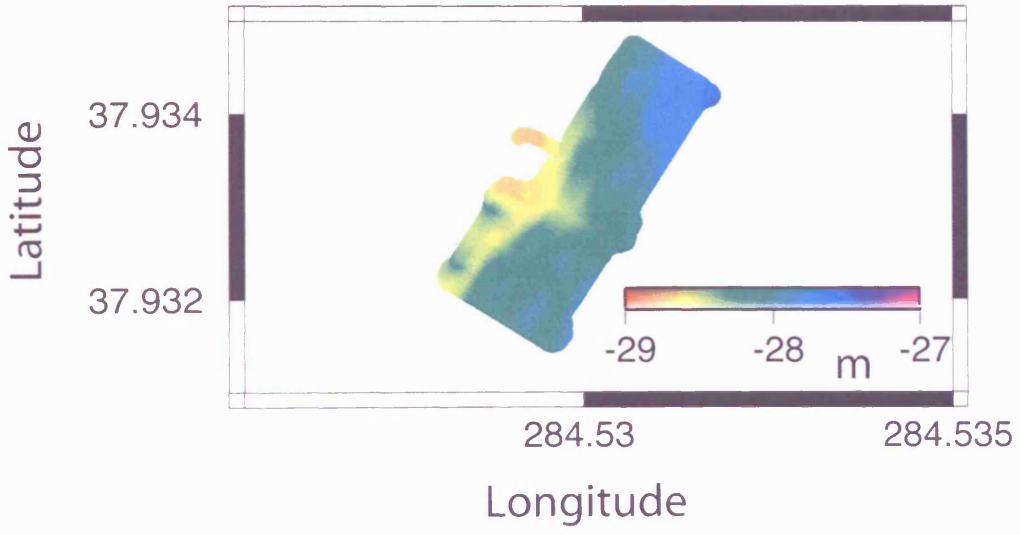

Figure 3.17: GPS truck survey of the Wallops runway.

3.3.11) LaRA flights

The LaRA flights took place on the 20th and 23rd May 2002 from Svalbard. Figure 3.18 shows the flight paths, which were designed to under-fly ERS2 and Envisat passes to within a few hours. On the 20th May, takeoff was at 09.28 and the last sea ice data were collected at 14.20, ERS over flew the LaRA flight path at 15.50. On the 23rd May, takeoff was at 12.00, and the P-3 arrived back in Svalbard at 18.00, ERS overflew at 15.55. The flight line on the 23rd May was extended as far north as possible, in order to

sample colder, thicker ice. As the latitudinal limit of ERS is 81.5°, there are no ERS measurements in this area.

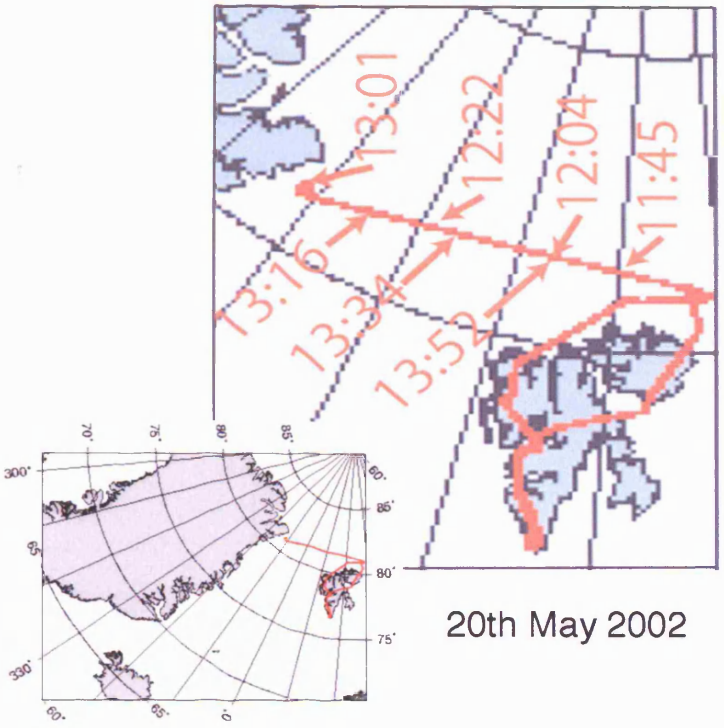

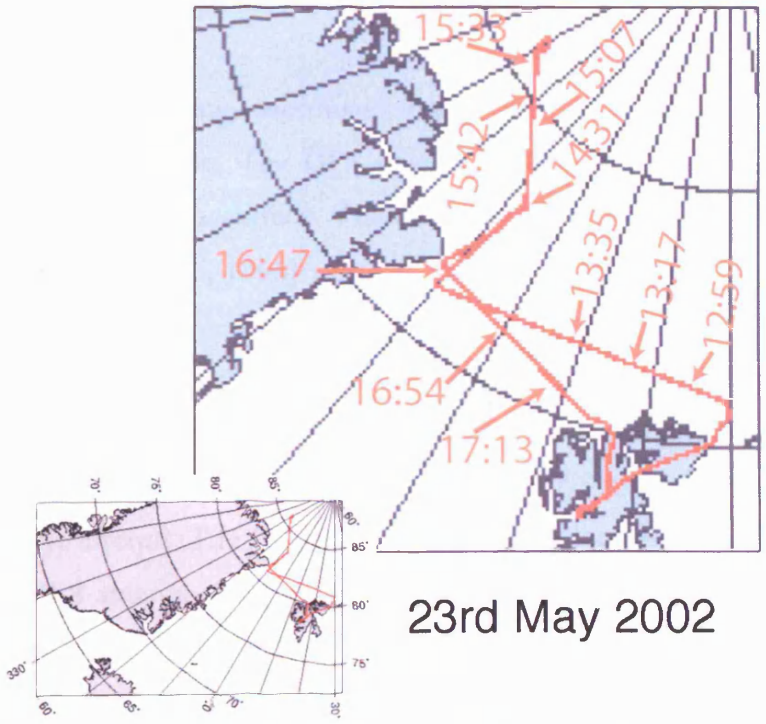

Figure 3.18: Locations of the LaRA flight lines. Top plot shows the flight line for the 20th May 2002 and the bottom plot show the flight line for the 23rd May 2002. Times during the flights are shown in red.

3.3.12) Georeferencing of measurements

All ATM, GPS and INS data and digital photographs were processed by NASA at the Wallops Flight Facility. The technique and coordinate transforms used to determine the coordinates of the point of intersection of the laser spot with the Earths surface with respect to the reference ellipsoid are described in Vaughn et al. (1996).

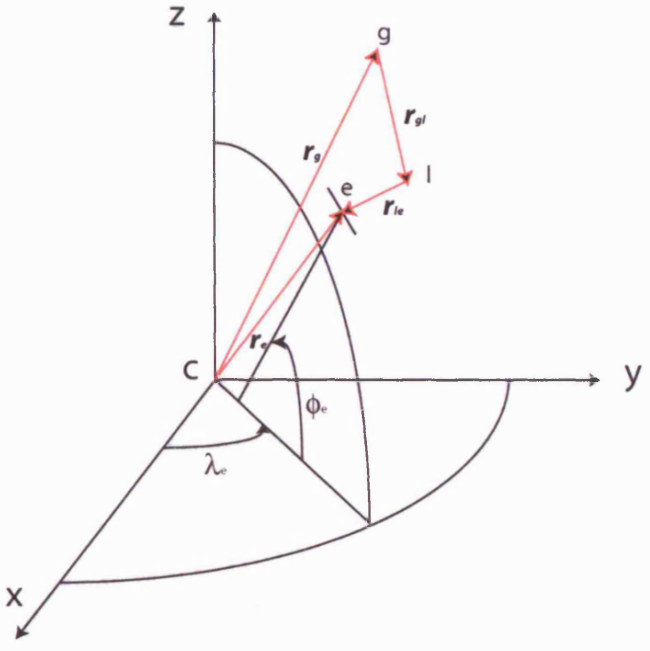

Figure 3.19: Georeferencing coordinate frame. C is the centre of the WGS-84 ellipsoidal coordinate frame. The GPS antenna is at **g**, the laser at **l** and the laser footprint at **e** on the Earths surface. The ellipsoidal coordinates of **e** are ($\mathbf{r_e}$, $\boldsymbol{\phi_e}$, $\boldsymbol{\lambda_e}$). [redrawn from Vaughn et al., 1996]

The position of the GPS antenna ($\mathbf{r_g}$) onboard the aircraft can be determined to a few centimetres accuracy in World Geodetic System (WGS-84) ellipsoidal coordinates, by combining the location from the GPS antenna and the INS measurements, which define the attitude of the aircraft. The vector ($\mathbf{r_{gl}}$) measures the location of the instrument with respect to the GPS antenna. This measurement is made in the local reference frame of the aircraft, and rarely changes when the instrument is installed on the same aircraft. The instrument is mounted in the aircraft with a bias in pitch, roll and heading (i.e. when the INS reads zero roll, the mounting angle of the instrument may be such that the roll is not zero for the instrument). This bias can change whenever the instrument or the

INS are reinstalled. This bias is estimated and corrected for by collecting data over a known, relatively flat, surface.

For the case of the ATM instruments, the geometry of the laser beam in the reference frame of the instrument (figure 3.20) must be determined. It is defined in terms of:

1) The rotation axis angle (β), which is relative to the laser beam coming from the source.
2) The scanner tilt angle (α), which is normal to the scanning mirror surface and is measured relative to the rotation axis.
3) The angle of rotation of the scan mirror about its axis is referenced to a point, which corresponds to the laser beam being directed toward the starboard wing. This angle is recorded by the sensor but must be adjusted to make the angle meaningful in the scanner reference frame. An adjustment (**scanner rotation zeroset**) is added to the recorded angle of rotation to make this adjustment.

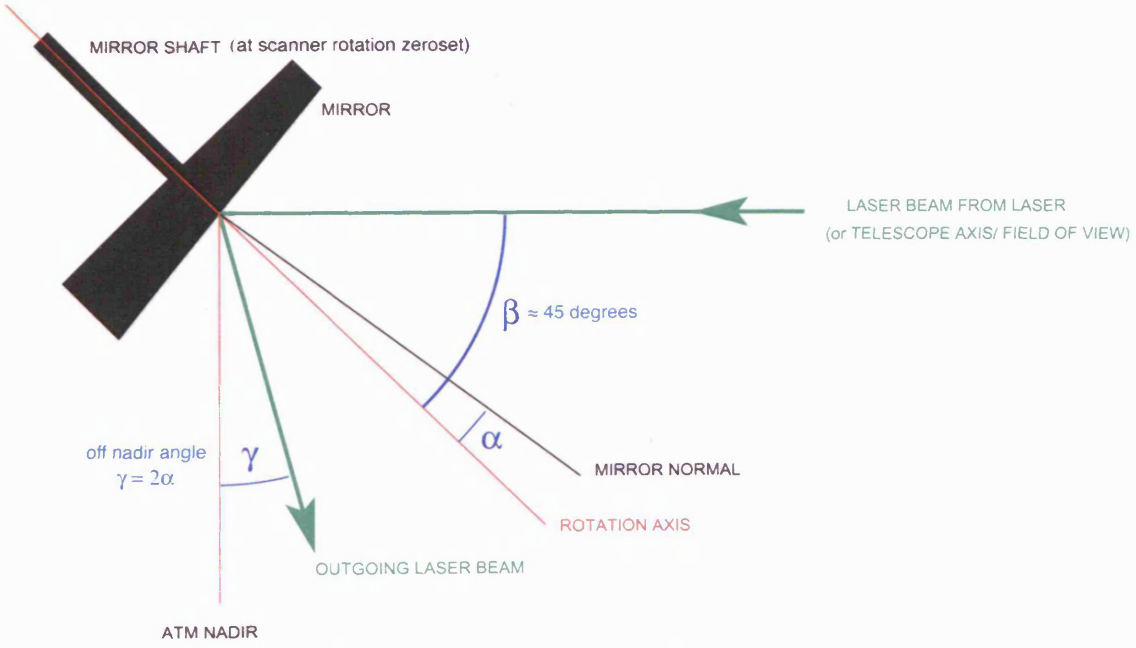

Figure 3.20: Forward looking cross-section showing the geometry of the ATMs. The scan mirror position is such that the laser beam is at its most starboard position (shaft position zero). [figure adapted from figure by Serdar Manizade, personal communication].

To calculate the position of the laser spot on the Earth's surface the vector between the ATM and the Earth's surface ($\mathbf{r}_{le}$), is used along with the information about the geometry of the laser beam. However, before the vector $\mathbf{r}_{le}$ can be used it must be corrected for range bias. The range bias is measured before and after every flight by reflecting a laser pulse off a mirror a known distance away from the instrument. Once all the biases have been computed, the laser point's location on the Earth's surface in the aircraft's reference frame are computed. These coordinates are then transformed into ellipsoidal coordinates by using the vector from the ATM to the Earth's surface ($\mathbf{r}_{le}$), the GPS antenna to the ATM ($\mathbf{r}_{gl}$) and the vector $\mathbf{r}_g$ that gives the location of the GPS antenna in ellipsoidal coordinates.

The D2P data files give the latitude and longitude of the nadir of the GPS antenna using the corrected GPS string from Wallops. APL found that the GPS time stamp was approximately 13 seconds ahead of the D2P time stamp and corrected for this offset by interpolating the GPS data in time. The locations are accurate to microseconds. [Carl Leuschen, personal communication]. Further processing must be done to locate the D2P footprint. This processing is described in chapter 5.

3.3.13) ATM data processing

The measurements from the ATMs, GPS and INS are processed individually at Wallops Flight Facility. GPS time tags are attached to each data set to synchronise them. The data are then combined to georeference the ATM data. All data are corrected for errors in time, pitch, roll and scan azimuth. The final version of the data gives the elevation of points on the ground, with respect to the reference ellipsoid, along with some aircraft information and laser parameters. The data have not been filtered so contain some unrealistic elevation estimates that are caused by reflection from very light clouds [Bill Krabill, personal communication].

3.3.14) ATM data format

The data are known as ATM QFIT data. Data are distributed as a binary file (for a description of the file see appendix 1), for each laser shot there is a data segment giving the;

1. Relative time (msec from the start of the file),
2. Laser spot latitude (degrees $\times 10^6$),
3. Laser spot longitude (degrees $\times 10^6$),
4. Elevation (mm with respect to the reference ellipsoid),
5. Start pulse signal strength,
6. Reflected laser signal strength,
7. Scan azimuth (degrees × 1000),
8. Pitch (degrees × 1000),
9. Roll (degrees × 1000),
10. UTC time.

Both ATMs operated in scanning mode during the calibration flights. ATM2 operated in profiling mode and ATM3 operated in scanning mode over the sea ice.

3.3.15) Digital photographs

The photographs were processed and distributed, on a CD, by the Wallops Flight Facility. During the flight the two cameras took pictures alternately. The pictures are stored on the CD in folders corresponding to the time they were taken. Each folder contains two sub-folders with the pictures from each camera and a text file named gps.txt. gps.txt describes the order of the photographs and gives the;

1. Photograph number,
2. Date,
3. Time,
4. Latitude,
5. Longitude,
6. Time between photographs (seconds),
7. Distance between photographs (nautical miles),
8. Bearing between photographs,
9. Speed (knots)

Equations 3.11 and 3.12 calculate the dimensions on the ground of a photograph in meters:

$$\Delta x_p = 2 \times 0.642 \times h \tag{3.11}$$

$$\Delta y_p = 0.667 \times \Delta x_p \tag{3.12}$$

where Δx_p is the along track dimension (m), Δy_p is the across track dimension and h is the elevation of the camera above the ground in meters.

3.3.16) D2P data processing

The D2P data was processed at APL and used the GPS and INS data processed at the Wallops Flight Facility to locate the data and to estimate changes in the vertical velocity of the aircraft (section 3.3.2).

3.3.17) D2P data format

D2P data sets are available on the password protected ftp server (srbdata3.jhuapl.edu), files are found in directory /yyyymmdd/processed and named Pyyyymmdd.xxx [Raney & Leuschen, 2003]. For each echo within the file flag; time, latitude, longitude, altitude, heading, pitch, roll, tracking range, reference, attenuation, pulse length, and bin size are given. Then a 2*2 (pulse length) array where the first column is the bin number[0,0,1,1,2,2,….,pulse length, pulse length], and the second column is I[0,2,4….,(2*pulse length)-1] and Q[1,3,5,….,2*pulse length], follows. A full description of the data format is given in appendix 2.

3.4) APL elevation calibration of D2P data

To calibrate the D2P data, APL used a sinc function to re-track the echoes recorded over the runway. They used the peak of the sinc function to estimate the elevation and then compared these estimates to the GPS elevation estimates. Figures 3.21 and 3.22 show the radar derived heights (black), after 23.98 m has been subtracted from them,

and the GPS heights (red), as a function of distance along the runway. The GPS heights are averaged over the antenna footprint.

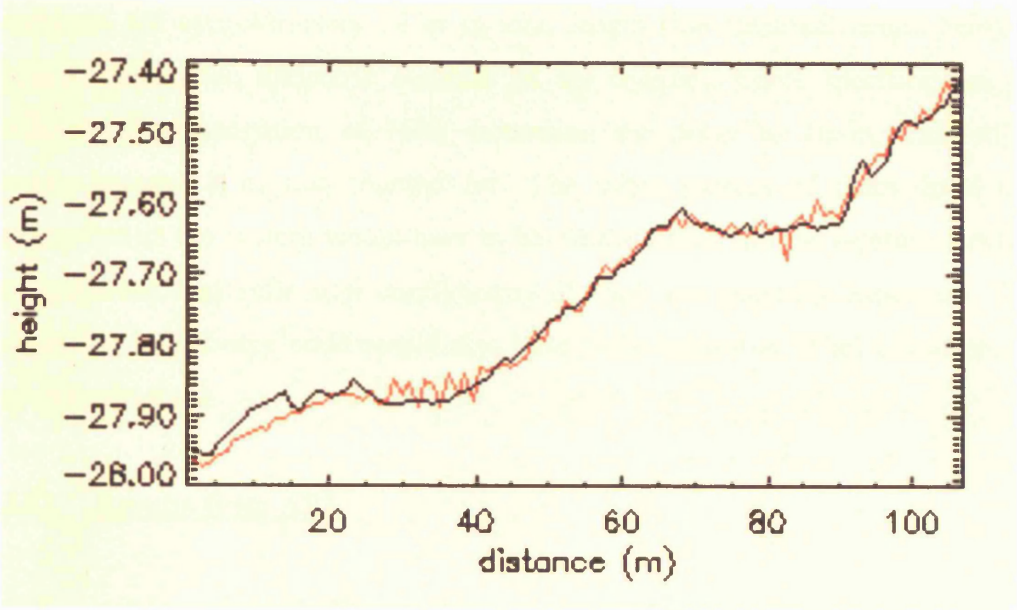

Figure 3.21: 300 m pass. [Raney & Leuschen, 2003]

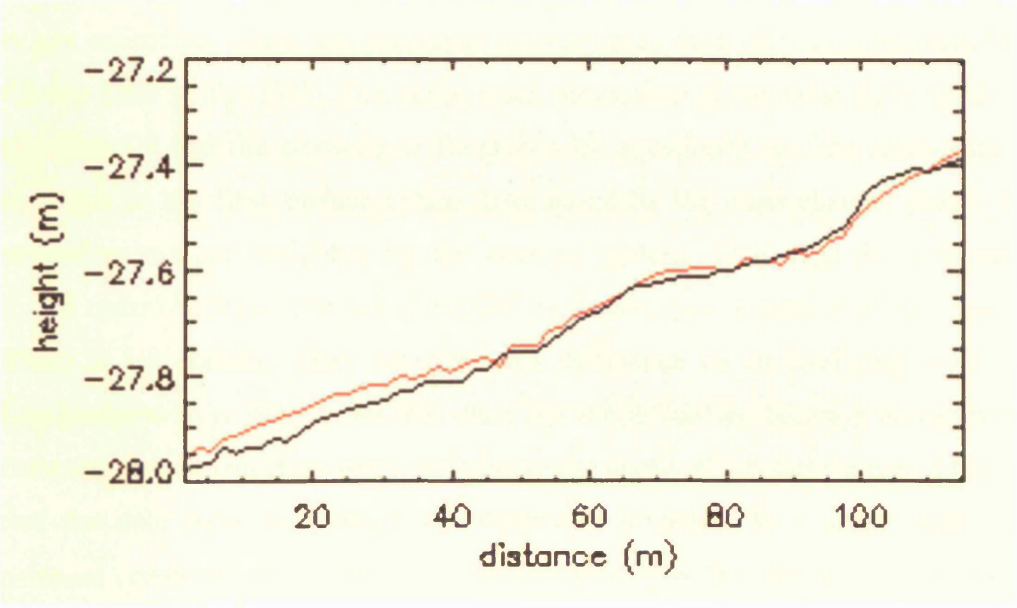

Figure 3.22: 600 m pass. [Raney & Leuschen, 2003]

Pass	Height	Pulse Length	D2P-GPS(mean)	D2P-GPS (std)
1	300 m	0.768 μs	23.9811 m	0.0173 m
2	600 m	1.536 μs	23.9674 m	0.0191 m

Table 3.3: Offset between D2P and GPS surveys of the Wallops runway. [Raney & Leuschen, 2003]

An offset of 23.98 m between the GPS and D2P runway surveys was found. There are a few possible sources of delays contributing to the 23.98 m. The cables to and from the antennas are approximately 12 m in total length (the electrical length being slightly longer due to the dielectric constant of the coaxial). Cable specifications give the velocity of propagation at 76%, increasing the delay to 16 m. This still leaves approximately 8 m unaccounted for. The other sources of delay have not been quantified as the system would have to be disassembled and the s-parameters (complex transmission and reflection coefficients) of each sub-assembly measured. The radar controller and source code would also have to be looked at. [Carl Leuschen, personal communication]

3.5) Results from APL

Raney and Leuschen (2003) use the re-tracking algorithm described above to estimate radar elevations along the experiment flight lines. These data are compared to ATM height estimates, which are calculated by averaging laser elevation data that fall within the footprint of the D2P. The along track dimension of the radar footprint is given by equation 3.9 and the cross-track dimension by equation 3.10. The cross-track pointing direction to the first surface return determined by the cross-channel phase. The laser measurements are weighted by the antenna pattern. They find the difference (laser minus radar) between the two elevation estimates, over a section of the Greenland Ice Sheet is 1.8 metres. They attribute this difference to an overlying layer of snow. Comparisons over sea ice are less clear but the difference between elevation estimates from the two instruments seem to indicate the depth of the snow cover. They conclude that the data have been relatively calibrated in height to ± 2 cm [Carl Leuschen, personal communication], and that the data sets show that elevation estimates from the two instruments may be identical or different depending on the surface conditions. Therefore elevation differences are not due to differences between the instruments themselves.

The use of a peak-power retracker, calibrated over the runway, assumes that the runway has the same backscatter characteristics and topography as the ice. This is not the case and both the different backscatter characteristics, and the topography of the ice will

change the echo shape. The height calibration of ± 2 cm is derived by calculating the standard deviation in the difference between the D2P and GPS measurements over the runway (see table 3.4). However, a ± 2 cm precision over the runway does not mean that the same error estimate applies to elevation measurements over a different surface with different backscatter characteristics and topography. Their investigation compares laser and radar elevation estimates, however, no cross-calibration of the laser and radar instruments over a known surface has been performed and an error estimate for the averaged laser data is not given. Such a calibration is fundamental to determining the relationship between the two instruments over the snow/ice system. Although this method provides a quick first look at the data sets and yields some encouraging results implying that the radar and laser are ranging to different surfaces, it is difficult to draw any firm geophysical conclusions from the investigation.

3.6) Summary

- Satellite radar altimeters can provide measurements of ocean topography, the marine gravity field, the ocean floor topography, wave height and wind speed. Laser altimeters can provide surface elevation maps, measure cloud heights and the vertical structure of clouds and aerosols.

- The LaRA field campaign has been described, the instruments used, the geolocation of the data and the data processing done by the Wallops Flight Facility and APL.

- The analysis performed by APL shows the potential of the LaRA data set to provide information on radar returns from the D2P and the combination of radar and laser altimetry. Although their investigation shows some interesting results it is difficult to draw any geophysical conclusions from it. It is the starting point for a more detailed and rigorous investigation. The purpose of the following chapters is to describe a comprehensive analysis of the LaRA data set, the methods used and the results produced.

4) Comparison of spaceborne radar altimetry and airborne laser altimetry over sea ice

4.0) Introduction

In this chapter we describe the first comparison of satellite radar altimetry (ERS-2) and airborne laser altimetry over sea ice. The experiment was done in collaboration with Sine Munk Hvidegaard from National Survey and Cadastre (KMS), Denmark.

Section 4.1 describes the experiment and section 4.2 describes the instruments. In section 4.3 we describe the laser interaction with the snow covered ice surface and the snow freeboard measurement from the laser altimeter. Section 4.4 describes the ice freeboard measurement from the radar altimeter. In order to investigate the differences between measurements from two different instruments, in sections 4.5 to 4.7 we explore the statistical properties of the data and determine reasonable scales in space and time at which to examine the data. The results are described in section 4.8 and show that the laser and radar are reflecting from different surfaces and that the magnitude of the difference decreases with increasing surface air temperature. This suggests that the penetration depth of the radar signal, into the snow, varies with temperature. The results also show the potential for computing Arctic wide snow depth maps by combining measurements from laser and radar altimeters. Snow depth maps will reduce the uncertainty in the computation of sea ice thickness from both laser [Wadhams et al., 1992] and radar (chapter 1, sections 1.5.3 and 1.6) measurements of sea ice freeboard, as well as providing a useful data set in terms of climate modelling.

4.1) The experiment

During April and May 2001 and May 2002, KMS collected airborne laser altimetry data, over sea ice, as part of a larger project to measure gravity on the Greenland continental shelf region [Forsberg et al. 2002] and as part of a joint gravity and ice mapping survey [Forsberg et al. 2003]. Figure 4.1 shows the locations and dates of the KMS airborne laser altimetry data and the ERS-2 spaceborne laser altimetry.

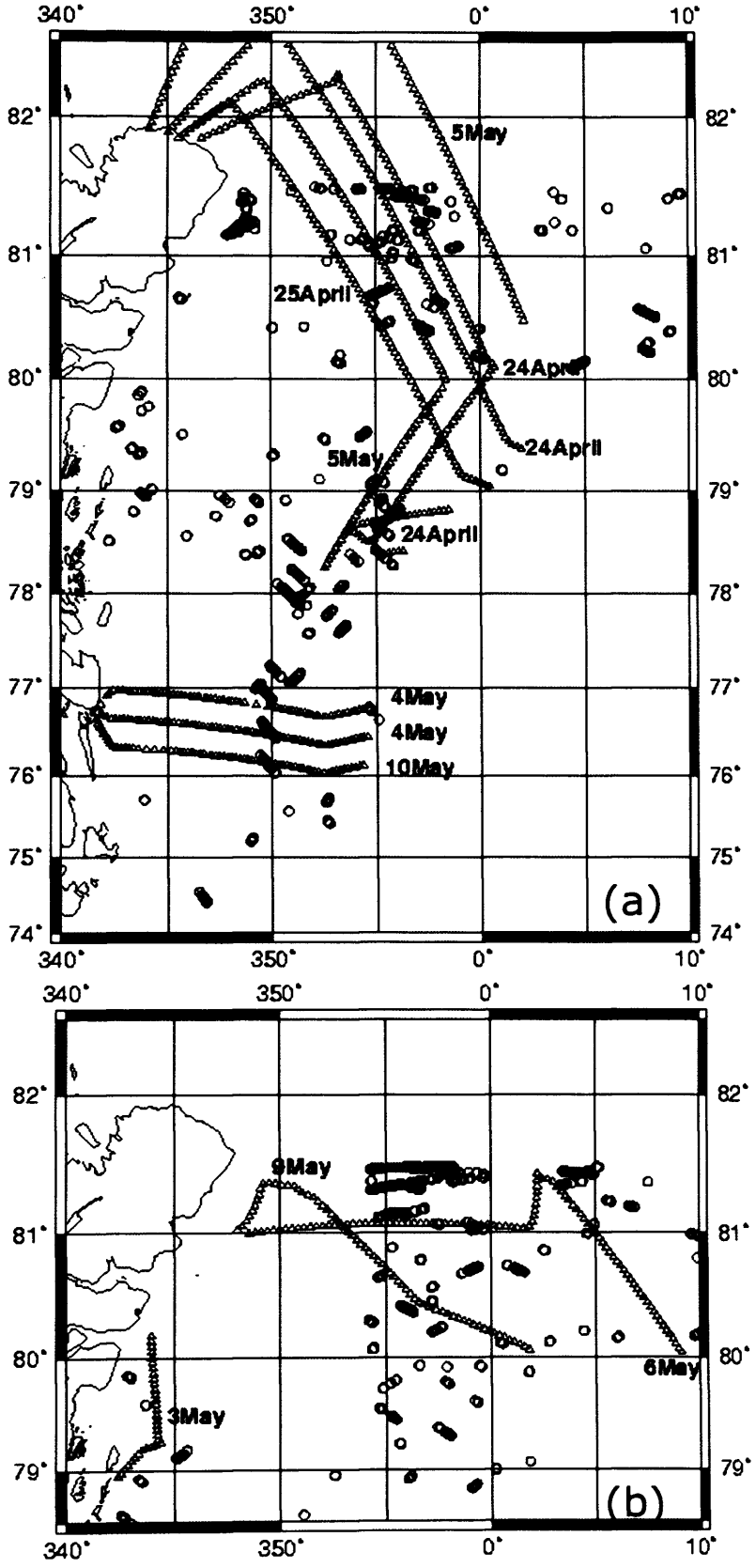

Figure 4.1: Study area with locations of ERS2 radar data [(a) 19/04/01 to 15/05/01 and (b) 28/04/02 to 14/05/02] shown by circles and locations of airborne laser data shown by triangles. Data from 2001 is shown in (a) and 2002 in (b).

4.2) Instruments

An Optech near-infrared laser altimeter was used for both KMS surveys. The altimeter operates at a wavelength of 904 nm, has a footprint of approximately 1 m and operates between 150 and 300 meters altitude. Additional data was gathered in 2002 from a scanning laser altimeter, operating at a wavelength of 900 nm. It provided the same measurements as the Optech laser but with a greater along track spacing.

ERS-2 carried a 13.8 GHz radar altimeter, further details of the altimeter specifications can be found in ERS (2003). ERS-2 operated at an altitude of 782 to 785 km and had a footprint of approximately 10 km in diameter.

4.3) Snow freeboard measurement from the laser altimeter

Many studies using laser altimetry are based on the assumption that the laser reflects from the first surface in its line of sight. In general, for the case of sea ice studies, the reflecting surface is not explicitly named. Wadhams et al., (1991), state that their laser profilometer (the Airborne Oceanographic Lidar operating at 355 and 532 nm) ranges to the sea ice surface but do not state whether the surface is snow covered. However, since the measurements were taken in May, between the North Pole and Greenland, and the Fram Strait, it is unlikely that the ice is snow free (see section 3.3.11 and table 4 in Wadhams et al. (1992)). Comiso et al. (1991) describe the same experiment and state that the laser altimeter reflects from the snow surface. Using the data from this experiment Wadhams et al. (1992), derive an expression relating the mean ice draft to mean freeboard, which can be measured by laser altimetry. Although it is not stated, it is inherent in their expression that the laser measures the elevation of the sea ice plus the snow, when it measures the freeboard. Hvidegaard and Forsberg (2002) also use this assumption to calculate sea ice thickness from elevation measurements their laser altimeter, which operates at 904 nm.

The measurement of the elevation of the snow and ice above the water (snow freeboard) is similar to the measurement of the sea ice freeboard described in chapter 1,section 1.5.1

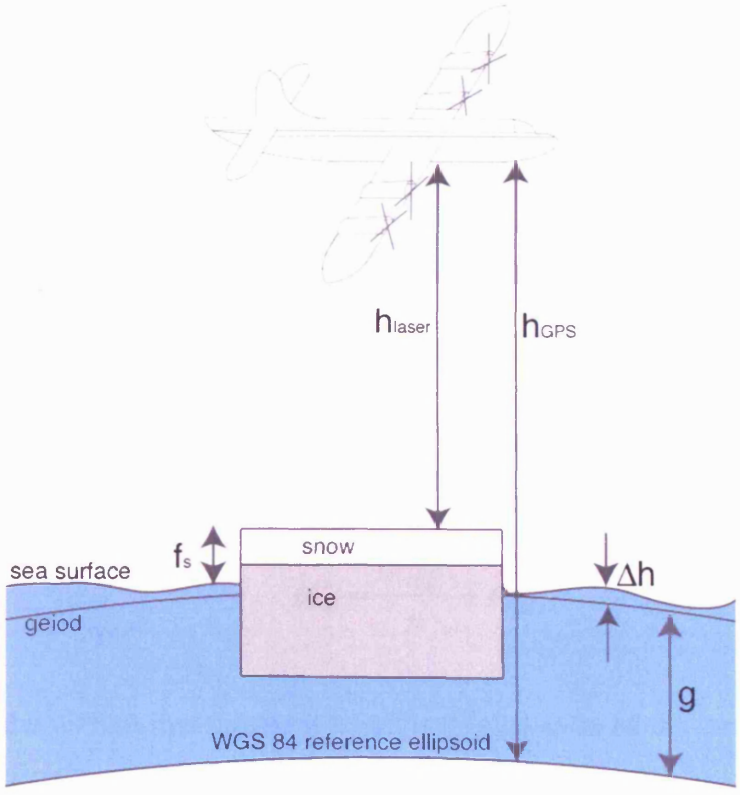

Figure 4.2: Schematic diagram of the measurement of snow freeboard from airborne laser altimetry. $\mathbf{f_s}$ is the snow freeboard, $\mathbf{h_{laser}}$ is the distance measured by the laser to the air/snow interface, $\mathbf{h_{GPS}}$ is the elevation of the aircraft above the reference ellipsoid, **g** is the geoid height with respect to the reference ellipsoid and **Δh** is the deviation of the sea surface from the geoid.

The snow freeboard (f_s) is given by equation 4.1:

$$f_s = h_{GPS} - h_{laser} - g - \Delta h \qquad (4.1)$$

where h_{GPS} is the height of the aircraft above the WGS 84 reference ellipsoid, h_{laser} is the laser range corrected for the effects of pitch and roll, g is the geoid height taken from a model derived from airborne gravity measurements by KMS and Δh describes the deviation of the sea surface from the geoid caused by errors in the geoid model, tides and mean and time variant sea surface topography. [Hvidegaard & Forsberg 2002]. Error estimates for individual laser measured freeboards are 13 cm (100 Hz data). This error reduces to 5 cm when the data are averaged as described in section 4.7 (reduced 0.1 Hz data).

4.4) Freeboard measurement from the radar altimeter

Coincident measurements of the freeboard were obtained from the radar altimeter onboard ERS2 [Laxon et al., 2003]. Section 1.5, in chapter 1, describes how these measurements were calculated and gives details of their accuracy and their sources of error. Section 1.5.3, in chapter 1, describes the retrieval error and chapter 2 discusses the assumption that the radar return originates from the snow/ice interface.

An approximate error on the sum of ice freeboard estimates can be obtained from equation 4.2:

$$\sigma_{\Sigma}^{2} = \frac{\sigma_{diff}^{2}}{n} + \sigma_{SLA}^{2} \tag{4.2}$$

Where σ_{diff} is the diffuse measurement noise, and is taken to be the standard deviation of freeboard estimates about the mean for a contiguous sequence. σ_{SLA} is the error in sea level estimation, and is taken to be the standard deviation of the estimates used to determine the sea surface elevation (above the mean sea surface). We use values estimated from repeat track analysis of 0.14 m for σ_{diff} and 0.022 m for σ_{SLA}. [Peacock & Laxon, personal communication]

4.5) Spatial scales for comparison

A series of freeboard measurements are not necessarily independent. Adjacent data points on a sea ice floe will exhibit similar thickness' within a certain spatial (and temporal) limit. The autocorrelation function (acf) can provide information on the spatial structure of a sampled profile. The normalised acf (at a certain lag) is given by equation 4.3:

$$acf_{(lag)} = \frac{\sum_{j}\sum_{i}(h_i - \bar{h})(h_j - \bar{h})}{\sigma^2} \tag{4.3}$$

where h_i is the measurement at location i, h_j is the measurement that occurs at location j, which is within a certain distance from i, $\bar{h}$ is the average measurement over the whole

data set and σ^2 is the variance of the measurement over the whole data set. The minimum distance between statistically independent data points occurs at the lag where the acf has its first zero [Eicken & Lange, 1989].

Few investigations have looked at the acf of sea ice elevation, thickness or draft. It is reasonable to assume that values given for the acf of sea ice draft and thickness would also be applicable to sea ice elevation as ice elevation is proportion to ice draft and thickness. Table 4.1 lists investigations into the acf of sea ice.

Author	Data type	Location	Sampling	Distance to 1st zero crossing
Rothrock & Thorndike (1980)	Submarine sonar (ice draft)	Beaufort Sea	6 m sampling interval	1100 m
Melling & Riedel (1995), Melling et al., (1995)	Moored upward looking sonar (ice draft)	Beaufort Sea	2 m field of view, measurement interval 15 secs., total profile length 50 km.[1]	300 m
Flato (1995)	Model (ice thickness)	Whole Arctic	160 km grid	300 km to 1000 km depending on location
Flato (1998)	Submarine sonar (ice draft)	Beaufort Sea	1m segments over 15 km of track	390 m
Flato (1998)	Submarine sonar from Wadhams (ice draft)	Greenland to the North Pole	100 km segments over 39,100 km of track	200 km

Table 4.1: Summary of acf investigations into sea ice.

[1] The moored sonar relies on the motion of the ice pack to provide new targets. The speed of the ice pack varies. The mean speed is 0.083 ms^{-1} and the maximum speed is 0.99 ms^{-1} in the Beaufort Sea [Melling et al., 1995]. Therefore the distance between samples can range between 1.25 m and 14.85 m.

As the results listed in table 4.1 do not give a common distance at which sea ice measurements become statistically independent and the results from Flato (1995) indicate the distance to the 1st zero crossing depends on location, we computed the acf of the ice elevation from 5 km averages of the laser data. The distance to the first zero crossing ranged from 50 to 100 km. Figure 4.3 shows the acf for 3 laser tracks.

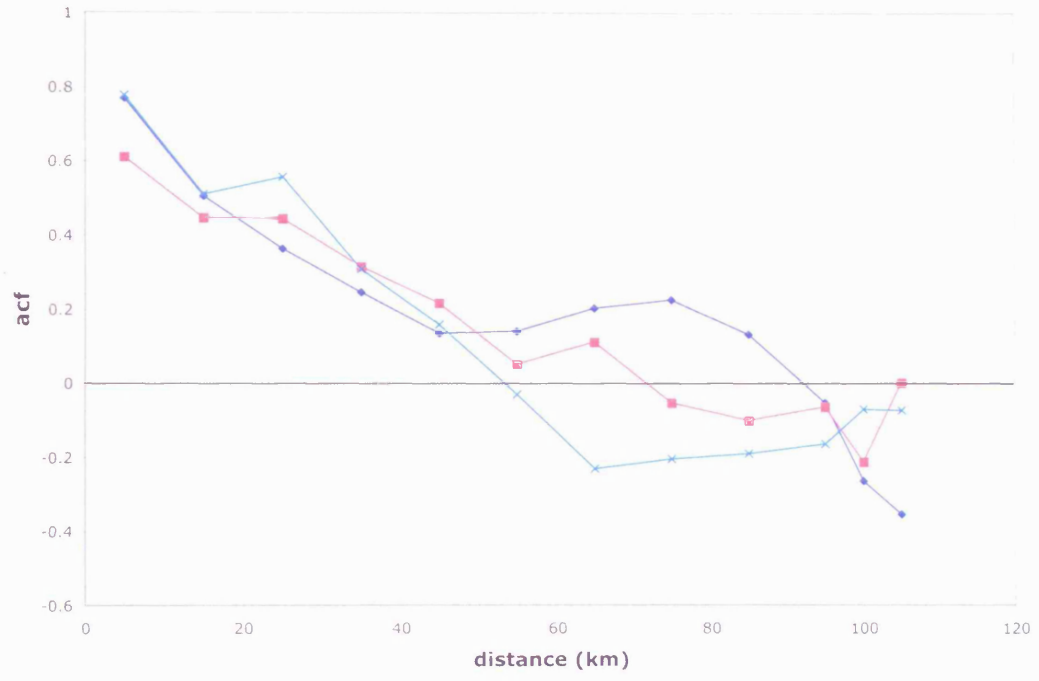

Figure 4.3: acf for laser estimates of snow freeboard.

Due to the low spatial density of the radar data we chose to compare data within 100 km of each laser point.

4.6) Temporal scales for comparison

To estimate the temporal correlation of the data sets we examined the ice drift velocities from drifting buoys from the International Arctic Buoy Program [IABP, 2000]. Typical velocities of 10-15 cm/s occur in the northern part of the study area in Spring. 15 cm/sec corresponds to about 65 km in 5 days. Considering the rapidly changing distribution of sea ice in the Fram Strait we chose a temporal search radius of 4 days.

4.7) Data averaging and errors

A 100 km moving average was computed over the laser data in an along track direction. The average elevation was computed at each datum point by taking the average of the elevations from points within ±50 km of the datum point (approximately 14000 points in each average). The averages were filtered to reduce data volume, we kept 0.1 % of the data giving us an elevation estimate every 6.5 km. For each estimate of snow freeboard from the laser data, the average radar derived ice freeboard was computed from all points falling within 100 km and 4 days of the laser point. All freeboard values below 0.05 m were excluded from both data sets to ensure that no open water values were included in the calculation. The difference between the two data sets (laser minus radar) was then computed for all averages that included at least 30 radar points. Taking an estimate of 0.05 m for the error on the laser data and using equation 4.2 to estimate the error on the radar data, assuming that the two data sets are independent and errors are added quadratically, the maximum error on the difference between the laser and the radar data is 0.06 m.

To investigate whether changes in the difference between the laser and radar elevations corresponded to temperature change, the daily maximum 2 m temperatures from the European Centre for Medium-Range Weather Forecasts (ECMWF) operational data [ECMWF, 2002] were averaged over the periods of the investigation and used to create a temperature contour map of the region.

4.8) Results

The differences in freeboards from the 2001 and 2002 flights, along with the temperature contours, are presented in Figure 4.4 (a) and 4.4 (b).

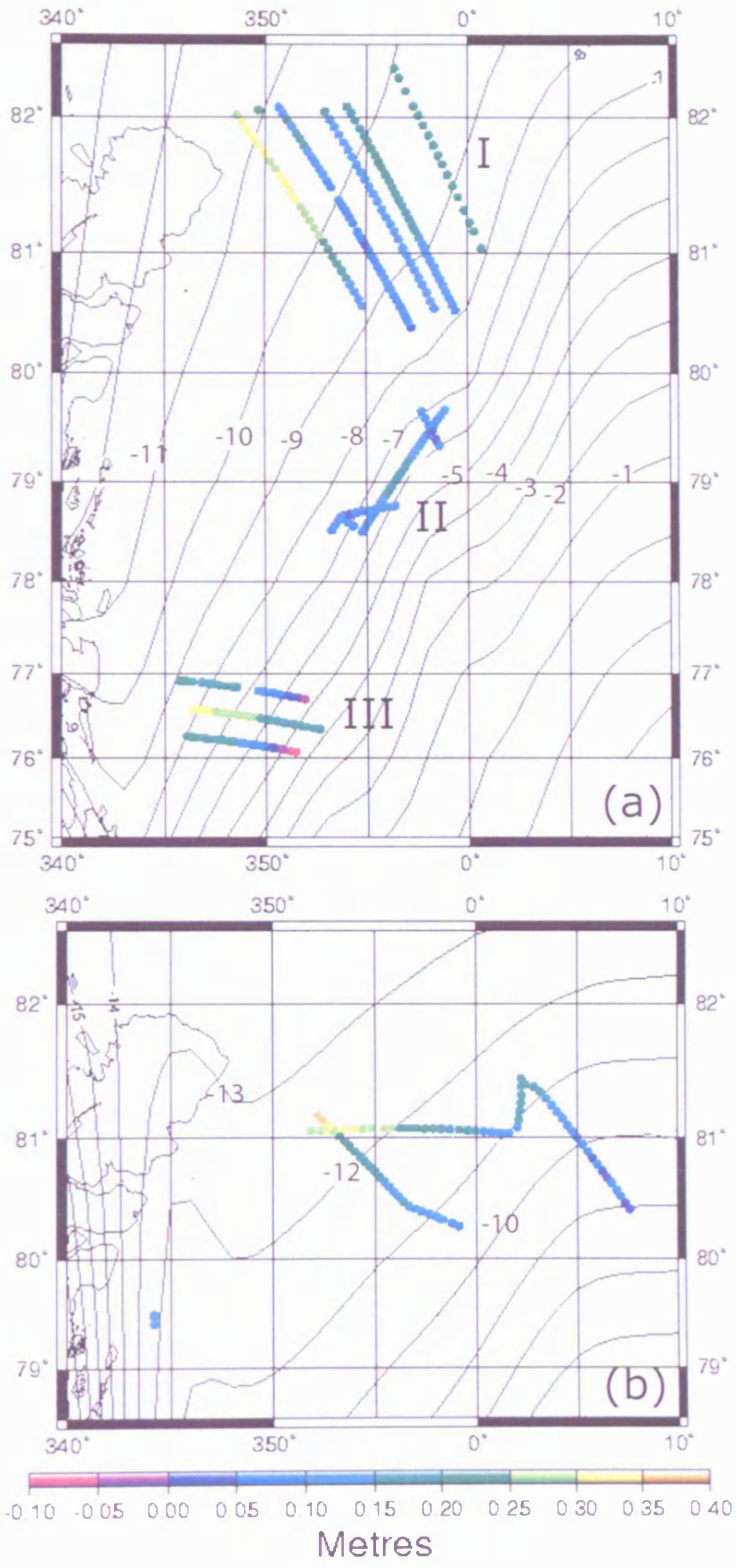

Figure 4.4: Snow freeboard minus ice freeboard for 2001 are shown in (a) and for 2002 in (b), along with contours showing the average maximum daily 2 m air temperature from ECMWF.

4.8.1) Differences between the laser and radar data sets

Figure 4.4 (a) shows the difference between the snow freeboard derived from the laser data and the freeboard derived from the radar data in 2001. The differences range from 0.10 and 0.35 m. The highest values are found close to the east coast of Greenland. Area I generally has the highest difference towards the northwest and differences decrease towards the southeast. In area II there is an agreement in the differences at the crossovers (where measurements with the laser altimeter were taken within one day of each other). Area III shows decreasing differences with distance as we move away from the coast. Here we see differences slightly below zero. They are caused by a combination of the measurement error and as a result of sampling differences.

Figure 4.4 (b) shows the difference between the snow freeboard derived from the laser data and the freeboard derived from the radar data in 2002. The differences range between 0.05 and 0.40 m and again the highest differences are in the west.

4.8.2) Comparisons with the temperature contours

Comparison with the temperature contours in figures 4.4 (a) and (b) show that as the air temperature increases the difference between the two data sets decreases.

4.8.3) Discussion

Figure 4.5 shows the snow depths predicted by Warren et al. (1999), we have annotated the diagram to show where the top of the experiment area is. The highest differences between the laser and radar elevation estimates (0.3 – 0.4 m) correspond well to the snow depths in figure 4.5.

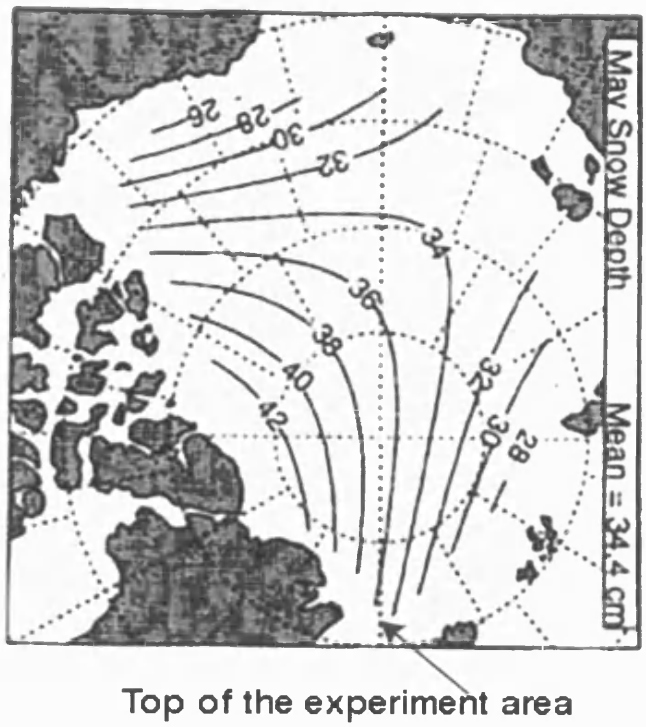

Figure 4.5: Mean snow depth for 1954-91 for May [Warren et al., 1999].

Comparing data from 2001 and 2002, we see the same size differences in area I (where we have data for both years), and the same relationship between the temperature and the differences between the two data sets. The temperatures in Figure 4.4 (b) are higher than those in the same location in 4.4 (a). However, comparisons of the ECMWF reanalysis data with observational data [Hagemann & Dümenil Gates, 2001] show differences between 1 and 5 degrees along the East Greenland coast. We expect similar differences in the operational data, however we expect the pattern of the temperature gradient to be correct. The results suggest that the radar signal does not penetrate to the snow-ice interface as the surface temperature increases towards zero. Although the differences between the laser and the radar measurements decrease with decreasing snow depth, we do not expect that the snow depth will be equal to zero over 100 km averages. Gow and Tucker (1987), estimate the average snow depth on multi-year ice floes to be 0.29 m between 78°20'N to 80°42'N latitude and 7°16'E to 7°10'W longitude during June and July 1984, and state that multi-year ice fraction is greater than 75% in that area. Evidence from Warren et al. (1999), indicates that three months after the formation of new-ice, snow depths on the new-ice will be equivalent to those

on older, multi-year ice. Warren et al. (1999) also state that the average snow depth on multi-year ice reaches a maximum in May.

4.9) Summary

- For the first time we have compared measurements from airborne laser and satellite radar altimeters over snow covered sea ice. We have analysed the spatial and temporal properties of snow freeboards and found scales within which it is reasonable to compare the two types of measurement. We find that the two independent measurements show comparable results with differences in areas close to the coast of Greenland similar to expected snow depths. We see that at most points the laser estimates are higher than the radar as would be expected. The results show a correlation between negative gradients in the differences and positive gradients in the 2 m air temperature, which suggests that the reflecting surface of the radar varies with temperature.

- Our results have implications for future planning of field campaigns to assess the accuracy of satellite estimates of sea ice freeboard from both radar and laser altimeters, such as those onboard CryoSat and ICESat. Sampling difficulties in our study could be resolved by designing aircraft flight lines to be coincident in space and time with satellite ground tracks. To validate winter measurements, data should be taken pre melt. Sampling over more homogeneous ice conditions would increase the temporal and spatial correlation scales.

- In addition, our study indicates the potential for estimating Arctic wide sea ice snow depth climatology and an ice thickness data set from coincident laser and radar altimetry during winter periods.

5) Analysis methods and cross-calibration

5.0) Introduction

In this chapter we describe the two new methods to compare the laser and radar data collected during LaRA. Section 5.1 describes the errors associated with the laser data. Section 5.2 describes the pre-processing of the radar data. Section 5.3 describes the UCL D2P re-tracking algorithm and section 5.4 describes the range calibration for the UCL D2P re-tracker. Section 5.5 discusses the limitations of the re-tracker and why it is necessary to build a radar simulator. Section 5.6 describes the UCL D2P power simulator and its calibration.

5.1) Analysis of ATM data

The georeferencing and processing of the ATM data is described in chapter 3, sections 3.3.12 and 3.3.13 respectively. However, the accuracy of the data sets must be assessed.

5.1.1) Accuracy of the ATM data

To investigate the accuracy of the data sets a similar method was employed to that used by Sallenger et al. (2003), to evaluate airborne lidar as a tool for quantifying beach change. The repeatability of the ATM surveys was determined by calculating the mean difference (μ) between the survey with the most data points and each of the other surveys. The standard deviation (σ) about the mean difference and the Root Mean Squared[1] (RMS) error were also calculated. σ is the random error and the RMS value is the total error – which reflects the mean difference and the random errors [Sallenger et al., 2003]. To derive the error associated with a single survey, it is assumed that every survey has the same sources of error. This means that, by partition of the errors, we can say that:

---

[1] $RMS = \sqrt{\frac{\sum_{i=1}^{n} x_i^2}{n}}$ where x is the difference between points.

$$\sigma_{ATM} = \frac{\sigma_{COM}}{2^{0.5}} \tag{5.1}$$

$$RMS_{ATM} = \frac{RMS_{COM}}{2^{0.5}} \tag{5.2}$$

where σ_{ATM} is the error associated with a single survey and σ_{COM} is the standard deviation of the differences between two surveys. As the footprint of the ATM pulse is approximately one metre, all data points lying within one metre of the comparison datum point were included in the calculations. Table 5.1 shows the total error (RMS error) for each of the ATM surveys. Therefore the maximum total error on a single laser point is 13 cm. When the points are averaged, as described in section 5.4.5, this error reduces.

ATM Survey	RMS_{ATM} (m)	Number of Observations
3rd May ATM3	0.1306	8479
6th May ATM2_1	0.1116	13670
6th May ATM2_2	0.0673	15749
6th May ATM2_3	0.0630	15490
6th May ATM3_1	0.0619	8619
6th May ATM3_2	0.0708	13215
6th May ATM3_3	Comparison flight	15895
All Flights	0.0907	75216

Table 5.1: Repeatability of ATM data over the Wallops runway.

5.1.2) ATM flight data

During the flights errors in the data from the INS cause errors in the elevation estimates from the ATMs. Data from the INS are used to geolocate the ATM data (see chapter 3, section 3.3.12). Data from the INS can contain time varying errors that occur during the course of the flight i.e. the value of pitch from the INS will contain time varying errors. Errors in the value of the pitch will affect the elevation estimate and result in coincident data points from fore and aft scans having different elevations. However, errors in the

pitch affect the fore and aft scans equally and oppositely and therefore can be corrected. Figure 5.1 shows this effect.

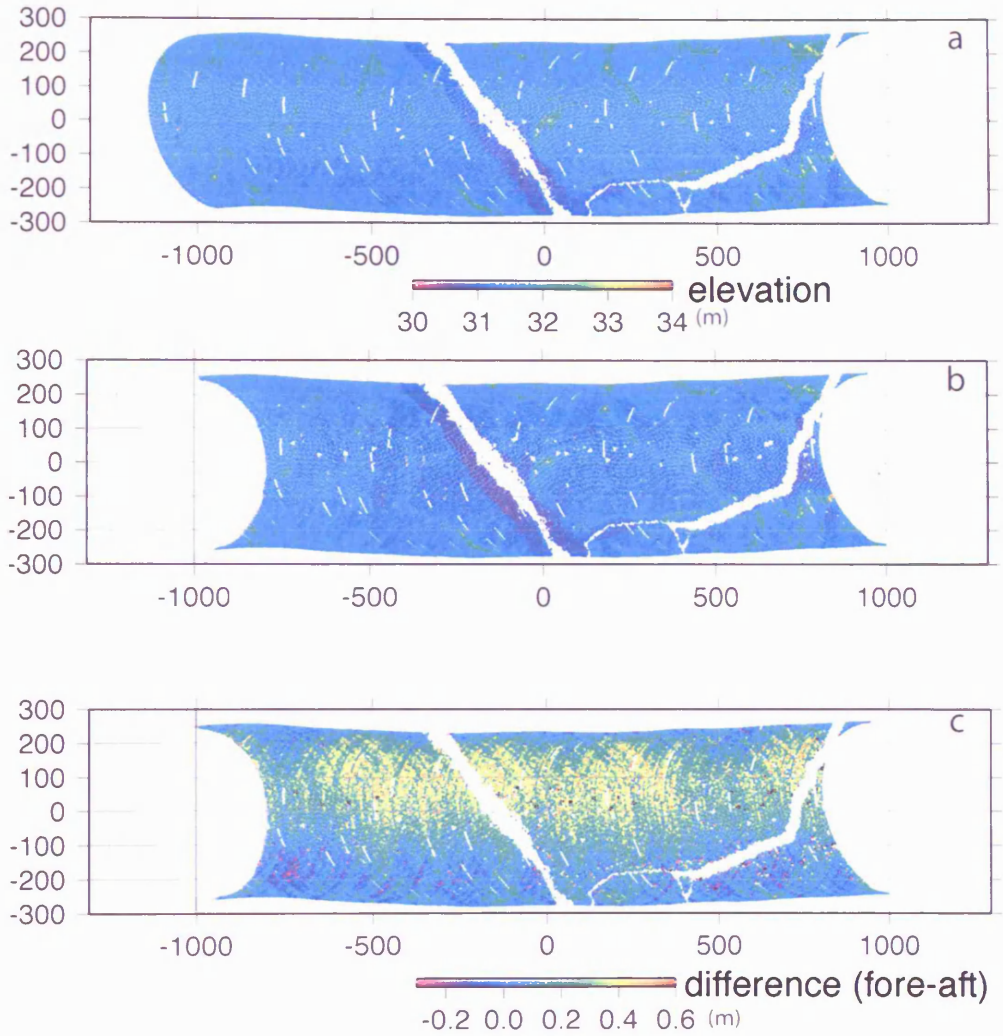

Figure 5.1: (a) section of track showing the elevation data, with respect to the reference ellipsoid, from the forward scan of ATM3 (b) same section of track showing the elevation data from the aft scan. Both (a) and (b) have been smoothed with a Gaussian smoother. (c) shows the difference in elevation between the forward and aft scans. (all units on the x and y axes are in metres)

Figure 5.1 shows laser elevations from ATM3 with respect to the reference ellipsoid; (a) shows data from the forward scan, (b) shows data from the aft scan and (c) shows the difference between the forward and aft scans. Differences range between –0.1 and 0.5 cm. This difference is caused by a pitch error of 0.06 degrees. Figure 5.2 shows the difference between fore and aft scans from a simulation of the ATM. The simulation

was performed over a flat surface, at an altitude of 600 m, with the ATM scanning at the same angle as ATM3. The simulator has a pitch error of 0.06 degrees added to the scanning geometry. The difference between the fore and aft scans calculated from the simulation is the same at the difference seen in figure 5.1.

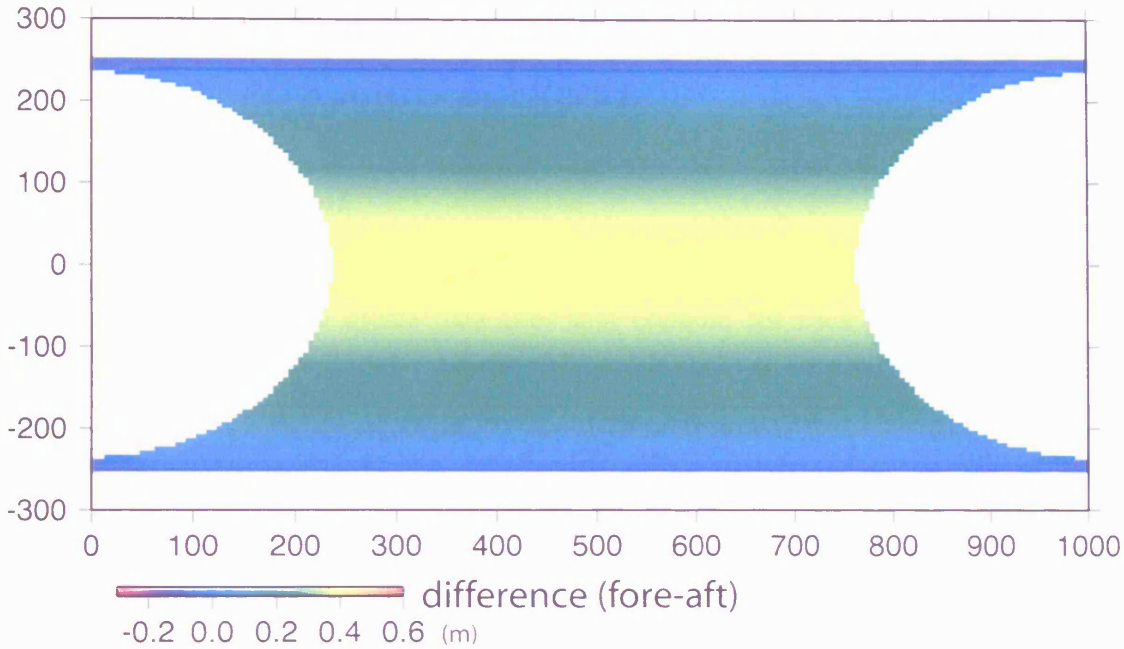

Figure 5.2: Simulated difference between fore and aft scans caused by a pitch error of 0.06 degrees.

The pitch error has an equal and opposite affect on the forward and aft sections of the scan. To remove the pitch error the data must be averaged and each average must include a contribution from the fore and aft part of the scan. Figure 5.1 also shows that the difference is slightly asymmetric. This indicates that there is an error locating the data due to an error in the measurement of the roll of the aircraft. When the data is averaged we also smooth the data set and this asymmetry is no longer apparent. We describe how the ATM data is averaged and smoothed in section 5.6.11.

5.2) Pre-processing and filtering of D2P data

Before the re-tracker or the power simulator were applied to the data, the power and phase were calculated from the APL files (5.2.1), and the data was filtered (5.2.2).

5.2.1) Power and phase calculation

The processed APL files do not give the power and phase values. These values must be calculated from the I and Q values (see chapter 3, section 3.3.17). The power and phase are calculated by:

$$power[i] = \sqrt{I[i]^2 + Q[i]^2} \quad (5.3)$$

$$phase[i] = a\tan(Q[i]/I[i]) \quad (5.4)$$

where $i = 0,1,2,...,length$.

We use this equation to create data files that contain, for each pulse, a header line giving:

Name	Type	Description
Flag	Integer	1 valid pulse, 0 invalid
Time	Integer	Seconds since 00:00
Latitude	Integer	Degrees × 10^6
Longitude	Integer	Degrees × 10^6
Altitude	Integer	Meters × 10^3
Heading	Integer	Degrees × 10^3
Pitch	Integer	Degrees × 10^3
Roll	Integer	Degrees × 10^3
Tracking range	Integer	Tracking range steps
Reference	Integer	Tracking shift
Attenuation	Integer	Receiver attenuation setting
Pulse length	Integer	Number of samples in pulse
Bin size	Integer	Meters × 10^3
Echo number	Integer	Sequential number of echo in file
Data Arrays		
Bin[1,...,pulse length]	Integer	Sample number
Power[1,...,pulse length]	Float	Power
Phase[1,...,pulse length]	Float	Phase

Table 5.2: Format of D2P data files after pre-processing performed at UCL

5.2.2) Filtering of D2P data

Four filters were applied to the D2P data. The number of points removed during each filter is given in appendix 3.

Filter 1:

The points in the processed data files from APL are given a flag. Flag=1 indicates that all the GPS data were available and that the radar was tracking. Flag=0 indicates that the GPS data were not available and/or the radar was not tracking. All points with Flag=0 were removed from the data set.

Filter 2:

Points with nonsensical pitch and roll values (e.g. values greater than 360°) were removed.

Filter 3:

Points crossing over 0° longitude were removed as they contained nonsensical longitude values.

Filter 4:

Points where the aircraft was turning were removed.

5.3) Re-tracking the D2P returns

In this section we describe the design of a new power re-tracking algorithm for returns from the D2P. Section 5.3.1 describes why re-trackers are necessary in radar altimetry and section 5.3.2 explains why existing re-trackers, used for other radar altimeters, are not suitable for the D2P radar altimeter. Section 5.3.3 describes the UCL D2P power re-tracking algorithm.

5.3.1) The use of re-trackers in radar altimetry

There are two reasons to employ re-tracking techniques in radar altimetry. Firstly, the radar tracking computer does not provide precise elevation estimates and secondly the waveform is sampled at discrete intervals that are larger than the resolution we desire.

Radar tracking

A tracking computer is used to keep the surface reflection at a fixed point in the range window. It achieves this by adjusting the delay time (a tracking shift) between the transmitted waveform and the deramping chirp (see figures 3.3 and 3.4 in chapter 3). However, the delay time does not always match the time taken for the waveform to travel to the surface and back to the altimeter, therefore the surface reflection point does not always arrive at the same point in the range window. This means that the radar tracking shift cannot be use to give a precise elevation estimate.

Sampling of waveforms

The returned waveform is sampled at discrete intervals. The spacing between each sample is called the range resolution. For example, the range resolution of the D2P is 0.208 m. However, we require a much better resolution to estimate the elevation of our surface so we rebuild the waveform using a function that closely approximates the waveform shape. This is known as re-tracking.

5.3.2) Existing re-tracking algorithms

Mathematically derived waveform models over the ocean [Brown, 1977] exist, however, there are no such models for sea ice. Although ERS collected data over sea ice no algorithm was specifically designed to re-track the sea ice data [Peacock & Laxon, 2004]. Envisat has four re-tracking modes, ocean, ice1, ice2 and a sea ice re-tracker. The sea ice re-tracker consists of a leading edge threshold detector [Laxon, 1994]. This technique is useful for comparing elevation estimates from successive orbits but is not suitable for the accuracy we require to compare elevation estimates from two different instruments (the radar and laser altimeters). An additional problem arises when we

consider using re-tracking algorithms employed by other radar altimeters. All operational satellite radar altimeters, to date, are conventional pulse limited altimeters. Therefore their waveform shape is different to data from the D2P (see chapter 3, figures 3.2 and 3.12). In chapter 3 we explained how and why the D2P echo shape varies from that of a conventional pulse limited altimeter. In brief, the D2Ps synthetic aperture along-track processing results in the whole of the beam limited footprint, in the along-track direction, contributing to the leading edge of the waveform, rather than to the trailing edge, as in conventional pulse limited altimetry. Because of this difference in the shape of the waveforms between the D2P and conventional pulse limited altimeters, the re-tracking algorithms from ERS etc. are not suitable for the D2P waveforms.

The CryoSat radar altimeter performs synthetic aperture processing in the along-track direction. However, the waveform shape from CryoSat varies from that of the D2P. Figure 5.3 shows an example of a model of the CryoSat waveform from Wingham et al., (2004). We have superimposed a D2P waveform (the same waveform is shown in figure 5.6), and scaled the echo power so that it is the same as the CryoSat waveform.

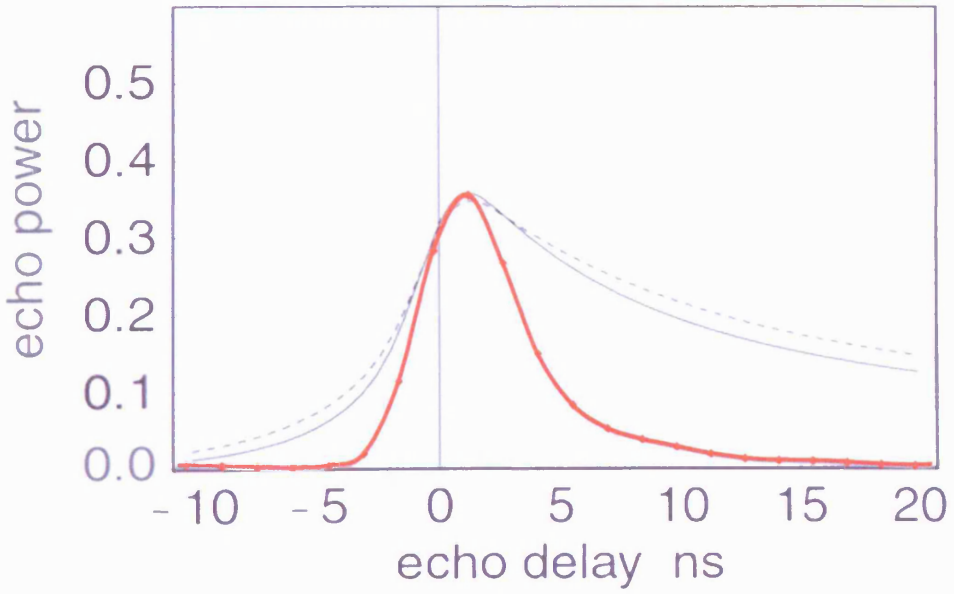

Figure 5.3: Modelled waveform shape for the CryoSat altimeter. The solid line is the waveform returned from a spherical surface and the dashed line is a waveform returned from a surface inclined to a sphere. [Wingham et al., 2004]. We have superimposed a typical D2P return (red line) for comparison. The D2P waveform has been scaled so that its echo power is equal to the modelled waveform. The position of the 0 delay for the D2P waveform is not exact.

The leading edge of the D2P waveform is steeper and the trailing edge falls off faster than the modelled CryoSat waveform. The differences in the shape of the waveforms are due to the differences in geometry of the spaceborne CryoSat altimeter and the airborne D2P. This means that we cannot use an approximation of the CryoSat model to re-track the D2P data.

5.3.3) UCL D2P re-tracking algorithm

The UCL D2P re-tracking algorithm is an empirically derived re-tracker designed to work with echoes conforming to the shape of typical echoes over a smooth surface, hereafter referred to as typical echoes. Figures 5.4 to 5.6 illustrate this type of echo.

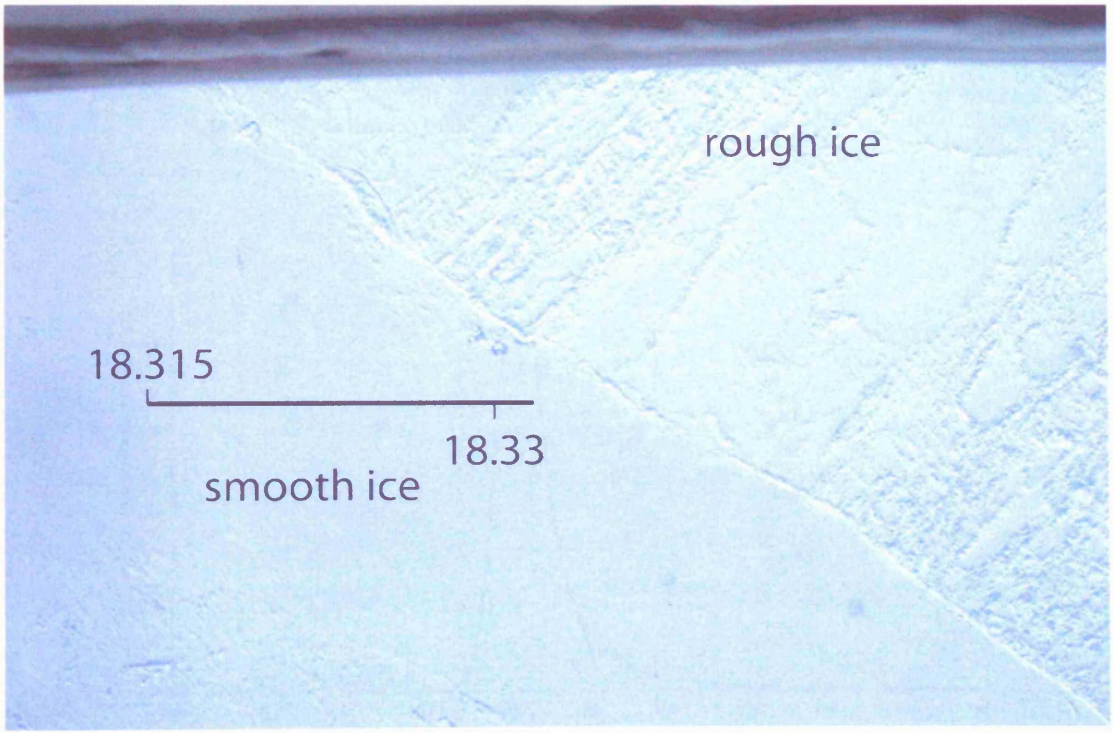

Figure 5.4: Photograph of sea ice showing both smooth and rough ice. Centre of photograph at 81.39° latitude and 18.33° longitude. The black line shows the location of the data shown in figure 5.5 over the smooth ice. The photograph covers an area of 770 m by 514 m. The black area at the top of the photograph is part of the aircraft.

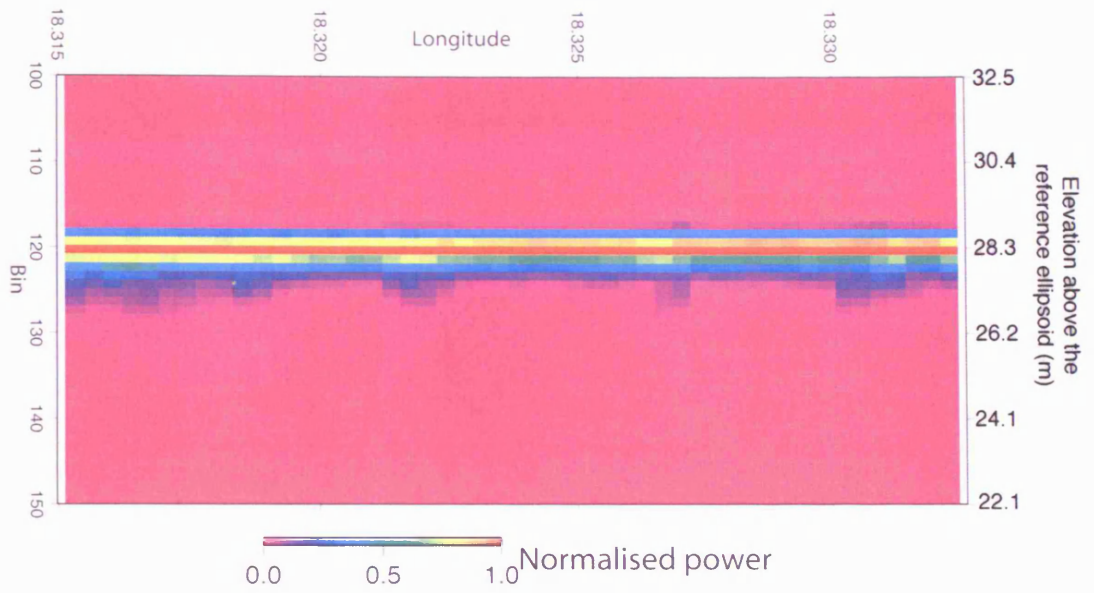

Figure 5.5: Z-scope plot of D2P power over smooth ice section (figure 5.4). The power has been normalised.

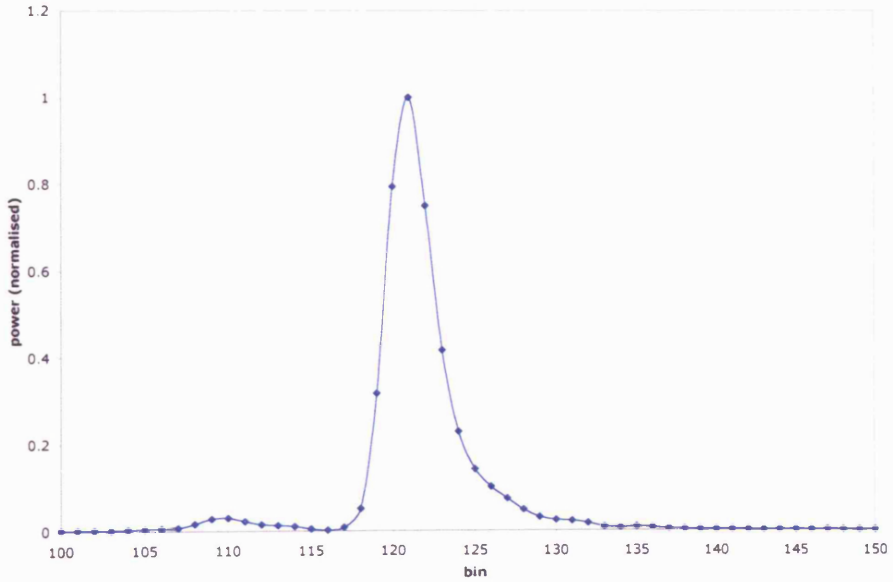

Figure 5.6: Echo at 18.316° longitude. The echo shape is typical of section shown in figure 5.5. Small rise at bin 110 appears in all data and therefore is likely to be an artefact of the radar.

Figure 5.7 shows the parameters used to re-track the echo.

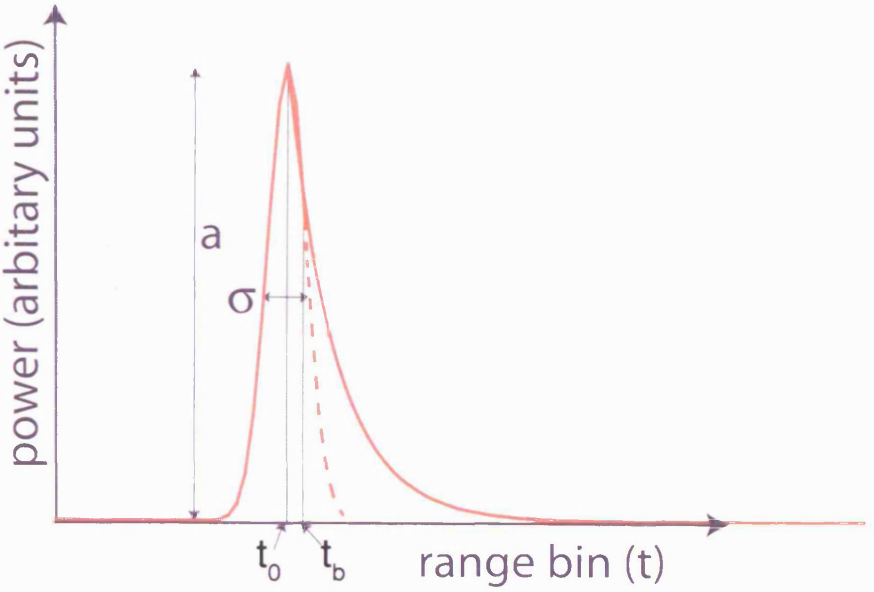

Figure 5.7: The UCL D2P re-tracking function. The solid red line shows the shape of the function. The first part of the function consists of a Gaussian with peak a and width σ. t_0 is the position on the x-axis of the peak, t_b is the position on the x-axis at which the second function takes over from the Gaussian. The second function is $ae^{-k(t-t_0)}$ where k is a constant.

We take our method for creating the UCL D2P re-tracker from Wingham[2] et al., (2004), appendix 1. The technique calculates a non-linear least squares fit to the data using an interpolating function (re-track function) that is designed to represent the CryoSat waveform. The re-track function consists of three functions that describe the shape of the CryoSat echo, which are joined by two linking functions, consisting of polynomials, to ensure that the re-track function is smooth and continuous. To re-track the D2P echoes, we changed the design of the interpolating function to represent the D2P echoes. We use two functions to describe the shape of the echo (figure 5.7) and one linking function.

Figure 5.8 shows the processing scheme for the UCL D2P re-tracking algorithm. The re-tracker uses the routine *mrqmin* from numerical recipes in C [Press et al., 1992]. *mrqmin* attempts to minimise the chi-squared value of a least squares fit between a set of data points and a non-linear function. The harness for *mrqmin* was taken from Vetterling et al., (1992) and modified by David Wallis (UCL). We then changed the harness into a sub routine, and created a new harness to: read in the D2P data files;

calculate the first guess parameters for the typical echo shape (σ, a, t_0 and k); read the best-fit parameters from *mrqmin*; and to calculate the elevation. The first guesses of the re-tracker parameters are described by equations (5.5) to (5.8) and the elevation is given by equation (5.28). We also designed a function (figure 5.7) to fit to the typical D2P echo shape. The algorithm to fit the echo shape uses the equations describing the typical echo shape and their partial derivatives. These are given by equations (5.9) to (5.27).

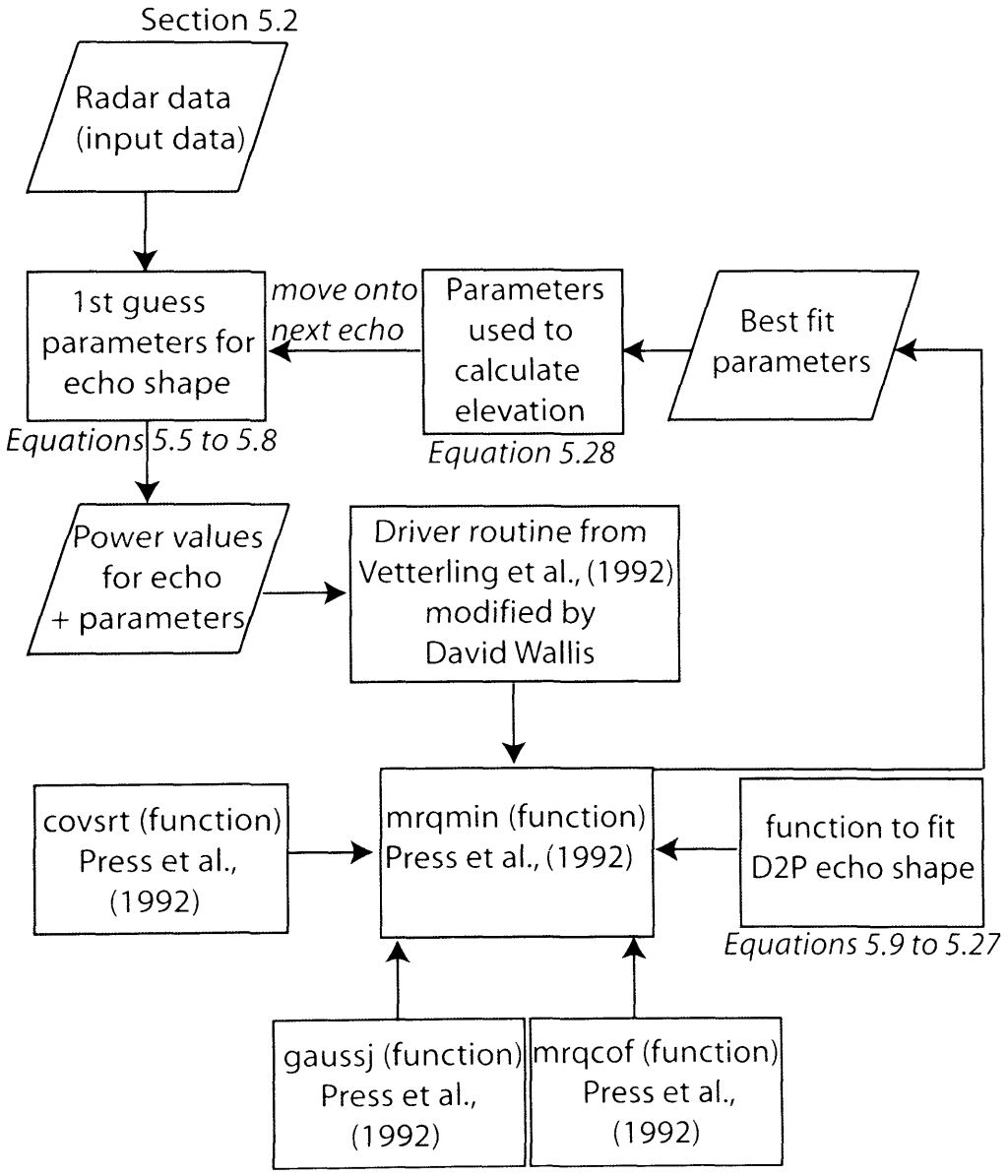

Figure 5.8: The UCL D2P re-tracking algorithm processing scheme.

First guess to the parameters

The function parameters are estimated from each D2P echo. a is taken to be the maximum power and it's position is used to estimate t_0. σ is estimated from the location of the first power estimate that is greater than half of the highest power, the location of the highest power and the general formula for a Gaussian (equation 5.5).

$$y = ae^{\frac{-(t-t_0)^2}{\sigma^2}} \tag{5.5}$$

therefore:

$$a/2 = ae^{\frac{-(t(j)-t(i))^2}{\sigma^2}} \tag{5.6}$$

where j is the (approximate) location of the half power point and i is the location of the peak power point. A first guess for σ is therefore given by:

$$\sigma^2 = \frac{-(t(j)-t(i))^2}{\ln(1/2)} \tag{5.7}$$

where k is given by:

$$k = \frac{t(i)-t(j)}{\sigma^2} \tag{5.8}$$

If the difference in location of the peak power and approximate half power is zero then σ equals 4 and k equals 0.5.

Re-tracking function

The re-tracking function must be smooth and continuous for all $t > t_0$, its first derivative must also be smooth and continuous. The shape of the re-tracking function, chosen to approximate the shape of a typical echo, consists of a Gaussian rise with a tail proportional to e^{-kt}, where k is a constant. A full description of the function is given by equation 5.9.

$$P(t) = ae^{-f(t)^2} \tag{5.9}$$

where

$$f(t) = f_n(t) = \frac{(t - t_0)}{\sigma} \qquad -\infty < t < t_0$$

$$f(t) = f_1(t) = a_3(t - t_0)^3 + a_2(t - t_0)^2 + \frac{1}{\sigma}(t - t_0) \qquad t_0 < t < (t_b + t_0)$$

$$f(t) = f_2(t) = (k(t - t_0))^{1/2} \qquad (t_b + t_0) < t < \infty$$

where t is the delay time, t_0 the time of the peak return and t_b the time at which f_1 is replaced by f_2. f_1 is a linking function between f_n and f_2 to ensure that the whole function is smooth and continuous. The constants a_3 and a_2 are derived using the following conditions, $f_1(t_0 - t_b) = f_2(t_0 - t_b)$ and $f_1'(t_0 - t_b) = f_2'(t_0 - t_b)$. Hence:

$$a_2 = -\frac{-5k\sigma + 4(kt_b)^{1/2}}{2\sigma t_b (kt_b)^{1/2}} \tag{5.10}$$

$$a_3 = -\frac{3k\sigma - 2(kt_b)^{1/2}}{2\sigma t_b^2 (kt_b)^{1/2}} \tag{5.11}$$

The 1st partial derivatives of the function must be smooth and continuous. The function has four variables a, σ, t_0 and k (t_b is calculated directly from k and σ, $t_b = k \times \sigma^2$). The partial derivatives of the re-tracking function are given by equations 5.12 to 5.27.

Partial derivatives of P_n:

$$\frac{\partial Pn}{\partial a} = e^{-\frac{(t-t_0)^2}{\sigma^2}} \tag{5.12}$$

$$\frac{\partial Pn}{\partial \sigma} = \frac{2ae^{-\frac{(t-t_0)^2}{\sigma^2}}(t - t_0)^2}{\sigma^3} \tag{5.13}$$

$$\frac{\partial Pn}{\partial t_0} = \frac{2ae^{-\frac{(t-t_0)^2}{\sigma^2}}(t-t_0)}{\sigma^2} \tag{5.14}$$

$$\frac{\partial P_n}{\partial k} = 0 \tag{5.15}$$

Partial derivatives of constants a_3 and a_2:

$$\frac{\partial a_2}{\partial \sigma} = -\frac{-5k + \frac{4k^2}{\sqrt{k^2\sigma^2}}}{2k\sigma^3\sqrt{k^2\sigma^2}} + \frac{k(-5k\sigma + 4\sqrt{k^2\sigma^2})}{2\sigma^2(k^2\sigma^2)^{3/2}} + \frac{3(-5k\sigma + 4\sqrt{k^2\sigma^2})}{2k\sigma^4\sqrt{k^2\sigma^2}} \tag{5.16}$$

$$\frac{\partial a_3}{\partial \sigma} = -\frac{3k - \frac{2k^2\sigma}{\sqrt{k^2\sigma^2}}}{2k^2\sigma^5\sqrt{k^2\sigma^2}} + \frac{3k\sigma - 2\sqrt{k^2\sigma^2}}{2\sigma^4(k^2\sigma^2)^{3/2}} + \frac{5(3k\sigma - 2\sqrt{k^2\sigma^2})}{2k^2\sigma^6\sqrt{k^2\sigma^2}} \tag{5.17}$$

$$\frac{\partial a_2}{\partial k} = -\frac{-5\sigma + \frac{4k\sigma^2}{\sqrt{k^2\sigma^2}}}{2k\sigma^3\sqrt{k^2\sigma^2}} + \frac{-5k\sigma + 4\sqrt{k^2\sigma^2}}{2\sigma(k^2\sigma^2)^{3/2}} + \frac{-5k\sigma + 4\sqrt{k^2\sigma^2}}{2k^2\sigma^3\sqrt{k^2\sigma^2}} \tag{5.18}$$

$$\frac{\partial a_3}{\partial k} = -\frac{3\sigma - \frac{2k\sigma^2}{\sqrt{k^2\sigma^2}}}{2k^2\sigma^5\sqrt{k^2\sigma^2}} + \frac{3k\sigma - 2\sqrt{k^2\sigma^2}}{2k\sigma^3(k^2\sigma^2)^{3/2}} + \frac{3k\sigma - 2\sqrt{k^2\sigma^2}}{k^3\sigma^5\sqrt{k^2\sigma^2}} \tag{5.19}$$

Partial derivatives of P_1 are:

$$\frac{\partial P_1}{\partial a} = e^{-(\frac{t-t_0}{\sigma} - \frac{(-5k\sigma+4\sqrt{k^2\sigma^2})(t-t_0)^2}{2k\sigma^3\sqrt{k^2\sigma^2}} - \frac{(3k\sigma-2\sqrt{k^2\sigma^2})(t-t_0)^3}{2k^2\sigma^5\sqrt{k^2\sigma^2}})^2} \tag{5.20}$$

$$\frac{\partial P_1}{\partial \sigma} = -2ae^{-(\frac{t-t_0}{\sigma}+(t-t_0)^2 a_2+(t-t_0)^3 a_3)^2}(\frac{t-t_0}{\sigma}+(t-t_0)^2 a_2+(t-t_0)^3 a_3) \quad (5.21)$$
$$(-\frac{t-t_0}{\sigma^2}+(t-t_0)^2\frac{\partial a_2}{\partial \sigma}+(t-t_0)^3\frac{\partial a_3}{\partial \sigma})$$

$$\frac{\partial P_1}{\partial t_0} = -2ae^{-(\frac{t-t_0}{\sigma}+(t-t_0)^2 a_2-(t-t_0)^3 a_3)^2}(-\frac{1}{\sigma}-2(t-t_0)a_2-3(t-t_0)^2 a_3) \quad (5.22)$$
$$(\frac{t-t_0}{\sigma}+(t-t_0)^2 a_2+(t-t_0)^3 a_3)$$

$$\frac{\partial P_1}{\partial k} = -2ae^{-(\frac{t-t_0}{\sigma}+(t-t_0)^2 a_2+(t-t_0)^3 a_3)^2}(\frac{t-t_0}{\sigma}+(t-t_0)^2 a_2+(t-t_0)^3 a_3) \quad (5.23)$$
$$((t-t_0)^2\frac{\partial a_2}{\partial k}+(t-t_0)^3\frac{\partial a_3}{\partial k})$$

Partial derivatives of P_2 are:

$$\frac{\partial P_2}{\partial a} = e^{-k(t-t_0)} \quad (5.24)$$

$$\frac{\partial P_2}{\partial \sigma} = 0 \quad (5.25)$$

$$\frac{\partial P_2}{\partial t_0} = ae^{-k(t-t_0)}k \quad (5.26)$$

$$\frac{\partial P_2}{\partial k} = ae^{-k(t-t_0)}(t-t_0) \quad (5.27)$$

The parameter t_0 is used to calculate the elevation, along with the *ref* value given in the header for each pulse. *ref,* when multiplied by the sampling interval (Si), gives the elevation of the centre of the range window above the reference ellipsoid. Therefore, to calculate the elevation:

$$elevation = (ref \times Si) + (((len/2) - t_0) \times Si) \quad (5.28)$$

where *Si*=0.208189 m and *len* is the number of bins in the range window.

5.4) UCL range calibration

We now describe the calibration method used for the UCL D2P re-tracking algorithm. We use the same method as APL. We then describe the results of the calibration.

5.4.1) Calibration method

The original offset correction of 23.98 m was calculated using a sinc re-tracking algorithm (chapter 3, section 3.4), and assuming that the peak of the function gave the position of the surface. The use of the alternative UCL D2P re-tracking algorithm means that the elevations must be re-calibrated.

Before the elevation estimates were re-calibrated, the D2P data longitudes, latitudes and altitudes were corrected as the values given in the data files were for the position of the GPS antenna rather than the radar antenna. All GPS data falling within the D2P footprint, with its centre at the radar nadir and dimensions given by equations 3.9 and 3.10 (chapter 3), were averaged. The GPS average was weighted with the antenna gain (see section 5.6.2 for a description of the antenna gain).

5.4.2) Calibration results

Figures 5.9 and 5.10 show the UCL, APL and GPS elevations along the runway. The outliers in the inset in figure 5.10 are caused by double peaked echoes of unknown origin (figure 5.11). The outliers were not included in the mean offset calculation in table 5.3.

Pass	Height	GPS-UCL (mean)	APL-UCL (mean)
1	300 m	0.02488057 m	0.0259418 m
2	600 m	0.04400917 m	0.02996341 m

Table 5.3: Offset between UCL re-tracker and the GPS survey and the APL re-tracker.

Therefore, to correct the elevation estimate for the UCL D2P re-tracker, we add 0.034 m to each elevation estimate.

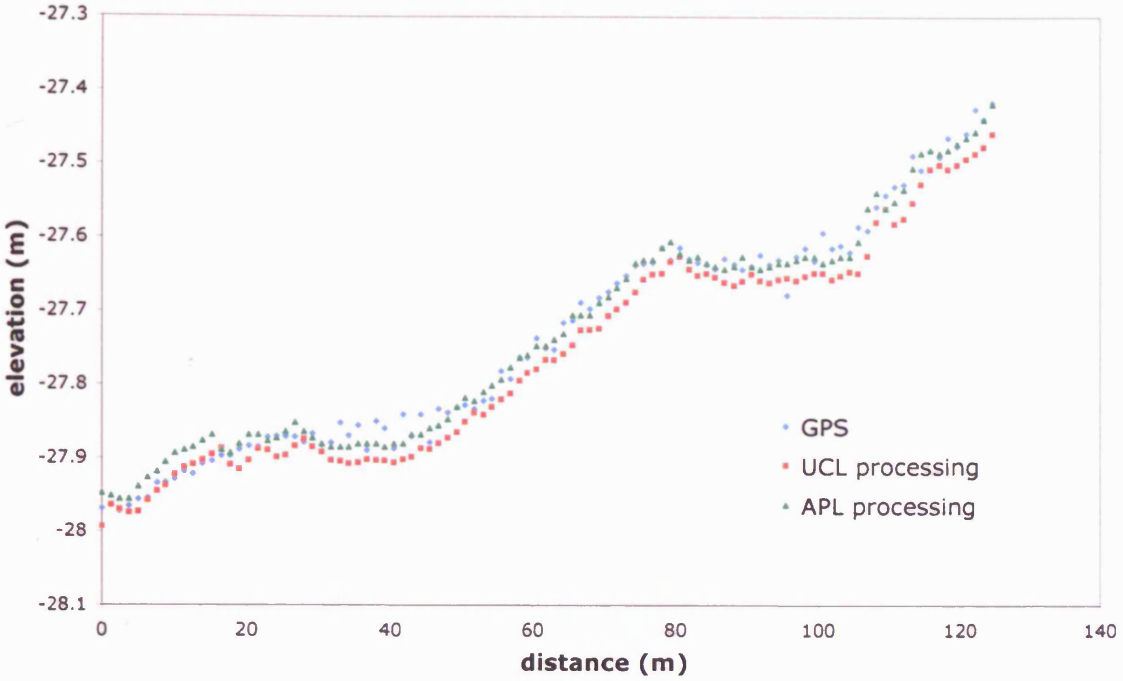

Figure 5.9: 300 m pass. GPS measurements averaged over radar footprint (blue). APL re-tracker elevation estimates with 23.98 m correction (green). UCL D2P re-tracker elevation estimates (red). Elevations are with respect to the reference ellipsoid.

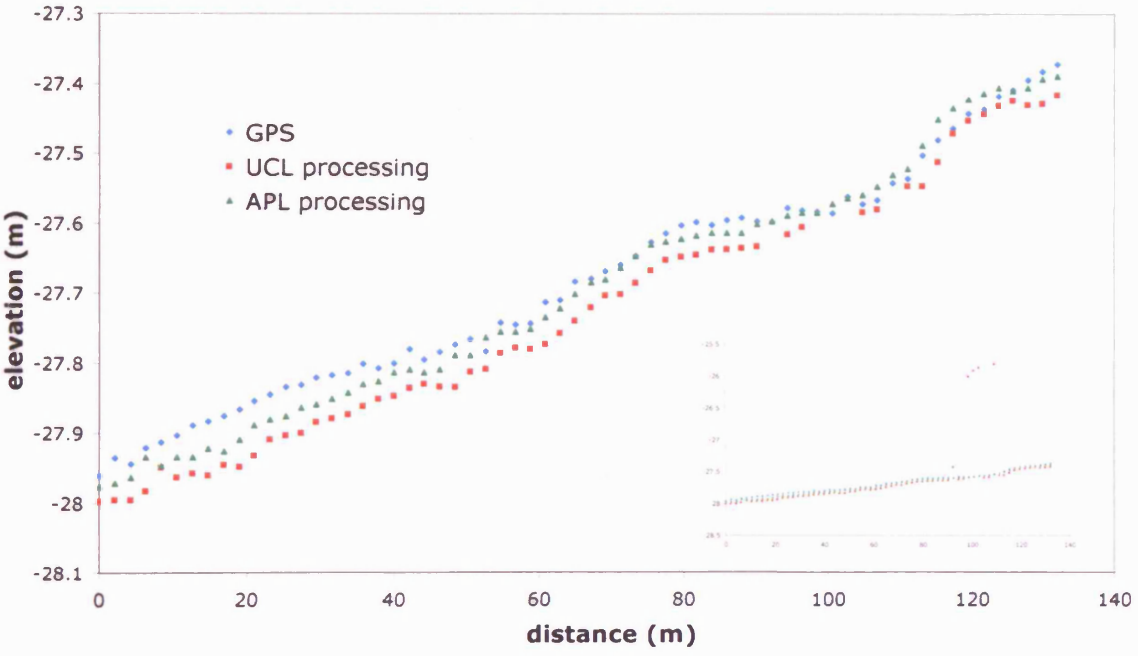

Figure 5.10: 600 m pass. GPS measurements averaged over radar footprint (blue). APL re-tracker elevation estimates with 23.98 m correction (green). UCL D2P re-tracker elevation estimates (red). Elevations are with respect to the reference ellipsoid. The inset figure shows the full data set over this section of track.

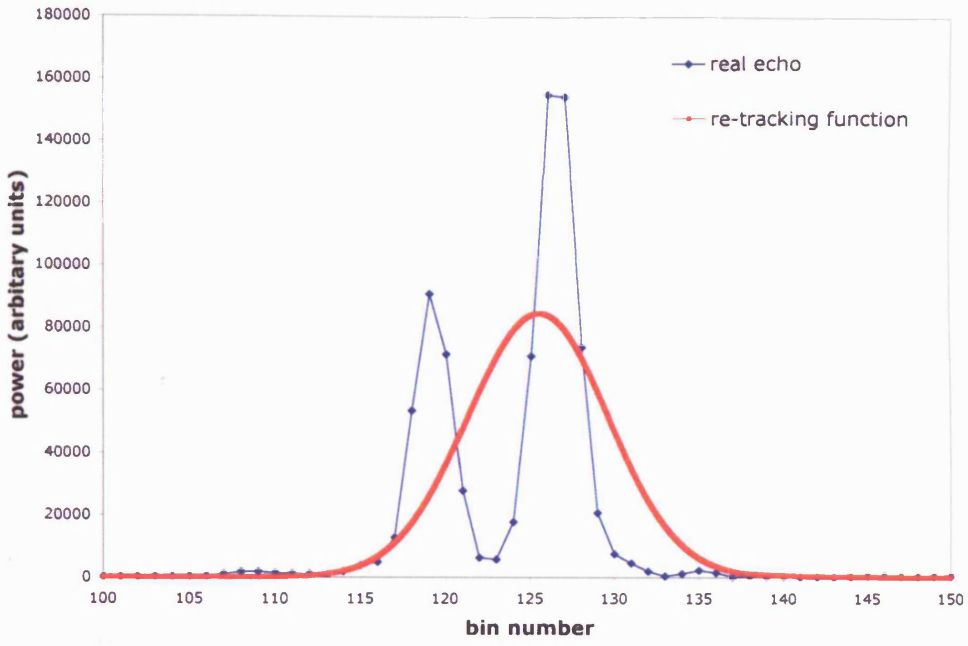

Figure 5.11: An example of double peaked echo from calibration flight.

5.4.3) Accuracy of the D2P data

The repeatability of the D2P data was determined by the method described in section 5.1.1. When comparing a datum point from the 300 m pass to data points from the 600 m pass, points lying within 2.4 m of the 300 m datum point were included in the calculations. 2.4 m is the width of the along-track footprint at 300 m altitude. When comparing a datum point from the 600 m pass to data points from the 300 m pass, points lying within 4.7 m of the 600 m datum point were included in the calculations. 4.7 m is the width of the along-track footprint at 600 m altitude.

D2P Survey	RMS_{D2P} (m)
300 m	0.0340
600 m	0.0355

Table 5.4: Repeatability of D2P data over the Wallops runway.

From table 5.4, we would expect a D2P repeat survey to give elevation estimates within 0.035 meters of the original survey. However, the purpose of writing a re-tracker is to compare the elevation estimates from the D2P to the elevation estimates from the ATM

data set. Therefore we must know how accurate our comparisons are. Sections 5.4.4 and 5.4.5 discuss this matter.

5.4.4) Comparisons between the ATM, D2P and GPS data sets

When comparing data from the D2P and ATM instruments collected during the LaRA campaign, only data collected simultaneously will be used. For this reason only data collected on the 3rd May, during the 600 m pass has been used to estimate the errors between the two data sets as this was the only calibration flight where data was recorded simultaneously.

The mean differences and standard deviations between the ATM, D2P and GPS data sets were computed using the same point inclusion criteria as described in section 5.4.3.

μ_{COM} (m)	σ_{COM} (m)	$RMS_{COM\,(m)}$
0.044176	0.096870	0.106468

Table 5.5: Mean difference, standard deviation and RMS error between the ATM3 survey taken on the 3rd May and D2P elevation estimates from the 600 m pass.

ATM/D2P Survey	μ_{COM} m (m)	σ_{COM} m (m)	$RMS_{COM\,(m)}$
3rd May ATM3	0.000868	0.120563	0.120563
6th May ATM2_1	0.012273	0.065659	0.066796
6th May ATM2_2	-0.065116	0.058115	0.087278
6th May ATM2_3	-0.037140	0.054755	0.066162
6th May ATM3_1	-0.097241	0.067041	0.118111
6th May ATM3_2	-0.111895	0.055094	0.124723
6th May ATM3_3	-0.068139	0.054991	0.087560
All Flights	-0.052654	0.089723	0.104032
D2P 300 m pass	-0.016980	0.051114	0.053861
D2P 600 m pass	0.043316	0.076553	0.087958

Table 5.6: Mean difference and standard deviation between ATM or D2P elevation estimates and GPS elevation estimates.

Summary of results

The results of the accuracy study are summarised in table 5.7. The largest standard deviations and RMS values from tables 5.1, 5.4, 5.5 and 5.6 have been taken to be the error on either the individual data sets or the error when comparing data sets.

	D2P	ATM
D2P	μ_{D2P} = -3 to 3 cm σ_{D2P} = 3 cm RMS_{D2P} = 3 cm	μ_{COM} = 4 cm σ_{COM} = 10 cm RMS_{COM} = 11 cm
ATM	μ_{COM} = 4 cm σ_{COM}= 10 cm RMS_{COM} = 11 cm	μ_{ATM} = -5 to 12 cm σ_{ATM} = 10 cm RMS_{ATM} = 13 cm
GPS	μ_{COM} = -2 to 4 cm σ_{COM} = 7 cm RMS_{COM} = 8 cm	μ_{COM} = -11 to 1 cm σ_{COM} = 12 cm RMS_{COM} = 12 cm

Table 5.7: Summary of accuracy results.

For the purpose of our study we are interested in the difference between the ATM and the D2P. The calibration data shows that over the runway that the maximum total error (RMS error) is 11 cm. This is comparing a single laser estimate within a D2P footprint.

5.4.5) Comparison of the average ATM elevation and the D2P elevation

Figure 5.12 shows two D2P footprints over the runway, and the coincident ATM data used to estimate the mean laser elevation over the footprint.

It is clear that, unless we observe a very smooth surface, the individual laser elevations will differ from the radar elevation. This sampling problem contributes to the RMS error between the two sets of elevations.

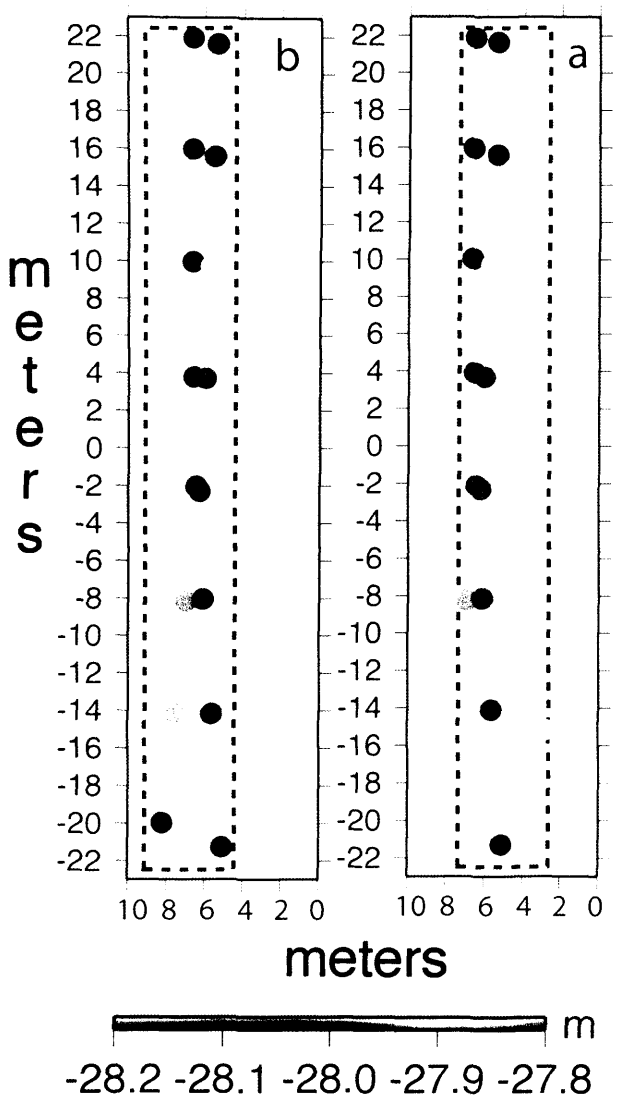

Figure 5.12: Two radar footprints (dashed rectangles) from the 600 m pass, with the laser elevations that fall within those footprints shown as coloured dots (to scale). The direction of flight is from right to left. The radar elevation estimate for a is –27.928 m and the mean laser elevation is –27.988 m, the radar elevation for b is –27.926 m and the mean laser elevation is –28.003 m.

Table 5.8 shows the mean difference, standard deviation and RMS error between the D2P elevation estimate and the ATM elevation estimate averaged over the D2P footprint.

μ_{COM} m	σ_{COM} m	RMS_{COM}	No. points in mean
-0.001723	0.023966	0.024028	12 to 17

Table 5.8: Mean difference, standard deviation and RMS error between D2P and the mean ATM elevation estimates.

Therefore the error between a D2P elevation estimate and a laser elevation estimate, consisting of an average of laser elevation estimates over the D2P footprint, is 2.4 cm. N.B. difference between the fore and aft scans (section 5.1.2) are not seen in the calibration data as they are caused by drift in the INS system which did not occur during the calibration flights. We expect the flight data to have the same error as the calibration data provided the differences in fore and aft scans are corrected for.

5.5) Limitations of the re-tracker

There are two major assumptions used in the re-tracker that could affect our elevation estimate. These are the assumption that the re-track point is at the peak of the return and that all echoes conform to the shape of a typical echo. We will now explain the problems associated with these two assumptions in detail.

1) The re-track point

We assume that the re-track point is at the peak of the return, and calculate our elevation estimates from this point. In reality the location of the re-track point depends on the surface height distribution. In chapter 3 we described the power returned to a conventional pulse limited altimeter from the sea surface, which has a Gaussian surface height distribution. For such a Gaussian surface, it is well know that it's re-track point is the half power point. Our re-tracker is calibrated at the peak of the return with elevation estimates over a runway. The surface height distribution of the runway is not the same as the surface height distribution over sea ice so the peak of the return may not correspond to the elevation of the sea ice.

2) The echo shape

We have assumed a typical echo shape for all our D2P returns. Figure 5.13 is a Z-scope plot of a series of returns from file number 8 on the 20th May. From the figure you can see that only the centre echoes on the along-track axis are typical echoes. Echoes either side do not have such a sharp power drop off.

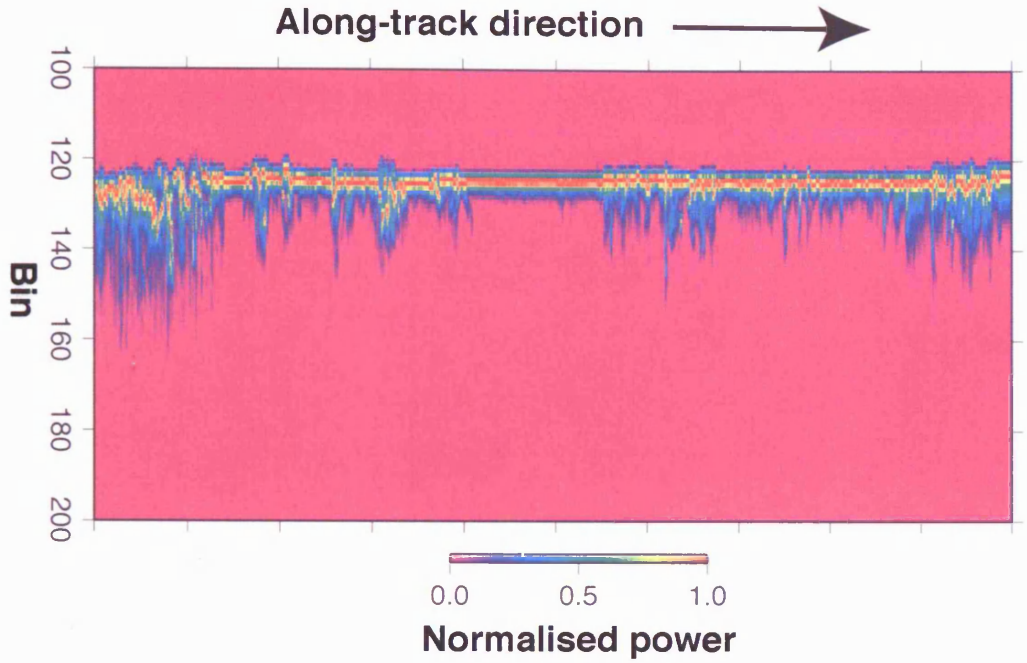

Figure 5.13: Z-scope plot of a section of track from file 8 on the 20th May.

Changes in the shape of the echo are due to changes in the pitch and roll of the aircraft and to the surface roughness changing (when the surface becomes rough the echoes tend to be wider). Our re-tracker is designed to cope with a typical echo shape, we do not know how it will perform when it attempts to re-track echoes wider echoes or indeed any echo shape that does not conform to the typical echo shape. We have seen the effect of applying the re-tracker to a double peaked echo shape in figures 5.10 and 5.11; the elevation estimates are too high. It is possible that we can filter out the echoes that do not conform to the shape of a typical echo, but this may seriously reduce our data volume.

By building a power simulator we avoid both of these problems and create a method that will provide a good fit to much of the data. The power simulator is designed to investigate whether we can see the laser and radar reflecting from different surfaces. We use the laser data to create a surface model (the laser ranges to the air/snow interface, or the air/ice interface when no snow is present) and simulate the D2P return over this surface. As the evidence presented in chapter two suggests that the radar reflects from the snow/ice interface we expect the return from the simulator to arrive earlier in the range window than the real D2P returns over the snow covered ice. The simulator takes

into account the pitch and roll of the aircraft, and therefore produces both typical and non-typical echoes. The data analysis does not require us to locate a re-track point as the full simulated echo shape is compared to the full real echo shape and the offset in the range window between them gives us an estimate of the difference in elevation between the laser/snow surface and the surface that the radar ranges to. The simulator creates a method to compare data from two different instruments that cannot be directly compared. In addition, by running the simulator over a flat, known surface, we will be able to find the re-track point for a typical D2P echo. As well as analysing the results from the simulator in their own right we can use the results to test the re-tracker. The re-tracker is a relatively quick and easy method to look at the LaRA data, therefore it could be a useful tool in comparing future data sets, but only if it provides reasonable elevation estimates. If the difference in elevation between the simulated echo and the real echo are similar to the difference between the elevation estimate from the re-tracker and the elevation estimate from the ATM data, then we can say that the re-tracker provides a reasonable elevation estimate.

The following sections describe the power simulator in detail.

5.6) The UCL D2P simulator

The UCL D2P simulator is designed to calculate a D2P radar echo from a surface constructed from the laser data. The position in the range window of the simulated echoes is then compared to the position in the range window of the real echoes (N.B. the size of the power of the simulated echoes is not calculated). An offset in the position (i.e. time) between the real and simulated echoes means that they are measuring different surfaces. The power integral is the basis of the simulator, and is given by equation 5.29:

$$\iint_A \frac{P(t)}{r^4} G^2(\theta,\phi)\beta(\theta_l)dA \qquad (5.29)$$

where A is area.

The power integral consists of three functions: $P(t)$, describing the power envelope as a function of time; $G(\theta,\phi)$, describing the antenna gain as a function of the facet orientation angles and $\beta(\theta_l)$, describing the weighting from the along track synthetic aperture processing as a function of look angle. The look angle and orientation angles are shown in figure 5.14.

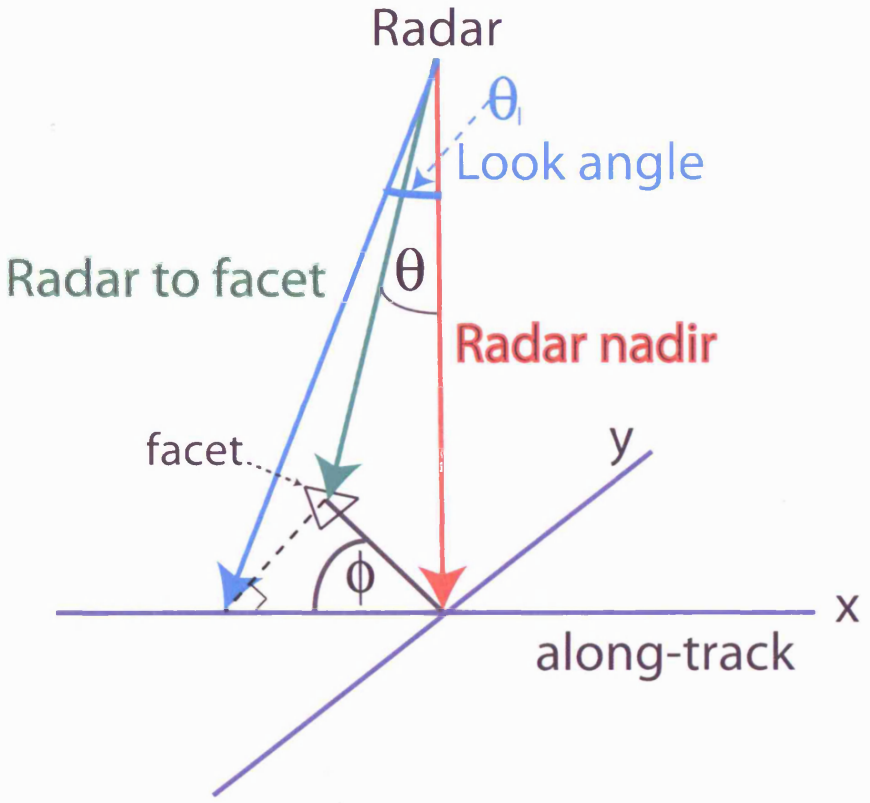

Figure 5.14: The facet orientation angles and the look angle.

We now describe each of the components of the power integral in detail.

5.6.1) The transmitted power envelope, *P(t)*

The transmitted power envelope is given by:

$$P(t) = \mathrm{sinc}^2(\Delta F \pi T) \qquad (5.30)$$

[Carl Leuschen, personal communication]

where ΔF is the instrument band width (360×10^6 Hz), and T is given by,

$$T = t - \frac{2r}{c} \tag{5.31}$$

where r is the range to the surface, t is the time at which the power is being measured and c is the speed of light. r is calculated from the magnitude of the vector between the D2P antenna and the facet.

$$r = \sqrt{z^2 + (x^2 + y^2)(1 + z^2/\mathrm{Re})} \tag{5.32}$$

where Re is the earth's radius.

5.6.2) The antenna gain, $G(\theta,\phi)$

The antenna gain (G) is a function of θ and ϕ, which describe the direction between the antenna bore-sight and the facet.

The following discussion is based on Peebles, (1998). $G(\theta,\phi)$ is the directive gain of the antenna and is defined as:

$$G(\theta,\phi) = \frac{\text{radiation intensity (W/Sr) in direction } (\theta,\phi)}{\text{average radiation intensity (W/Sr)}} \tag{5.33}$$

$$= \frac{\rho(\theta,\phi)}{P_{rad}/4\pi} \tag{5.34}$$

where P_{rad} is the total radiated power and $\rho(\theta,\phi)$ is the radiation intensity pattern.

The D2P has a rectangular antenna, the gain of which is given by $\rho(\theta,\phi)$:

$$\rho(\theta,\phi) = \frac{P_{rad}A}{\lambda^2}\left[\frac{1+\cos\theta}{2}\right]^2 \mathrm{sinc}^2\left[\frac{a\pi}{\lambda}\sin\theta\cos\phi\right]\mathrm{sinc}^2\left[\frac{b\pi}{\lambda}\sin\theta\sin\phi\right] \tag{5.35}$$

where a and b are the lengths of the sides of the antenna. For the D2P a=0.3 m and b=0.15 m. λ is the radar wavelength (0.022 m), and A_a is the area of the antenna. Therefore $G(\theta,\phi)$ is given by:

$$G(\theta,\phi) = \frac{4\pi A_a}{\lambda^2}\left[\frac{1+\cos\theta}{2}\right]^2 \operatorname{sinc}^2\left[\frac{a\pi}{\lambda}\sin\theta\cos\phi\right]\operatorname{sinc}^2\left[\frac{b\pi}{\lambda}\sin\theta\sin\phi\right] \quad (5.36)$$

5.6.3) The beam function, $\beta(\theta_l)$

As described in chapter 3, section 3.3.2, the D2P uses synthetic aperture processing in the along track direction. This means that the radar emits bursts of 16 coherent pulses, which form a long, synthetic aperture in the along-track direction. As the synthetic processing is only performed in the along-track direction, β is a function of the look angle (θ_l) only. The result of the synthetic processing is to narrow the along-track footprint, thereby improving the horizontal resolution of the elevation estimate. The signal to noise ratio of the elevation measurement is improved by multi-looks at each point on the ground from consecutive bursts. Each coherent pulse intersects the antenna gain pattern and the power envelope at a different location, this results in a slightly different shape of power return from each pulse.

To derive the power contribution from the synthetic processing we consider a linear array of N sources. Each source is separated by a distance Δx, given by:

$$\Delta x = \frac{v}{prf} = 0.086m \quad (5.37)$$

where v is the velocity of the aircraft (150 ms^{-1}) and prf is the pulse repetition frequency (1750 Hz).

The field equation for a linear array of sources is given by, [Peebles, 1998 & Stutzman & Thiele, 1998].

$$F_m = \sum_{n=0}^{N-1} e^{i2n(k\Delta x \sin\theta_l - \frac{\pi m}{N})} \tag{5.38}$$

where $k = \frac{2\pi}{\lambda}$, λ is the wavelength, Δx is the distance between coherent pulses, N is the number of pulses in a coherent burst (16) and m is the pulse number in the burst for which the field equation is being calculated. To calculate the power contribution from each of the 16 pulses equation 5.38 can be simplified and converted to power as follows [Peebles, 1998 & Stutzman & Thiele, 1998].

Let:

$$\beta = 2(k\Delta x \sin\theta_l - \frac{\pi m}{N}) \tag{5.39}$$

Therefore:

$$F_m = \sum_{n=0}^{N-1} e^{in\beta} \tag{5.40}$$

The series is:

$$F_m = 1 + e^{i\beta} + e^{i2\beta} + ... + e^{i(N-1)\beta} \tag{5.41}$$

Multiplying by $e^{i\beta}$ gives:

$$F_m e^{i\beta} = e^{i\beta} + e^{i2\beta} + ... + e^{iN\beta} \tag{5.42}$$

Subtracting 5.40 from 5.41 gives:

$$F_m(1 - e^{i\beta}) = (1 - e^{iN\beta}) \tag{5.43}$$

$$F_m = \frac{(1 - e^{iN\beta})}{(1 - e^{i\beta})} = \frac{(e^{iN\beta} - 1)}{(e^{i\beta} - 1)} = \frac{e^{iN\beta/2}}{e^{i\beta/2}} \frac{e^{iN\beta/2} - e^{-iN\beta/2}}{e^{i\beta/2} - e^{-i\beta/2}} \tag{5.44}$$

$$F_m = e^{i(N-1)\beta/2}\frac{\sin(N\beta/2)}{\sin(\beta/2)} \tag{5.45}$$

To find the power (P_m) we multiply by the complex conjugate:

$$P_m = \frac{\sin^2(N(k\Delta x\sin\theta_l - \frac{\pi m}{N}))}{\sin^2(k\Delta x\sin\theta_l - \frac{\pi m}{N})} \tag{5.46}$$

as:

$$e^{i(N-1)\beta/2}e^{i(N-1)\beta/2^*} = 1 \tag{5.47}$$

Figure 5.15 shows the power contribution from each beam as a function of distance, for the radar located above 0 on the x-axis.

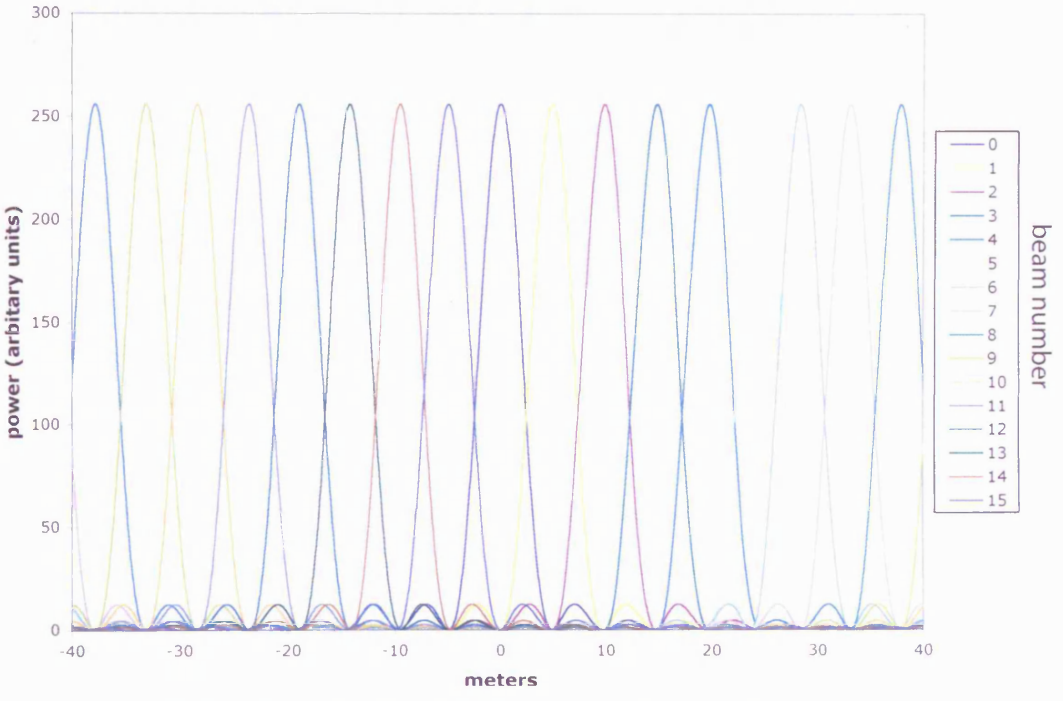

Figure 5.15: Power contribution from each coherent pulse within a burst as a function of distance from the radar nadir. The distance along the x-axis is calculated by taking the tangent of the look angle and multiplying by the radar altitude.

The dimension of the along-track footprint (Δx_{D2P}) is defined as the distance between peaks in figure 5.15 and is given by:

$$\Delta x_{D2P} = \frac{h \times prf \times c}{2 \times N \times v \times fc} \tag{5.48}$$

[Carl Leuschen, personal communication]

where h is the altitude of the radar, prf is the pulse repetition frequency (1750 Hz), c is the speed of light, v is the aircraft velocity (150 ms^{-1}) and fc is the radar frequency (13.9 GHz).

Our equation for the power contribution from the synthetic aperture processing is a simplification of the process as, although we are calculating returns from multiple angles we are not calculating the total number of looks over each footprint. Our simulator assumes that there is a distance of one across-track footprint (3.9 m at an altitude of 500 m) between each burst of pulses. Therefore each power return has 16 components, one from each coherent beam. In reality there is a distance of $\Delta x \times N$ between each burst, 1.375 meters. This means that each point on the ground can be seen by 25 consecutive bursts, and the beams from each burst overlap. To model this effect we would have to include 'beam steering' (chapter 3, section 3.3.2) which means that we would locate a point on the surface, and as the aircraft moves the beams would be steered (i.e. the look angle is adjusted) so that the beams would always line up and could be easily summed. The higher look rate of the D2P serves to reduce the signal to noise ratio. The simulator does not have noise, and as we are comparing the shapes of the real and simulated echoes rather than the power value we do not think that it is necessary to include the extra looks. By making the assumption that the bursts do not overlap and by calculating 16 beams (or looks) for each footprint we still include the complexity that the shape of the mean power is a function of look angle.

5.6.4) Combining $P(t)$, $G(\theta,\phi)$ and $\beta(\theta_i)$

Figure 5.16 shows how the three components of the power integral combine to produce a power return.

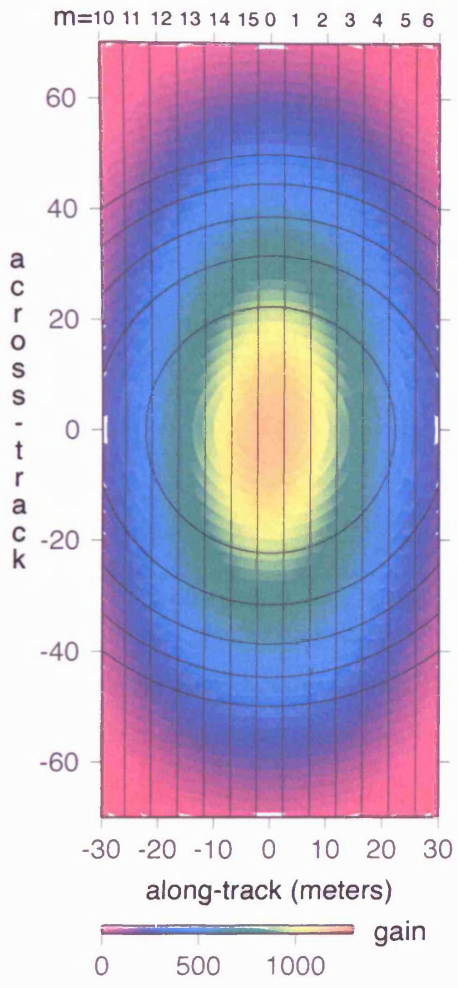

Figure 5.16: Components of the power integral. The graded coloured area shows the variation of the antenna gain. The vertical lines show the width of the along-track footprint, due the along-track processing, $\beta(\theta_l)$. The circles show the range rings.

Figure 5.17 shows the power returned from individual beams and illustrates how the change in look angle affects each power contribution.

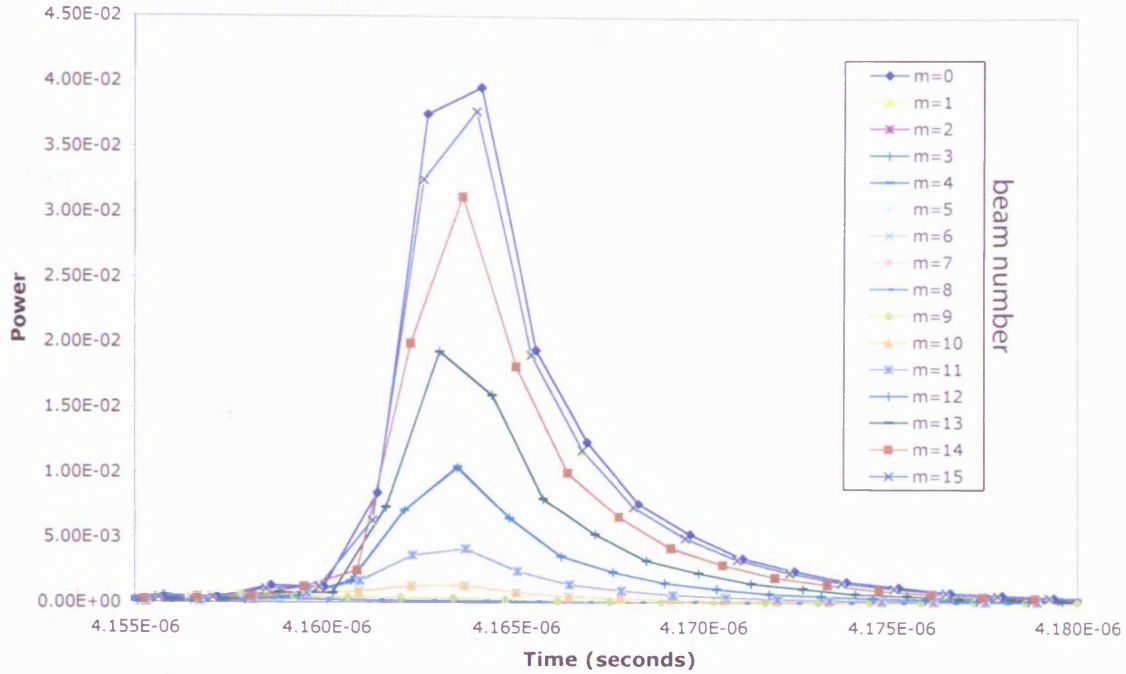

Figure 5.17: Power return from individual beams over a flat surface with no pitch, roll or yaw and no antenna mounting angle (see section 5.6.6). Beam m=0 returns the highest power as it passes through the centre of the gain pattern. Beams equal distance either side of m=0 are equal in power.

In order to produce figure 5.17 the timing of the power return from each beam was adjusted to account for the curvature of the pulse, as illustrated in figure 5.18 and given by equation 5.49.

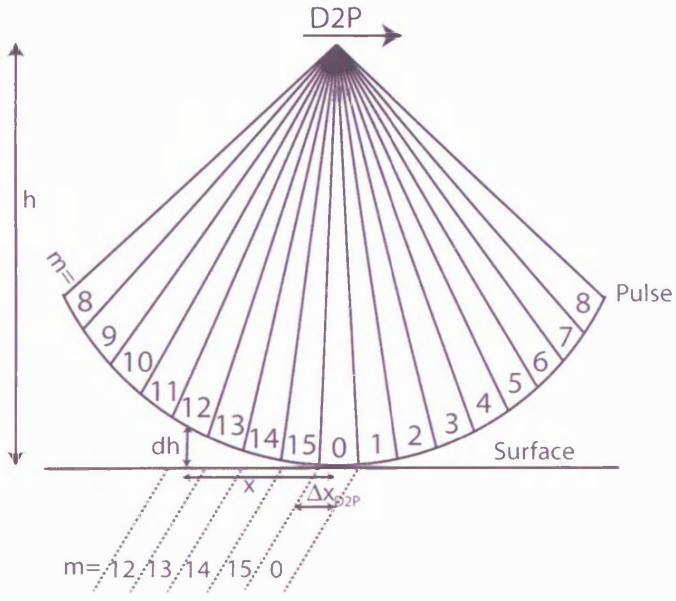

Figure 5.18: Illustration of time correction calculation, Δx_{D2P}, dh and h are in meters.

$$
\begin{aligned}
&if \quad m <= 8 \qquad x = m \times \Delta x_{D2P} \\
&if \quad m > 8 \qquad x = (16 - m)\Delta x_{D2P} \\
&dh = \sqrt{x^2 + h^2} - h \\
&time\_correction = 2 * dh / C
\end{aligned}
\tag{5.49}
$$

5.6.5) Locating the radar nadir

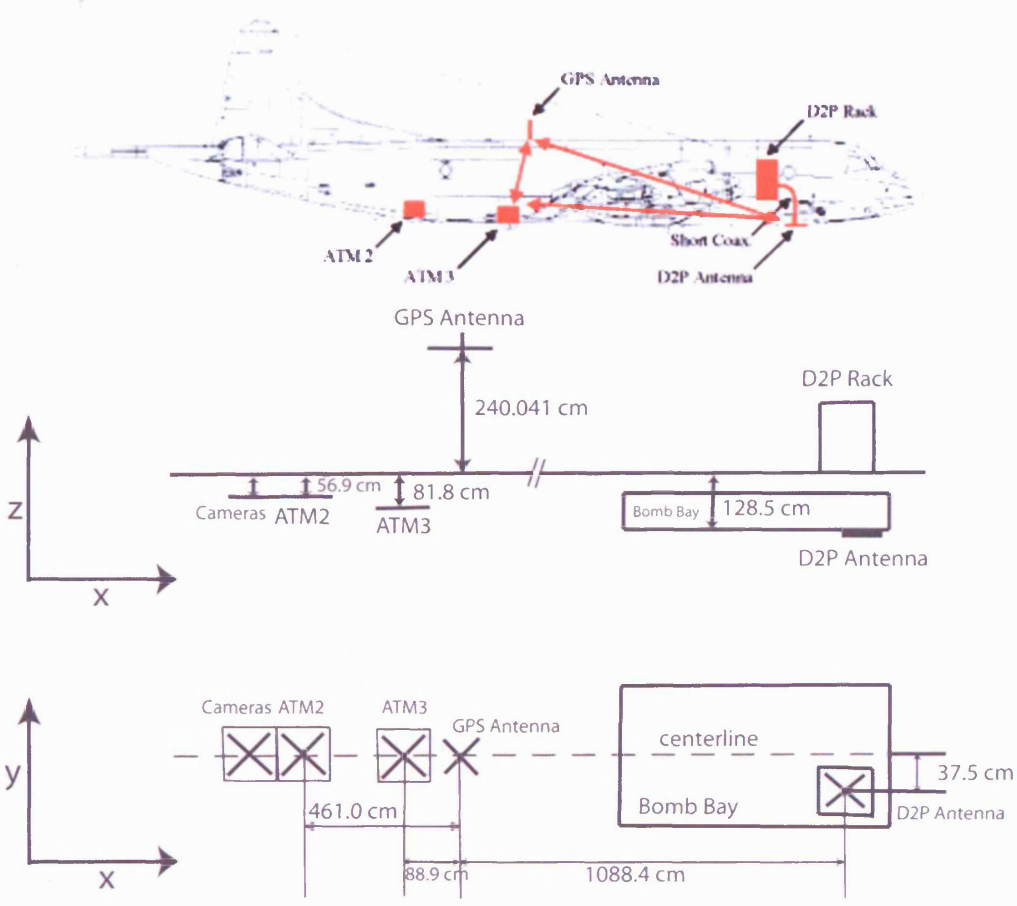

Figure 5.19: Sensor layout in the P-3 aircraft, adapted from Raney and Leuschen (2003).

The processed radar data (APL) locates the return at the GPS antenna rather than at the D2P antenna. In order to compare results from the simulator to the processed data sets, the radar nadir was calculated using the information in figure 5.19.

5.6.6) Locating the antenna boresight

The antenna is mounted as shown in figure 5.20. This means that the antenna boresight is not in line with the D2P nadir.

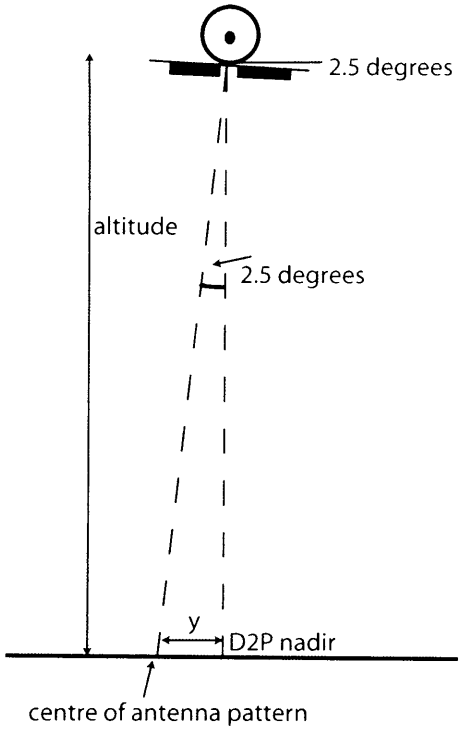

Figure 5.20: Shows the effect of the 2.5° off pointing of the D2P antenna (direction of flight coming out of the page). For a nominal altitude of 500 m the offset (y) of the centre of the antenna pattern from the D2P nadir is 21.8 m.

5.6.7) The pitch, roll and yaw of the aircraft

A change in pitch, roll or yaw will change the position of the antenna boresight or the antenna pattern. Positive roll corresponds to the starboard wing pointing down, and shifts the boresight to the port side of the antenna. Positive pitch corresponds to the aircraft nose up, and shifts the boresight forward of the antenna. Positive yaw corresponds to a rotation to the right. A change in yaw would not shift the boresight, but it would rotate the antenna pattern around the boresight.

Yaw

Yaw, the angle between the line of flight and the direction that the aircraft is pointing in, is not given as a parameter in either the radar or laser data files. However, the heading, defined as the orientation of the INS relative to true north, is given. To calculate the yaw we calculate the bearing between consecutive points, and subtract this value from the heading. Figure 5.21 shows the yaw values for both days of data.

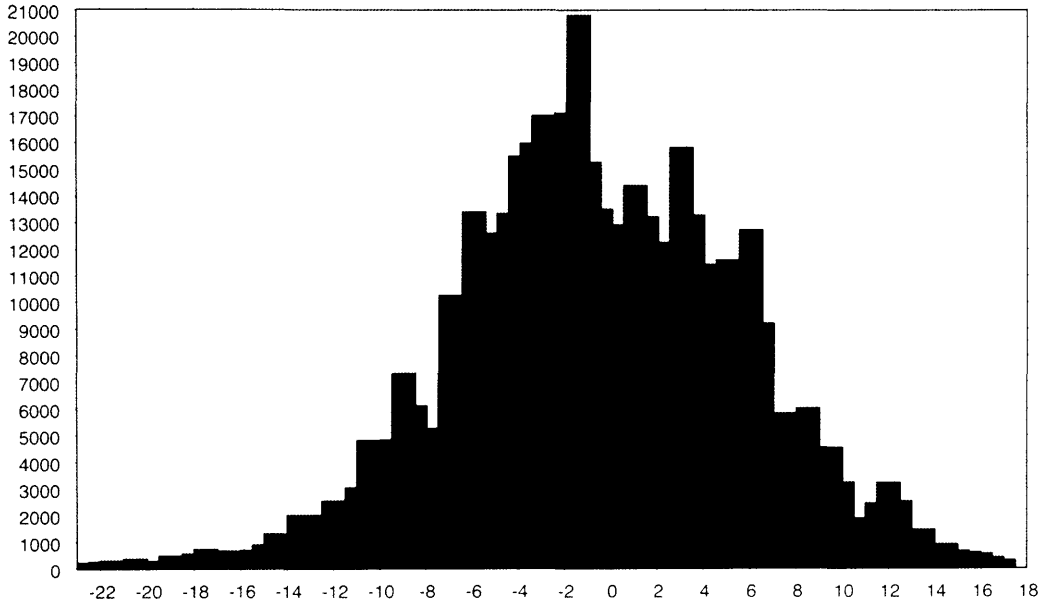

Figure 5.21: Yaw, in degrees, for all LaRA data.

The maximum yaw is -23°, figure 5.22 shows the rotation of the antenna pattern caused by a yaw of -23°. For comparison an antenna pattern with zero yaw is shown.

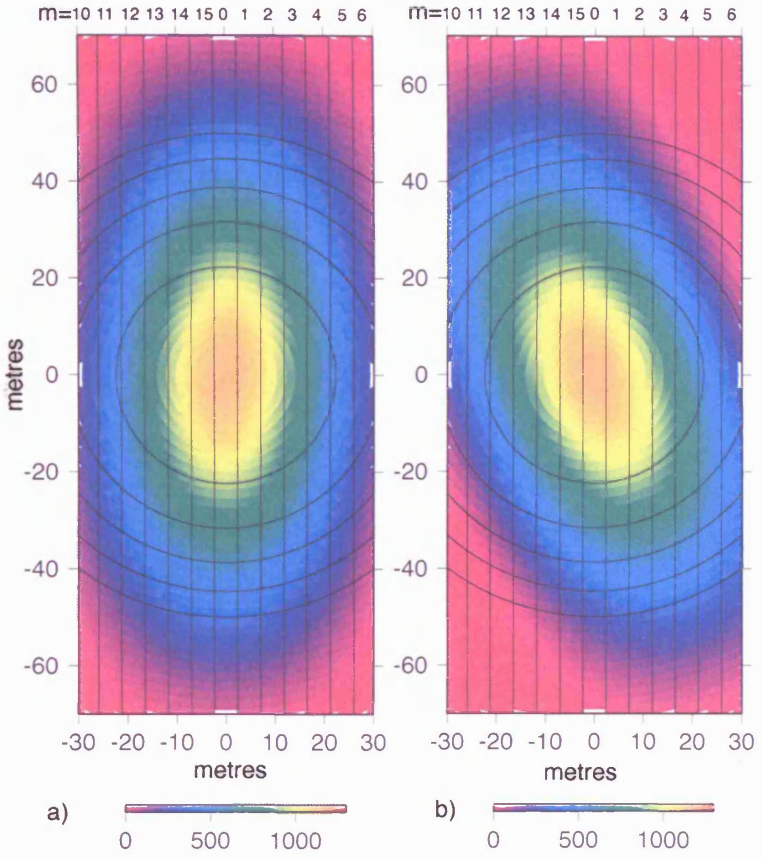

Figure 5.22: a) Location of the antenna pattern for zero yaw, b) locations of the antenna pattern for -23° yaw.

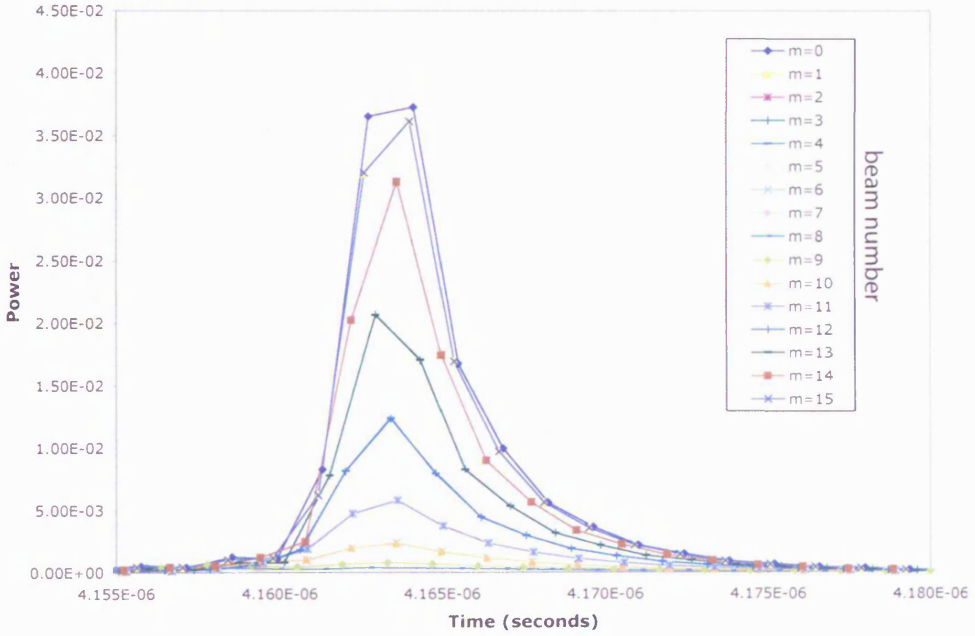

Figure 5.23: Power return from individual beams over a flat surface with a yaw of 23°. When compared to figure 5.17, it can be seen that although the magnitude of the power is slightly different for each beam, the shapes of the returns are the same.

Figure 5.23, when compared to figure 5.17, shows how the shift in the antenna pattern changes the magnitude of the power return but does not affect the shape of each beam significantly. As we are computing the shape of the return rather than the value of the power we do not need to include variations in yaw in the simulator.

Pitch and roll

Figure 5.24 shows the pitch and roll values from a section of track from the 20th. The values are typical over the whole data set.

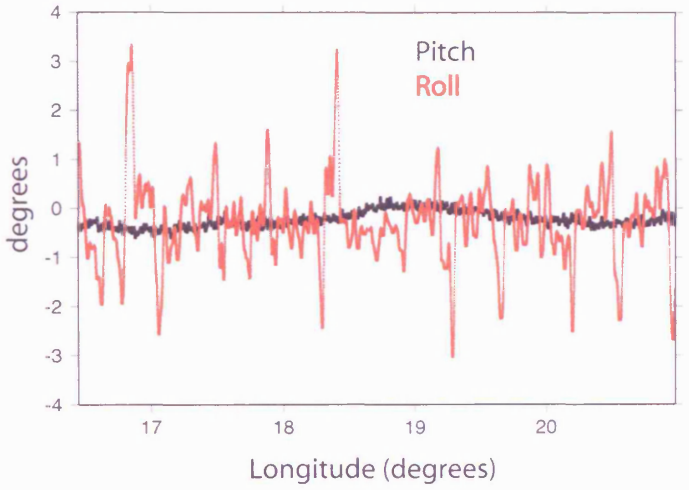

Figure 5.24: Pitch (black) and roll (red) values for a section of track from the 20th.

The maximum pitch is approximately ±0.5°. At a nominal altitude of 500 m a pitch of 0.5° will cause the antenna gain pattern to shift by 4.4 m in the along-track direction, which is greater than the along-track footprint. This alters the shape of the beams (figure 5.25) as m=0 is no longer located in the centre of the antenna gain pattern.

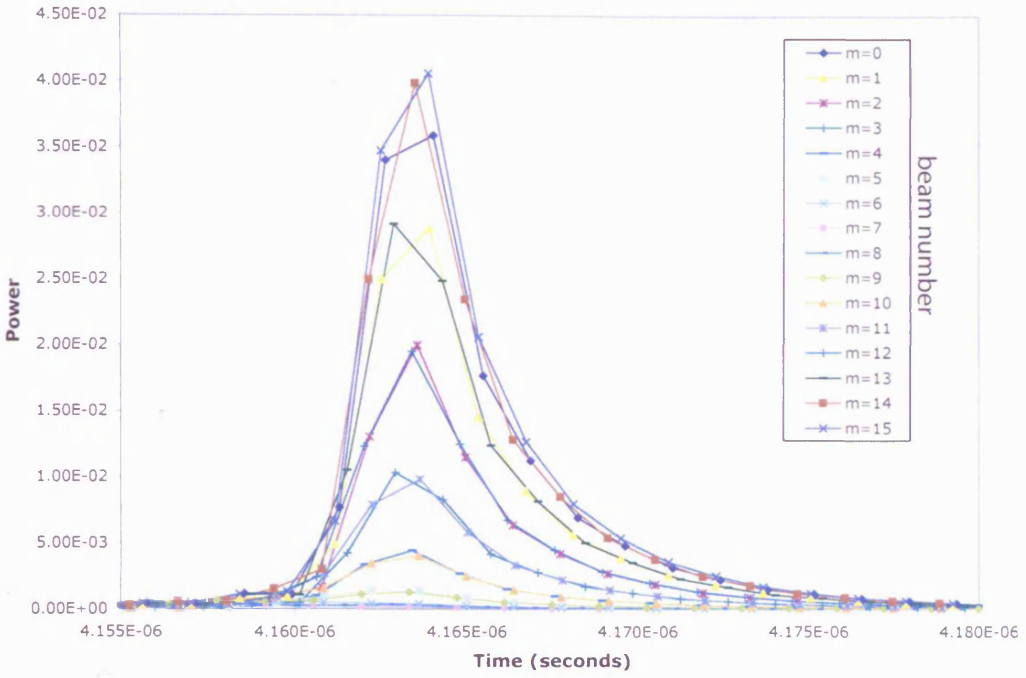

Figure 5.25: Power return from individual beams over a flat surface with a pitch of 0.5°.

The maximum roll is approximately ±3.0°. Combined with the antenna mounting angle (-2.5°), the maximum offset of the antenna gain pattern in the across-track direction, at a nominal attitude of 500m, is 48 m. The effect on the power beams is shown in figure 5.26.

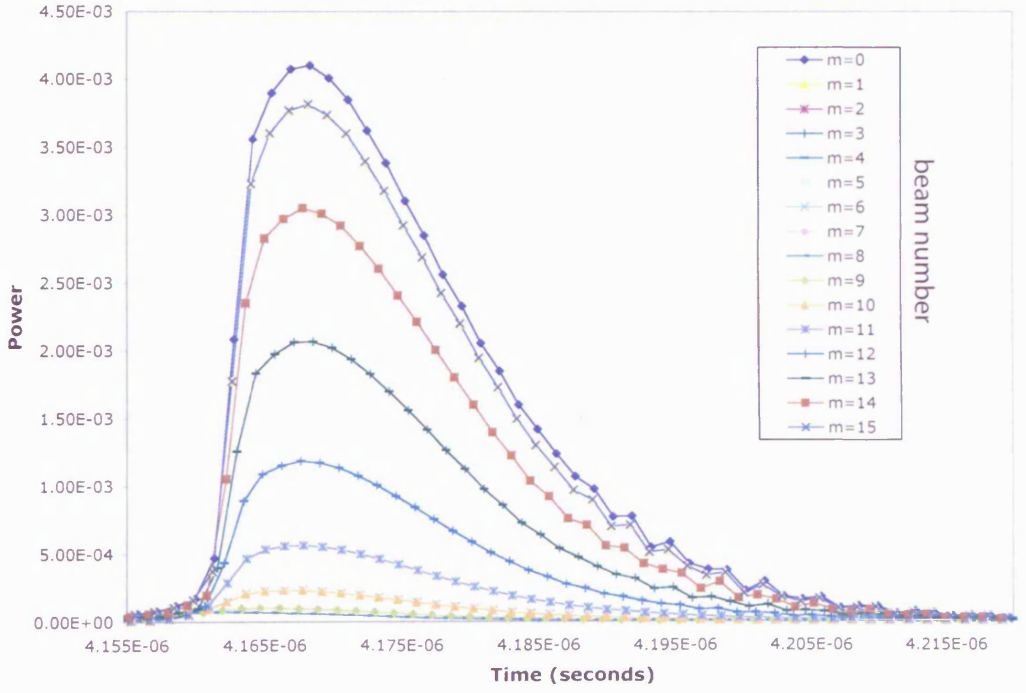

Figure 5.26: Power return from individual beams over a flat surface with a roll of –3.0° and antenna mounting angle of –2.5°. Note the change of x and y scales.

Figure 5.26 shows that the magnitude of the power decreases and a lager amount of power is received later in time, when the aircraft experiences roll. These effects are due to the roll causing the centre of the antenna gain pattern to shift out of the 1st range ring. Therefore, returns received later in time are multiplied by a higher gain than those received earlier in time.

As pitch and roll affect the shape of the power returns they are both included in the simulator.

5.6.8) Approximating the power integral as a sum

The power integral (equation 5.29) can be approximated as a sum provided the surface area elements (facet), over which the sum is performed, are small enough. The simulator creates a surface grid from the laser altimeter data (described in section 5.6.11). The grid is set up on a Cartesian coordinate system, with units of metres. For example, a 5 metre grid consists of elevation estimates every 5 meters in the x and y directions. An area element is defined by dividing a square of 4 points into two triangles, as illustrated in figure 5.27.

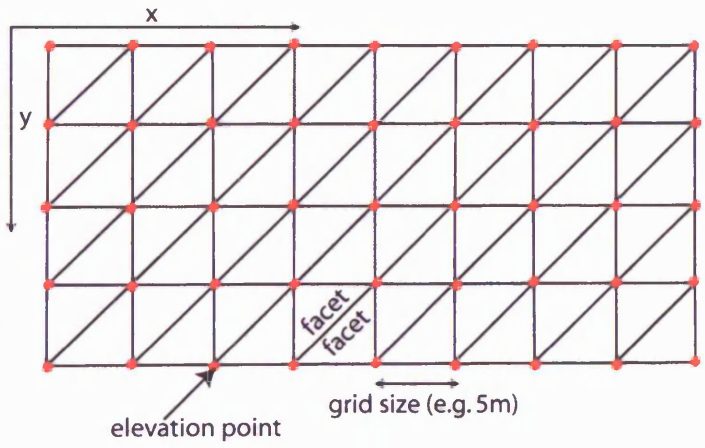

Figure 5.27: Surface grid and area element arrangement.

As the transmitted pulse expands over the surface the pulse annulus (see chapter 3, figure 3.2) decreases in width, if the facets cross over the edge of the annulus then an error is introduced into the power calculation. Figure 5.28 shows the power return (without $G(\theta,\phi)$ and $\beta(\theta_i)$) for different grid sizes. A Gaussian power transmit envelope is used rather than a sinc pulse for simplicity.

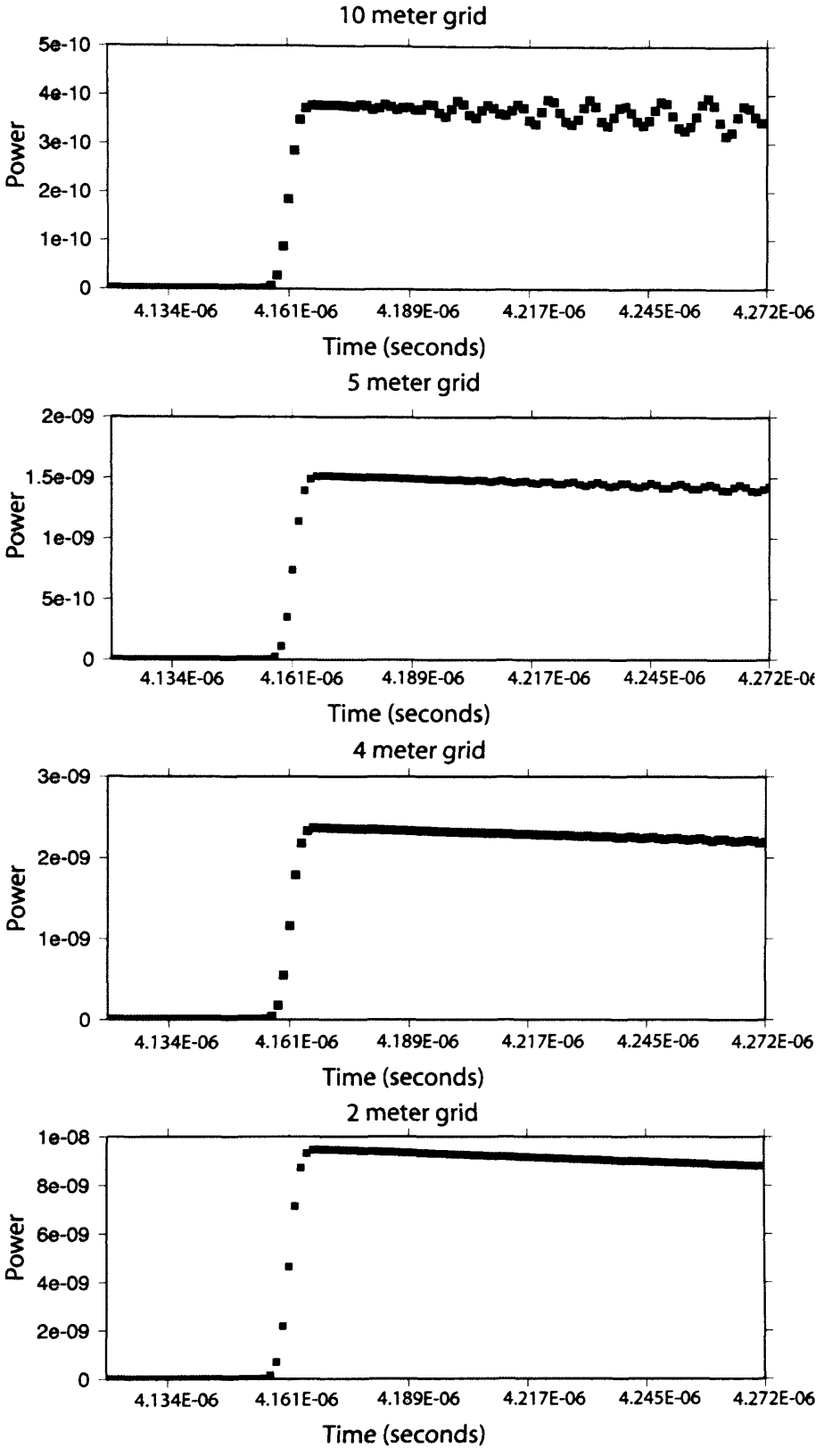

Figure 5.28: The top plot shows the power return from 10 metre grid. The return becomes noisy in the trailing edge. A gradual reduction in the noise level is shown through the 5 metre, 4 metre and 2 metre plots. Measurements are taken with the same altitude, pulse lengths aircraft position and surface as for figures 5.23, 5.25 and 5.26.

A grid size of 4 metres is used in the simulator. Although the 2 metre grid produces a slightly smoother return, using a 2 metre grid rather than a 4 metre grid does not effect our results, and the extra computing time require to run the simulator with a 2 metre grid is too large. Figure 5.26 shows power returns with the maximum roll offset, significant power is not received after 4.215 μsecs, the power return from a 4 meter grid is smooth after this time and therefore can be used in the simulator.

5.6.9) Simulator processing scheme

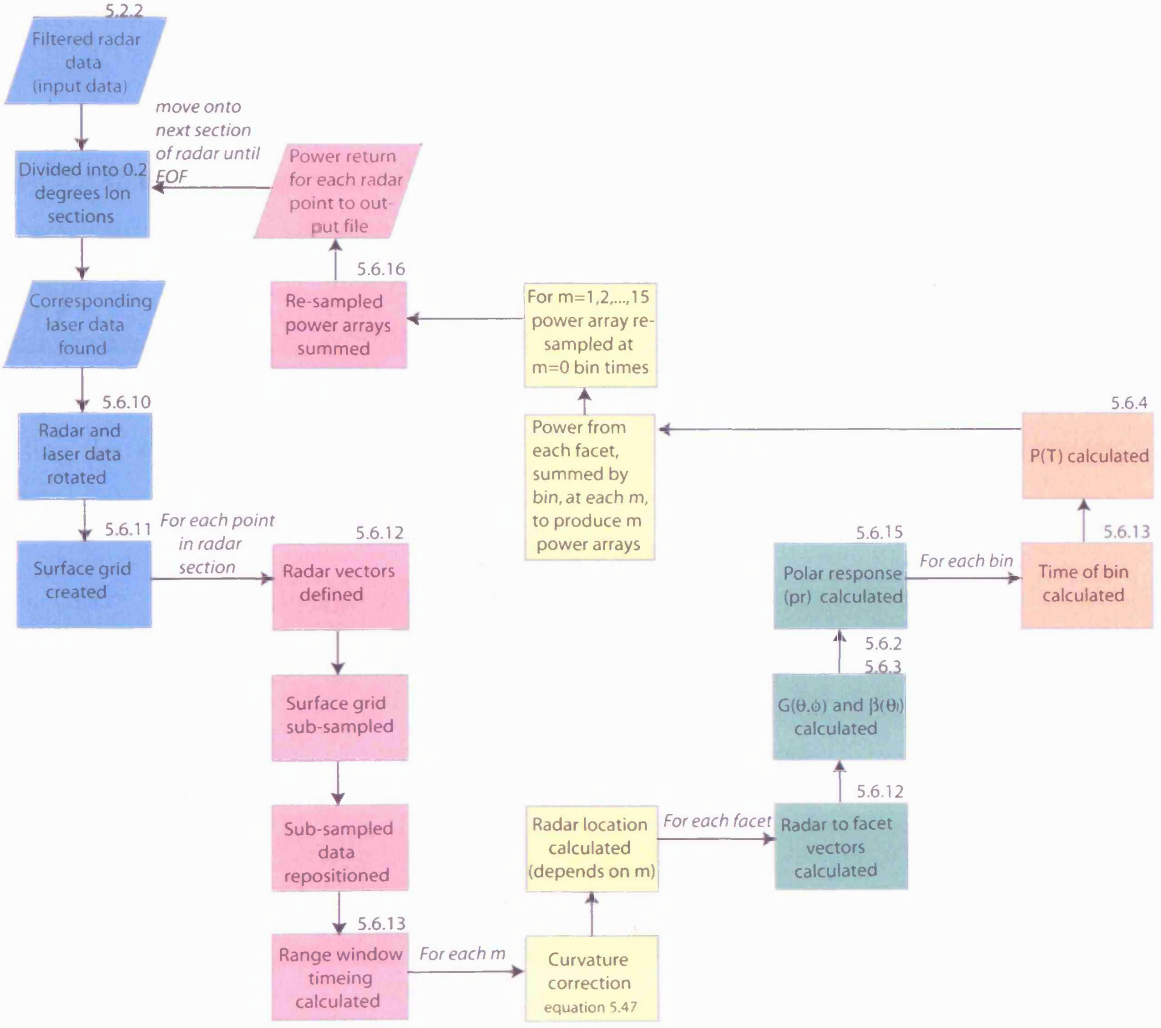

Figure 5.29: The simulator processing scheme. Blue indicates processes performed on the input data, pink indicates processes performed for every radar point, yellow indicates processes performed for every beam, green for every facet and orange for each bin in the range window. The numbers refer to the section where the individual process is described.

Filtered radar data (section 5.2.2) is read into the simulator, divided into sections to speed up processing time, and the corresponding laser data located. Sections 5.6.10 to 5.6.17 describe the major processes in detail.

5.6.10) Rotating the data sets

The laser and radar data sets are transformed and rotated onto a Cartesian grid so that the flight line is at a constant y value. The input data consists of longitude and latitude of the GPS antenna (the correction for the location of the D2P antenna is applied later), and the longitude, latitude and elevation of the ATM3 laser points.

We use an oblique mercator projection and take our method from Snyder (1982). We use the spherical transform, rather than the more precise elliptical transform, to reduce computing time. The use of the spherical transform is justified as we transform a short section of track (0.2° longitude), therefore the maximum offset between a point transformed using the spherical transformation and a point transformed using the elliptical transformation is 0.04 m. Figure 5.30 shows a section of track transformed using the spherical transformation (top plot) and the elliptical transformation (bottom plot).

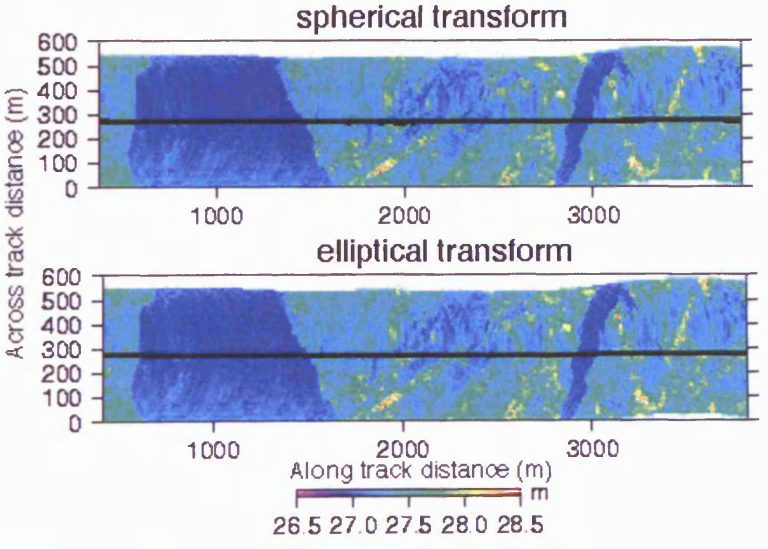

Figure 5.30: Spherical transformation (top), and elliptical transformation (bottom). The black line is the aircraft nadir and the coloured area is the laser surface elevation measurement.

The oblique mercator for a sphere can be pictured by wrapping a cylinder around a sphere so that it touches the surface along the great circle path chosen as the central line. We use our flight line as the great circle path. Equations 5.50 to 5.55 give the transformation:

Take two points that lie upon the central line, with latitudes and longitudes (ϕ_1, λ_1) and (ϕ_2, λ_2) and longitude increasing easterly. The location of the pole of the transformation (ϕ_p, λ_p) is calculated by:

$$\lambda_p = \tan^{-1}[(\cos\phi_1 \sin\phi_2 \cos\lambda_1 - \sin\phi_1 \cos\phi_2 \cos\lambda_2)/ (\sin\phi_1 \cos\phi_2 \sin\lambda_2 - \cos\phi_1 \sin\phi_2 \sin\lambda_1)] \quad (5.50)$$

$$\phi_p = \tan^{-1}[-\cos(\lambda_p - \lambda_1)/\tan\phi_1] \quad (5.51)$$

For any point with latitude and longitude (ϕ,λ), its x and y position is given by:

$$x = R\tan^{-1}\{[\tan\phi\cos\phi_p + \sin\phi_p \sin(\lambda - \lambda_0)]/\cos(\lambda - \lambda_0)\} \quad (5.52)$$

$$y = \frac{R}{2} In[(1 + A)/(1 - A)] \quad (5.53)$$

where R is the polar radius and A and λ_0 are given by:

$$A = \sin\phi_p \sin\phi - \cos\phi_p \cos\phi \sin(\lambda - \lambda_0) \quad (5.54)$$

$$\lambda_0 = \lambda_p + \pi/2 \quad (5.55)$$

[Snyder, 1982]

Figure 5.31 shows a section of data in its original latitude/longitude coordinates and then in its Cartesian coordinates after it has been transformed and rotated. The black line is the location of the GPS antenna nadir and the coloured points are surface elevation estimates from ATM3.

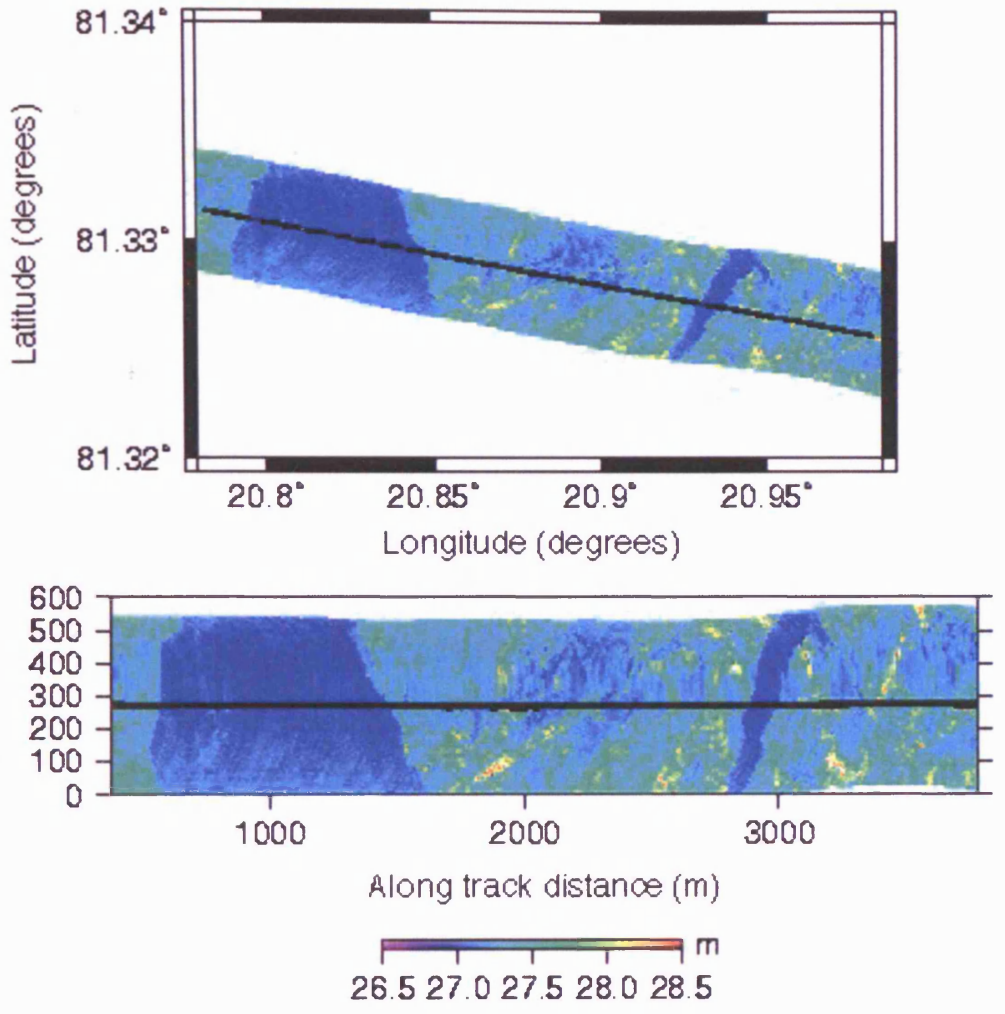

Figure 5.31: ATM3 elevation estimates (coloured surface) and GPS antenna nadir locations (black line). The top plot shows the data in its original coordinate system. The bottom plot shows the data after it has been rotated and transformed into a Cartesian coordinate system.

5.6.11) The surface grid

The surface grid was created from the ATM3 laser data as follows. Section 5.1.2 describes how differences in elevation occur in the fore and aft scans, at co-located points. This problem is resolved when the surface grid is created. Once the data has been transformed and rotated (section 5.6.10), it is separated into fore and aft scans. Two grids are then created, one using the elevation estimates from the fore scan and one using the elevation estimates from the aft scan. The grid is 4000 meters by 600 meters and has points every four metres (section 5.6.8). A Gaussian function is used to smooth

the data to each grid point. The two grids are then averaged only at points where there is data from both fore and aft scans. Figure 5.32 shows the same data as figures 5.30 and 5.31 after it has been separated into fore and aft scans and smoothed. In figures 5.30 and 5.31 evidence of the scan pattern can be seen. In figure 5.32 this effect is no longer apparent.

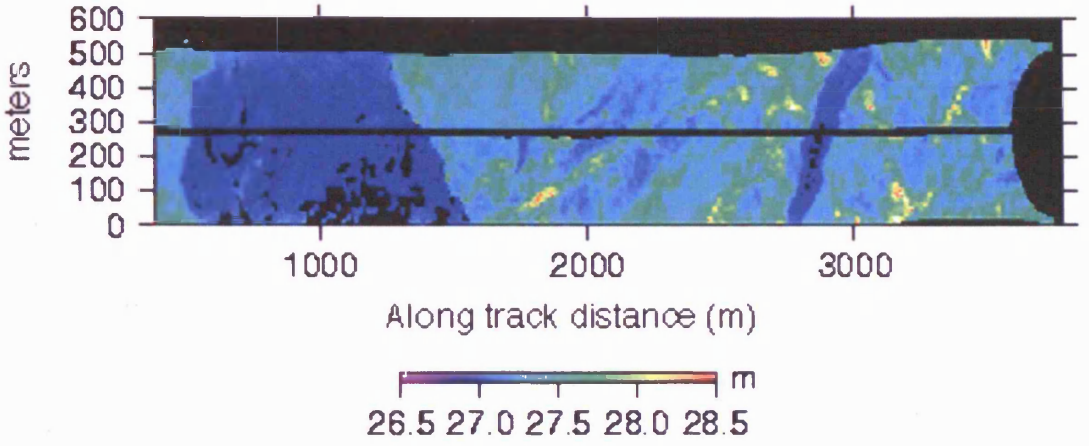

Figure 5.32: ATM3 elevation estimates (coloured surface) and GPS antenna nadir locations (black line) after the data has been transformed and rotated and the ATM data have been smoothed. Black areas within the surface are locations where data from both fore and aft scans is not available.

5.6.12) The coordinate system

In this section we describe the simulator coordinate system and how the radar and surface are located within it. The coordinate system is illustrated in figure 5.33. We already have a surface grid and the location of the GPS nadir in Cartesian coordinates. We also have the altitude of the aircraft for each of the GPS points. The altitude of the aircraft and the surface elevation are both given as elevations above the reference ellipsoid, therefore z=0 in the coordinate system corresponds to the reference ellipsoid.

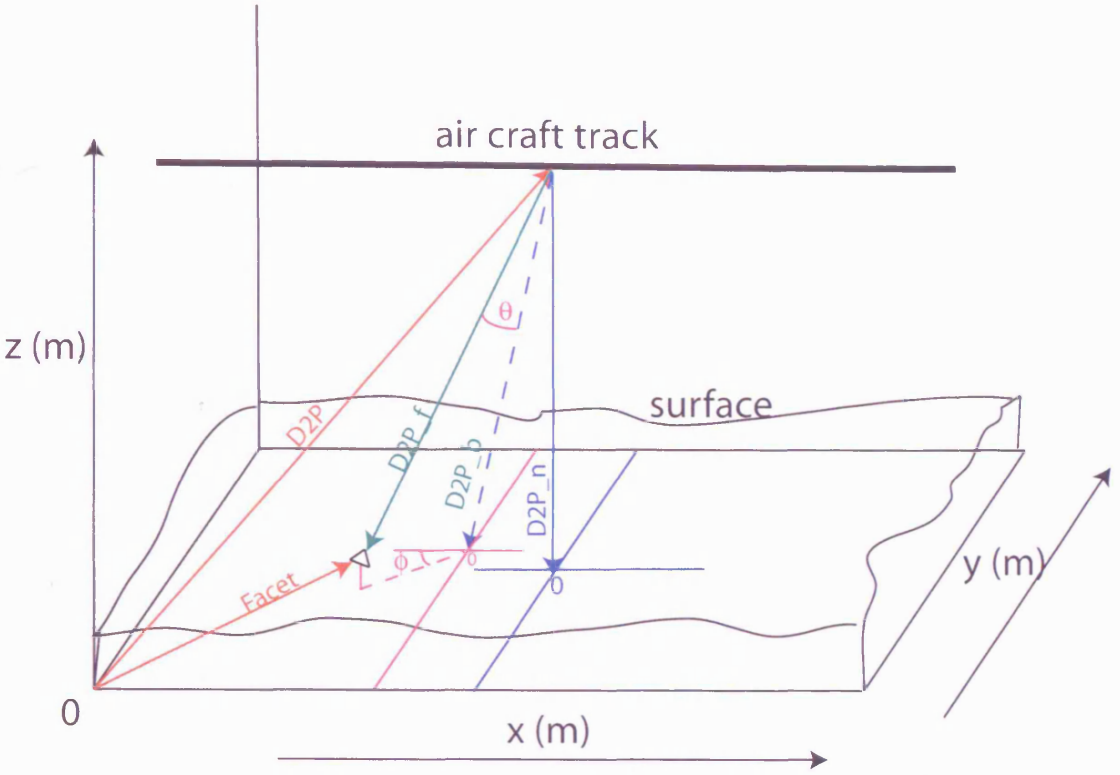

Figure 5.33: Simulator coordinate system.

To locate the D2P antenna we add the offset (figure 5.19) between the GPS and the D2P antennas. This addition is simple as the offset is given in metres and the GPS antenna position has been transformed into metres. The location of the antenna is shown by vector **D2P** and the antenna nadir is shown by vector **D2P_n** (figure 5.33). Next we locate the antenna boresight. The pitch will change the location of the boresight in the x direction and the roll and antenna mounting angle will change the location of the boresight in the y direction. Vector **D2P_b** shows the location of the antenna boresight. Each facet is created from three points (located by **r1**, **r2**, and **r3**) on the surface grid (figure 5.27). Using vector calculus we calculate the location of the centre of the facet from **r1**, **r2** and **r3**. The centre of the facet is shown by vector **Facet** (figure 5.33). Next we calculate the vector between the D2P antenna and the facet (vector **D2P_f**). As the **D2P** and **Facet** are both located from the origin of the coordinate system we can use vector calculus again to calculate **D2P_f**. The antenna gain is a function of θ and ϕ. θ is the angle between **D2P_b** and **D2P_f** and can be calculated from vector calculus. The method used to calculate ϕ is shown in figure 5.34:

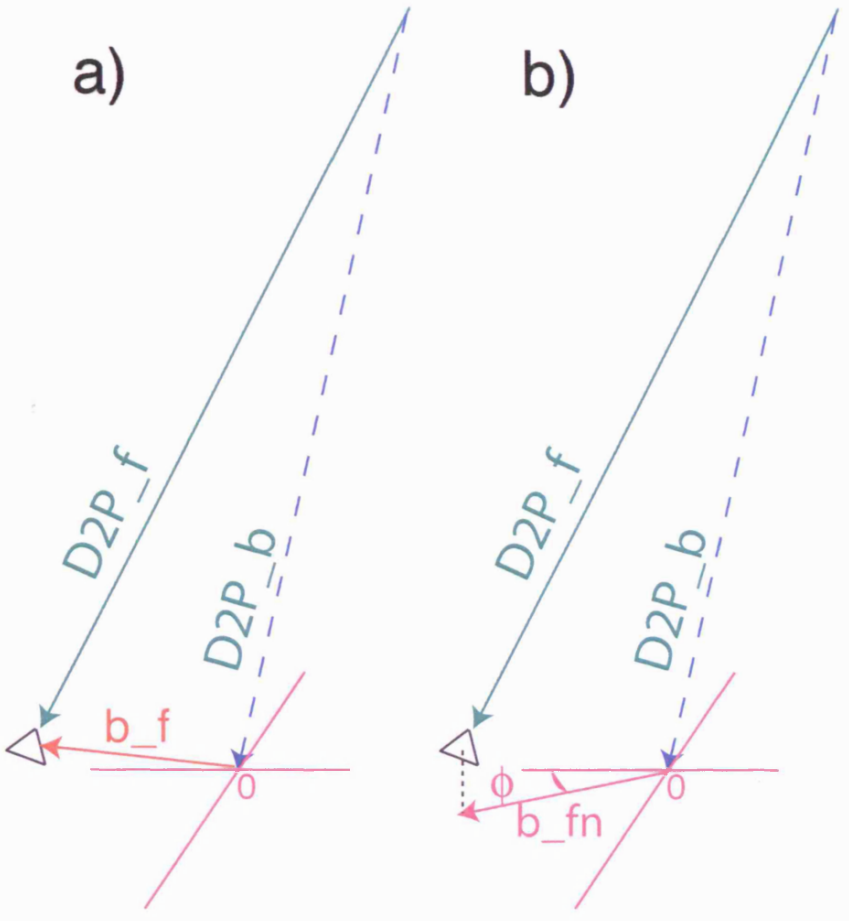

Figure 5.34: ϕ calculation.

a) calculate the vector (**b_f**) between the boresight (**D2P_b**) and the facet (**D2P_f**) using by subtracting **D2P_b** from **D2P_f**.

b) Project **b_f** onto the xy coordinate system (e.g. **b_f.z** = 0.0) to make the vector **b_fn** and find its angle (ϕ) with the x axis.

β is a function of θ_l. θ_l only changes in the along-track direction (x axis). Therefore, to calculate it, we take the **D2P_n** and set the y coordinate to zero and take the **D2P_f** and set the y coordinate to zero then calculate the angle between the modified vectors. The final angle we calculate is the angle for the polar response (θ_{pr}). As we have used triangular facets we can compute the vector normal to the facet and then find the angle between it and **D2P_f**.

5.6.13) Timing the range window

The simulator is designed to create a range window and sample the power with the same timing as the D2P. In the APL processed radar data sets, each pulse has a reference number (*ref*), which gives the elevation of the centre of the waveform above the reference ellipsoid. Using this number and the sampling interval (*Si*) we calculate the timing of the range window.

First we calculate the distance (in metres) to the arrival of the centre of the range window at the D2P:

$$dc = 2(\mathbf{D2P.z} - (ref \times Si)) \qquad (5.56)$$

where *Si*=0.208189 metres and **D2P.z** is the altitude of the D2P antenna.

We next calculate the distance to the start of the range window:

$$ds = dc - (len \times Si) \qquad (5.57)$$

where *len* is the number of bins in the range window.

We then convert to time by dividing by the speed of light (c). The first power value is recorded at time *ds/c*.

5.6.14) Sampling the power echo

In chapter 3, section 3.3.2 we described how the D2P samples the return waveform and the subsequent processing. The received signal is sampled every 6 nseconds, after pulse compression the sampling interval is equal to 1/ΔF (section 3.1.6). Before the range FFT is performed the waveform is zero padded by a factor of two. This means that the sampling interval after the FFT is 1/2ΔF. Therefore we also sample the power return at 1/2ΔF.

5.6.15) The polar response

The variable pitch and roll can cause the centre of the antenna gain pattern to shift away from the D2P nadir and out of the early range rings. This means that, in the simulator, we receive larger amounts of power at later times in the range window. This situation is unrealistic over a smooth ice surface. In reality, as we moved away from the antenna nadir, and the pulse intersected the facets at angles decreasing from 90°, we would expect to see less energy returned despite the shifted gain pattern. Over a rough ice surface the situation could change depending on the orientation of the facets. If the facets were orientated in such a way as to direct energy back toward the antenna then we would expect larger power returns later in time and visa versa. Figures 5.35 to 5.38 show an example of a power return over a rough section of ice, with a pitch of –0.208° and roll –1.18° (N.B. there is also an antenna mounting angle of –2.5° that is added to the roll angle and offsets the centre of the gain pattern in the y direction). Figure 5.35 shows the surface and the D2P nadir (black square). The elevation of the surface varies by three meters.

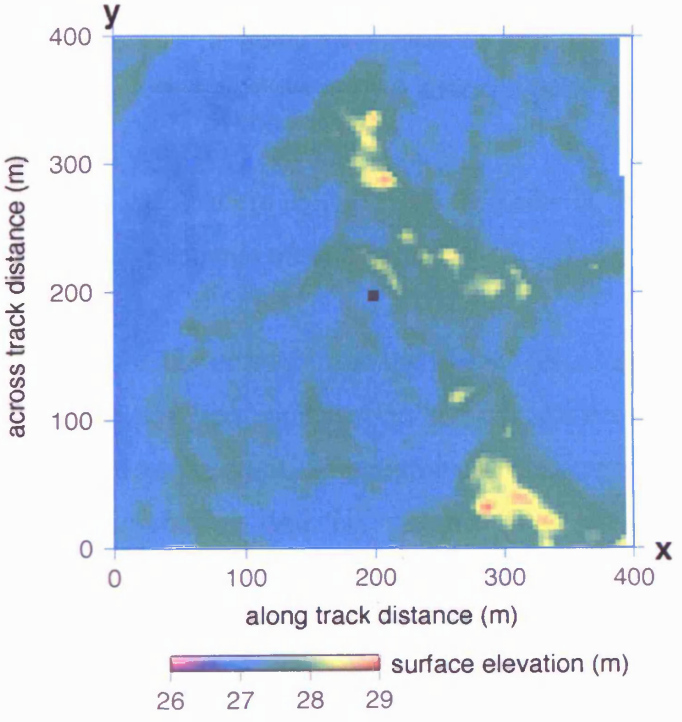

Figure 5.35: Section of the data centred on 81.34° latitude and 20.94° longitude. The black square in the centre of the figure, is the D2P nadir, and elevations are with respect to the reference ellipsoid.

Figure 5.36 shows the off set of the gain pattern due to –0.208° in pitch (-5.69 m in the x direction from the nadir location) and the offset due to the roll (-1.18°) and the antenna mounting angle (-2.5°) in the y direction (62.74 m from the nadir location).

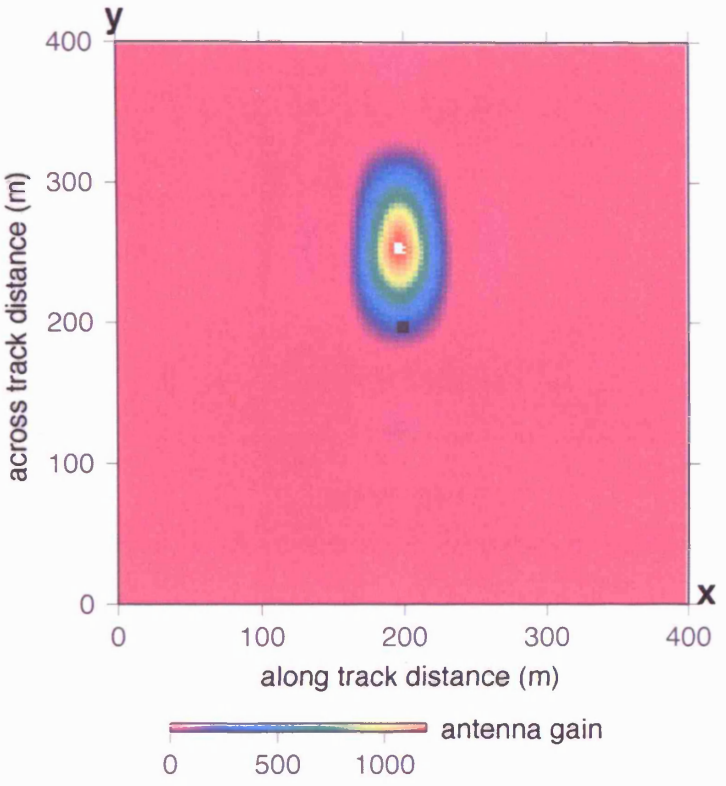

Figure 5.36: The antenna gain pattern shifted from the nadir of the D2P (black square) because of the pitch, roll and antenna mounting angles.

Figure 5.37 shows the real echo returned from the surface (blue) and the simulated echo (red). No polar response has been included in the calculation. The simulated echo initially has the same form as the real echo but peaks much later in time (increasing bin number corresponds to increasing time i.e. distance from the D2P nadir). This is because as we move further away from the nadir the gain increases making the power received later in time greater than the power received earlier in time. This effect is mitigated in the real echo as the polar response decreases (in general) as we move away from the nadir.

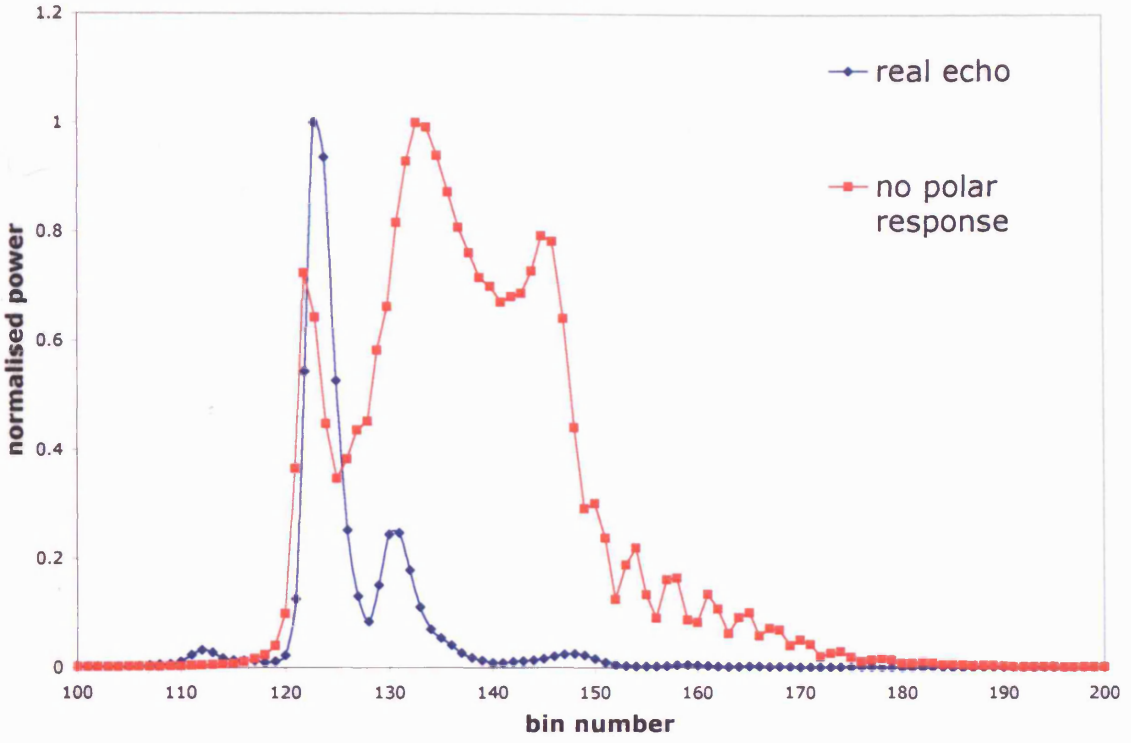

Figure 5.37: Real D2P echo (blue) and simulated echo with no polar response (red).

It is clear that we need to model the polar response in the simulator to approximate the shape of the real echoes. To achieve this we calculate the angle between the normal to the facet and the D2P antenna (θ_{pr}) and set a polar response angle (ϕ_{pr}), which governs the rate of decrease of the polar response (*Pr*), i.e. as we move further away from the D2P nadir, θ_{pr} increases and *Pr* decreases. *Pr* is given by equation 5.58:

$$\mathrm{Pr} = e^{-\left(\frac{\theta_{pr}}{\phi_{pr}}\right)^2} \qquad (5.58)$$

Figure 5.38 shows the real echo and three simulated echoes, each with a different polar response angle.

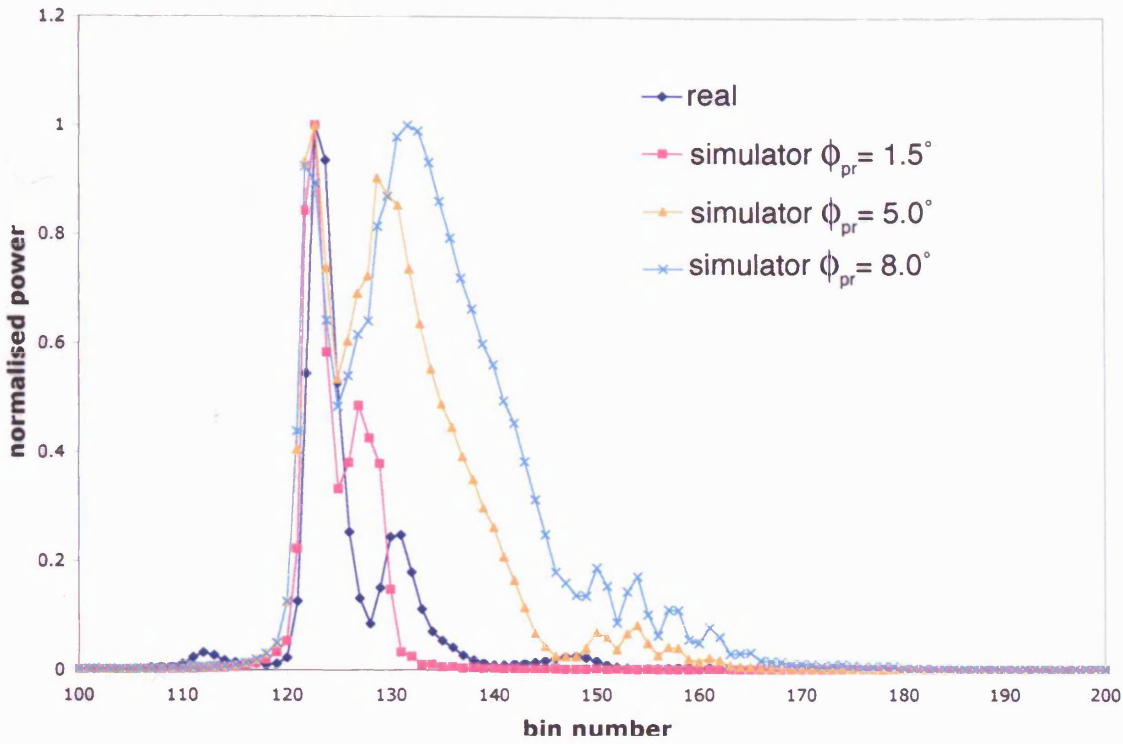

Figure 5.38: Real echo (dark blue) and simulated echoes with varied polar response angles. ϕ_{pr}=1.5° for the pink echo, 5° for the orange echo and 8° for the light blue echo.

The echoes with ϕ_{pr}=1.5° and 5° approximate the shape of the real echo better than ϕ_{pr}=8°, both peaks are in line, and both have smaller second peaks. The position of the second peak for ϕ_{pr}=5° is in line with the real echoes second peak where the second peak for ϕ_{pr}=1.5° occurs too early. ϕ_{pr}=8° bears a close resemblance to the simulated echo with no polar response, with its second peak larger than its first. We do not know the exact polar response of each surface reflector so recreating the real echo perfectly is not possible in this context. We have chosen a polar response angle of 5° for our simulator as this angle will allow the simulator to create both typical and non-typical echoes.

5.6.16) Re-sampling the echoes

As described in figure 5.17, the simulator produces m power arrays. These power arrays are summed to produce the total power array for the radar point. However, due to the curvature correction, each of the m power array bins occurs at a slightly different time.

We have to re-sample the power arrays at the same time, so we can sum the power contribution at each bin to produce the total power array.

We take our method from Porat (1997). To re-sample the power array we use Shannon's Reconstruction Theorem, which states that for a function $x(t)$ can be represented by its periodic samples $x(nT_s)$, where n is the sample number and T_s is the sampling interval:

$$x(t) = \sum_{-\infty}^{+\infty} x(nT_s)\mathrm{sinc}\left(\frac{t - nT_s}{T_s}\right) \tag{5.59}$$

If we consider a point in time that coincides with a sample point, say $t=n_0T_s$ then:

$$\mathrm{sinc}\left(\frac{n_0T_s - nT_s}{T_s}\right) = \delta[n - n_0] \tag{5.60}$$

and

$$\sum_{-\infty}^{+\infty} x(nT_s)\mathrm{sinc}\left(\frac{t - nT_s}{T_s}\right) = x(nT_s) \tag{5.61}$$

If we now chose a point t located between n_0T_s and $(n_0+1)T_s$ then none of the values in the sinc function will be zero, but the points closer to n_0T_s will contribute more to the sum than the points father from n_0T_s, since sinc is a decaying function.

However, in equations 5.59 to 5.61 the sinc function must be computed between minus infinity and infinity and therefore cannot be used in its current form. To overcome this problem we use a windowed sinc function, i.e. we multiply the sinc function with a function that is zero outside some extent. There are many functions that exist to this purpose (see Poularikas (1999), for examples), after trying different windows we found that the results were the same, and chose to use a $\cos^3$ window as it was simple to compute. Figure 5.39 shows an example of a return from m=4, re-sampled at the times from m=0.

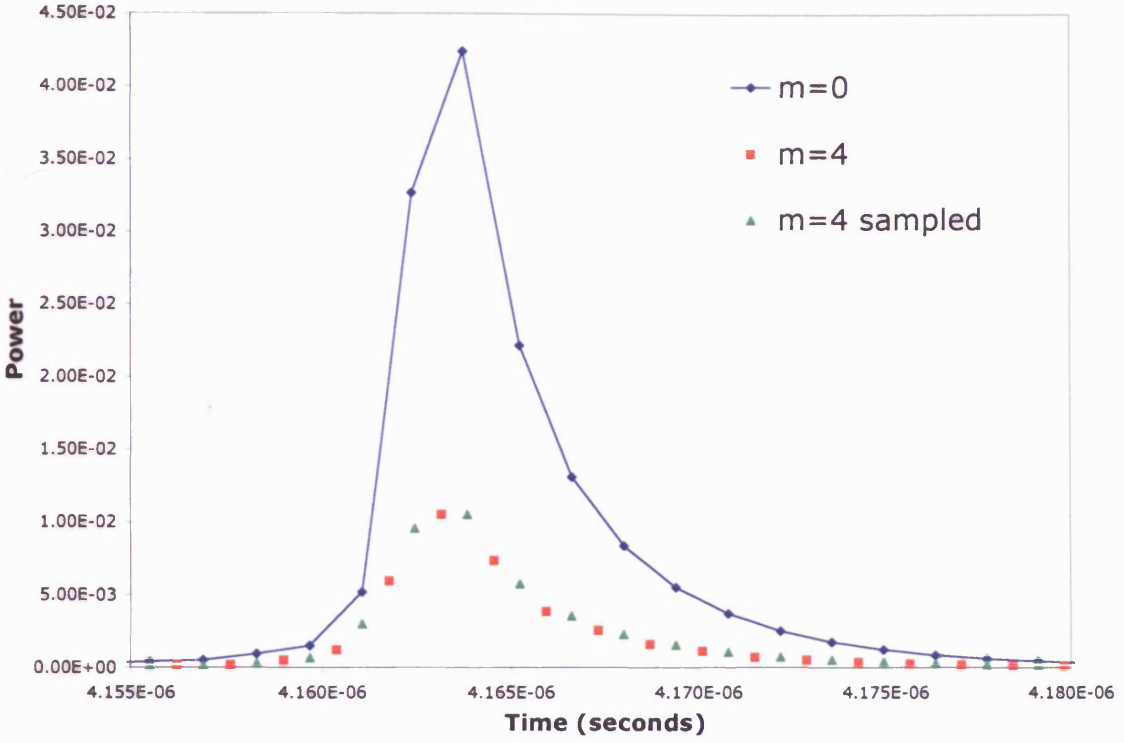

Figure 5.39: Example of a re-sampled power return. Plot shows the power return at m=0 (blue), lines between points are draw for ease of viewing. The red points show the original power return from m=4 and the green points show the re-sampled m=4 at the m=0 times.

5.6.17) The final simulated power echo

Once the power contributions from all 16 beams have been summed the total power echo is printed to an output file. Figure 5.40 shows an example of a power echo over a flat surface with no pitch and roll or antenna mounting angle. The re-track point is also shown (red line), and lies between the half power point and the peak.

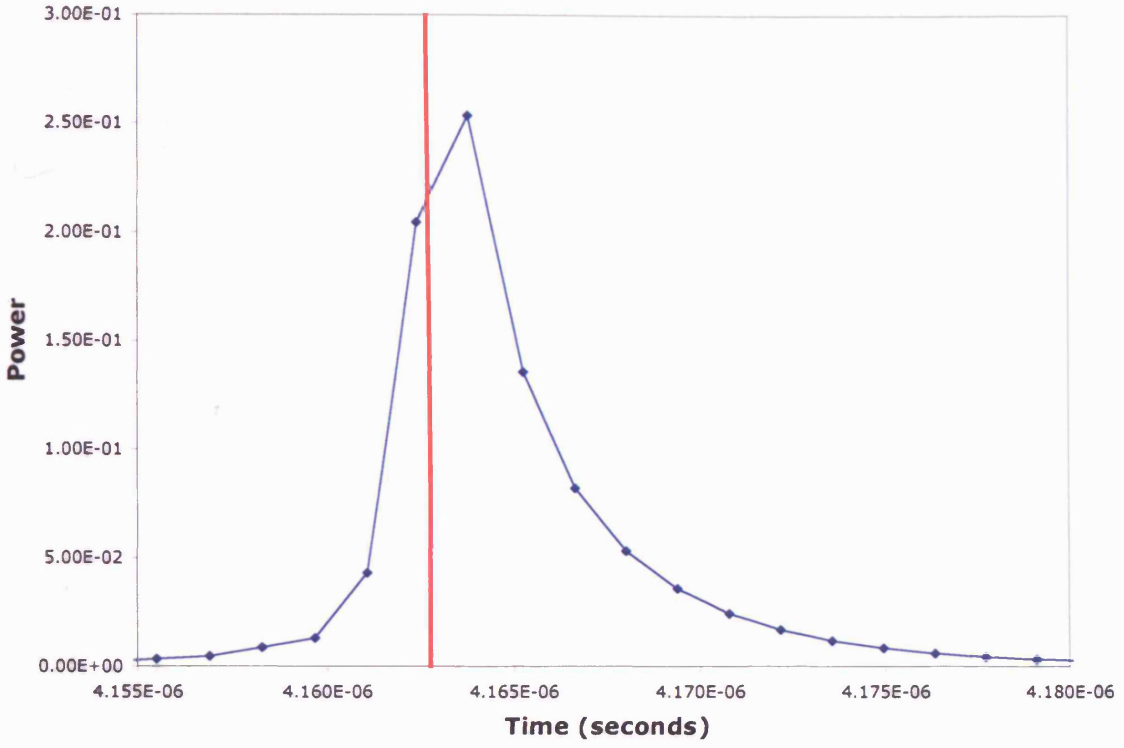

Figure 5.40: Total power return over a flat surface, with no pitch and roll and no antenna mounting angle. The red line shows the re-track point.

5.6.18) Comparing the real and simulated echoes

In sections 5.5 and 5.6 we explained that our method to compare the simulated echoes would involve comparing the echo shape across the whole range window, and calculating the offset between the simulated and real power returns. An offset in the position of the real and simulated echoes, corresponds to an offset in time, which corresponds to an offset in range (i.e. an offset means that the power returns are coming from different surfaces). Figure 5.41 shows the echo comparison processing scheme.

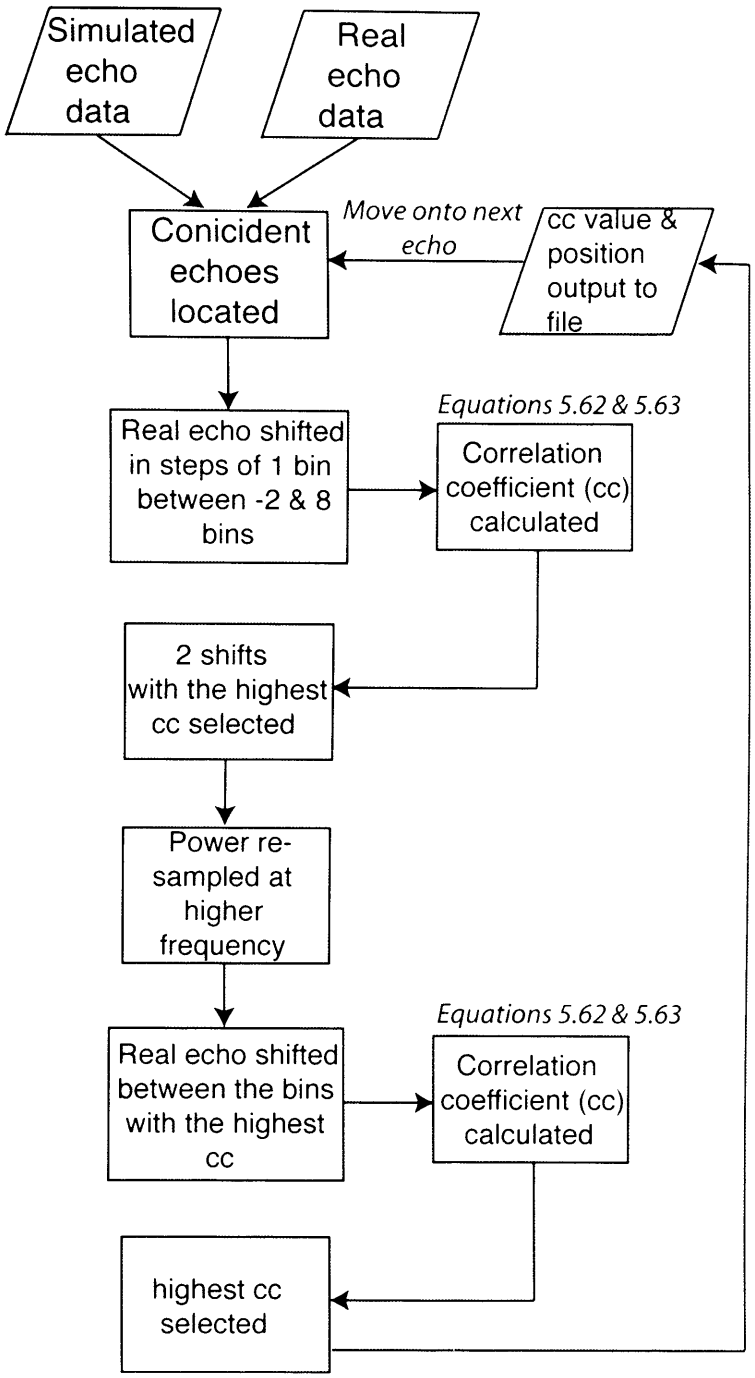

Figure 5.41: The echo comparison processing scheme.

The echoes are compared by calculating their correlation coefficient (cc), which is given by equations 5.62 and 5.63. [Bevington & Robinson, 1992]

$$cc = \frac{\mathrm{cov}(x,y)}{\sigma_x \sigma_y} \tag{5.62}$$

where x is the real echo array, y is the simulated echo array, *cov(x,y)* is the covariance of x and y, and σ_x and σ_y are the standard deviations of x and y. *cov(x,y)* is given by:

$$\text{cov} = \frac{1}{n}\sum_{i=1}^{i=n}(x_i - \bar{x})(y_i - \bar{y}) \tag{5.63}$$

where $\bar{x}$ and $\bar{y}$ are the mean values of x and y.

For each pair of echoes, the power values from the real echo are shifted bin by bin, between –2 bins and 8 bins. At each shift the correlation coefficient between the real and simulated echoes is calculated. When all the integer bin shifts have been completed, the highest and second highest correlation coefficients (bin2) are found. The bin shift pertaining to the second highest correlation coefficient provides the starting point for the factional bin shifts. The power values in each array are re-sampled at a frequency 40 times higher than the original sampling frequency (i.e. samples are taken every 0.005 m in range). The real array is repositioned at the bin2 shift. It is then shifted along each of the newly sampled points, and the correlation coefficient calculated at each shift. The highest correlation coefficient marks the point where the two echoes match the best. The value of the highest correlation coefficient and at which shift it occurs are printed to the output file and the process is repeated for the next echo.

5.6.19) Calibrating the simulator

In section 5.6.18 we described how the simulated echoes are compared to the real echoes. For this method to provide an accurate estimate of the difference in elevation between the laser surface and the surface measured by the radar over sea ice, the position of the echoes in the range window must match when the radar and the laser are measuring the same surface. As we described in chapter 3, section 3.3.10, only one calibration flight simultaneously collected ATM3 and D2P data over the Wallops runway, therefore we use these data sets to determine the bias between the real and simulated data. The calibration data was processed as any data over sea ice would be processed with the exception that we repeated the simulation ten times, varying the value of the polar response angle (ϕ_{pr}) between 0.5° and 5°. The variation of ϕ_{pr} was performed to investigate firstly, what polar response best fitted the calibration data and secondly, what affect an incorrect value of ϕ_{pr} had on the correlation coefficient, and the offset between echoes. Figure 5.42 shows an example of a real echo (black) from the calibration data set and simulated echoes calculated from different values of ϕ_{pr}.

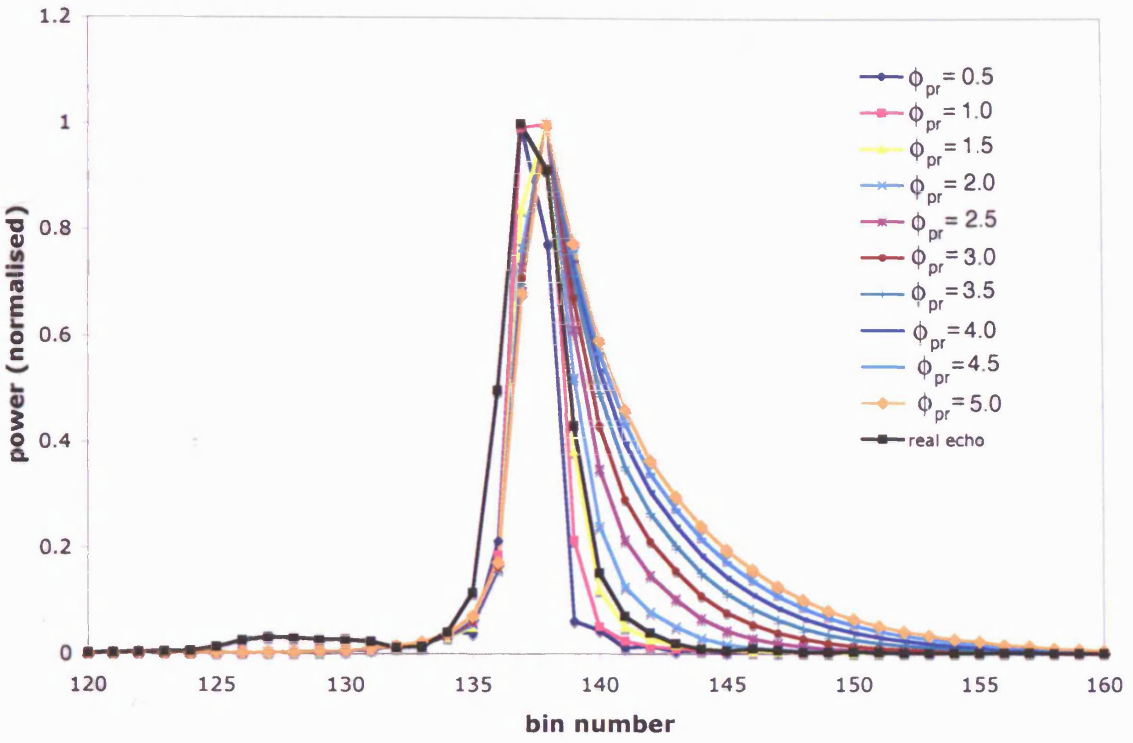

Figure 5.42: Calibration data. Real echo (black) simulated echoes (colours) for varying polar responses.

Figure 5.43 shows the average correlation coefficient (equation 5.62) between the real and simulated echoes for varying ϕ_{pr}.

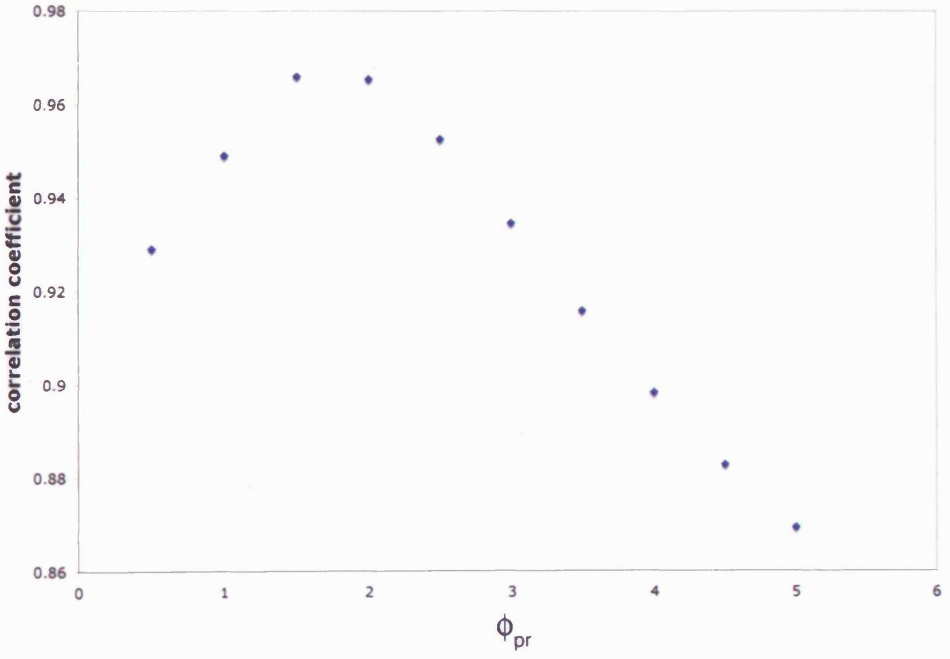

Figure 5.43: Average correlation coefficient between the real and simulated calibration echoes, for varying ϕ_{pr}.

Figure 5.44 shows the average offset in meters between the real and the simulated calibration echoes, for varying ϕ_{pr}.

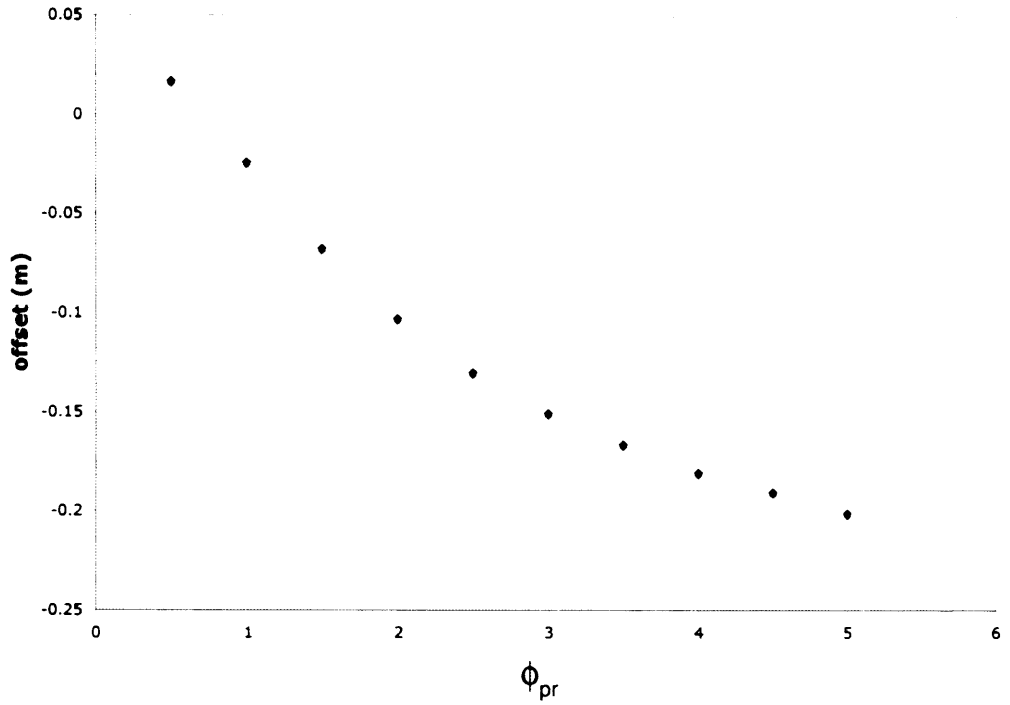

Figure 5.44: Average offset between the real and simulated calibration echoes, for varying ϕ_{pr}.

ϕ_{pr}=1.75° provides the highest correlation coefficient and was found by fitting a 6th order polynomial to the data in figure 5.43, and finding the maximum of the curve. We use ϕ_{pr}=1.75° to calculate the bias between the real and the simulated echoes. For ϕ_{pr}=1.75°, the offset is -0.087 m, therefore 0.087 m is added to offset between the real and simulated echoes over sea ice. As ϕ_{pr}=5.0 (section 5.6.15) will not provide the most realistic value of ϕ_{pr} for all of the sea ice data, we will only include echoes where the correlation coefficient is above 0.95 in our analysis. To estimate the maximum error on the elevation difference calculated from echoes with a 0.95 or above correlation coefficient we calculate the values of ϕ_{pr} for which the correlation coefficient equals 0.95, and use these values of ϕ_{pr} to estimate the offset error from figure 5.44. The correlation coefficient is equal to 0.95 at ϕ_{pr} = 1.01° and 2.58° . The offset for ϕ_{pr} = 1.01°is -0.025 and for ϕ_{pr} = 2.58° is -0.133 meters. Therefore the error on the difference estimate for a single echo is ± 0.06 m.

5.6.20) The effect of speckle

The D2P power echo is the result of the summation of many returns from single scatterers. As scatterers are located at different positions on the surface and the D2P receiver is moving, the phase of the return from each scatterer will be different causing the received signal to change with time. This fluctuation in the received signal is known as fading or speckle [Franceschetti & Lanari, 1999]. Speckle reduces with increased averaging. In section 5.6.3 we described how each point on the ground is seen by 16 coherent echoes, comprising a burst, and that the velocity of the aircraft means that each point can be seen by 25 consecutive bursts. Therefore the mean D2P power echo, for each point, is formed from 400 looks. Following Laxon and Rapley (1987), the power from a single bin of a 400 pulse sum return waveform, $v_{400}(i)$, will be Gaussian distributed with a variance given by:

$$\sigma^2(v_{400}(i)) = \frac{V(i)^2}{400} \qquad (5.64)$$

where $V(i)$ is the mean power of the bin.

To simulate speckle on the simulated waveforms we calculate a random error with a Gaussian distribution in accordance with equation 5.64, and add this error to each power estimate. Figures 5.45 and 5.46 show Z-scope plots of (a) the real D2P data, (b) the simulated data without speckle and (c) the simulated data with speckle. Figure 5.45 shows a long section of track with varying surface types and figure 5.46 shows a short section of track over smooth ice with typical returns. We show two sections of track to examine whether adding speckle over a smooth surface with typical echoes has a greater effect than adding speckle over a variable surface.

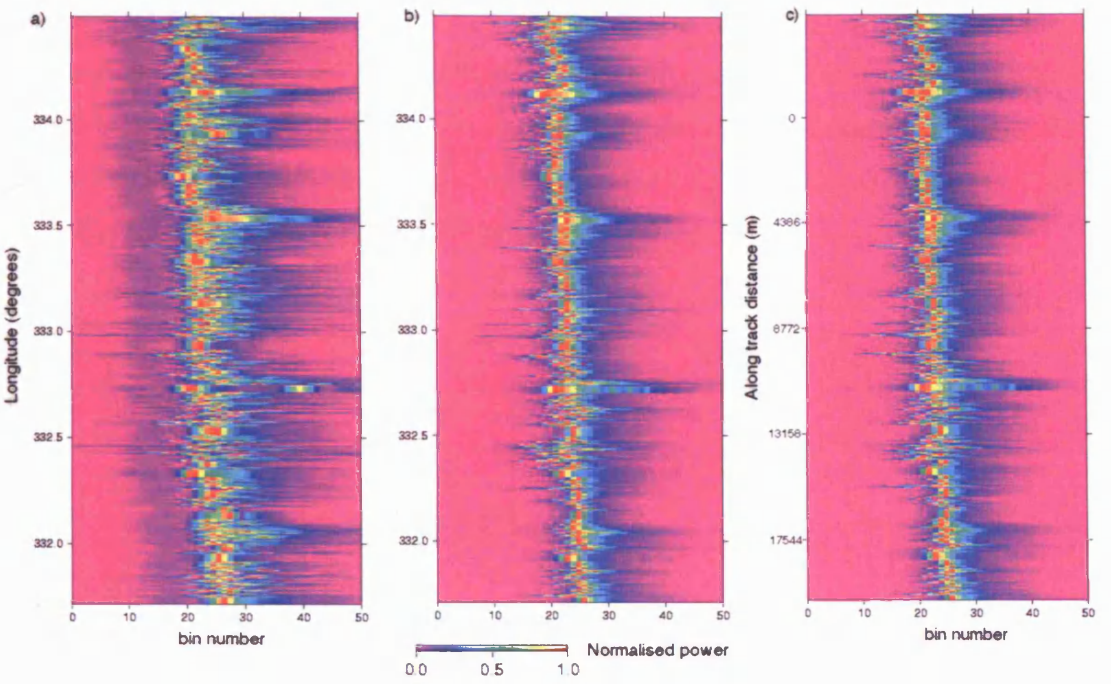

Figure 5.45: Z-scope plots over a long section of track with variable surface types.(a) shows the real D2P data, (b) shows the simulated data without speckle and (c) shows the simulated data with speckle.

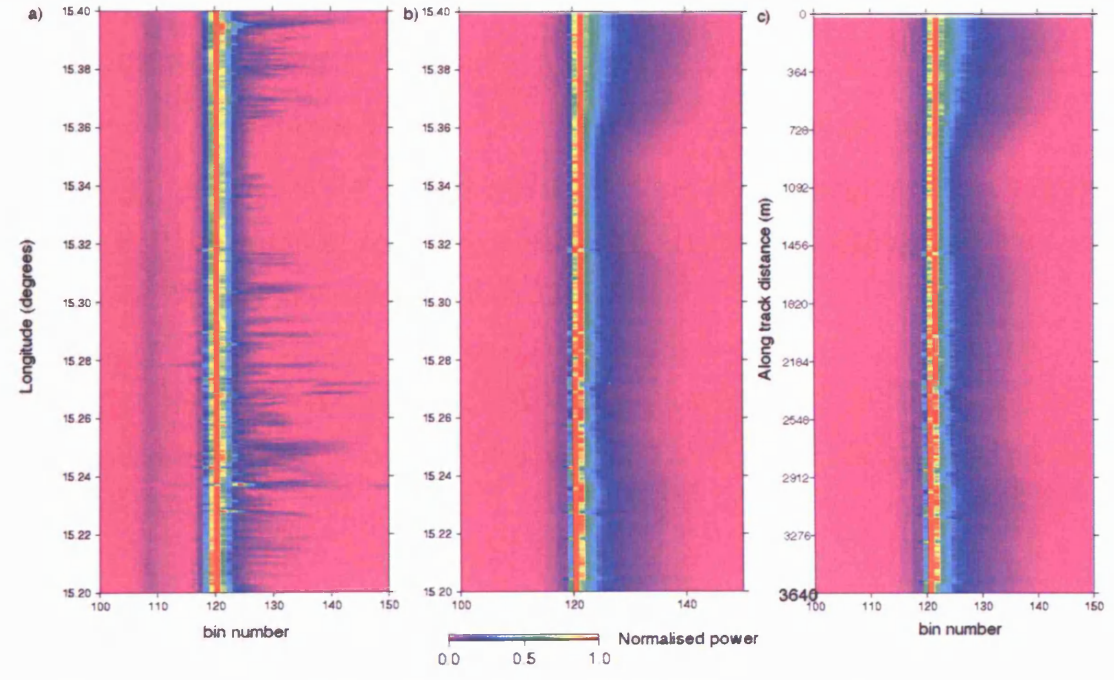

Figure 5.46: Z-scope plots over a smooth section of track, consisting of mainly typical echoes.(a) shows the real D2P data, (b) shows the simulated data without speckle and (c) shows the simulated data with speckle.

Figures 5.45 and 5.46 show that although adding speckle makes a slight difference to the simulated return it does not produce the variability seen in the real data. To estimate the effect of speckle on the cross correlation of the data sets, we correlate the simulated echo with the simulated echo with added speckle. Figure 5.47 shows histograms of the offset between simulated echoes with and without speckle.

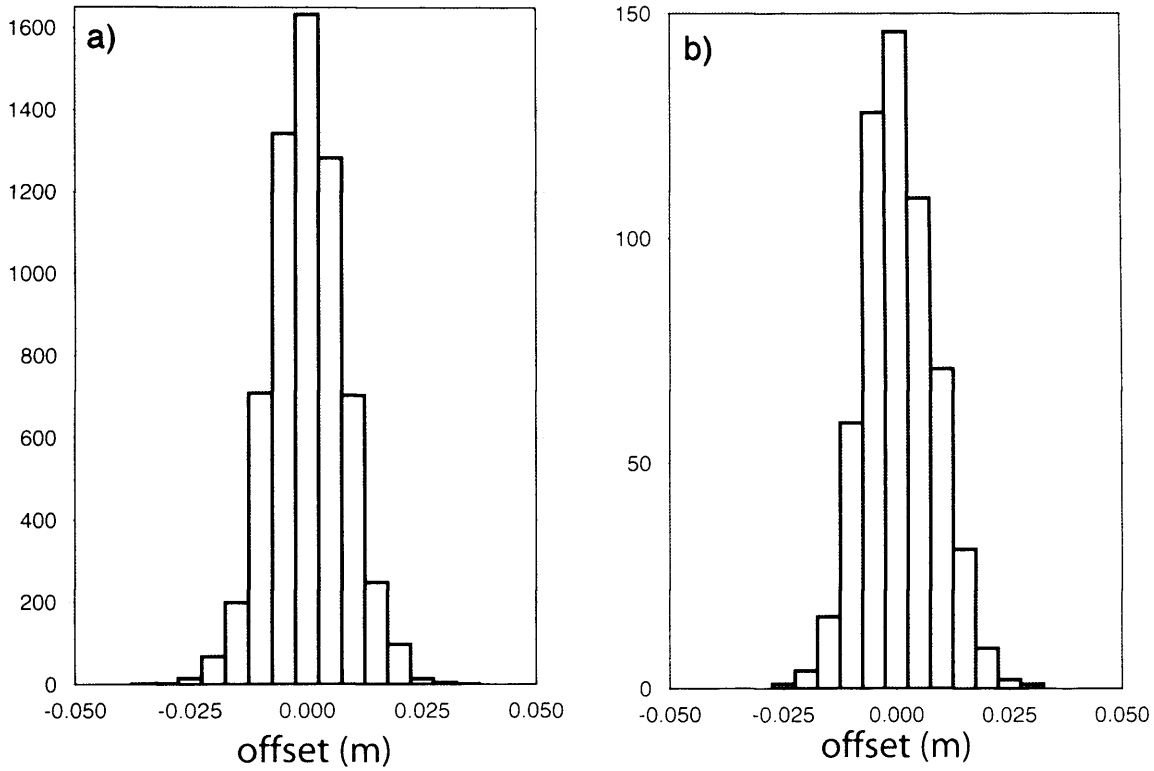

Figure 5.47: Histogram of the difference in offset in the range window between simulated echoes with out speckle and simulated echoes with speckle. a) shows data from figure 5.45 and b) shows data from figure 5.46.

Figure 5.47 shows the variability (i.e. the standard deviation of the histograms) in the offset caused by speckle is approximately 0.01 m. Therefore we add 0.01 m to our error estimate of ± 0.06 m.

5.7) Summary

Overview

- In this chapter we have described two new methods for analysing the data collected during the LaRA field campaign. The first method was a new re-tracking algorithm (the UCL D2P re-tracking algorithm) based on the typical shape of a D2P return. The second method was a radar simulator (the UCL D2P simulator), which provided a new method to compare two coincident data sets collected by different instruments.

In-detail

- We have assessed the accuracy of the ATM3 laser altimetry data set and found differences in the fore and aft scans due to errors in the INS value of pitch. We have corrected these errors by creating a surface grid from the ATM3 data with gird point elevations consisting of elevation estimates from both the fore and aft scans.

- We have designed a new re-tracking function for typical D2P echoes. We have described the re-tracking algorithm processing scheme. We have calibrated the re-tracker over a known surface and estimated an error of ± 2.4 cm when comparing re-tracked radar elevation estimates to ATM3 laser elevation estimates, averaged over the D2P footprint.

- We have discussed the limitations of the re-tracker: 1) The unknown re-track point and 2) the assumption that all echoes conform to the shape of a typical echo. We have described how the UCL D2P simulator overcomes both of these limitations by 1) comparing the full simulated echo shape to the full real echo shape and using the offset between them in the range window to estimate the difference in elevation between the laser/snow surface and the surface the radar ranges to, and 2) by including pitch and roll, and by simulating echoes over a real surface, the simulator creates both typical and non-typical echoes.

- We have designed a power simulator to calculate a D2P echo from a surface constructed from the laser data. We have described the simulator processing

scheme and the components of the power simulator in detail. We have described a method to compare the elevation difference between the real and simulated echoes by computing their offset in the range window. We have calibrated the simulator. We have assessed the effect of having a constant polar response angle for all facets on the offset between the real and simulated echoes. We have estimated an error on the offset of ± 0.06 m. We have assessed the effect of speckle on the offset and found that it introduced an additional 0.01 m to our error estimate, therefore the total error estimate on the offset is ± 0.07 m.

6) Comparison of simulated and observed radar echoes over sea ice

6.0) Introduction

In this chapter we take 6 example sections, and discuss how well the simulator reproduces the real data, and where the simulator fails to reproduce the real data. We look at how the real and simulated data change when the aircraft experiences large amounts of pitch and roll. We examine the offset in the range window between the real and simulated returns. The offset will indicate if the radar and the laser are measuring different surfaces (chapter 5,sections 5.6.18 and 5.6.19). We calculate the correlation coefficient between the offset and the aircraft parameters of pitch, roll and altitude to examine whether the offset is due to the simulator not modelling the effects of these parameters correctly. Finally we look for drifts in the calibration of the radar data (recall the D2P was calibrated once over a runway, 17 days before the LaRA flights).

6.1) Location of comparison areas

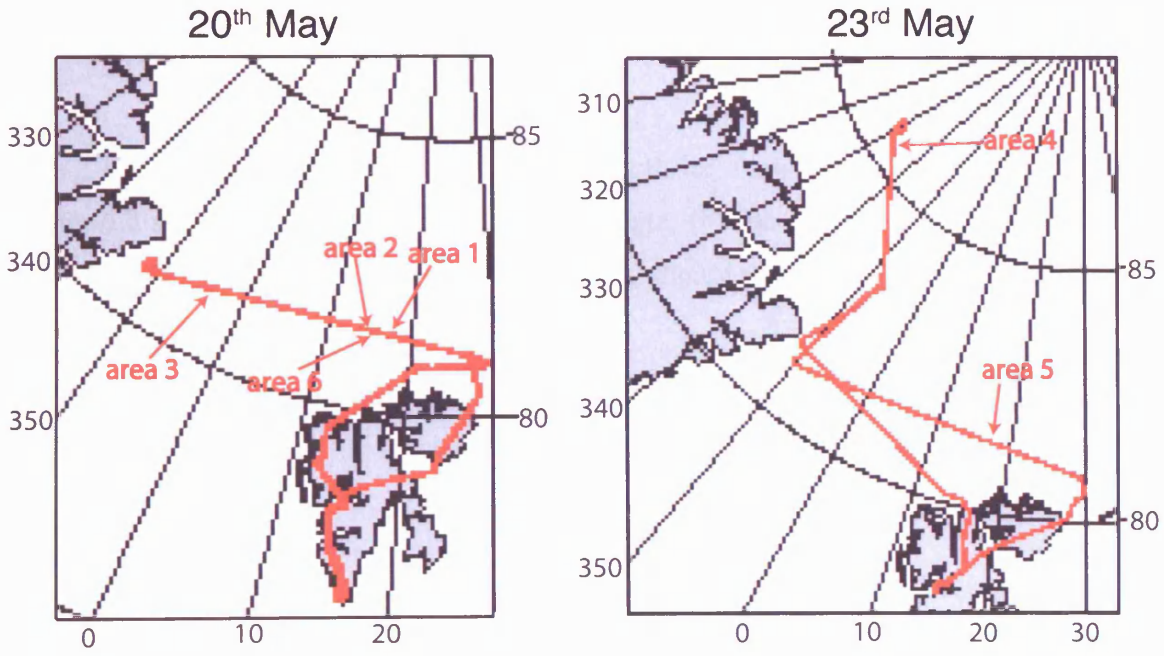

Figure 6.1: Location of study areas.

Due to the large number of data points we have chosen to show sections of the track over different ice regimes, from both days of data collection, rather than the whole data set. Figure 6.1 shows the location of each of our study areas.

For each area we show Z-scope plots of the normalised power for the real and simulated data. The top axis of the Z-scope shows the location of the data in longitude and along track distance (m). The side axis shows the bin number. The bin number has been adjusted according to the *ref* value, given for each data point. The adjustment is the same for the real and simulated data and means that all the range windows line up. Power at a higher bin number corresponds to a lower elevation with respect to the reference ellipsoid. Each bin corresponds to 0.208189 m in elevation. For areas 1,3,4,5 and 6 we show the offset between the real and the simulated data. A positive offset means that the simulator is measuring a higher surface (with respect to the reference ellipsoid) than the radar i.e. the laser is reflecting from a higher surface than the radar. Only offsets with a correction coefficient of 0.95 or greater are shown (see section 5.6.19, chapter 5). The calibration offset of 0.087 m has been added, the offsets have not been smoothed and adjacent offsets are connected by a straight line.

6.2) Area 1

Area 1 is a slightly extended section of the smooth ice shown in chapter 5, figure 5.4. Figure 6.2 shows zscope plots of (a) the D2P data, (b) the simulated data and (c) the offset between the simulated and real echo and d) digital imagery of the ice over which the measurements were taken.

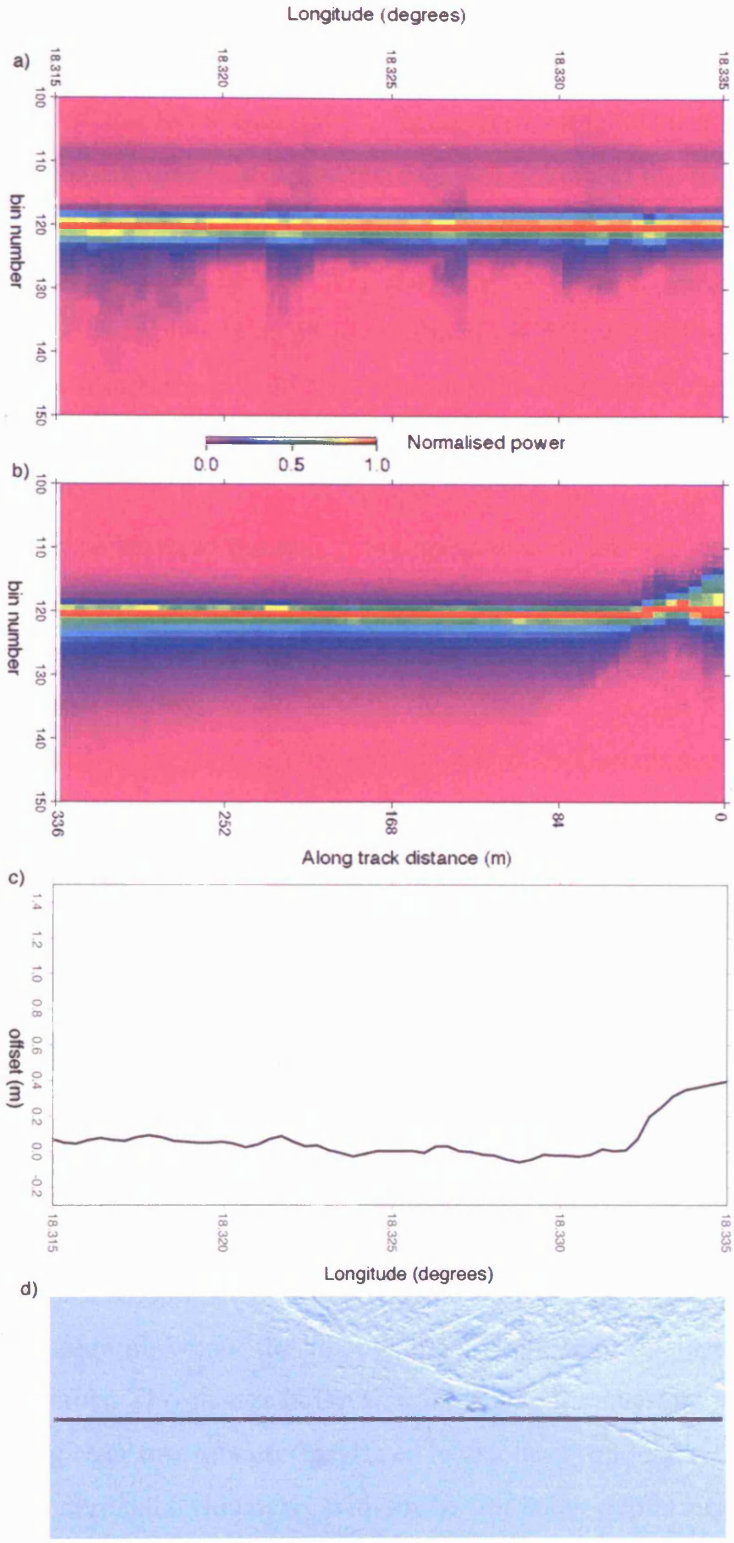

Figure 6.2: Z-scope plots a) from the D2P and b) from the simulator. c) shows the offset between the real and simulated echoes. d) is the digital imagery of the ice over which the measurements were taken. The black line shows the flight path. The imagery has been stretched in the along track direction and cropped in the across track direction.

Comparing the real data (a) and the simulated data (b), we see a faint purple line extending across the plot at bin 109 in the real data but not in the simulated data. This line is an artefact of the radar (chapter 5, figure 5.6) rather than a return from the surface, therefore the simulator does not recreate it. Looking at the return, the peak of the return occurs in the same bin for the real and simulated data, which implies they are measuring the same surface. In fact this may not be correct, elevation difference inferred from the Z-scope plots is quantised at the bin width of 0.208 m, therefore there could be an elevation difference between the simulated data and the real data of up to 0.208 m. This is why we must either retrack the data or correlate the two echoes at a higher sampling frequency than the D2Ps sampling frequency of 0.208 m, and then compare the difference between the two. It is also noticeable that the leading edge of the simulated data is narrower and the trailing edge wider than the real data by one bin. The wider trailing edge can be explained by the polar response angle. We applied a polar response angle of five degrees to all our data (see chapter 5, section 5.6.15), we chose this value as it would allow us to create echoes over both smooth and rough surfaces, and to recreate the effects of roll on the return (i.e. if the polar response angle were smaller then we would not get a high return from off nadir locations when the aircraft underwent roll). The trailing edge is too wide over this section of data as the polar response angle is too large over the section. Figure 6.3 shows profiles of a real and simulated echoes. The re-sampled (bottom) plot on figure 6.3 shows that although the leading edge simulated echo is slightly narrower that the real echo, the difference is very small.

The final feature to note in figure 6.2 is the change on the right hand side of the simulated data from a smooth surface to a rougher surface. The change corresponds to the area in the photograph where the smooth snow changes to rougher snow. The real data does not show this. The change in the simulated data is consistent with the depth of the snow increasing over this section (measured by the laser) and the radar continuing to measure the ice underneath. However, without in-situ snow depth measurements, it is not possible to confirm this.

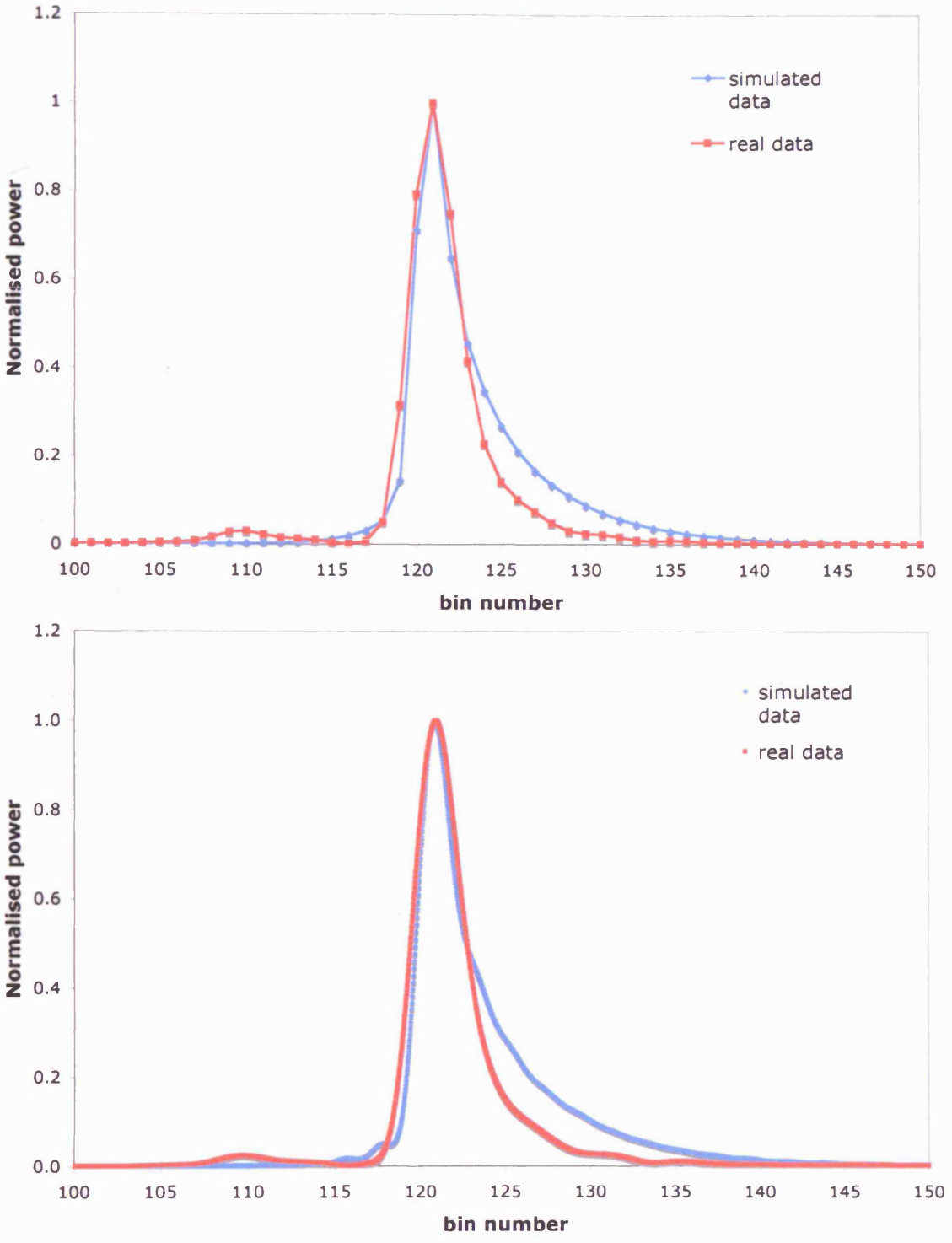

Figure 6.3: A real (red) and simulated (blue) echo positioned at 18.316° longitude. The top plot shows the data point at each range bin and the bottom plot shows the re-sample echoes sampled 40 times per bin.

6.3) Area 2

We have chosen area 2 to show an example of how the real data and the simulated data behave when we have large variations in the aircraft parameters of pitch, roll and altitude.

Figure 6.4 a) and b) shows that the simulator recreates the effect of a large change in the pitch, roll and altitude. The trailing edge of the simulated data is too narrow in this case. This is because the polar response angle is too small over this section of track. However, the main shape of the return echo and the variability in its shape and position on the range window is simulated well.

Where the aircraft experiences large values of pitch and roll the centre of the antenna gain pattern is shifted away from the nadir position and out of the first pulse ring. For example: At longitude 14.85° the aircraft roll is -14°, with the antenna mounting angle of -2.5°, the offset of the centre of the antenna pattern is 183 m to the starboard side of the nadir position. The antenna gain pattern tends to zero at approximately 60 m from its centre (see chapter 5, figure 5.16), so this means that the power returned from facets at nadir is negligible compared to the power returned from facets located at the centre of the shifted gain pattern. The travel time for the power from facets at the centre of the gain pattern is longer than the travel time from facets at nadir, therefore the main return occurs at a higher bin compared to the data that is not subjected to large roll values.

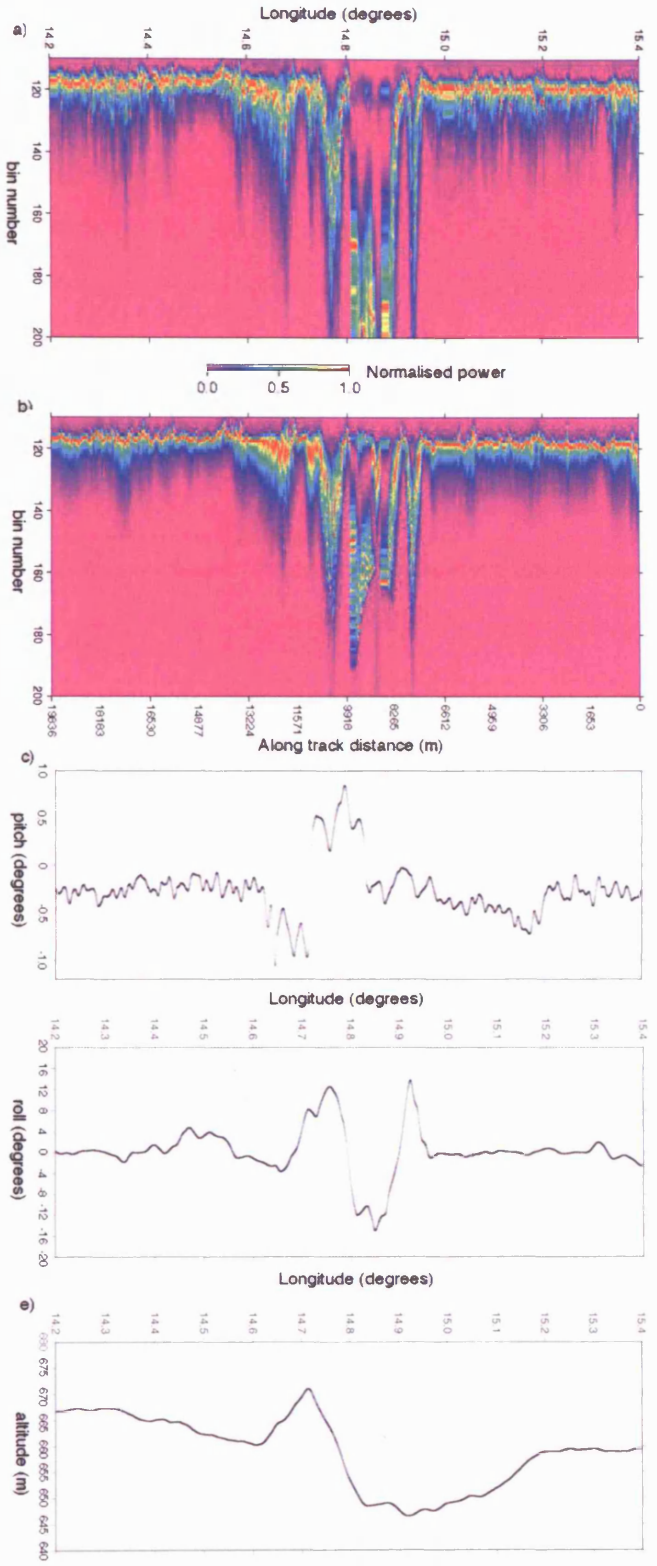

Figure 6.4: Z-scope plots show the normalised power a) from the D2P and b) from the simulator. c) shows the pitch of the aircraft d) shows the roll of the aircraft and e) show the altitude of the aircraft.

We would expect some differences in the shape of the real and simulated echo due to the position of the laser data relative to the aircraft nadir during large variations of the roll. When the aircraft experiences positive/negative roll the instruments see the surface to the port/starboard side of the aircraft rather than being centred on nadir. Figure 6.5 shows the nadir position of the aircraft (black line) and the laser surface elevation estimates (coloured points), for the section of track shown in figure 6.4.

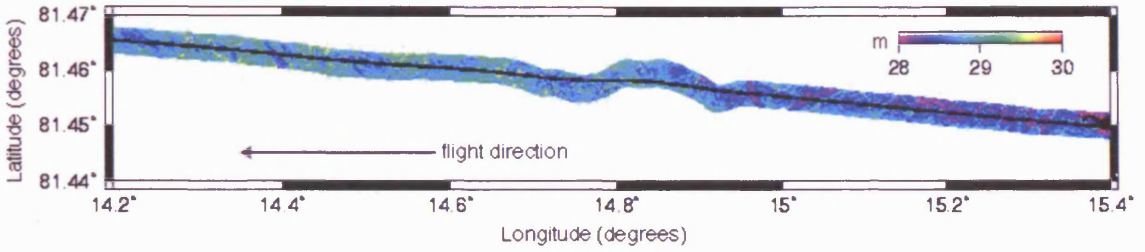

Figure 6.5: Laser elevations and aircraft nadir position for section of track shown in figure 6.4.

Figure 6.5 shows that, at 14.85° longitude, the laser data is almost entirely to the starboard side of the aircraft. In reality the D2P will record returns from both the port and starboard side of the aircraft but as we do not have surface data (laser data) to the port side of the aircraft we cannot simulate the return from this part of the surface. Therefore we would not expect the simulated and real return to be exactly the same. This issue illustrates a limitation of the simulator: we cannot simulate an echo realistically in an area where we have insufficient laser data.

The variation in pitch is much smaller than the variation in roll over this section (± 1° compared with ± 16°). ± 1° will shift the centre of the antenna pattern fore or aft of the nadir position by only 10.5 m. This will alter the shape of the return from individual beams (see chapter 5, figure 5.25), and can be easily simulated. The change in altitude will cause the timing of the range window to shift. The simulator is designed to create a range window and sample the power with the same timing as the D2P (chapter 5, section 5.6.13), therefore the simulator is able to re-create the effect of changes in altitude on the return echo.

In chapter 5, section 5.2.2, we described how the D2P data was filtered. From the evidence presented above it is clear that we should also remove data where we have large values of roll. Figure 6.6 shows a histogram of the roll values for the two LaRA flight days.

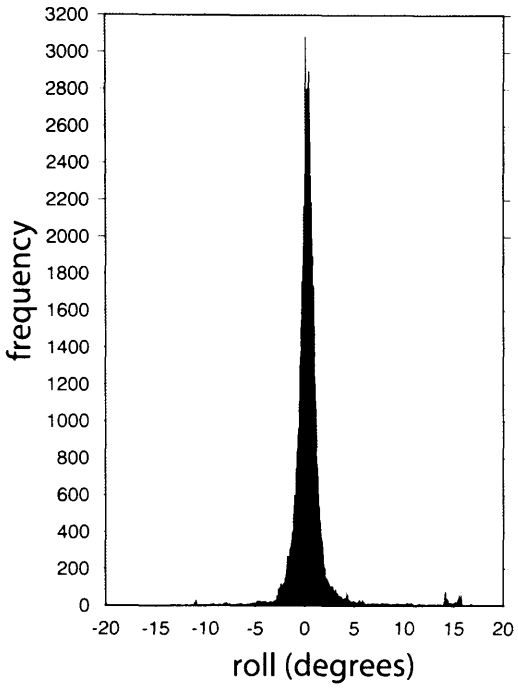

Figure 6.6: Histogram of roll values from the two days of LaRA flights.

Based on figures 6.4 and 6.6 we have decided to remove data points with a roll greater than ± 5°.

6.4) Area 3

Area 3 is a long, continuous section of ice only broken by one lead. We chose this section to look at the offset between the real and the simulated echoes and to see if the offset was related to the aircraft parameters of pitch, roll and altitude. The purpose of this comparison was to check that the offset between the real and simulated data was not simply due to the simulator incorrectly modelling the effects of these parameters. Figure 6.7 shows the Z-scope plots of the real and simulated data and the offset between the real and simulated echoes. Figure 6.8 shows two examples of the digital imagery over area 3. Image 1 is typical of the whole section and image 2 shows the only lead of the section. Their locations are shown in figure 6.7 on the lower x-axis in b).

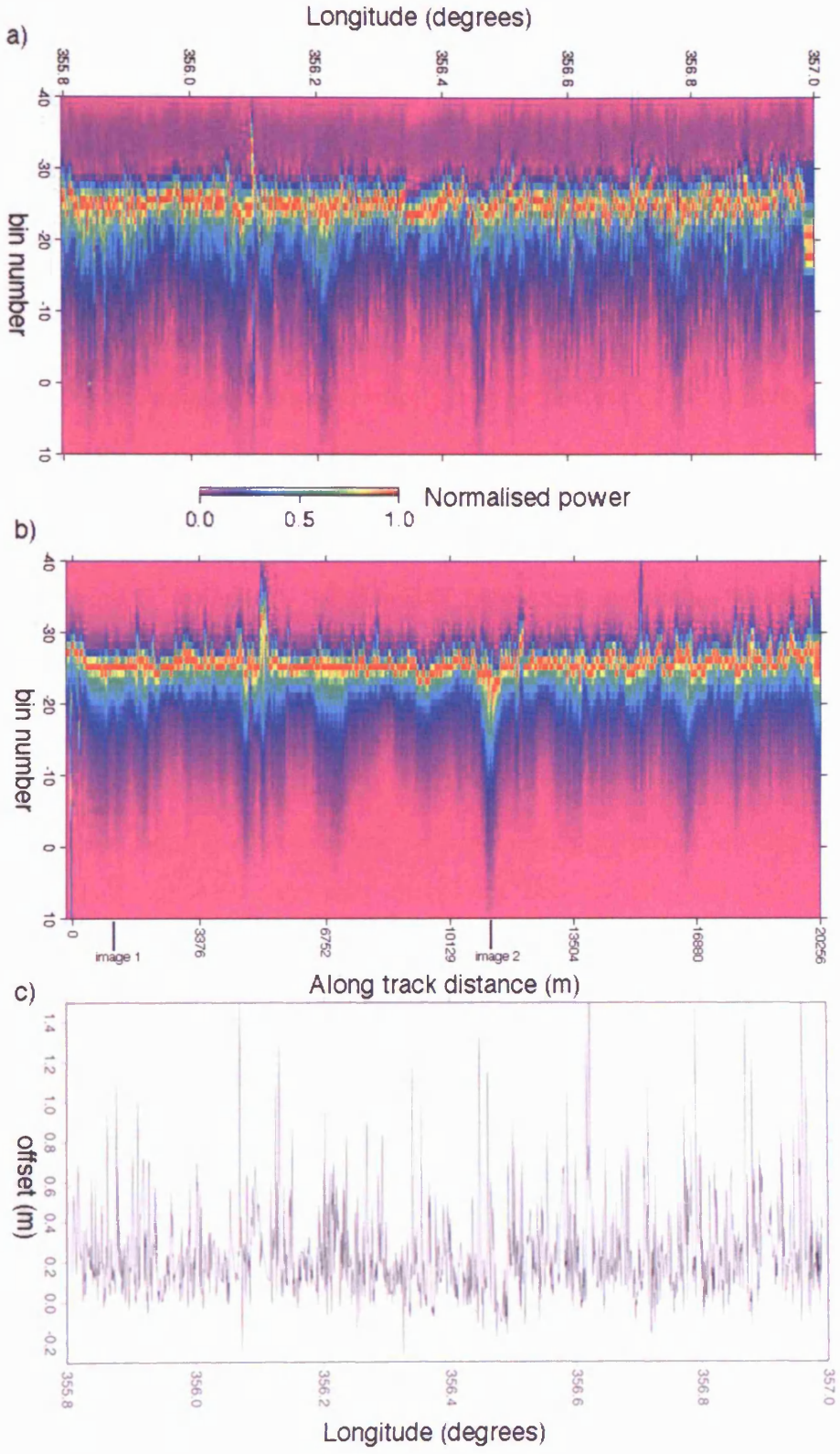

Figure 6.7: Z-scope plots show the normalised power from a) the D2P and b) the simulator. Lines on the bottom x-axis mark the locations of the digital imagery shown in figure 6.8. c) shows the offset between the real and simulated data.

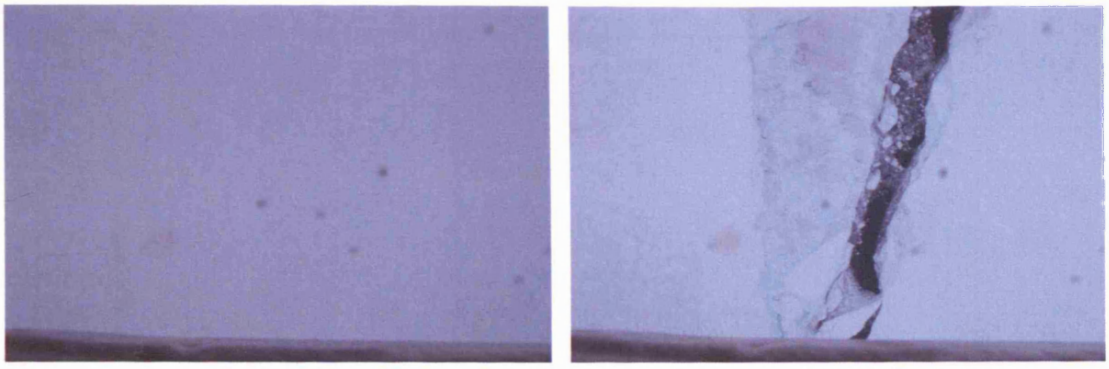

image 1 image 2

Figure 6.8: Digital imagery. Image 1 shows a typical view of the snow/ice (355.87° longitude). Image 2 shows the one lead (356.49° longitude) of the section. Locations of the images are shown in figure 6.7.

Comparing figure 6.7 a) and b), the simulator reproduces the change in position of the peak bin over the section. It is noticeable that the real data (a) is more variable than the simulated data (b), we attribute this variability to a fluctuating polar response over the surface which is not modelled in the simulator.

Figure 6.9 shows the offset between the real and simulated echoes vs. a) roll, b) pitch and c) altitude. There is no significant correlation between the offset and the aircraft parameters. We repeat this experiment with data from the 23rd ,in a different area, in section 6.5

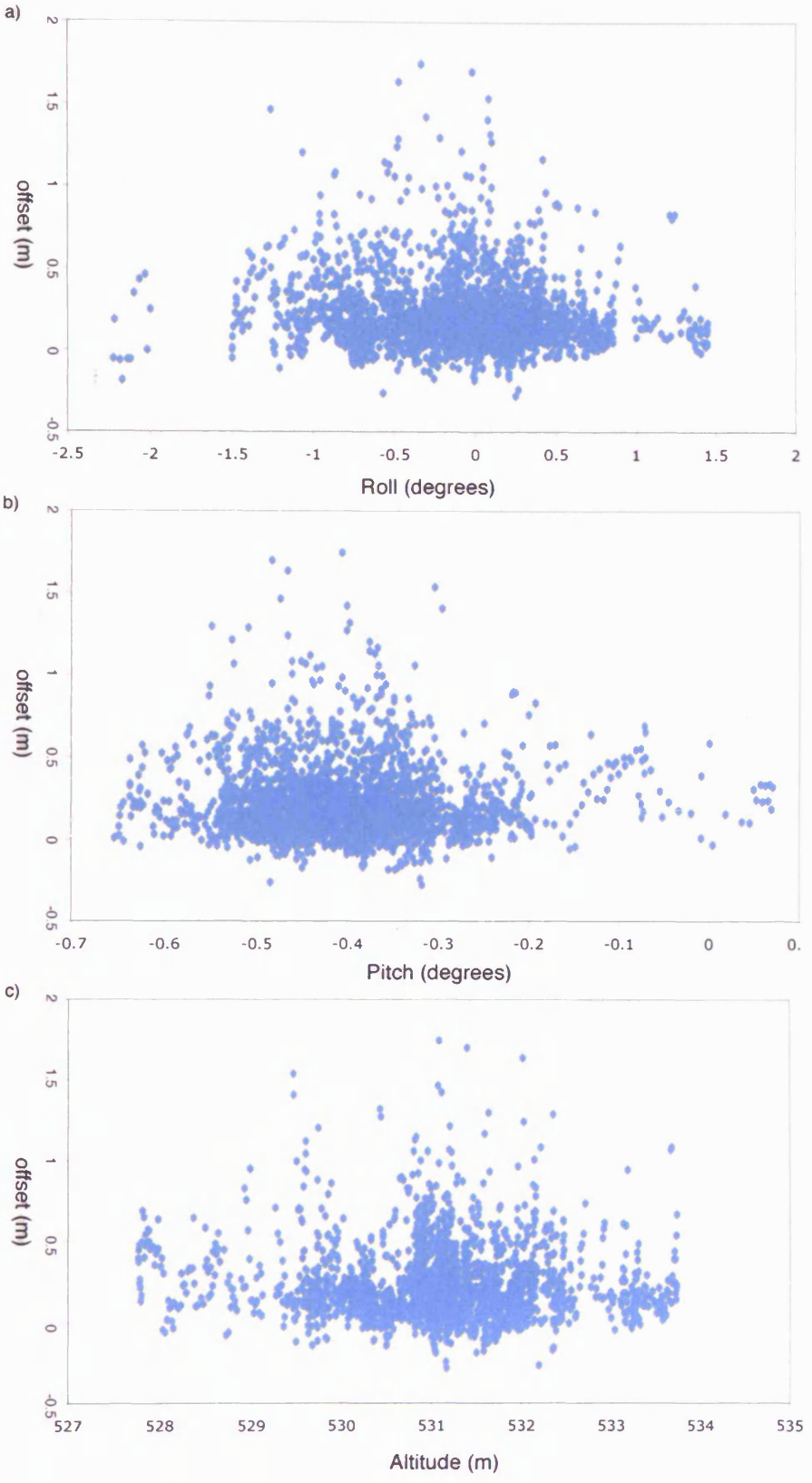

Figure 6.9: The offset vs. a) roll, b) pitch and c) altitude. The correlation coefficient for a) is -0.10974, b) -0.013954 and c) -0.057493.

6.5) Area 4

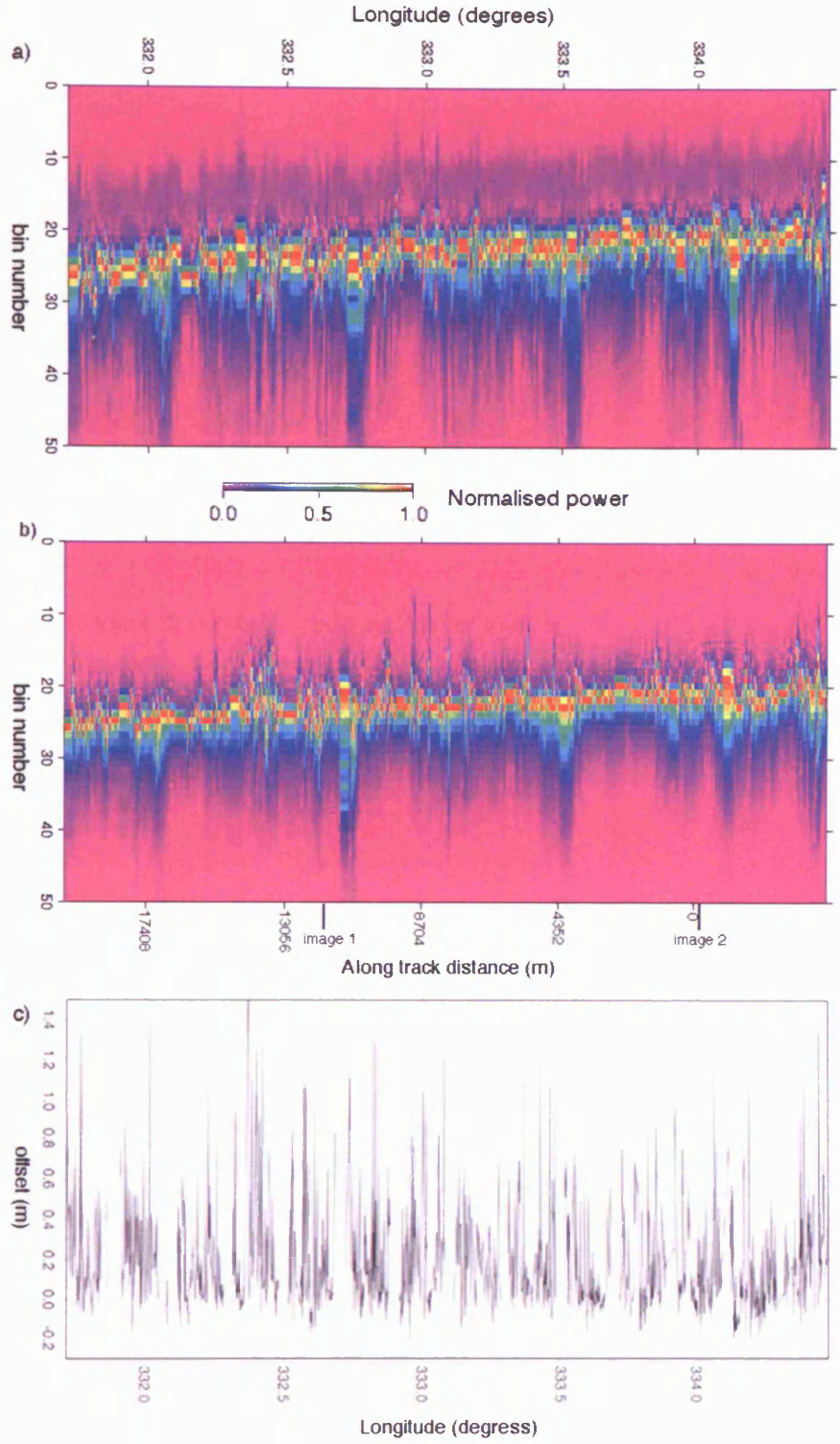

Figure 6.10: Z-scope plots show the normalised power from a) the D2P and b) the simulator. Lines on the bottom x-axis mark the locations of the digital imagery shown in figure 6.11. c) shows the offset between the real and simulated data.

Area 4 is situated to the north of Greenland and is a long, continuous section of ice broken only by two leads (located at 322.58° longitude and 333.32° longitude).

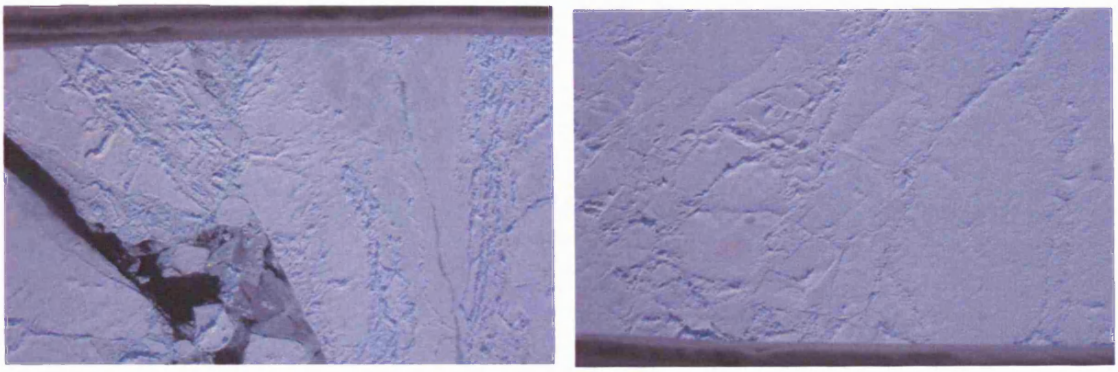

image 1 image 2

Figure 6.11: Digital imagery. Image 1 shows the lead positioned at 322.58° longitude. Image 2 shows a typical view of the snow/ice (333.98° longitude). The location of the imagery is shown in figure 6.10 b) on the lower x-axis.

Figure 6.12 shows that, again, we see no significant correlation between the offset and the aircraft parameters.

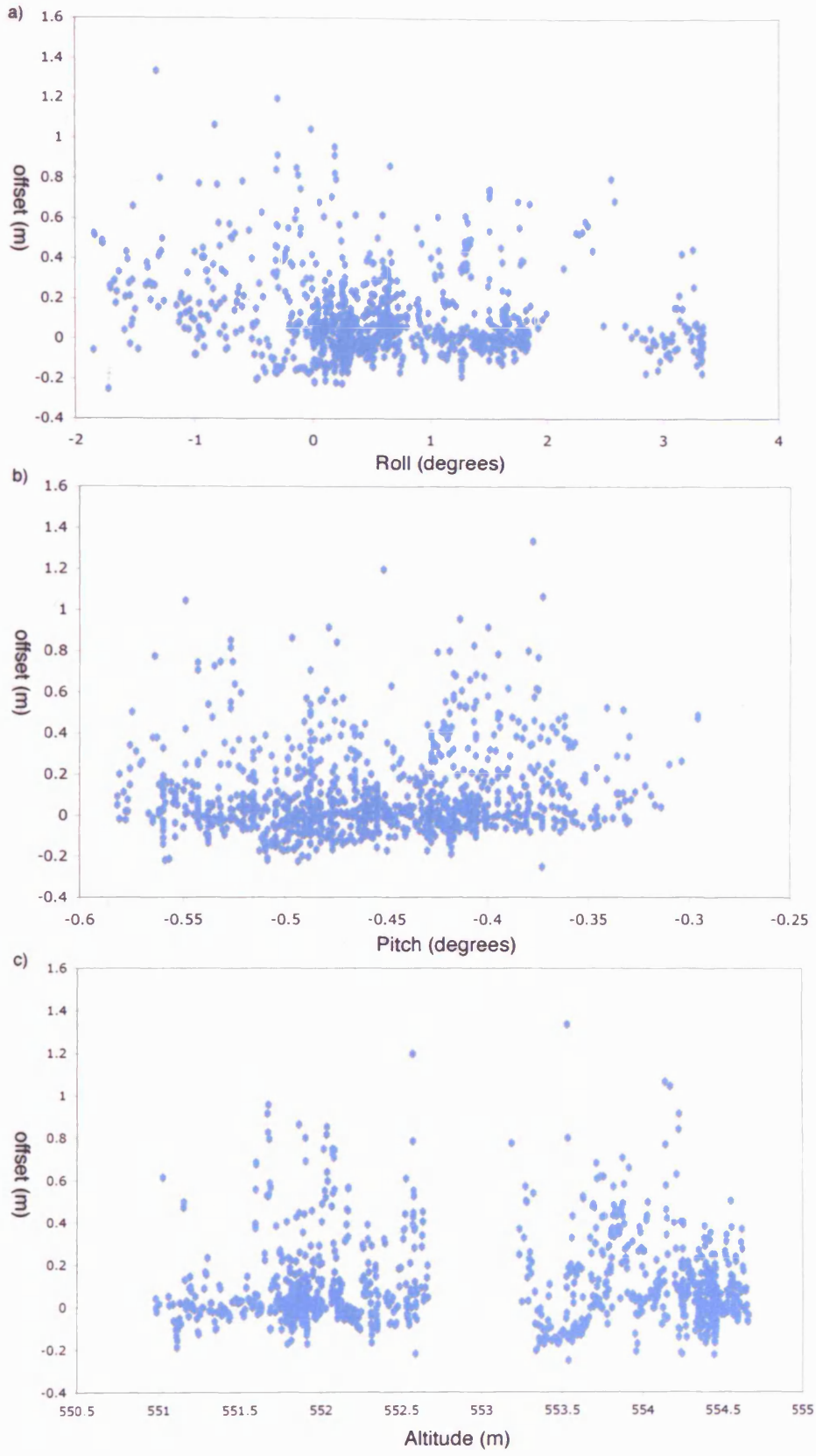

Figure 6.12: The offset vs. a) roll, b) pitch and c) altitude. The correlation coefficient for a) is -0.170826, b) 0.119072 and c) 0.001077.

6.6) Area 5

Figure 6.13 shows a section of track over a mixed surface regime, consisting of snow covered ice and bare ice.

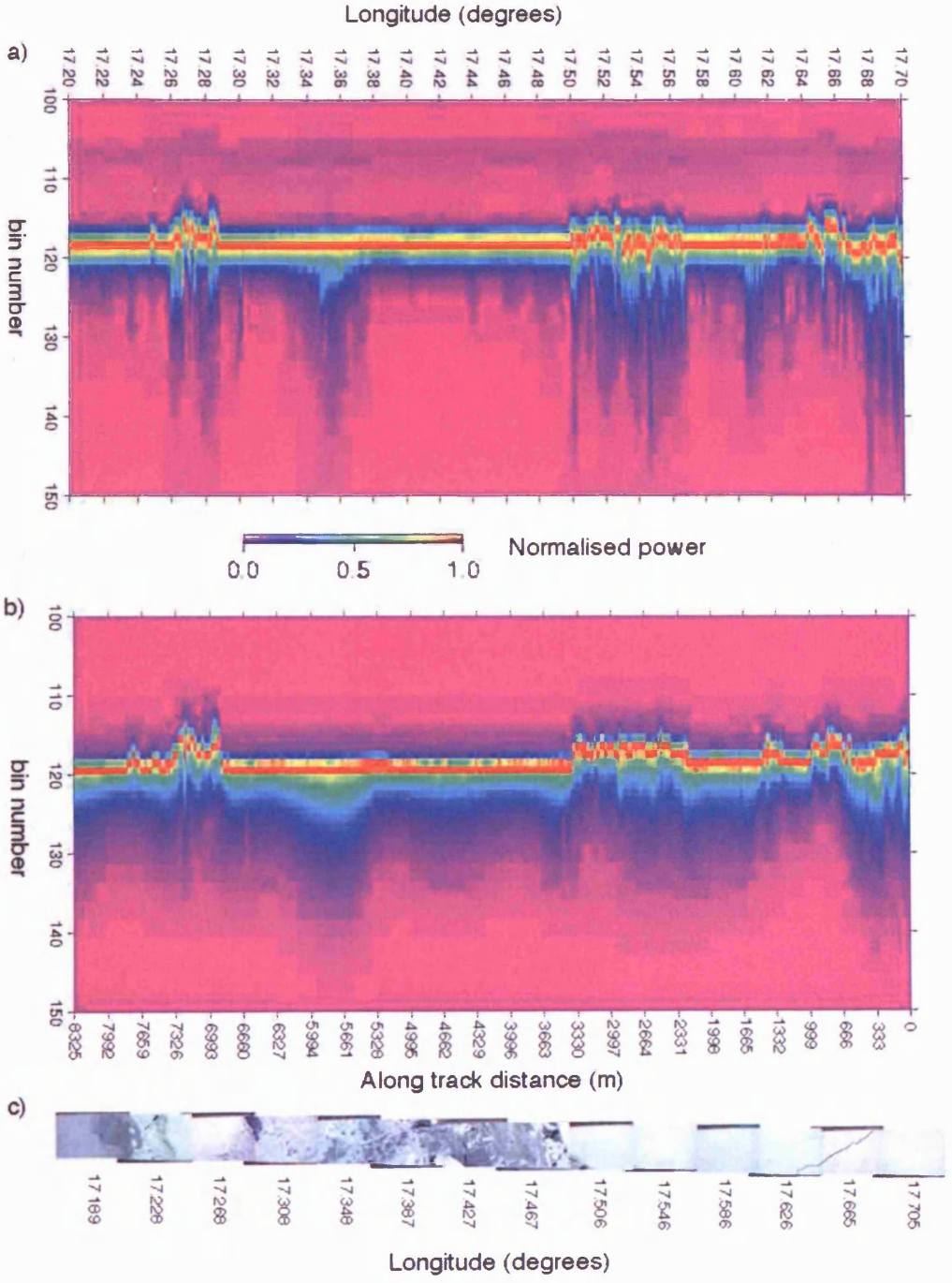

Figure 6.13: Z-scope plots show the normalised power a) from the D2P and b) from the simulator. c) shows the digital imagery of the ice over which the data shown in a) and b) were collected. The imagery is shown in clearer detail in figure 6.14.

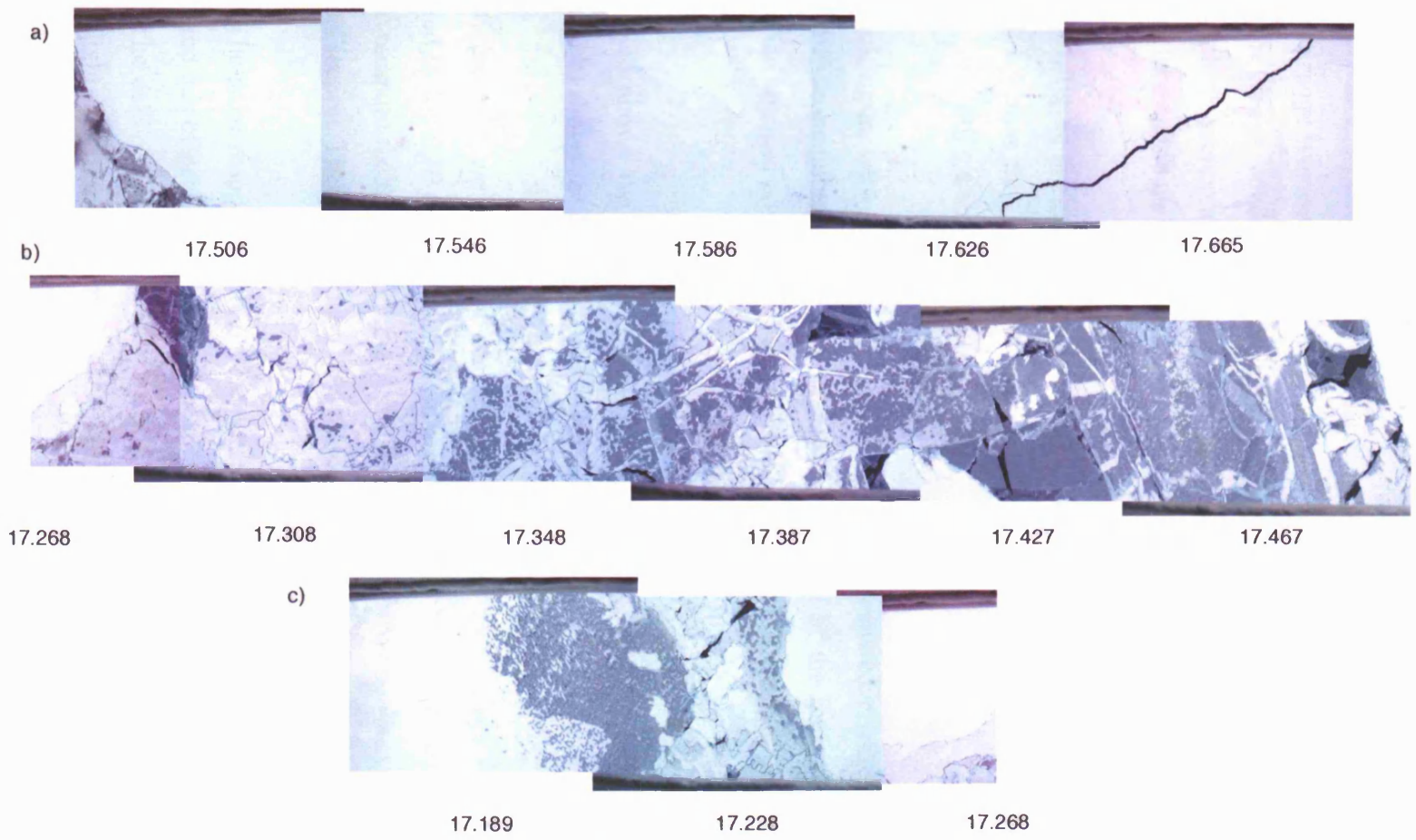

Figure 6.14: Photographs over area 5 divided into a) snow covered ice, b) thin ice and c) mixed thin and snow covered ice. The longitudes locate the centre of each photograph.

Section a), figure 6.14 shows snow covered ice between 17.7° longitude and 17.5° longitude. The Z-scope plots from this section show both variable position of the peak bin in the range window, indicating a rough surface and constant position of the peak bin in the range window, indicating a smooth surface. Careful inspection of the photographs in section a) shows a variable surface but it is difficult to see the roughness of the surface and to tie it to the Z-scope plots.

Section b), figure 6.14 shows thin, snow free, ice between 17.5° longitude and 17.29° longitude. Across this section the position of the peak in both the Z-scope plots is constant, indicating a smooth surface

Section c), figure 6.14 shows a mixture of thin ice and snow covered ice. Comparison with the Z-scope plots shows that, as before, the peak of the return over the snow covered ice changes position in the range window and is at a constant position over the thin ice.

Figure 6.15 shows the offset between the real and the simulated data. a) shows the offset and b) shows the digital imagery over the section.

From figure 6.15 we see that the laser surface appears to be lower than the surface measured by the D2P over the thin ice. In reality we would expect both the laser and the radar to measure the top of the thin ice and therefore the offset between them to be zero over this section. There are two possible reasons for this offset:

1. The polar response angle of five degrees is too wide for the returns over thin ice and this effects the estimate of the offset between the real and simulated data.
2. The calibration of the radar has drifted in the 17 days between the calibration flights at Wallops and the LaRA flights in the Arctic.

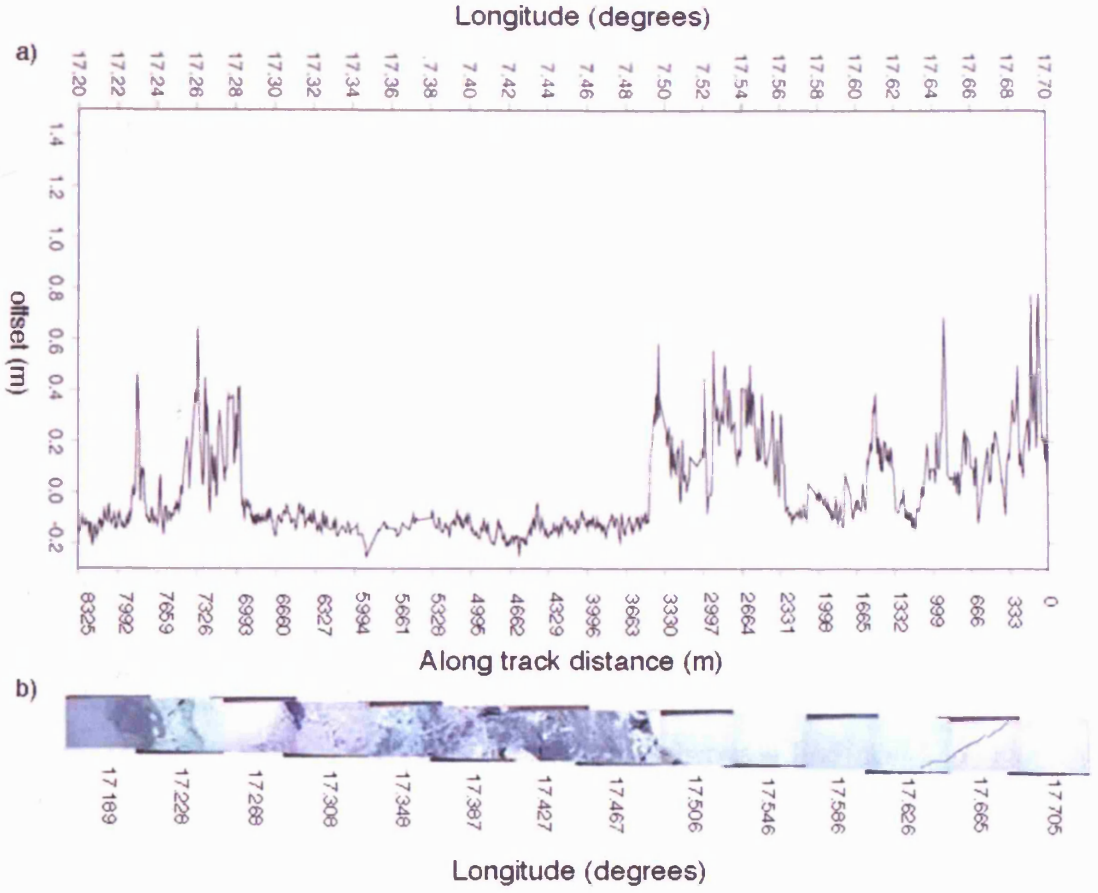

Figure 6.15: Offset between the simulated and the real data. A positive offset means that the surface measured by the simulator (i.e. the laser surface elevation map) is higher than the surface measured by the D2P. a) shows the offset, b) shows the digital imagery.

To test 1. we took the thin ice section and simulated the returns, changing the polar response angle (ϕ_{pr}) to find the most appropriate value. We then calculate the offset between the simulated and real data, for each polar response angle.

As in chapter 5, section 5.6.19, we found the highest correlation coefficient by fitting a sixth order polynomial to the plot of ϕ_{pr} vs. correlation coefficient. We use the same method here and find that a polar response angle (ϕ_{pr}) of 2.82° provides the highest correlation coefficient. ϕ_{pr}=2.82° corresponds to an offset of -0.171 m. This means that the average offset between the simulated and the real data. over the thin ice is -0.171 m. It is important to note that the offsets shown in figure 6.15 have had the calibration offset of 0.087 m added to them and therefore, when we include the calibration offset, the average offset over the thin ice is approximately -0.084 m. Using ϕ_{pr}=5°, we get an

offset of -0.207 m, therefore only 0.036 m (from -0.171—0.207) of the difference between the real and the simulated data, over the thin ice can be explained by the use of a greater polar response angle. 0.036 m is well within our error estimate of ± 0.06 m calculated in chapter 5, section 5.6.19. Therefore we have 0.048 m of offset unaccounted for. Area 6, described in section 6.7, shows another example of measurements over thin ice.

6.7) Area 6

Figure 6.16 shows two zscope plots of real data at the same longitude. a) shows the out bound pass and b) shows the return pass.

Figure 6.16 shows that although the outbound and return pass were separated by 2 hours, features in the Z-scope plot from the outbound pass are also seen in the Z-scope plots for the return pass. In particular, the flat section between 17.5° and 17.7° longitude in a) can be seen between 17.4° and 17.6° longitude in b). Figure 6.17 shows the digital imagery over this section from the outbound pass a) and the return pass b).

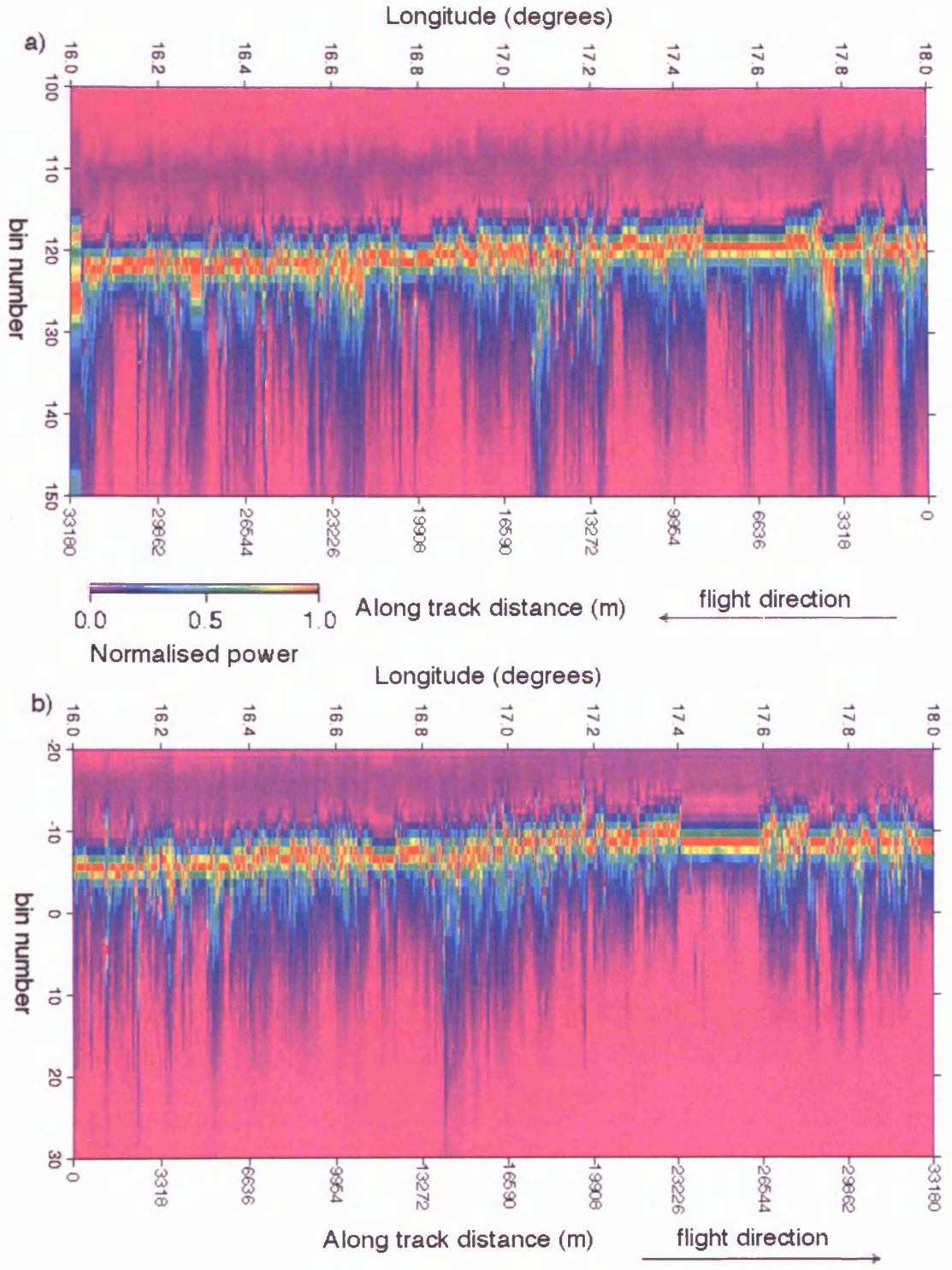

Figure 6.16: Z-scope plots of the normalised power from the D2P at the same longitude. a) shows the outbound pass and b) show the return pass. The two passes are separated by 2 hours.

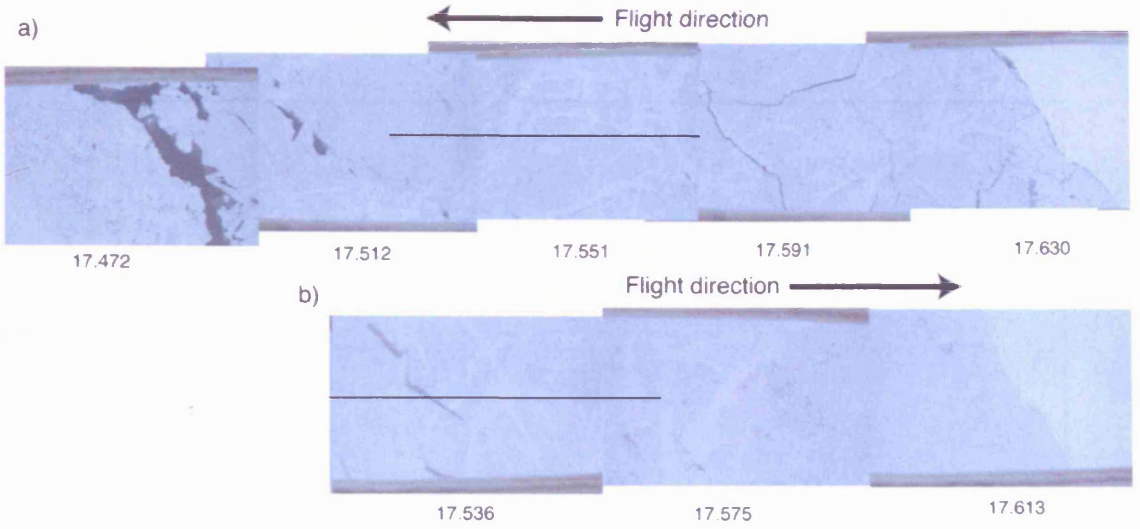

Figure 6.17: digital imagery over flat section of ice a) shows the outbound flight and b) shows the return flight. The longitude is given for the centre of each photograph.

Unfortunately, cloud cover obscured the photographs over much of the return pass and meant that laser data was only collected over a short section of the thin ice. Comparison of 6.17 a) and b) tells us that the return flight did not pass over exactly the same ice and the outbound flight, but due to the similar patterns on the ice from both passes and to the similar shape of the edge of the thin ice (seen in the far right imagery), we believe that we a seeing the same area of ice in both passes. The black line in b) marks the section of track over which we have data from the return pass. In order to compare data from the two passes we selected a section of track from the outbound pass that was the same distance away from the thin ice edge as the section of track from the return pass. The section is marked by the black line in a).

Figure 6.18 shows the offset for a) the outbound pass and b) the return pass. Comparing figure 6.18 with 6.15, the offset in all three cases over thin ice is negative and in most cases is between -0.10 m and -0.20 m. To check the effect of an incorrect polar response angle we repeat the experiment described in section 6.6 over the outbound pass. We use the outbound pass as it contains more data and we can extend the study area over the whole section of thin ice.

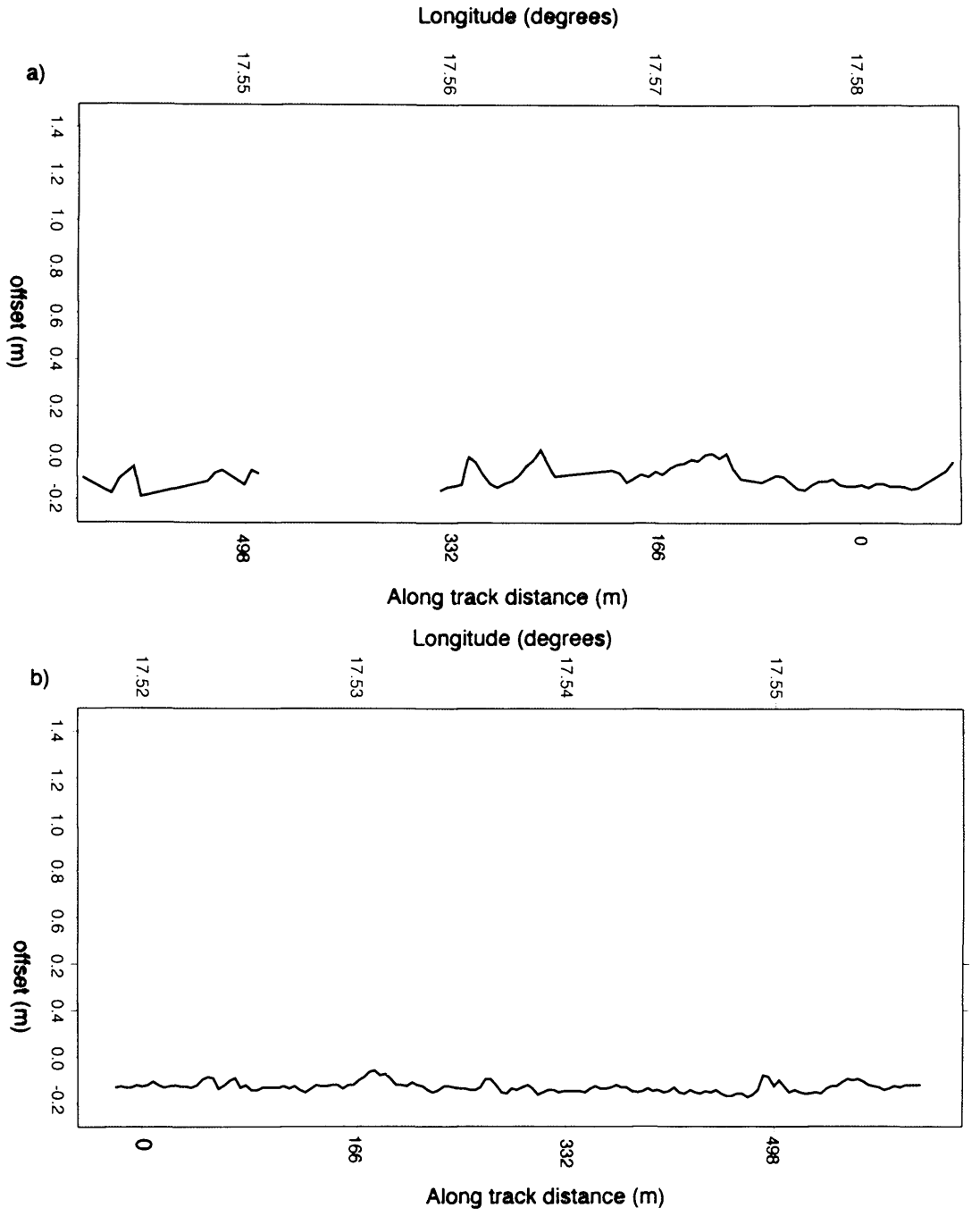

Figure 6.18: Offset between the simulated and the real data. A positive offset means that the surface measured by the simulator (i.e. the laser surface elevation map) is higher than the surface measured by the D2P.

The offset over the section for the best fit polar response angle (ϕ_{pr}= 4°) is -0.172 m (for area 5 it was -0.171 m). Using the 5° polar response angle we get an offset of -0.19 m. Therefore, after adding the calibration offset and taking into account the fixed polar response angle, the unaccountable offset over the thin ice is -0.067 m (for area 4 it was -

0.048). Both areas show similar offsets, therefore a drift in calibration could be the cause. However, as no calibration of the D2P was performed in the Arctic, we cannot confirm this and as the unaccountable offset is small compared to the offset between the laser and the radar over snow covered ice, we have not adjusted our data.

6.8) Summary

- The simulator reproduces the shape to the real echoes well compared to the retracker. It is able to model the effects of variable aircraft parameters and produce typical and non-typical echo shapes.

- The use of a constant polar response means that the simulator does not reproduce all of the variability seen in the real data and that the trailing edge of the simulated echo is often too wide or too narrow compared to the real data. However, our error estimates for the measurement of the offset between the real and simulated data have taken this into account (chapter 5, section 5.6.19). The error on an offset estimate is ±0.07 m. As the offsets between the simulated data and the real data, shown in this chapter, are typically 0.2 m, we believe that we are seeing an elevation difference between the real and simulated data.

- We have shown that the elevation difference we see between the real and simulated data is not due to the simulator incorrectly modelling the effects of changes in the aircraft parameters. Sections 6.4 and 6.5 showed long sections of track over mainly unbroken ice. There was no significant correlation between the aircraft parameters and the offset.

- By locating areas of, thin, snow free ice we have examined the offset between the simulated and real data to attempt to determine any drift in the calibration of the radar. The results imply that the radar calibration drifted by between 0.05 and 0.07 m between the calibration flights and LaRA. However, as no calibration of the D2P was performed in the Arctic, we cannot confirm this and we have not adjusted our data.

7) Elevation differences between radar and laser altimeter data over sea ice

7.0) Introduction

In this chapter we take a wider look at the offset between the simulated and real echoes. We have divided the study area into three regions, as shown in section 7.1, and have taken examples from each region. Dividing the study area allows us to look for regional variations in the offset. Section 7.2 describes the data presented in this chapter and the analysis methods used. Section 7.3 shows a map of sea ice drift, used to estimate the ice drift between outbound and return passes with coincident longitudes. Sections 7.4 to 7.6 analyse data from each of the regions shown in figure 7.1. Section 7.7 compares measured snow depth distributions to the offset between the laser and the radar. Section 7.8 shows offset maps for the whole of the processed data set. In section 7.9, we evaluate the UCL D2P re-tracker. Finally, in section 7.10, we estimate the impact of using the laser/radar difference on the ice thickness calculation.

7.1) Study regions

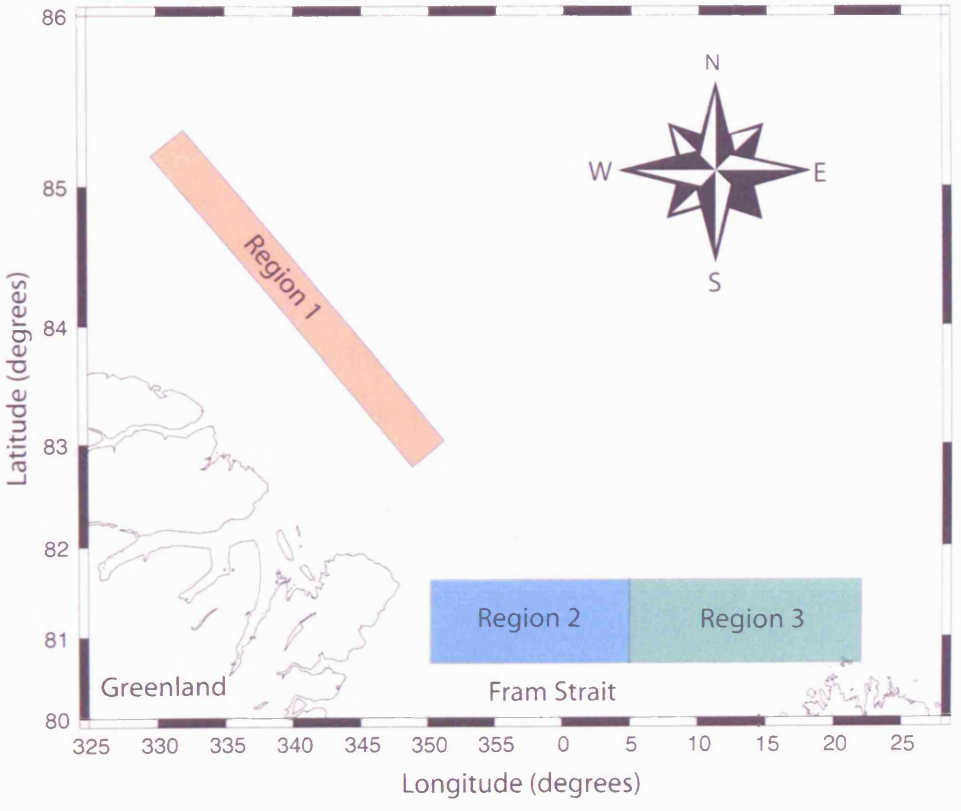

Figure 7.1: Map showing study regions.

We have divided the data into three study regions. Region 1 is situated to the north of Greenland and includes data between 330° and 350° longitude and 83° and 85° latitude. Region 2 is in the west Fram Strait and includes data between 350° and 5° longitude and 80.5° and 81.5° latitude. Region 3 is in the east Fram Strait and includes data between 5° and 22° longitude and 80.5° and 81.5° latitude.

7.2) Data description and analysis methods

During our discussion about the offset in each region we show various plots of the offset between the real and the simulated data. The offset is the position of the simulated data in the range window minus the position of the real data in the range window. Therefore a positive offset tells us that the laser is measuring a higher surface (with respect to the reference ellipsoid) than the radar. The offset is given in meters and the calibration adjustment of 0.087 m has been added. The offset has not been averaged and the error estimate on each offset is ±0.07 m (see chapter 5). The plots and histograms of the offsets show both positive and negative offsets. Negative offsets arise from areas over thin ice where there is little or no snow cover (see chapter 6, sections 6.6 and 6.7), and as a result of the ± 0.07 m error estimate. Gaps in the data are caused by: the filtering applied to the radar data set (chapter 5, section 5.5.2); the additional filtering of points with a roll greater than 5° (chapter 6, section 6.3); a lack of laser data caused by the presence of cloud cover or open leads. At the ATM wavelength of 532 nm, energy is not returned from the surface of calm water, but is forward scattered into the water column, therefore the energy returned to the altimeter will give an elevation estimate that is lower than the surface of the water or no energy at all will be returned to the altimeter. If the water surface is rippled then the altimeter may receive a strong return from the surface. When the altimeter is operating in scanning mode it more susceptible to these problems. [Bill Krabill, personal communication]. While looking at the laser data we found no scanning laser returns over open water.

During our analysis we compute the autocorrelation function of the offset using equation 4.3 in chapter 4. We also compute the correlation coefficient of the offset between spatially coincident tracks using equations 5.62 and 5.63, in chapter 5. The correlation coefficient was computed by taking the longitude values from shorter pass

and finding the offset at those longitude values in the longer pass, by linear interpolation.

7.3) Sea ice drift

Figure 7.2 shows sea ice drift velocities from derived from the NASA QuickSCAT/SeaWinds scatterometer and the SSM/I brightness temperature maps from the NSIDC. This figure is used to estimate sea ice drift between outbound and return passes located at the same longitudes.

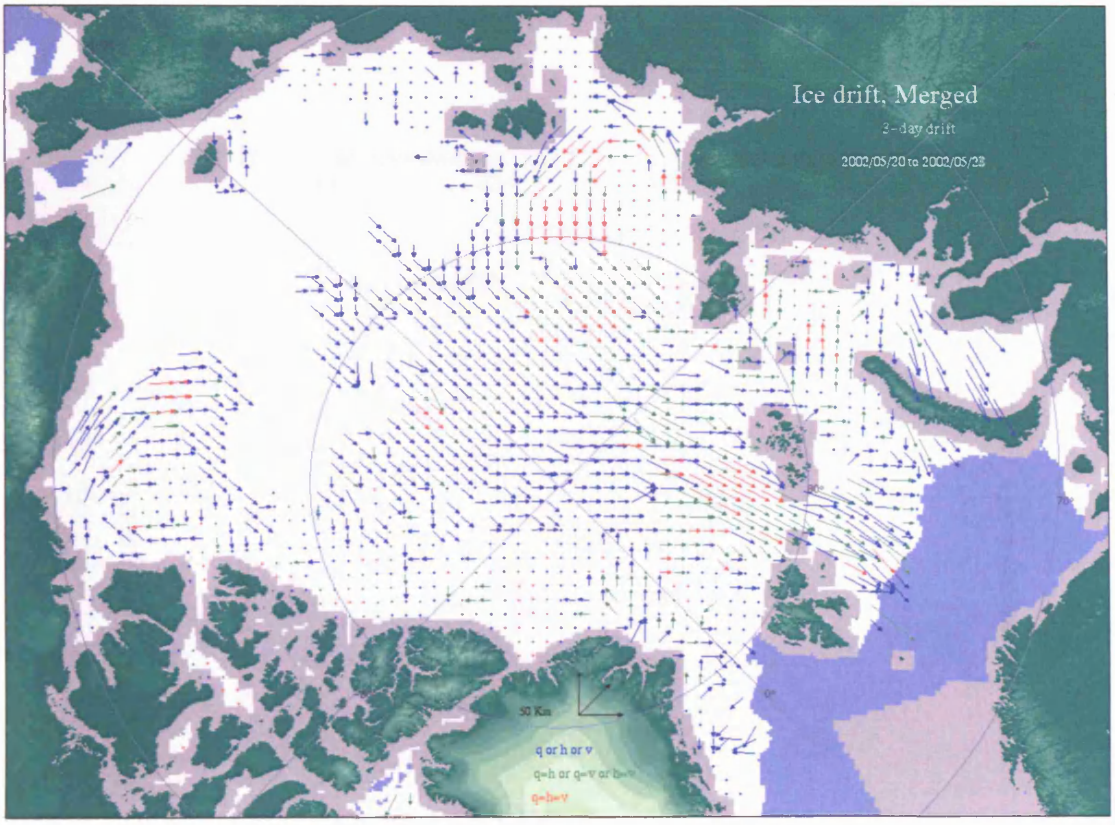

Figure 7.2: Sea ice drift velocities. The arrows show the 3-day drift between 20/05/02 and 23/05/02. [Ezraty & Piolle, 2004]

7.4) Region 1

Figure 7.3 shows the locations of the data points north of Greenland for the outbound and return passes on the 23rd May. The colour scale indicates the value of the offset at each of these points. The passes are separated by approximately 30 minutes.

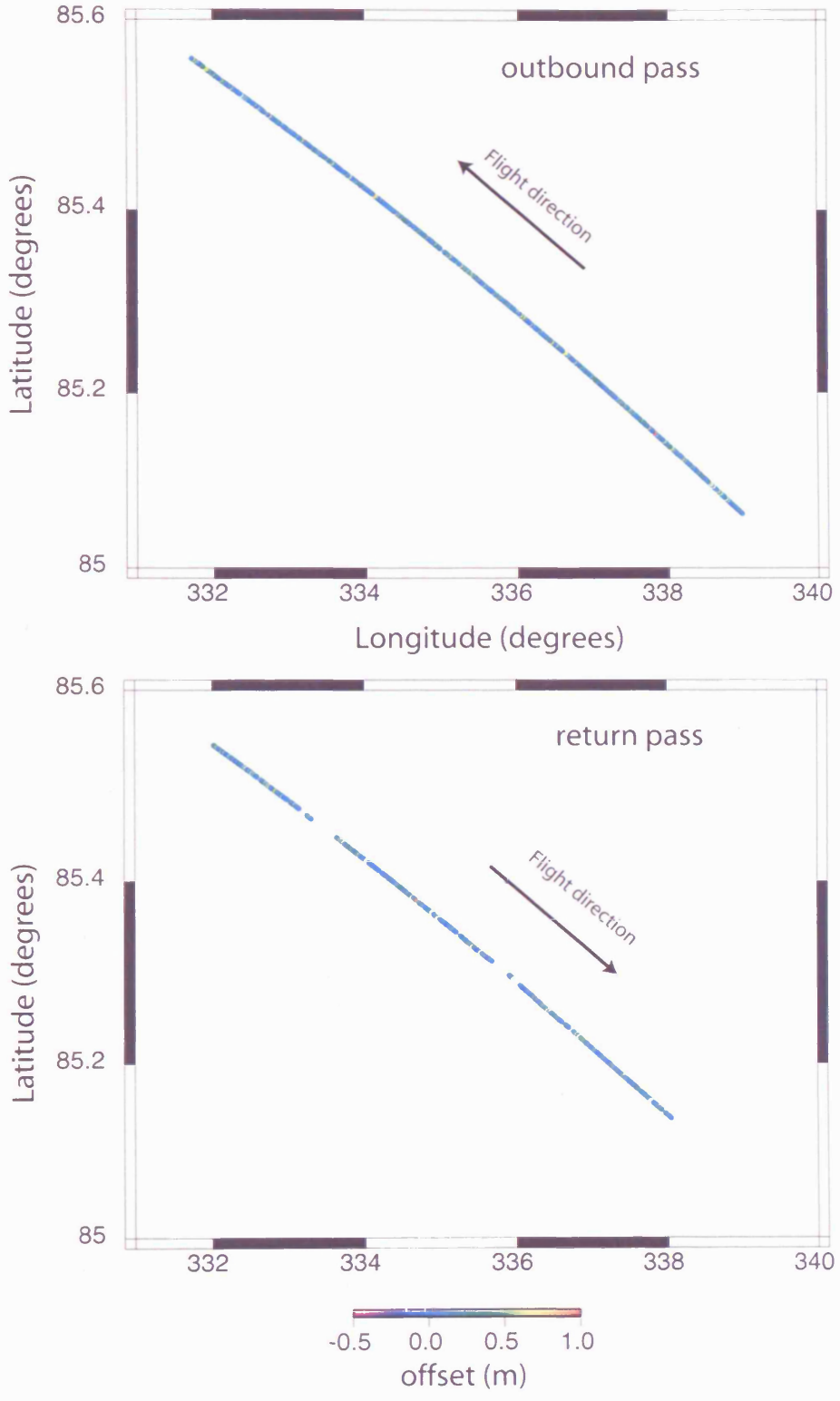

Figure 7.3: Region1, north of Greenland, offset between the simulated data and the real data.

The outbound and return passes are separated by 36 m with the return pass located at a slightly higher latitude than the outbound pass. From figure 7.2, we estimate that the ice would have drifted north by 50 m in the time between the passes. Therefore we estimate that the across track distance between passes was approximately 14 meters. Figure 7.4 shows the offset between the real and simulated data as a function of along track distance.

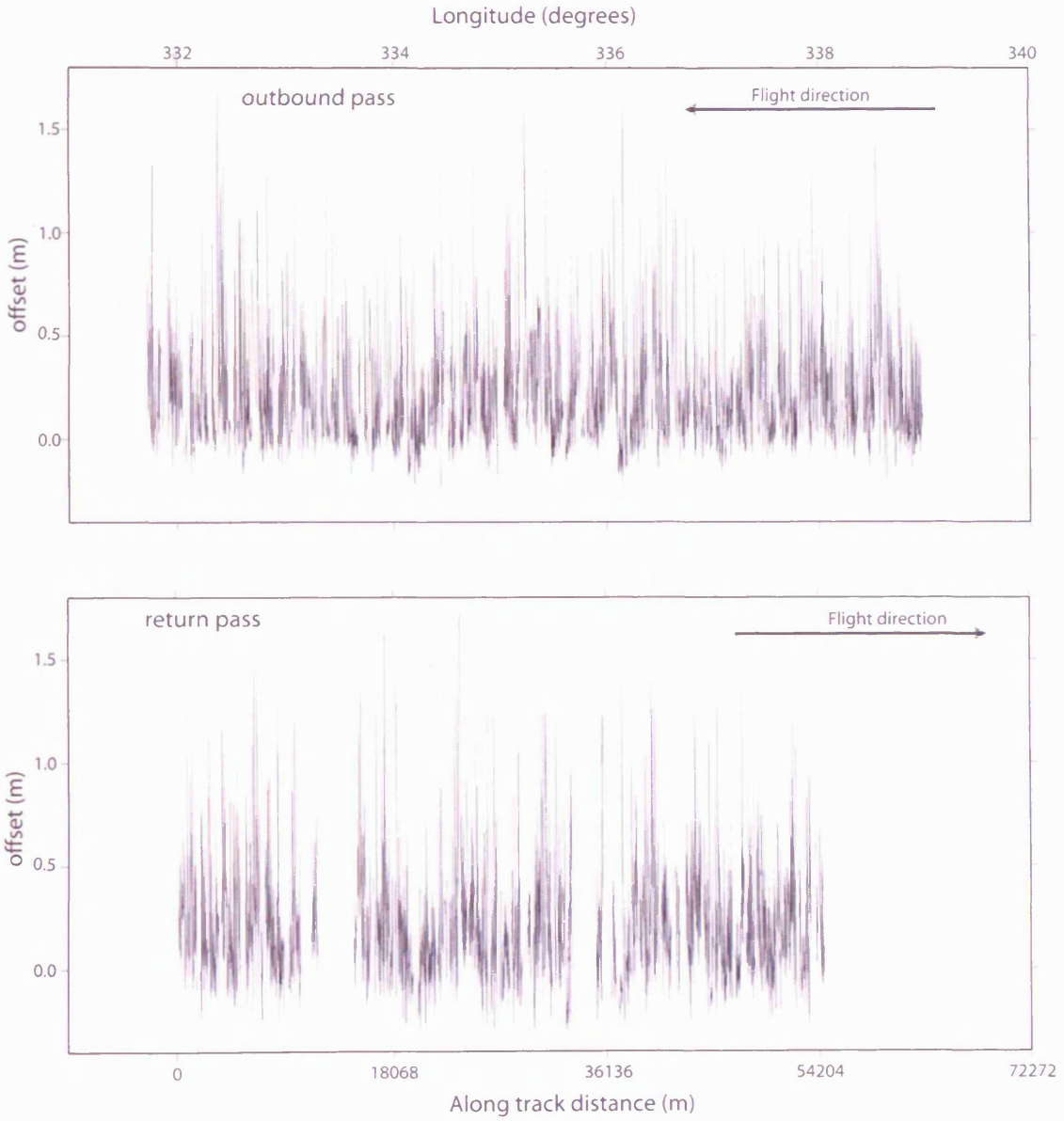

Figure 7.4: Region 1, north of Greenland, offset between the simulated data and the real data as a function of along track distance.

The average offset for the outbound pass is 0.187 m and its standard deviation is 0.267 m. The average offset for the return pass is 0.2 m and its standard deviation is 0.221 m. The correlation coefficient between the outbound and return pass is 0.126.

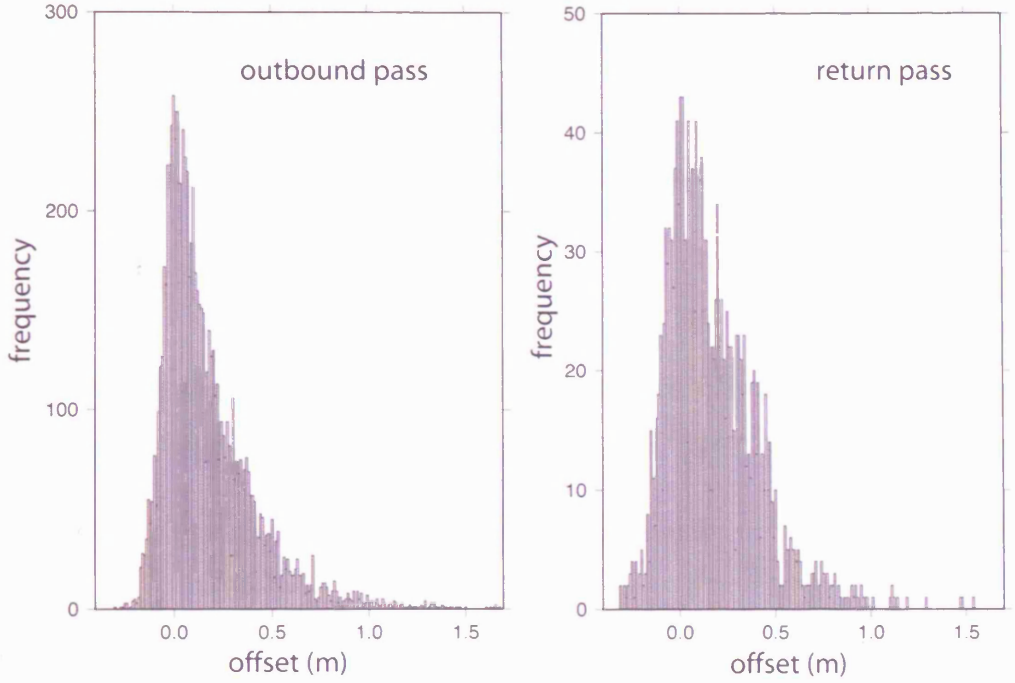

Figure 7.5: Region 1, offset frequency histograms.

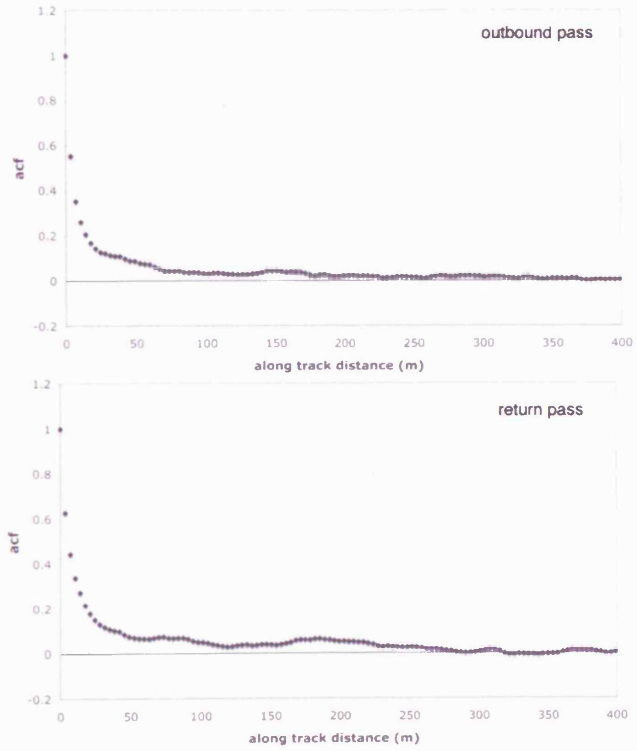

Figure 7.6: Region 1, the offset acf.

Figure 7.6 shows the acf for region 1. It shows that in the along track direction the offset between the radar and the laser de-correlates over a relatively short distance. The correlation coefficient (0.126) calculated for the data shown in figure 7.4 is the across track correlation coefficient, as the outbound and return passes were separated by approximately 14 m. It is interesting to note from figure 7.6, that the acf at 14 m is approximately 0.2, indicating that the offset in the along track direction de-correlates at approximately the same rate as the offset in the across track direction.

7.5) Region 2

Figure 7.7 shows the location of the data points and their offset, for region 2. The data were collected on the 20th May and separated in time by approximately 1 hour.

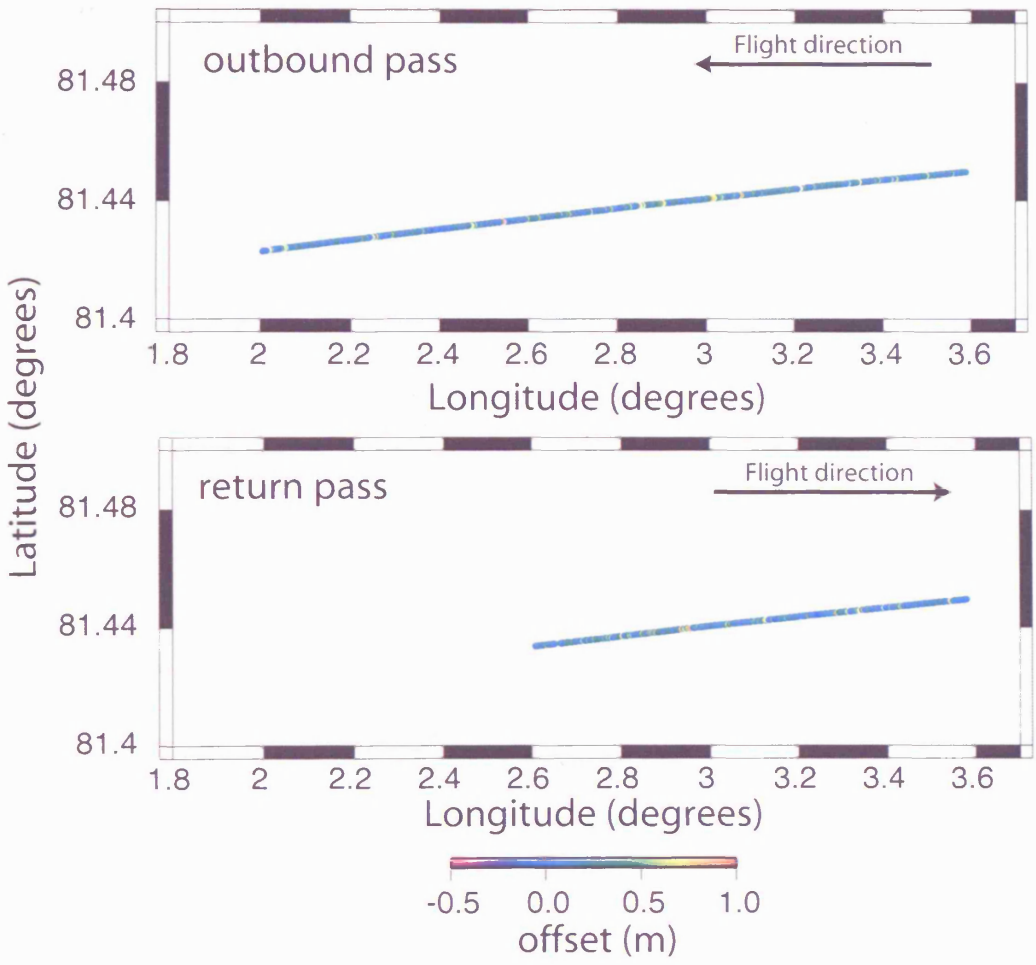

Figure 7.7: Region 2, west Fram Strait, offset between the simulated data and the real data.

The outbound and return passes are separated by 30 m with the outbound pass located at a slightly higher latitude than the return pass. Figure 7.2 suggests very little ice drift in this region, therefore we estimate that the across track separation between passes is 30 meters. Figure 7.8 shows the offset between the real and simulated data as a function of along track distance.

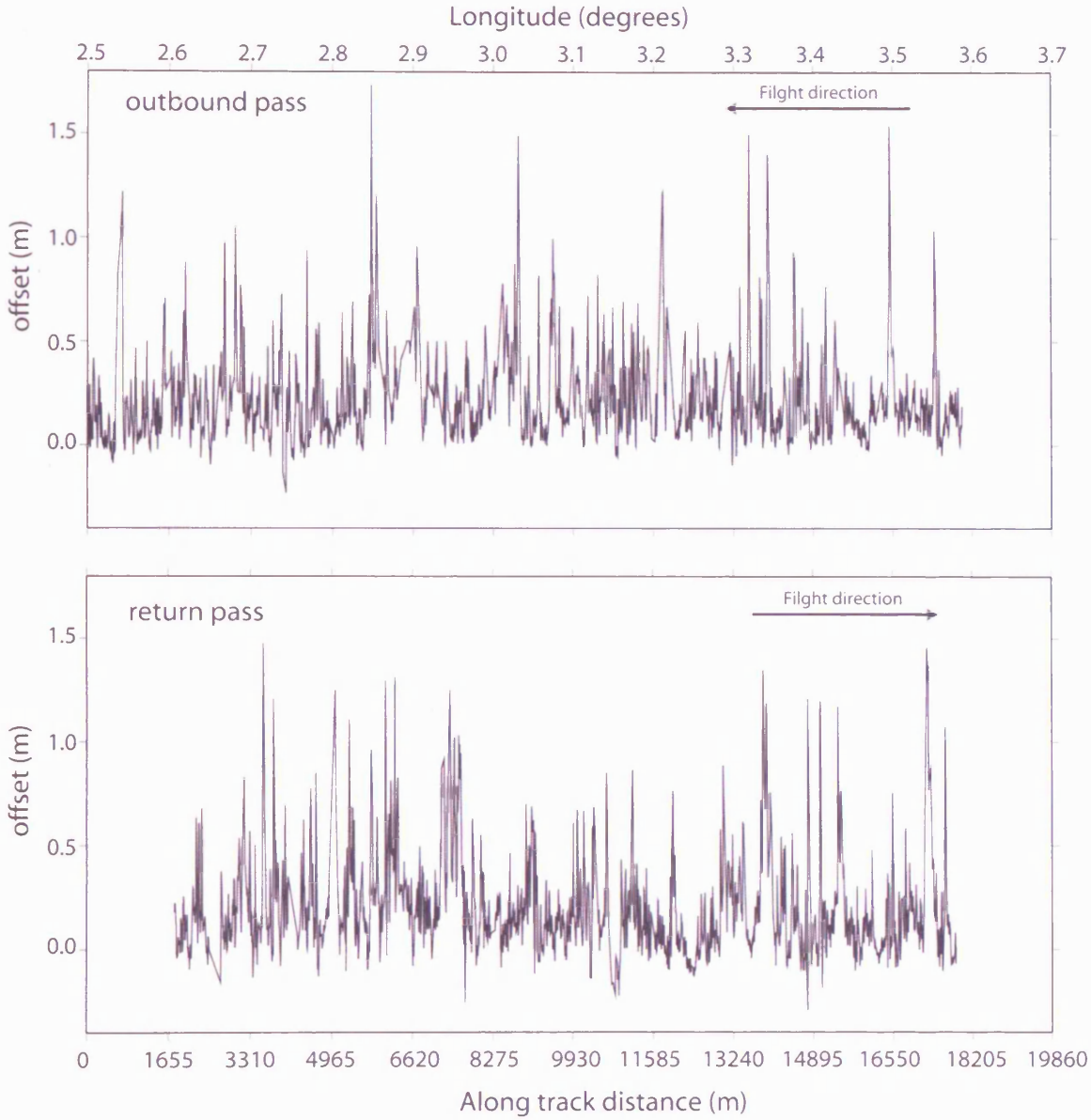

Figure 7.8: Region 2, west Fram Strait, offset between the simulated data and the real data as a function of along track distance.

The average offset for the outbound pass is 0.176 m and its standard deviation is 0.224 m. The average offset for the return pass is 0.260 m and its standard deviation is 0.223 m. The correlation coefficient between the outbound and return pass is 0.012.

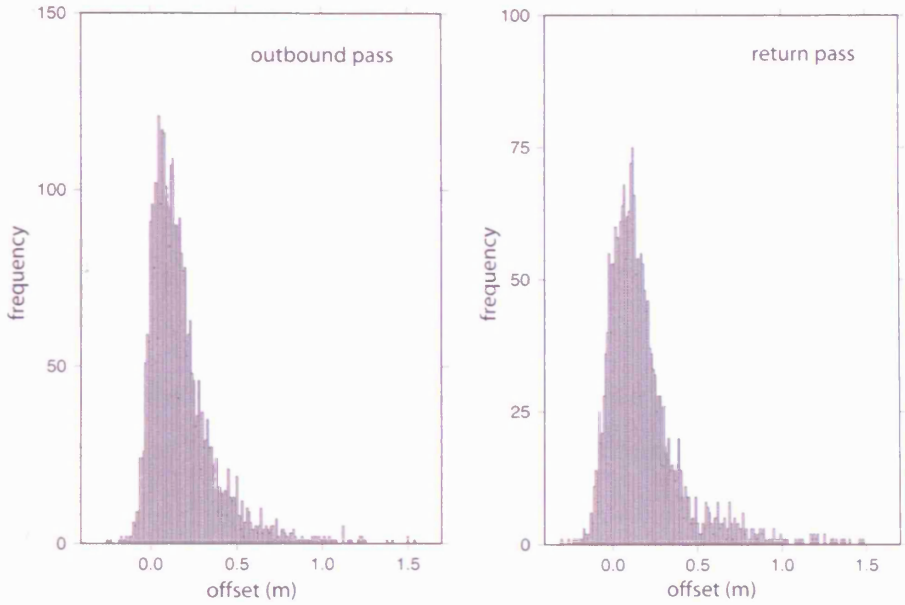

Figure 7.9: Region 2, offset frequency histograms.

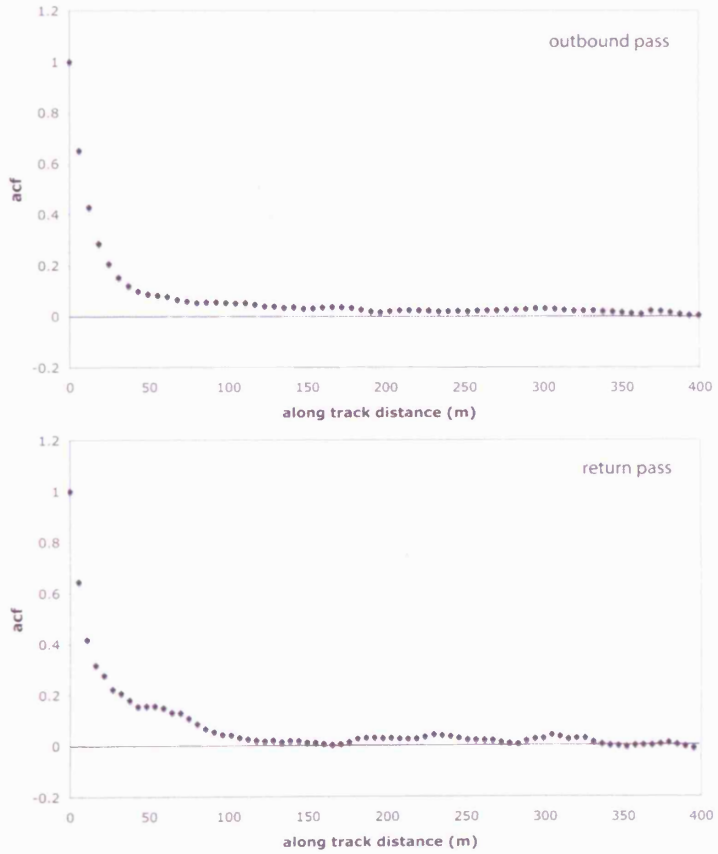

Figure 7.10: Region 2, the offset acf.

Figure 7.10 shows the acf for region 2. As for region 1, it shows that in the along track direction the offset between the radar and the laser de-correlates over a relatively short distance. The across track correlation coefficient calculated for the data shown in figure 7.8 is 0.012, with an across track separation between passes of approximately 30 m. From figure 7.10, that the acf at 30 m is approximately 0.15 (outbound pass) or 0.21 (return pass), which indicates that the offset in the across track direction de-correlates at a faster rate than the offset in the along track direction.

7.6) Region 3

Figure 7.11 shows the locations of the data points and their offset, for region 3. The data were collected on the 20th May and separated by approximately 2 hours.

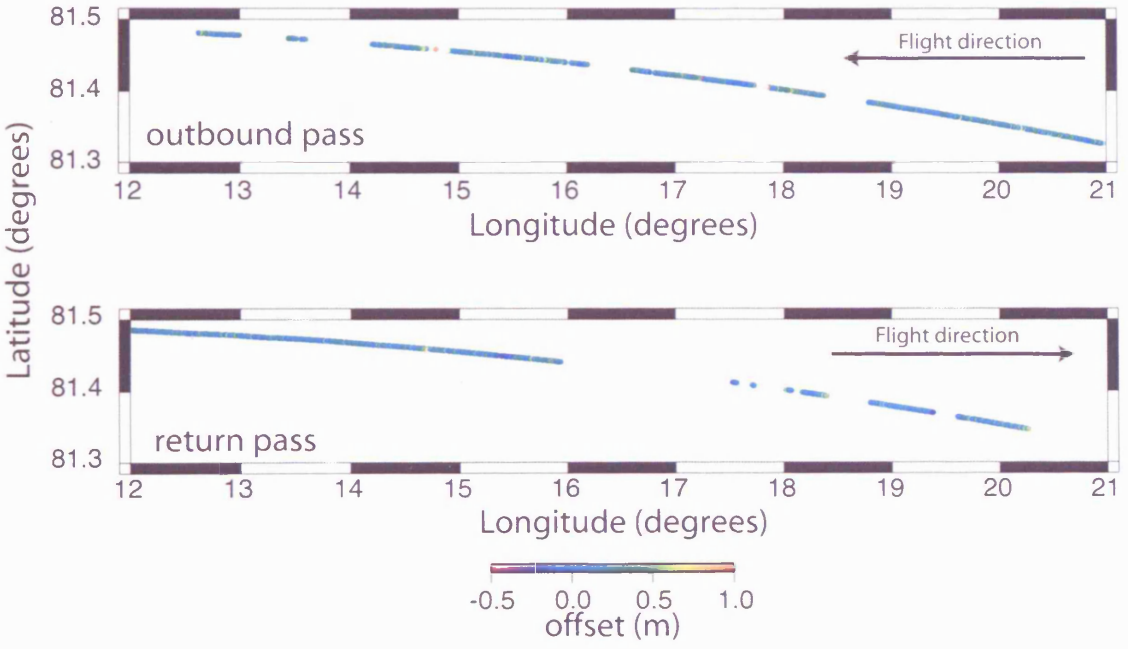

Figure 7.11: Region 3, east Fram Strait, offset between the simulated data and the real data.

The outbound and return passes are separated by 40 m with the outbound pass located at a slightly higher latitude than the return pass. Figure 7.2 suggests very little ice drift in this region, therefore we estimate that the across track separation between passes is 40 meters. Figure 7.12 shows the offset between the real and simulated data as a function of along track distance.

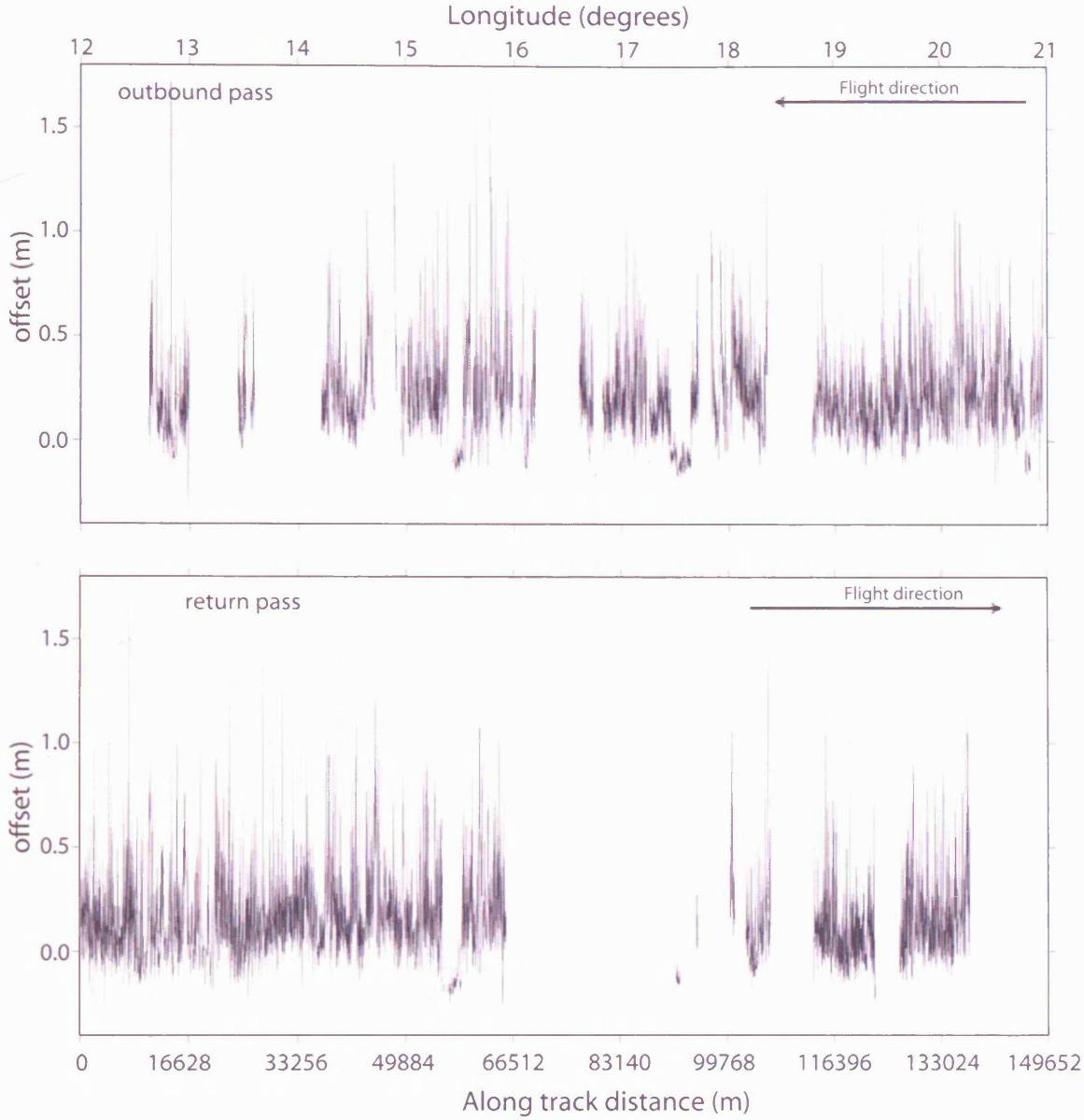

Figure 7.12: Region 3, west Fram Strait, offset between the simulated data and the real data as a function of along track distance.

The average offset for the outbound pass is 0.141 m and its standard deviation is 0.195 m. The average offset for the return pass is 0.239 m and its standard deviation is 0.213 m. The correlation coefficient between the outbound and return pass is 0.15.

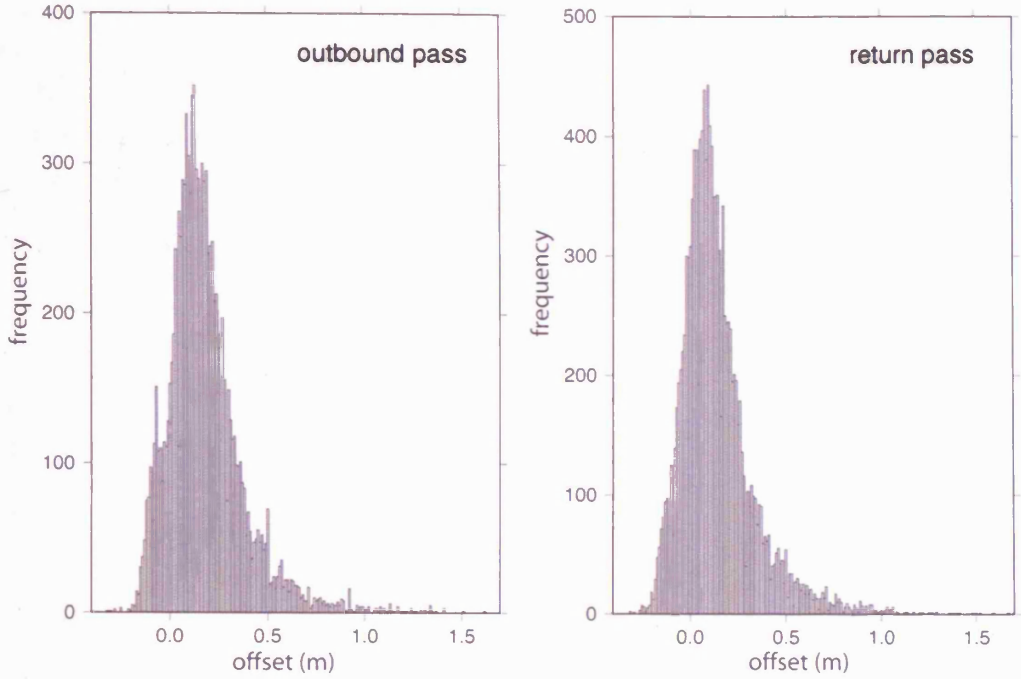

Figure 7.13: Region 3, offset frequency histograms.

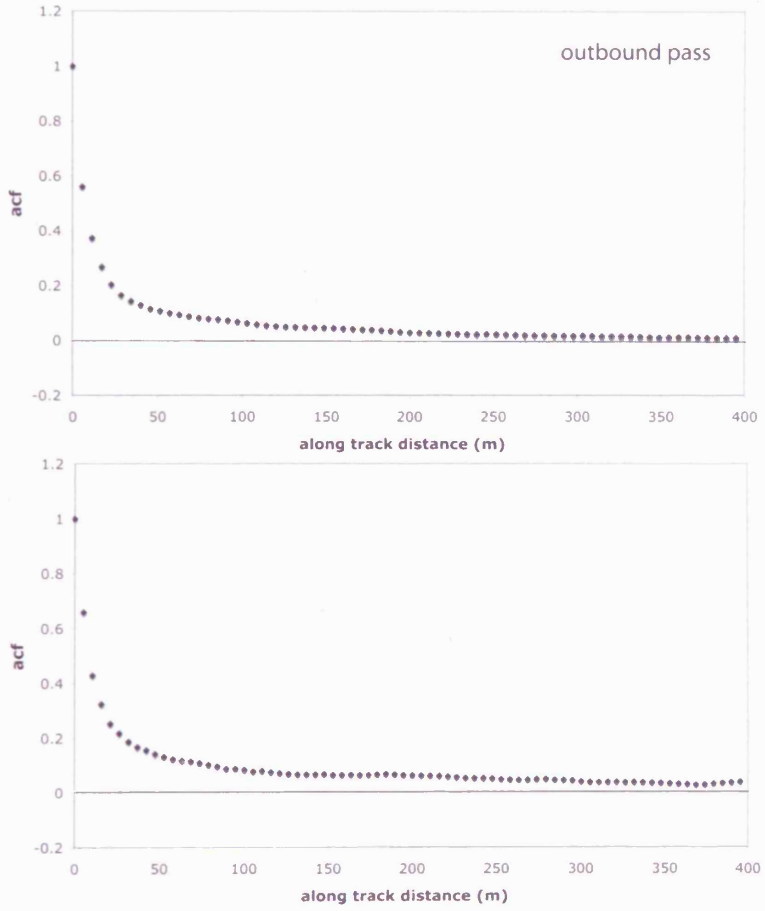

Figure 7.14: Region 3, the offset acf.

As this section of track contains many gaps we take a section that is continuous in both the outbound and return pass from figure 7.11, and repeat the correlation and acf calculations. Figure 7.15 shows the offset as a function of along track distance.

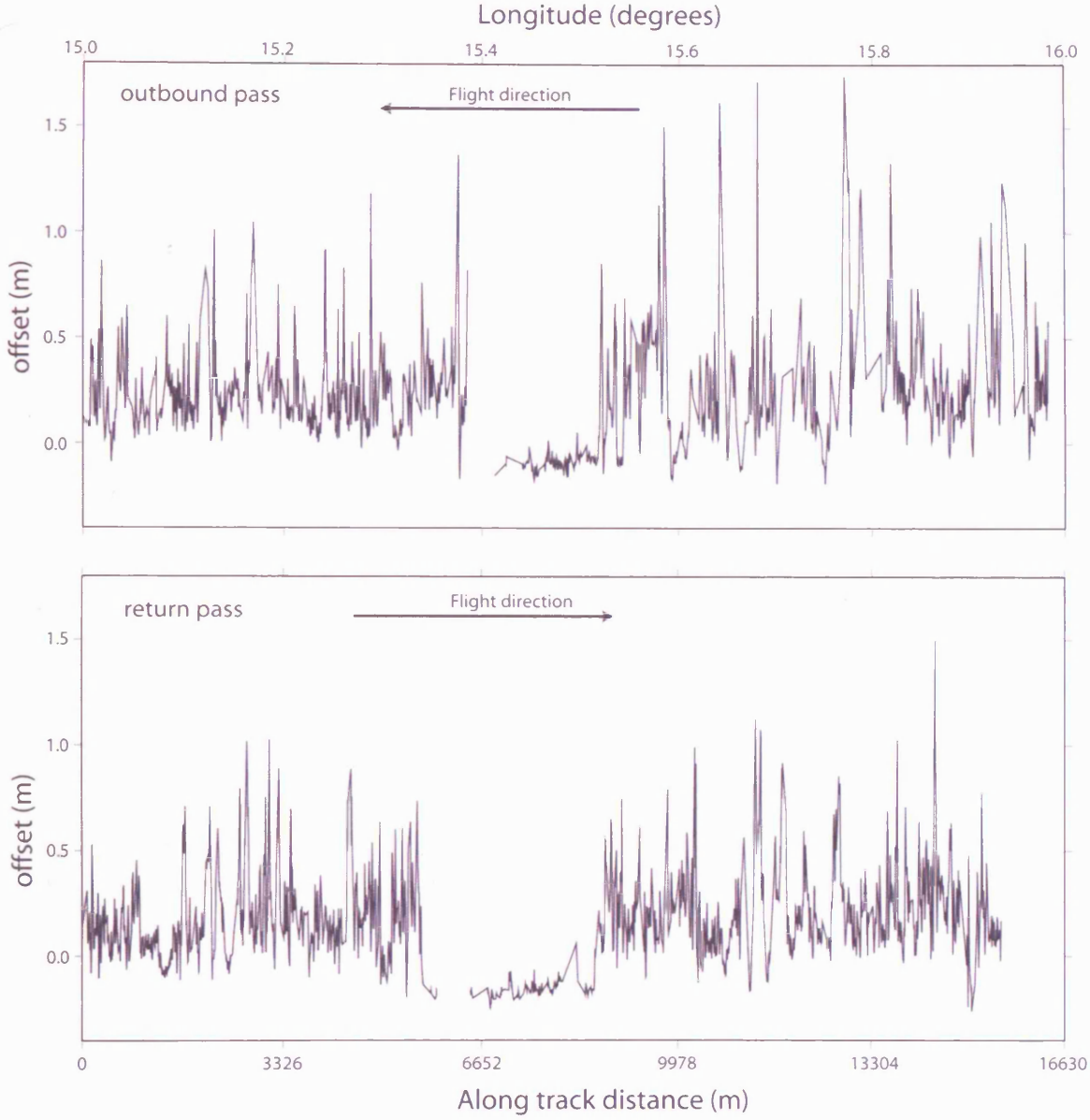

Figure 7.15: Region 3, west Fram Strait, offset between the simulated data and the real data as a function of along track distance.

The average offset for the outbound pass is 0.154 m and its standard deviation is 0.215 m. The average offset for the return pass is 0.260 m and its standard deviation is 0.266 m. The correlation coefficient between the outbound and return pass is 0.12.

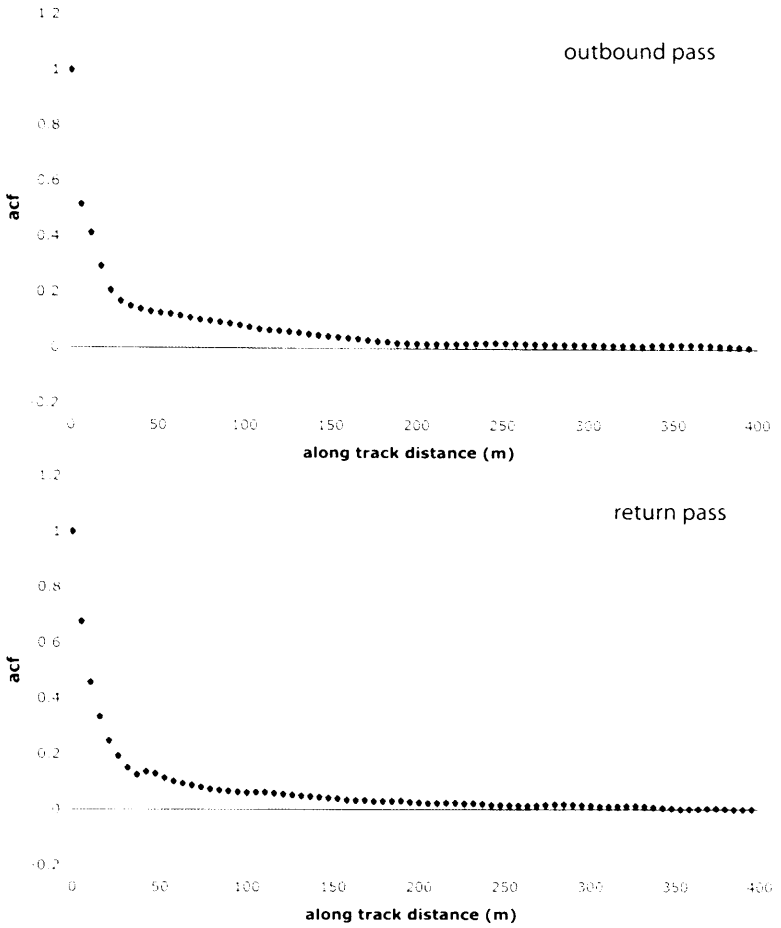

Figure 7.16: The acf for region3, 15° to 16° longitude.

Figure 7.16 shows the acf for region 3. As for regions 1 and 2, it shows that in the along track direction the offset between the radar and the laser de-correlates over a relatively short distance. The across track correlation coefficient calculated for the data shown in figure 7.15 (the short section of track) is 0.12 and for the data shown in figure 7.12 (the long section of track) is 0.15. The across track separation between passes is approximately 40 m. From figure 7.16, that the acf at 40 m is approximately 0.14 (short section) and from figure 7.14, the acf at 40 m is approximately 0.15 (long section of track). Therefore, as for region 1, the offset in the along track direction de-correlates at approximately the same rate as the offset in the across track direction.

7.7) Measured snow depth distribution over sea ice

In-situ snow depth data was not collected during LaRA so we cannot say that the offsets we see between the laser and the radar are due to the snow layer. However, we can compare the offset to snow depth measurements from other field experiments to investigate whether the offset has a similar size and distribution to measured snow depth.

Figures 7.17 and 7.18 show measured snow depth distributions. Figure 7.17 is taken from Colony et al., (1998), and shows snow depth measurements from the Russian North Pole drifting station program. Stations were situated at locations over the Arctic basin (see figure 1, Colony et al., 1998) and the program ran between 1954 and 1991. Figure 7.18 is taken from Sturm et al., (2002), and shows snow observations taken between October 1997 and October 1998 in the Beaufort Sea as part of the Surface Heat Budget of the Arctic Ocean (SHEBA) experiment.

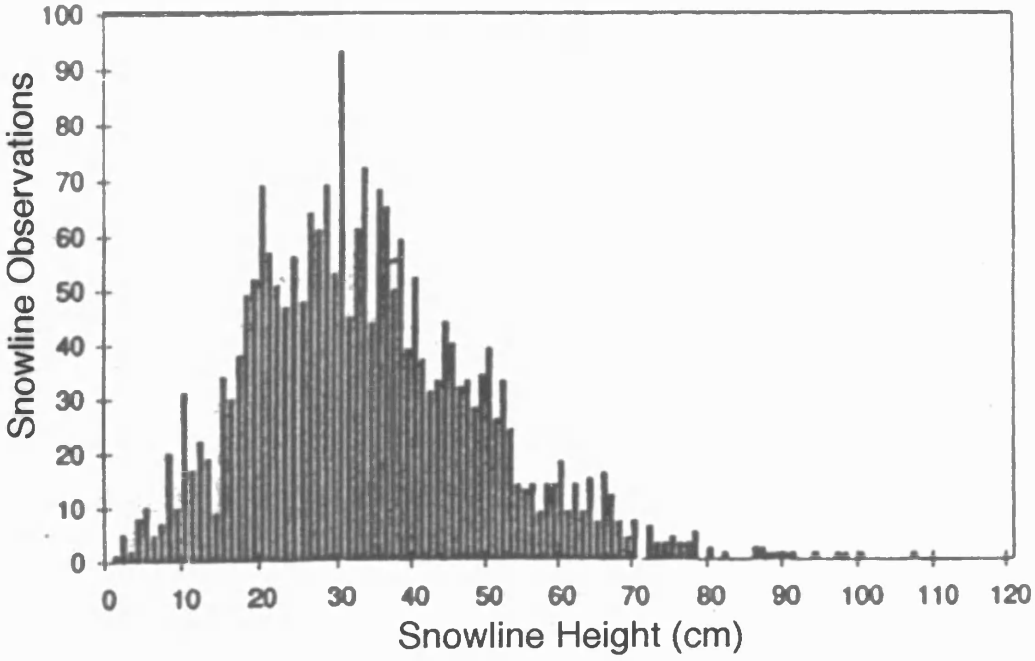

Figure 7.17: Distribution of snow heights from snow lines in April. The mean value is 31.4 cm and the standard deviation is 15.5 cm. [Coloney et al., 1998]

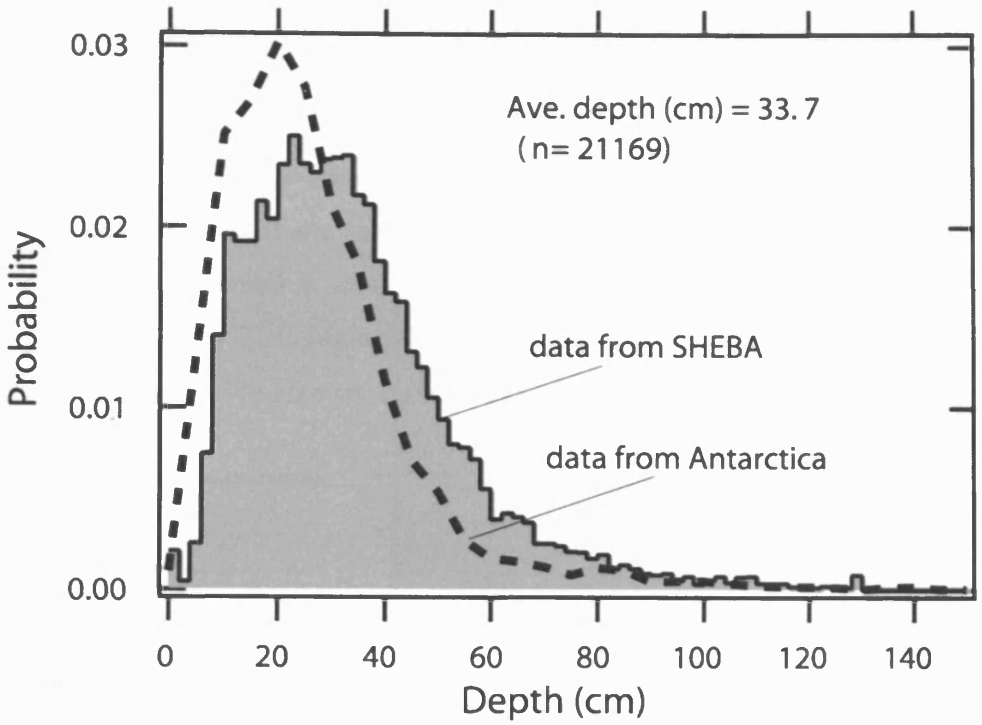

Figure 7.18: The probability distribution function (PDF) for all SHEBA snow depths, compared with a PDF for snow on ice in the Bellinghausen, Ross and Admundsen seas in the Antarctic. The mean depth is 33.7 cm and the standard deviation is 19.3 cm. [Sturm et al., 2002]

The mean snow depth in figure 7.17 is 0.314 m and 0.337 m in figure 7.18. The mean offset is 0.20 m. Although it is lower than the mean snow depths, is comparable to the snow depth values shown in figures 7.17 and 7.18. The shape of the offset distribution shown in figures 7.5, 7.9 and 7.13 is similar to the PDF of snow depths in figure 7.18. The distributions have a steep rise to the peak and a slower falloff at higher snow depths. Figure 7.17 also has a similar falloff at higher snow depths but has a shallower rise to the peak.

In addition Sturm et al., (2002) examine the spatial variability of the snow depth. They found that snow depths over a flat section of multi year ice varied by a factor of six over distances as short as 20 m. Further investigation showed that the snow depth varied at 20 m regardless of the ice type. The correlation coefficients and acf plots of the offset have also shown short correlation lengths in both the along track and across-track directions, similar in size to those found by Sturm et al., (2002).

7.8) Offset maps for the LaRA field campaign

Figures 7.19 and 7.20 show the offset for the flights taken on the 20th May and the 23rd May respectively. The offsets are plotted with the daily maximum 2 m temperatures from ECMWF (see chapter 4, section 4.7). Although the temperature contours from the 23rd are approximately 7° C higher than those from the 20th, the values of the offset on both days are similar. We also see no regional variation in the offset.

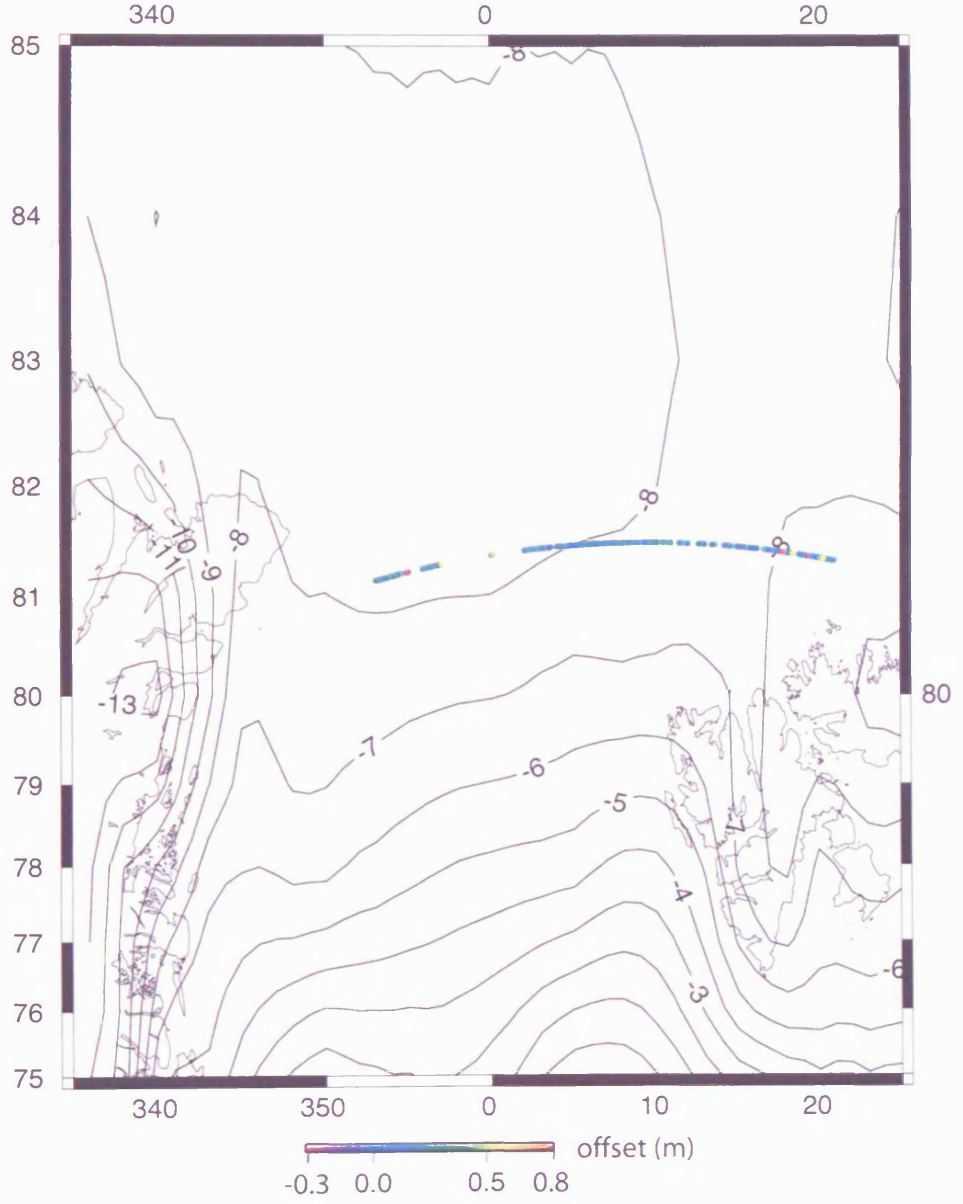

Figure 7.19: Offset map showing all data from the 20th May 2002, along with contours showing the average maximum daily 2 m air temperature from ECMWF.

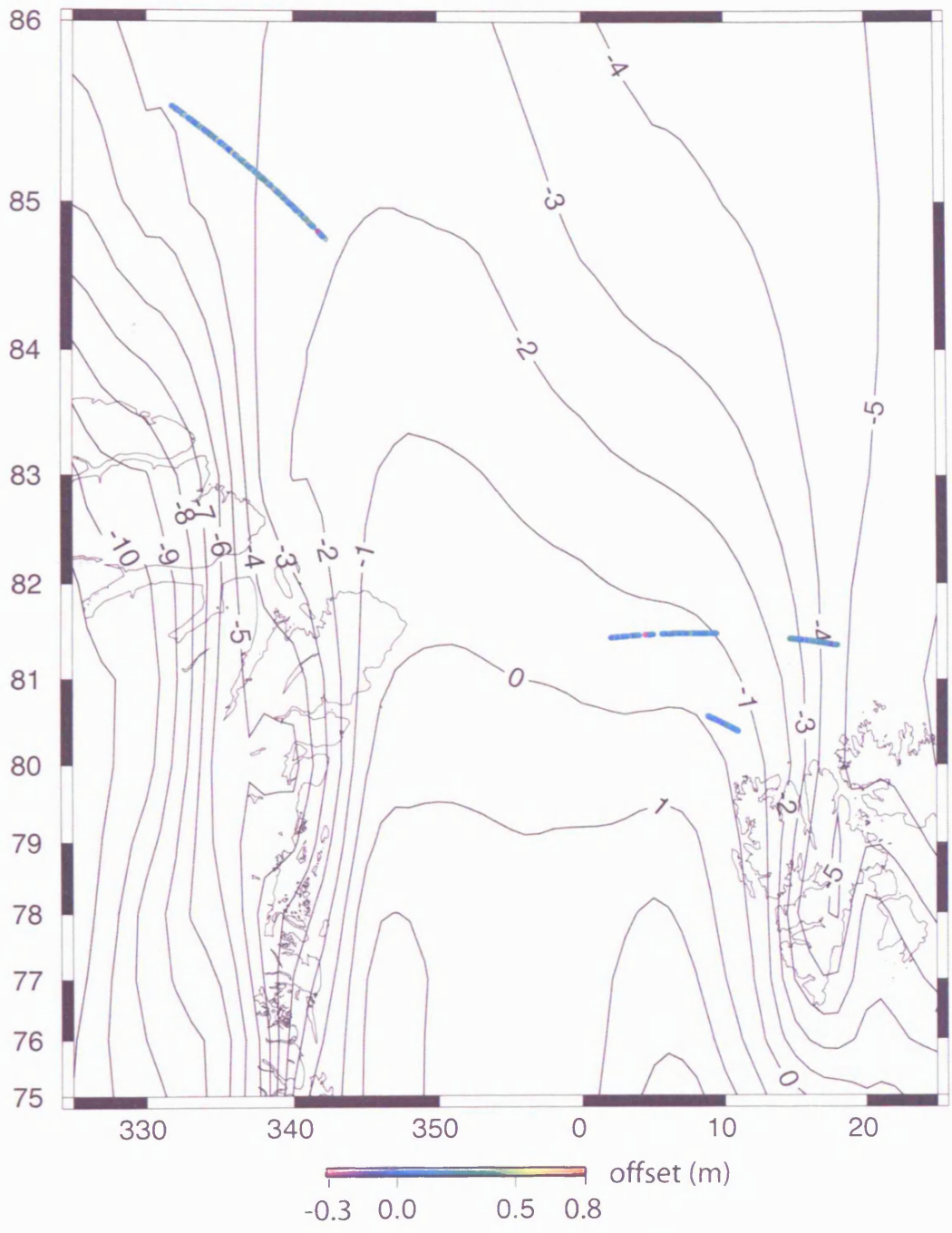

Figure 7.19: Offset map showing all data from the 23rd May 2002, along with contours showing the average maximum daily 2 m air temperature from ECMWF.

7.9) Evaluation of the UCL D2P re-tracker

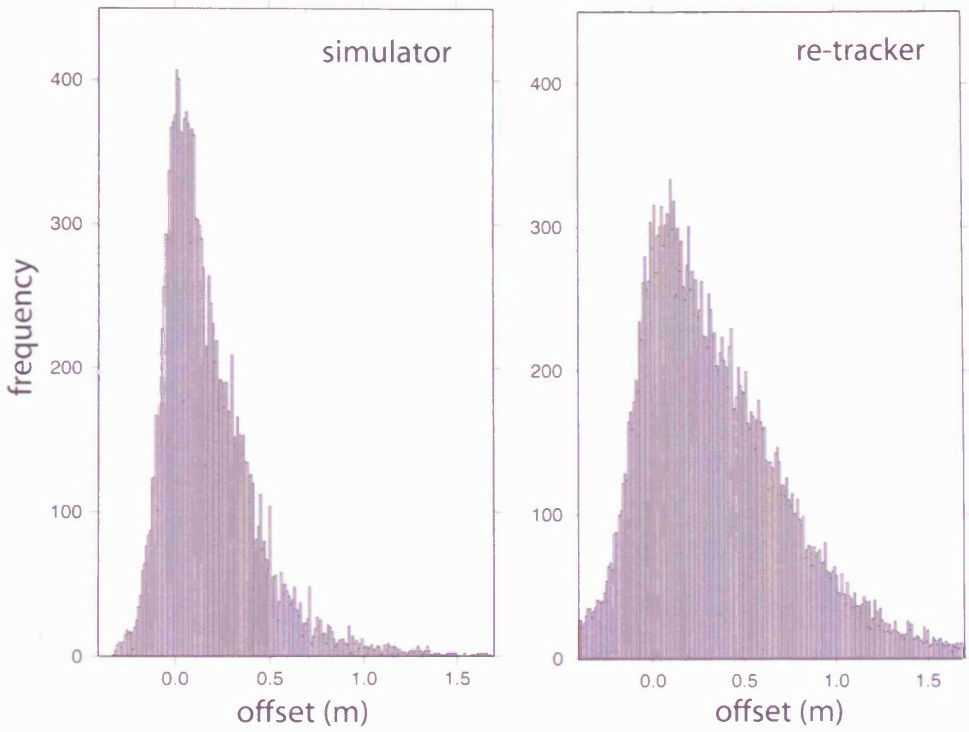

Figure 7.21: Histogram of offsets from the simulated data and the re-tracked data from region 1.

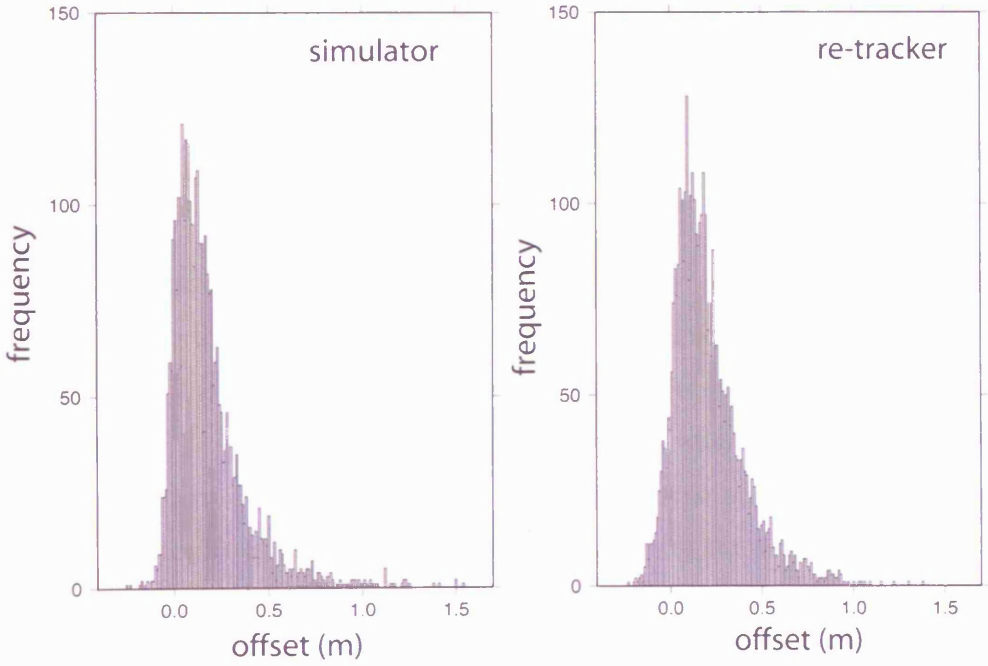

Figure 7.22: Histogram of offsets from the simulated data and the re-tracked data from region 2.

Figures 7.21 and 7.22 show examples of the distribution of offsets calculated from the simulator (simulated echo minus real echo) and from the re-tracker (average laser elevation over the D2P footprint minus the re-track radar elevation estimate). Both figures show that the offset estimates from the re-tracker have a wider distribution than the offset estimates from the simulator. This suggests that the re-tracker is both overestimating and underestimating the elevation of the D2P data. Figure 7.23 shows a non-typical echo (blue) and the re-tracking function fit to that echo (red).

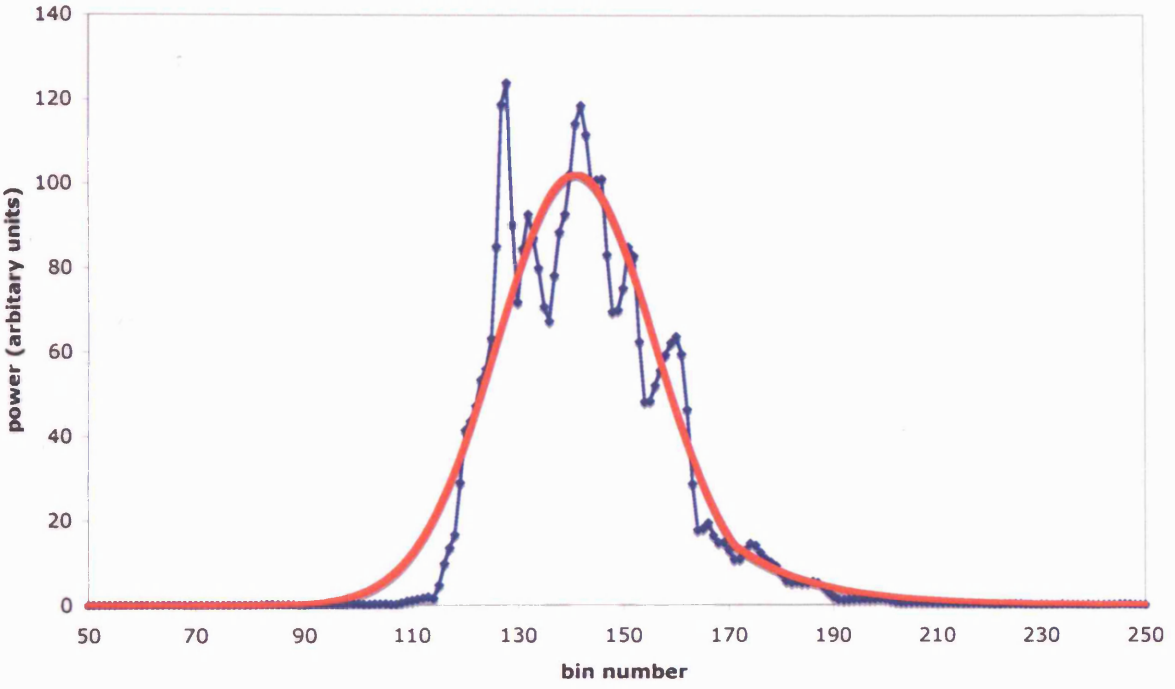

Figure 7.23: Example of the re-tracking function fit to a non-typical echo.

The re-racking function tends to place its self at the centre of the echo. It is the leading edge of the return that gives us an elevation estimate. Therefore, when re-tracking a non-typical echo, the elevation estimate is unrealistic. For example, the re-track echo shown in figure 7.23 has an elevation estimate of 14 m, where the surrounding ice has an elevation of 20 m. Non-typical echoes result from large values of aircraft roll (see figure 5.26, chapter 5) or from rough surfaces. Figure 7.24 shows that, even if we filter out all points with a roll greater than 5°, the re-tracked data will still contain unrealistic elevation measurements due to not-typical echoes from rough surfaces.

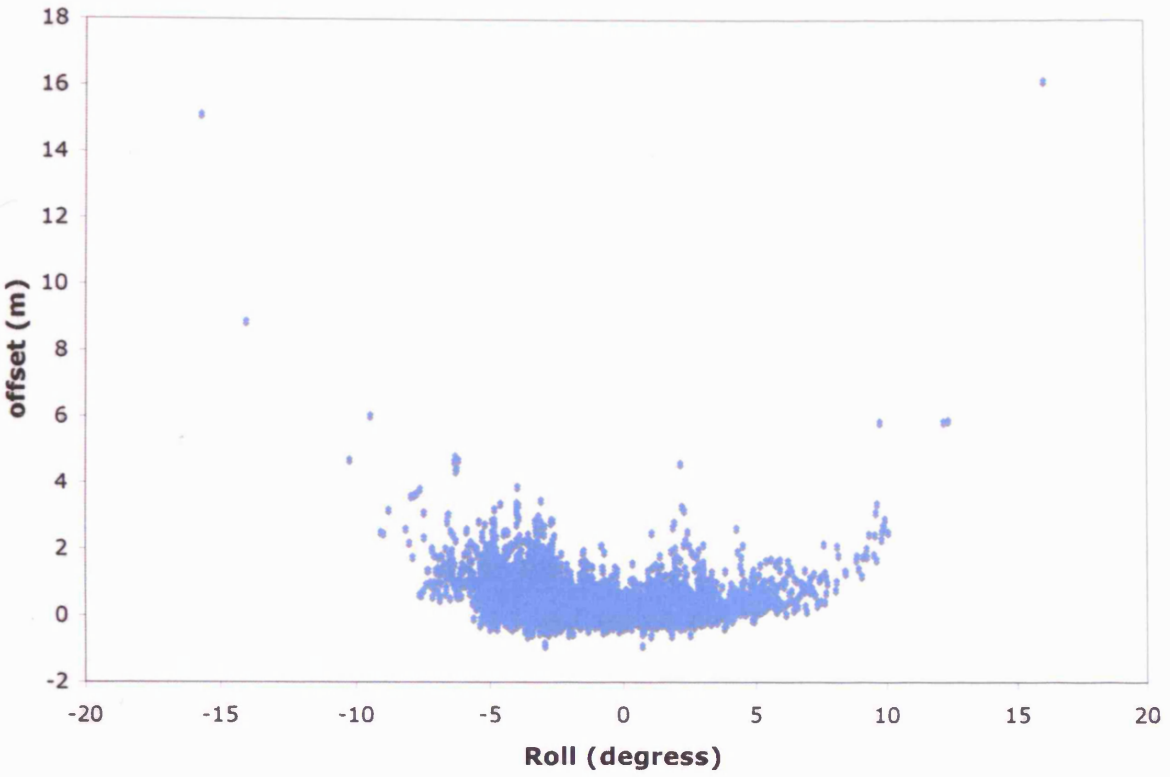

Figure 7.24: The difference (offset) in elevation between the re-tracked radar echoes and the laser elevation estimates, as a function of roll.

Future re-trackers for airborne D2P data over sea ice should take into account the variability of the D2P echo shape. If the re-tracker uses an interpolating function over the whole return, the roll of the aircraft should be a parameter of that function. Alternatively, a leading edge re-tracker could be used. The simulator provides a useful tool for designing a new re-tracker. We have already shown the position of the re-track point for a D2P echo over a flat surface, with the antenna pattern centred at nadir (figure 5.40, chapter 5). By changing the surface roughness and the location of the centre of the antenna pattern we can investigate how the echo shape and the re-track point change.

7.10) An estimate of the impact of using the laser/radar difference on the ice thickness calculation

In this section we assume that the laser-radar difference is equal to snow depth and we take the error on the laser-radar derived snow depth to be equal to the accuracy in determining the difference between the laser and the radar elevations (± 0.07 m). Applying this error in snow depth to the ice thickness error estimates from radar

altimetry (equation 1.3) and laser altimetry (equation 1.5), results in the error decreasing from ± 0.45 m to ± 0.37 m (a decrease of 0.08 m) for the radar case, and the error decreasing from ± 0.78 m to ± 0.55 m (a decrease of 0.23 m) for the laser case.

LaRA was designed to under-fly ERS2 (see section 3.3.11 chapter 3). Figure 7.25 a) shows a section of coincident LaRA/ERS2 track where the airborne laser (elevations shown) and radar altimetry data are available and ERS2 sea ice freeboard estimates are available (red crosses). 7.25 b) shows the snow depth at each of the ERS2 freeboard locations. The Climatology snow depth is inferred from Warren *et al.,* (1999) and the LaRA snow depth is calculated by taking a weighted average of the difference between the laser and radar elevations within the ERS footprint. 7.25 c) shows the sea ice thickness calculated using equation 1.1 and taking the ERS2 freeboard estimate, the constant values for water and sea ice density (given in section 1.5.1, chapter 1), the snow density from Warren *et al.,* (1999) and the snow depth either from the climatology or from the LaRA data. b) shows that, while the climatology estimate of snow depth is relatively constant across the section of track, the LaRA derived snow depths are higher than the climatology on the left hand side of the figure and lower than the climatology on the right hand side of the figure. This suggests that spatial variability in snow depth may exist which is not resolved by the climatology, in-situ snow depth measurements would be useful to confirm this. In c) we see the same relationship between with the sea ice thickness estimates derived from the two different snow depth estimates. However, without in-situ snow depth and ice thickness data, we cannot say which method provides the more accurate estimate of sea ice thickness.

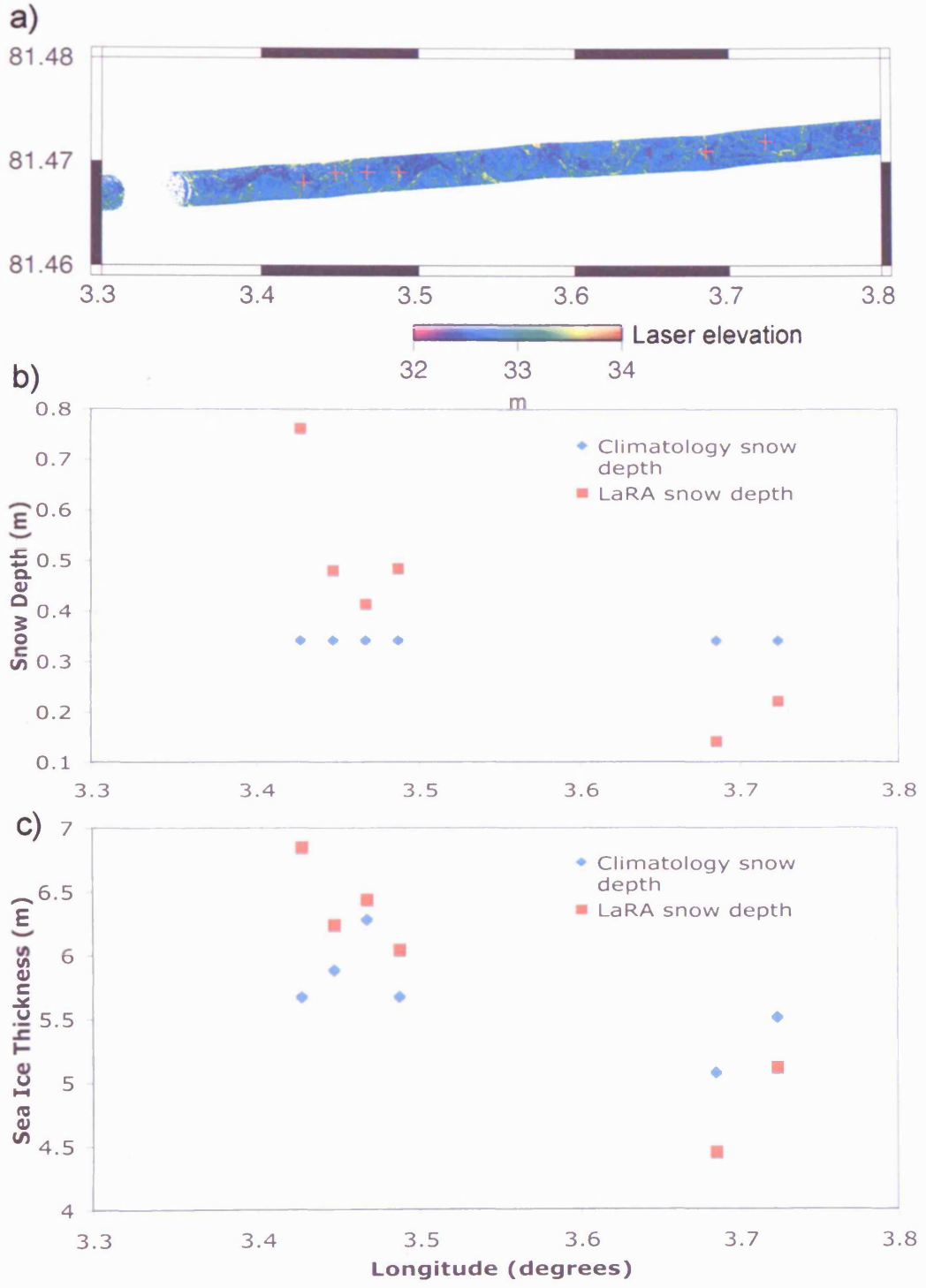

Figure 7.25: a) shows a section of coincident LaRA/ERS2 track with the laser elevations and ERS2 sea ice freeboard estimates (red crosses). 7.25 b) shows the snow depth at each of the ERS2 freeboard locations from the climatology and from the LaRA laser/radar difference. 7.25 c) shows the sea ice thickness calculated using the snow depth from either the climatology or from the LaRA data.

7.11) Summary

- We have shown that the laser elevations are consistently higher than the radar elevations over snow covered sea ice. This is consistent with the hypothesis that the radar penetrates to the snow/ice interface. However, with out in-situ data we cannot confirm this.

- We have shown that the elevation difference between the laser and the radar is consistent with observed snow depth. And that the distribution of the offset compares well to snow depth distribution.

- We have shown that the offset between the laser and the radar de-correlates over short distances (50 meters or less), in both the along track and across track directions. This has implication for planning future field campaigns, in that extreme care must be taken, when comparing measurements for different platforms to ensure that they are looking at the same section of ice.

- We have, perhaps surprisingly, seen no regional variation in the offset.

- We have shown that the UCL D2P re-tracker over-estimates the offset between the laser and the radar when re-tracking non-typical echoes. We have suggested that the re-tracker could be re-designed, using the simulator to explore the effects of surface roughness and the location of the antenna pattern, on the leading edge of the return and the re-track point.

- We have shown that if we assume an error in snow depth of ± 0.07 m (i.e. snow depth is equal to the laser elevation minus the radar elevation) then the over all error in ice thickness, derived from a satellite radar altimeter, decreases from ± 0.45 m to ± 0.37 m (a decrease of 0.08 m) and the error in ice thickness derived from a satellite laser altimeter, decreases from ± 0.78 m to ± 0.55 m (a decrease of 0.23 m).

8) Conclusions

8.0) Introduction

In this final chapter we summarise the work presented in this thesis. In section 8.1 we state the achievements of this thesis. In section 8.2 we assess the methods used in this thesis. In section 8.3 we give suggestions for future field campaigns based on what we have learnt from LaRA. Finally, in section 8.4 we suggest directions for future work.

8.1) Achievements

- We have completed the first quantitative comparison of coincident airborne radar and laser altimetry over sea ice.

- We have estimate the difference in elevation estimates from a radar and laser altimeter with and accuracy of ± 0.07 m.

- We have shown for the first time that the laser elevations are consistently higher than the radar elevations over snow covered sea ice, which is consistent with the hypothesis that the radar penetrates to the snow/ice interface.

- We have shown that the differences in the elevations between the laser and the radar are consistent with observed snow depth. And that the distribution of the offset compares well to snow depth distribution from in-situ data.

- We have shown that if we assume an error in snow depth of ± 0.07 m (i.e. snow depth is equal to the laser elevation minus the radar elevation) then the over all error in ice thickness, derived from a satellite radar altimeter, decreases from ± 0.45 m to ± 0.37 m (a decrease of 0.08 m) and the error in ice thickness derived from a satellite laser altimeter, decreases from ± 0.78 m to ± 0.55 m (a decrease of 0.23 m). In-order to validate sea ice models, we require basin wide ice thickness measurements with an accuracy of ± 0.5 m, in-order to analyse trends in sea ice thickness we must be-able to detect changes in sea ice thickness of 4

cm per year on a basin wide scale. Therefore, while we can use satellite radar altimetry estimates of sea ice thickness to validate sea ice models, the error on the ice thickness estimation from both satellite radar and laser altimetry must be reduced further in-order determine trends in sea ice thickness with confidence.

- We have shown that the offset between the laser and the radar de-correlates over short distances (50 meters). This has implications for planning future field campaigns, in that extreme care must be taken when comparing measurements from different platforms to ensure that they are looking at the same section of ice.

- We have provided valuable insights into the complexities of combing laser and radar measurements over sea ice from an airborne platform, and highlighted the problems and solutions of the task.

- We have developed and assessed two new methods, the UCL D2P re-tracker and the UCL D2P radar simulator, to compare coincident data from different instruments that measure different surfaces.

8.2) Assessment of methods

In chapter 5 we presented two methods for analysing coincident airborne laser and radar altimetry.

The first of these methods was the UCL D2P re-tracking algorithm based on the typical shape of a D2P return. We then averaged the laser elevation data over the radar footprint and compared the offset between the two measurements. The re-tracker provided a useful first look at the data and suggested that the laser and radar were measuring different surfaces. However, although the re-tracker gives similar offset estimates to the simulator when re-racking typical echoes, it gives unrealistic radar elevations, and therefore large offsets, when re-tracking non-typical echoes. This is due to the fact that the re-tracker cannot account for varying topography and, in its present form, does not account for the roll of the aircraft.

The second method was a radar simulator. The simulator provided a new method to compare two coincident data sets collected by different instruments. This was achieved by generating a surface model from the laser data, which was then used to synthesise the radar echo. The simulator created both typical and non-typical echoes and reproduced the effects of roll, pitch and variable surface roughness. Difference between the simulated data and the real data were due to the fact that we set a constant polar response over all ice types. We have shown that the range offset between the simulated and real data is not related to the pitch, roll and altitude of the aircraft. This adds weight to the argument that the offsets we see between the two instruments are of geophysical origin. We have shown that the calibration of the radar is likely to have drifted between the calibration flights and the LaRA flights, which occurred 17 days after the calibration flights. This cannot be confirmed as the D2P was not re-calibrated during LaRA. We think it is of paramount importance that the radar is regularly calibrated during the field work, as well as before and after.

8.3) Suggestions for future field campaigns

The work presented in this thesis has highlighted a number of issues related to the collection of field data over Arctic sea ice. Here we summarise these issues and suggest ways in which the data collection could be improved in future field campaigns.

8.3.1) Calibration of the radar

All instruments should be calibrated before and after the flights. Calibration of the laser altimeters was performed before and after each flight, however the radar altimeter was calibrated at the Wallops Flight Facility, in Virginia, USA, 17 days before the flights in the Arctic and no subsequent calibration was performed. Our analysis shows a possible offset in the radar calibration, which highlights the fact that the radar should be calibrated before and after each flight to reduce uncertainty in the elevation estimates. We suggest that, apart from using a GPS truck survey of the runway to calibrate the data as described in chapter 5, corner reflectors could also be placed at known locations on snow covered sea ice to calibrate the radar and to gain further insights into the degree of penetration into the snow layer. For studies comparing measurements from laser and radar altimeters it is important that two instruments can be cross calibrated.

Therefore both instruments should be calibrated over the same known surface (i.e. a runway).

8.3.2) The laser altimeters

During LaRA the P3 carried two laser altimeters, ATM2 operated in profiling mode and ATM3 operated in scanning mode. During our analysis we only used data from ATM3. The reason for this was that we saw differences in the fore and aft scans due to errors in the INS value of the aircraft pitch. As the fore and aft scans were effected equally and oppositely by the pitch error, we could correct the data for the error. However, it was not clear if these errors were present in the ATM2 data, and because we wanted to average the laser data over the radar footprint or create a surface grid, the data from ATM2 was not used. In future it would be better to have both lasers operating in scanning mode so that all of the data could be utilised.

It would also be useful to use a laser that does not penetrate into the water column such as the 904 nm laser used by Hvidegaard and Forsberg (2002). Laser elevation estimates over open water would provide extra tie points between the radar and the laser (we used snow free thin ice as tie points).

8.3.3) In-situ snow depth measurements

Although we have compared the difference between the laser and the radar qualitatively with snow depth measurements, without in-situ snow depth measurements, we cannot say if, by differencing the radar elevation estimate from the laser elevation estimate, we are measuring snow depth. We also cannot say that the radar penetrates to the snow/ice interface. Our results may be consistent with these hypotheses but without in-situ data we cannot state them as fact. In future experiments, it is desirable to collect coincident snow depth and temperature measurements to allow a quantitative comparison to be made.

8.3.4) Date of the flights

As shown by figures 7.19 and 7.20 in chapter 7 the air temperature in May can be above zero degrees in the Fram Strait. In order to look at the difference between the penetration characteristics of the radar and the laser it is important that the snow layer has not melted or even partially melted. The evidence presented in chapter 2 tells us that the presence of even a small amount of water in the snow layer strongly effects its dielectric properties, and indicates that radar measurements over wet snow will only provide information on the snow layer and not on the ice. We suggest that March or April would be a more suitable time of year to perform such experiments. The mean temperature in the Arctic is -29°C between November and April and this period precludes any melting of the snow cover [Colony et al., 1998].

8.3.5) Location of the flights

The LaRA flights mainly occurred in the Fram Strait, which is a major ice out flow region of the Arctic. Figure 7.2 shows that the ice drift in this region is not uniform, which makes it difficult to sample the same section of ice in repeat passes. The ice motion in this region becomes an even greater issue when trying to compare measurements from sensors located on different platforms. Ice in the Fram Stait is very mixed as it comes from different regions of the Arctic. This makes interpretation more difficult. We suggest that area to the north west of Greenland, where we see little ice motion, would be a better region for such experiments.

8.4) Directions for future work

8.4.1) Design a new re-tracker for D2P measurements

LaRA provided us with a unique opportunity to study spatially and temporally coincident elevation estimates from laser and radar altimetry. These data sets allowed us to build a simulator and compare like with like (a real echo with a simulated echo) rather than a re-tracked elevation estimate (radar) with an averaged elevation estimate (laser). However, this will not always be the case. The simulator allows us to see what parameters influence the radar return and therefore what parameters should be included

in a re-tracker for use when scanning laser data are not available. For example, we found the roll of the aircraft strongly influenced the shape of the returns and that high roll values gave us non-typical echo shapes. The simulator can also tell us the position of the re-track point over a flat surface (chapter 5, figure 5.38), further experiments would tell us how the position of the re-track point varies over a rough surface and with the aircraft parameters. The simulator has the potential to be used to design a re-tracker for D2P data that can be used when no laser data is present.

8.4.2) Estimate sea ice thickness from the LaRA data set

In-order to estimate sea ice thickness from the LaRA data set we would first need to design a new re-tracker (section 8.4.1) to estimate the elevation of the sea ice and sea surface. Secondly we would need to find the elevation of the sea surface. This could be done either by using the digital photographs to locate areas of open water and finding the corresponding elevation estimates over those areas or by analysing the differences in the returns over open water and ice and using those echo characteristics to automate the process. Once the sea surface elevation had been calculated then the ice freeboard could be found in the same way as described in section 1.5.1 (chapter 1). The ice thickness could then be calculated using equation 1.1 and by taking the difference between the laser and the radar to be equal to the snow depth.

8.4.3) Combining data from ICESat and CryoSat

Analysis of the data collected during LaRA shows the potential of combing satellite laser and radar altimetry measurements over sea ice from ICESat and CryoSat. Combination of ICESat and CryoSat data will be particularly valuable if ICESat can be steered onto a CryoSat ground track, and if spatially and temporally co-incident airborne laser and radar altimetry measurements can be acquired.

References

Aagaard, K., and E. C. Carmack, The Role of Sea Ice and Other Fresh Water in the Arctic Circulation, *Journal of Geophysical Research,* Vol. 94, C10, pp 14,485-14,498, October 15, 1989.

Ahrens, C. D., Essentials of Meteorology – An Invitation to the Atmosphere, West Publishing Company, 1993.

Barnola, J. M., D. Raynard, Y. S. Korotkevich and C. Lorius, Vostok Ice Core Provides 160,000-Year Record of Atmospheric CO_2, *Nature,* 329 (6138), 1518-1530, 1996.

Barry, R. G., M. C. Serreze, J. A. Maslanik and R. H. Preller, The Arctic Sea Ice-Climate System: Observations and Modelling, *Reviews of Geophysics,* 31, 4, pp 397-422, November, 1993.

Beaven, S. G., G. L. Lockhart, S. P. Goginei, A. R. Hosseinmostafa, K. Jezek, A. J. Gow, D. K. Perovich, A. K. Fung and S. Tjuatja, Laboratory measurements of radar backscatter from bare and snow-covered saline ice sheets, *Int. Journal of Remote Sensing,* 16(5), pp 851-876, 1995.

Bertie, J., H. Labbe and E. Whalley, Absorptivity of Ice I in the Range 4000 – 30 cm^{-1}, *J. Chem. Phys.,* 50, p 4508, 1969.

Bevington, P. R., and D. K. Robinson, Data Reduction and Error Analysis for the Physical Sciences, Second Edition, McGraw-Hill, Inc., 1992.

Bourke, R. H., and A. S McLaren, Contour Mapping of Arctic Basin Ice Draft and Roughness Parameters, *Journal of Geophysical Research,* Vol. 97, C11, pp 17,715-17,728, November 15, 1992.

Bourke, R. H. & R. G. Paquette, Estimating the Thickness of Sea Ice, *Journal of Geophysical Research,* Vol. 94, NO. C1, pp 919-923, January 15, 1989.

Brown, G. S., The Average Impulse Response of a Rough Surface and its Applications, *IEEE Trans. Antennas & Propagation,* Vol. AP-25, no. 1, 67-74, 1977.

Brown, J., A. Colling, D. Park, J. Phillips, D. Rothery and J. Wright, Ocean Circulation, Ed. G. Bearman, Butterworth-Heinemann, Reed Educational and Professional Publishing Ltd., 1998.

Bufton, J. L., Laser Altimetry Measurements from Aircraft and Spacecraft, *Proceedings of the IEEE,* Vol. 77, 3, pp 463-477, March 1989.

Carsey, F. D., R. G. Barry and W. F. Weeks, Introduction, In: *Microwave Remote Sensing of Sea Ice, Geophys. Monogr. Ser., vol. 68,* Ed. F. Carsey, Washington D.C., 1992.

Carson, D. J., Climate modelling: Achievements and prospects, *Quarterly Journal of the Royal Meteorological Society, Part A,* VOL. 125, 553, pp 1-27, January, 1999.

Chelton, D. B., E. J. Walsh and J. L. MacArthur, Pulse Compression and Sea Level Tracking in Satellite Altimetry, *Journal Atmos. Oceanic Technol.,* vol. 6, pp. 407-438, June 1989.

Childers, V. A., D. C. McAdoo, J. M. Brozena & S. W. Laxon, New gravity data in the Arctic Ocean: Comparison of airborne and ERS gravity, *Journal of Geophysical Research,* Vol. 106, B5, pp 8871-8886, May 10, 2001.

Clark, P. U., N. G. Pisias, T. F. Stocker and A. J. Weaver, The Role of the Thermohaline Circulation in Abrupt Climate Change, *Nature*, Vol. 415, Feb. 21, 2002

Colony, R., V. Radionov and F. J. Tanis, Measurements of precipitation and snow pack at Russian North Pole drifting stations, *Polar Record,* 34 (188), 3-14, 1998.

Comiso, J. C., P. Wadhams, W. B. Krabill, R. N. Swift, J. P. Crawford and W. B. Tucker III, Top/Bottom Multisensor Remote Sensing of Arctic Sea Ice, *Journal of Geophysical Research,* Vol. 96, C2, pp 2693-2709, February 15, 1991.

Comiso, J. C., D. J. Cavalieri and T. Markus, Sea Ice Concentration, Ice Temperature, and Snow Depth Using AMSR-E Data, *IEEE Transactions on Geoscience and Remote Sensing*, Vol. 41, No. 2, February 2003.

Csathó, B, R. H. Thomas and W. B. Krabill, Mapping Ice Sheet Topography with Laser Altimetry in Greenland, *BPRC Technical Report Number 96-01,* BYRD Polar Research Centre, The Ohio State University, Columbus, Ohio, 1996.

Culdip, W., and M. Milnes, Overview of altimeter data processing at the UK Earth Observation Data Centre, Int. Journal of Remote Sensing, 15, pp 871-887, 1994.

Cumming, W., The Dielectric Properties of Ice and Snow at 3.2 cm, *J. Appl. Phys.,* 23, pp 768-733, 1952.

Curry, J., J. Schramm and E. Ebert, Sea Ice-Albedo Climate Feedback Mechanism, *Journal of Climate,* 8(2), 240-247, Feb., 1995.

Drinkwater, M. R., and G. B. Crocker, Modelling Changes in the Dielectric and Scattering Properties of Young Snow-Covered Sea Ice at GHz Frequencies, *Journal of Glaciology,* Vol. 34, No. 118, 1988.

Eicken H., and M. A. Lange, Sea Ice Thickness Data: The Many Vs. The Few, *Geophysical Research Letters,* Vol. 16, No. 6, pp 495-498, June 1989.

Eicken, H., W. B. Tucker III and D. K. Perovich, Indirect measurements of the mass balance of summer Arctic sea ice with an electromagnetic induction technique, *Annals of Glaciology,* Vol. 33, pp 194-200, 2001.

ECMWF, "ECMWF Operational Analysis data (March 1994 – present)", British Atmospheric Data Centre, 2002, http://badc.nerc.ac.uk/data/ecmwf-op, 2002.

ESA, "ERS 1 and 2" *esa, observing the earth,* 24th February 2003, http://www.esa.int/export/esaSA/GGGWBR8RVDC_earth_0.html, 19th December 2003.

ESA, "Altimeter Design", *esa Earth Observation,* 11th July 2003, http://earth.esa.int/rootcollection/eeo4.10075/altimeter_design.html#func, 19th March 2004.

ESA, "Envisat Instruments", *Envisat,* 21st January 2005, http://envisat.esa.int/instruments/ra2, 25th January 2005.

Evans, S., Dielectric Properties of Ice and Snow – A Review, *J. Glaciol.,* 5, pp 773-792, 1965.

Ezraty, R., and J. F. Piolle, "Gridded sea-ice drift vectors (PSI-DRIFT)", IFREMER, CERSAT, 2004, http://www.ifremer.fr/cersat/en/data/overview/gridded/psidrift.htm#description, 15th March 2005.

Flato, G. M., Spatial and temporal variability of Arctic ice thickness, *Annals of Glaciology,* 21, pp 323-329, 1995.

Flato, G. M., The Thickness Variable in Sea-Ice Models, *Atmosphere-Ocean*, 36 (1), 29-36, 1998.

Forsberg, R., A. Olesen, K. Keller and Møller, Airborne Gravity Survey of Sea Areas around Greenland and Svalbard, *KMS Technical Report,* No. 18, 2002.

Forsberg, R., K. Keller, S. M. Hvidegaard and A. Olesen, ESAG-2002, European airborne gravity and lidar survey in the Arctic Ocean, *KMS Technical Report,* No. 21, 2003.

Franceschetti, G., & R. Lanari, Synthetic Aperture Radar Processing, *CRC Press,* 1999.

Golden, K. M, M. Cheney, K-H Ding, A. K. Fung, T. C. Grenfell, D. Isaacson, J. A. Kong, S. V. Nghiem, J. Sylvester and D. P. Winebrenner, Forward Electromagnetic Scattering Models for Sea Ice, *IEEE Transactions on Geoscience and Remote Sensing,* Vol. 36., 5, September 1998.

Gordon, C., C. Cooper, C. A. Senior, H. Banks. J. M, Gregory, T, C, Johns, J. B. F, Mitchell and R. A, Wood, The simulation of SST, sea ice extents and ocean heat transports in a version of the Hadley Centre coupled model without flux adjustments, *Climate Dynamics,* 16(2-3): 147-168, Feb 2000.

Gow, A. J., and W. B. Tucker III, Physical Properties of Sea Ice Discharged from the Fram Strait, *Science,* Vol. 236, pp 436-439, April 24, 1987.

Gray, A. L., R. K. Hawkins, C. E. Livingstone, L. Drapier Arsenault and W. M. Johnstone, Simultaneous Scatterometer and Radiometer Measurements of Sea-Ice Microwave Signatures, *IEEE Journal of Oceanic Engineering,* Vol.)E-7, No. 1, January 1982.

Gregory, J. M., P. A. Stott, D. J. Cresswell, N. A. Rayner, C. Gordon and D. M. H. Sexton, Recent and Future Changes in Arctic Sea Ice Simulated by the HadCM3 AOGCM, *Geophysical Research Letters,* Vol. 29, 24, 2175, doi:10.1029/2001GL014575, 2002.

Guenther, G. C., A. G. Cunningham, P. E. LaRocque and D. J. Reid, Meeting the Accuracy Challenge in Airborne Lidar Bathymetry, *Proc. 20th EARSeL Symposium: Workshop on LIDAR Remote Sensing of Land and Sea,* European Association of Remote Sensing Laboratories, Dresden, Germany, June 16-17, 2000.

Hadley Centre, http://www.met-office.gov.uk/research/hadleycentre/models/modeldata.html, 2004.

Hallikainen, M, and D. P. Winebrenner, The Physical Basis for Sea Ice Remote Sensing, In: *Microwave Remote Sensing of Sea Ice, Geophys. Monogr. Ser., vol. 68,* Ed. F. Carsey, Washington D.C., 1992.

Hallikainen, M., Review of the Microwave Dielectric and Extinction Properties of Sea Ice and Snow, *Geoscience & Remote Sensing Symposium, IGARSS '92, International,* Vol. 2, pp 961-965, 1992.

Hagemann, S., and L. Dümenil Gates, Validation of the Hydrological Cycle of ECMWF and NCEP reanalysis using the MPI hydrological discharge model, *Journal of Geophysical Research,* Vol. 106, pp 1503-1510, 2001.

von Hippel, A. R., Dielectric Materials and Applications, MIT Press, Cambridge, MA, 1954.

Houghton, J. T.,G. J. Jenkins and J. J. Ephraums, *Climate Change, The IPCC Scientific Assessment,* Report prepared for the IPCC by working group I, Cambridge University Press, 1990.

Houghton, J. T., Y. Ding, D. J.Griggs, M. Noguer, P. J. van der Linden, X. Dai, K. Maskell and C. A. Johnson, *Climate Change 2001: The Scientific Basis*, Contribution of Working Group 1 to the Third Assessment Report of The Intergovernmental Panel on Climate Change, Cambridge University Press, 2001.

Hvidegaard, S. M., and R. Forsberg, Sea-ice thickness from airborne laser altimetry over the Arctic Ocean north of Greenland, *Geophysical Research Letters,* Vol. 29, 20, 1952, doi:10.1029/2001GL014474, 2002.

IABP, "Polar Science Centre, International Arctic Buoy Program", International Arctic Buoy Program (IABP), 11th October 2000, http://iabp.apl.washington.edu, Oct. 2002.

Ishizu, M., Airborne/Spaceborne Laser Altimeter, *Journal of the Communications Research Laboratory,* Vol. 49, 2, pp 89–107, 2002.

Jensen, J. R., Angle Measurement with a Phase Monopulse Radar Altimeter, *IEEE Transactions on Antennas and Propagation,* Vol. 47, no. 4, April 1999.

Jezek, K. C., D. K. Perovich, K. M. Golden, C. Luther, D. G. Barber, P. Gogineni, T. C. Grenfell, A. K. Jordan, C. D. Mobley, S. V. Nghiem and R. G. Onsott, A Broad Spectral, Interdisciplinary Investigation of the Electromagnetic Properties of Sea Ice, *IEEE Transactions on Geoscience and Remote Sensing,* Vol. 36, No. 5, pp 1633-1641, September 1998.

JPL, "Part III", *TOPEX/Poseidon On-line Tutorial,* 9 February 2002, http://topex-www.jpl.nasa.gov/education/tutorial3.html, 19th December 2003.

JPL, "Seasat 1978", 10th February 1998, http://southport.jpl.nasa.gov/scienceapps/seasat.html, 25th January 2005.

Koh, G., Complex dielectric constant of ice at 1.8 GHz, *Cold Regions Science and Technology,* 25, pp 119-121, 1997.

Kovacs, A., and J. S. Holladay, Sea-ice thickness measurement using a small airborne electromagnetic sounding system, *Geophysics,* Vol. 55, No. 10, pp 1327-1337, October 1990.

Kovacs, A., D. Diemand and J. J. Bayer. Jr., Electromagnetic Induction Sounding of Sea Ice Thickness, *CRREL Report,* 96-6, 1996

Krabill, W. B., W. Abdalati, E. B. Frederick, S. S. Manizade, C. F. Martin, J. G. Sonntag, R. N. Swift, R. H. Thomas and J. G. Yungel, Aircraft Laser Altimetry Measurement of Elevation Changes of the Greenland Ice Sheet: Technique and Accuracy assessment, *Journal of Geodynamics,* 34, pp 357-376, 2002.

Krabill, W. B., and C. F. Martin, Aircraft Positioning Using Global Positioning System Carrier Phase Data, *Journal of The Institute of Navigation,* Vol. 34, 1, Spring 1987.

Kreyscher, M., M. Harder, P. Lemke and G. M. Flato, Results of the Sea Ice Model Intercomparison Project: Evaluation of Sea Ice Rheology Schemes for use in Climate Simulations, *Journal of Geophysical Research,* Vol. 105, C5, pp 11,299-11,320, May 15, 2000.

Kwok, R., H. J. Zwally and D. Yi, ICESat observations of Arctic sea ice: A first look, *GRL,* vol. 31 L16401, doi:10.1029/2004GL020309, 2004.

Lamb, J., Measurements of the Dielectric Properties of Ice, *Trans. Faraday Soc.,* 42A, pp 238-244, 1946.

Lamb, J., and A. Turney, The Dielectric Properties of Ice at 1.25 cm Wavelength, *Proc. Phys. Soc.,* Section B, 62, pp 272-273, 1949.

Laxon, S. W., Sea ice altimeter processing scheme at the EODC, *Int. Journal of Remote Sensing,* 15, 915-924, 1994.

Laxon, S. W., N. Peacock and D. Smith, High Interannual Variability of Sea Ice Thickness in the Arctic Region, *Nature,* Vol. 425, pp 947-950, doi:10.1038/nature02050, October 30, 2003.

Laxon, S. W., and C.G. Rapley, Radar Altimeter Data Quality Flagging, *Adv. Space Res.,* Vol. 7, No. 11, pp. (11)315)-(11)318, 1987.

Ledley, T. S., Sea Ice: A factor in influencing climate on short and long time scales, in: *Ice in the climate system,* Ed. W. R. Peltier, 1993.

Lemke, P., W. D. Hibler, G. Flato, M. Harder and M. Kreyscher, On the Improvement of Sea-Ice Models for Climate Simulations: The Sea Ice Model Intercomparison Project, *Annals of Glaciology*, 25, pp 183-187, 1997.

Lepparanta, M., Physics of Ice-Covered Seas, Vol 1, *Helsinki University Press/University Printing House,* 1998

Lindsay, R. W., Changes in the modelled ice thickness distribution near the Surface Heat Budget of the Arctic Ocean (SHEBA) drifting ice camp, *Journal of Geophysical Research*, Vol. 108, No. C6, 3194, doi:10.1029/2001JC000805, 2003.

Luthcke, S. B., S. Ekholm, J. B. Blair, Introduction, *Journal of Geodynamics,* 34, pp 343-345, 2002.

Lytle, V. I., K. C. Jezek, A. R. Hosseinmostafa and S. P. Gogineni, Laboratory backscatter measurements over sea ice with a snow cover at Ku band, *IEEE Trans. Geoscience and Remote Sensing,* 31(5), pp 1009-1016, 1993.

Mahesh, A., J. D. Spinhirne, D. P. Duda and E. W. Eloranta, Atmospheric Multiple Scattering Effect on GLAS Altimetry-Part II: Analysis of Expected Erros in Antarctic Altitude Measurements, *IEEE Transactions on Geoscience and Remote Sensing,* Vol. 40, 11, pp 2353-2362, November 2002.

Mantripp, D., Radar Altimetry, in The Determination of Geophysical Parameters from Space, Ed. N. E. Fancey, I. D. Gardiner and R. A. Vaughan, Scottish Universities Summer School in Physics and Institute of Physics Publishing, Bristol and Philadelphia, 1996.

Mätzler, C., and U. Wegmüller, Dielectric Properties of fresh-water ice at microwave frequencies, *J. Phys D: Appl. Phys.,* 20: 1623-1630: Erratum 1988, 21:1660, 1987.

McIlveen, R., Fundamentals of Weather and Climate, Chapman & Hall, 1992.

Melling, H and D. A. Riedel, The Underside Topography of Sea Ice over the Continental Shelf of the Beaufort Sea in the Winter of 1990, *Journal of Geophysical Research,* Vol. 100, C7, pp 13,641-13,653, July 15, 1995.

Melling, H., P. H. Johnston, and D. A. Riedel, Measurement of the draft and topography of sea ice by moored subsea sonar, *J. Atmos. Oceanic Technol.,* 12, 589-602, 1995.

McIlveen, R., Fundamentals of Weather and Climate, Chapman and Hall, 1995

McLaren, A. S., The Under-Ice Thickness Distribution of the Arctic Basin as Recorded in 1958 and 1970, *Journal of Geophysical Research,* Vol. 94, C4, pp 4971-4983, April 15, 1989.

McLaren, A. S., R. G. Barry and R. H. Bourke, Could Arctic ice be thinning? *Nature*, Vol. 345, p 762, 28 June, 1990.

McLaren, A. S., J. E. Walsh, R. H. Bourke, R. L. Weaver and W. Wittmann, Variability in sea-ice thickness over the North Pole from 1977 to 1990, *Nature,* Vol. 358, 16 July, 1992.

National Snow and Ice Data Centre. 1998. Submarine Upward Looking Sonar Ice Draft Profile Data and Statistics. Boulder, CO: National Snow and Ice Data Centre/World Data Centre for Glaciology. Digital media., 1998.

Parashar, S. K., A. W. Biggs, A. K. Fung and R. K. Moore, Investigation of Radar Discrimination of Sea Ice, *Proceedings of the 9th International Symp. On Remote Sensing of the Environment,* Ann Arbor, MI, Vol.1, pp 323-332,15-19th April 1974.

Peacock, N. R., and S. W. Laxon, Sea surface height determination in the Arctic Ocean, *Journal of Geophysical Research,* Vol. 109, C07001, doi:10.1029/2001JC001026, 2004.

Peebles, Jr. P. Z, Radar Principles, John Wiley & Sons, Inc., 1998.

Perovich, D. K. and A. J. Gow, A quantitative description of sea ice inclusions, *Journal of Geophysical Research,* Vol. 101, No. C8, pp 18,327-18,343, August 15, 1996.

Perry, J., and A. Straition, Revision of the "Dielectric Constant" of Ice in the Millimetre-Wave Spectrum, *J. Appl. Phys.,* 44, p 5180, 1973.

Porat, Boaz, A course in digital signal processing / Boaz Porat. New York : John Wiley & Sons , 1997.

Poularikas, Alexander D: The handbook of formulas and tables for signal processing, Boca Raton, Fla : CRC Press : Springer : EEE Press , 1999

Press, W. H., S. A. Teukolsky, W. T. Vetterling and B. P. Flannery, Numerical Recipes in C. The Art of Scientific Computing, Second Edition, Cambridge University Press, 1992.

Prinsenberg, S. J., I. K. Peterson and S. Holladay, Comparison of airborne electromagnetic ice thickness data with NOAA/AVHRR and ERS-1/SAR images, *Atmosphere-Ocean,* 34(1), p 185-205, Mar 1996.

Raney, R. K., The Delay/Doppler Radar Altimeter, *IEEE Transactions on Geoscience and Remote Sensing,* Vol. 36, no. 5, September 1998.

Raney, R. K., Radar Altimetry, in *Wiley Encyclopaedia of Electrical and Electronic Engineering,* Vol. 17, Ed. J. G. Webster, New York: John Wiley and Sons, pp 547-560, 1999.

Raney, R. K., and J. R. Jensen, The New Generation of Radar Altimeters: Proof of Concept, Final Report, *NASA Instrument Incubator Program (IIP), Contract NAS5-97271, Task Order 015,* August 2001.

Raney, R. K., LaRA-2002 Implementation Plan, *Johns Hopkins University, Applied Physics Laboratory,* 22 April 2002.

Raney, R. K., and C. Leuschen, Technical Support for the Deployment of Radar and Laser Altimeters during LaRA 2002, *Johns Hopkins University, Applied Physics Laboratory,* March 2003.

Rees, W. G. Physical Principles of Remote Sensing, *Cambridge University Press,* 2001.

Reid, G. C., Solar Variability and the Earth's Climate, *In: Solar Variability and Climate,*, Ed. E. Friis-Christensen, C. Fröhlich, J. D. Haigh, M. Schüssler and R. von Steiger, Kluwer Academic Publishers, 2000.

Rossiter, J., and J. S. Holladay, Ice-Thickness Measurement, In: Remote Sensing of Sea Ice and Icebergs, Ed. S. Haykin, E. O. Lewis, R. K. Raney and J. Rossiter, 1994.

Rothrock D., and A. Thorndike, Geometric Properties of the Underside of Sea Ice, *Journal of Geophysical Research,* 85, C7, 3933-3963, 1980.

Rothrock, D. A., Ice Thickness Distribution – Measurement and Theory, In *The Geophysics of Sea Ice,* Ed. N. Untersteiner, New York, Plenum Press, NATO ASI series, Series B, Physics, v.146, 1986.

Rothrock, D. A., Y. Yu and G. A. Maykut, Thinning of the Arctic Sea-Ice Cover, *Geophysical Research Letters,* Vol. 26, 23, pp 3469-3472, December 1, 1999.

Rothrock, D. A., J. Zhang and Y. Yu, The Arctic Ice Thickness Anomaly of the 1990s: A Consistent View from Observations and Models, *Journal of Geophysical Research,* Vol. 108, No C3, 3083, doi:10.1029/2001JC001208, 2003.

Rudels, B., The Thermohaline Circulation of the Arctic Ocean and the Greenland Sea, *Phil. Trans. R. Soc. Lond.* A., 352, 287-299, 1995.

Sallenger, Jr. A. H., W. B. Krabill, R. N. Swift, J. Brock, J. List, M. Hansen, R. A. Holman, S. Manizade, J. Sontag, A. Meredith, K. Morgan, J. K. Yunkel, E. B. Frederick and H. Stockdon, Evaluation of Airborne Topographic Lidar for Quantifying Beach Changes, *Journal of Coastal Research*, 19, 1, pp 125-133, Winter, 20003.

Schanda, E., Physical Fundamentals of Remote Sensing, *Springer-Verlag, Berlin, Heidelberg, New York, Tokyo*, 1986.

Snyder, John P: Map projections used by the U.S. Geological Survey, Washington : U.S. G.P.O, 1982

Steward, E. G., Fourier Optics: An Introduction, *John Wiley & Sons,* 1987.

Stiles, W. H., and F. T. Ulaby, The Active and Passive Microwave Response to Snow Parameters 1. Wetness, *Journal of Geophysical Research,* Vol. 85, C2, pp 1037-1044, Feb. 20, 1980.

Stimson, G. W., Introduction to Airborne Radar, *Hughes Aircraft Company, El Segundo, California,* 1983.

Stogryn, A., Equations for Calculating the Dielectric Constant of Saline Water, *IEEE Trans. Microwave Theory Techn.,* MIT-19, pp 733-736, 1971.

Strass, V. H., Measuring Sea Ice Draft and Coverage with Moored Upward Looking Sonars, *Deep-Sea Research I,* 45, pp 795-818, 1998.

Sturm, M., J. Holmgrem and D. K. Perovich, Winter snow cover on the sea ice of the Arctic Ocean at the Surface heat Budget of the Arctic Ocean (SHEBA): Temporal evolution and spatial variability, *Journal of Geophysical Research,* Vol. 107, NO. C10, 8074, doi:10.1029/2000JC000400, 2002.

Stutzman, W. L., and G. A. Thiele, Antenna Theory and Design, *John Wiley & Sons, Inc.,* 1998.

Tucker III, W. B., A. J. Gow and W. F. Weeks, Physical Properties of Summer Sea Ice in the Fram Strait, *Journal Geophysical Research,* Vol. 92, C7, pp 6787-6803, June 30, 1987.

Tucker III, W. B., D. K. Perovich, A. J. Gow, W. F. Weeks and M. R. Drinkwater, Physical properties of sea ice relevant to remote sensing, In: *Microwave Remote Sensing of Sea Ice, Geophys. Monogr. Ser., vol. 68,* Ed. F. Carsey, Washington D.C., 1992.

Tucker III, W. B., and J. W. Weatherly, Evidence for rapid thinning of sea ice in the western Arctic Ocean at the end of the 1980s, *Geophysical Research Letters,* Vol. 28, 14, pp 2851-2854, July 15, 2001.

Ulaby, F. T., R. K. Moore and A.K. Fung, Microwave Remote Sensing – Active and Passive, Volume II – Radar Remote Sensing and Surface Scattering and Emission Theory, Addison-Wesley Publishing Company, 1982.

Ulaby, F. T., R. K. Moore and A.K. Fung, Microwave Remote Sensing – Active and Passive, Volume III – From Theory to Applications, Addison-Wesley Publishing Company, 1986.

Untersteiner, N., Ed., The Geophysics of sea ice, New York, Plenum Press, NATO ASI series, Series B, Physics, v.146, 1986.

Vant, M. R., R. B. Gray, R. O. Ramseier and V. Makios, Dielectric Properties of Fresh and Sea Ice at 10 and 35 GHz, *J. Appl. Phys.*, 45, pp 4712-4717, 1974.

Vant, M. R., R. O. Ramseier and V. Makios, The complex-dielectric constant of sea ice at frequencies in the range 0.1-40 GHz, *J. Appl. Phys.*, 49(3), pp 1264-1280, March 1978.

Vaughn, C. R., J. L. Bufton, W. B. Krabill & D. Rabine, Georeferencing of airborne laser altimeter measurements, *Int. J. Remote Sensing,* Vol. 17. 11, pp 2185-2200, 1996.

Vaughan, R. A. and A. P. Cracknell, Remote Sensing and Global Climate Change, 1994.

Vazquez, J., "History of Altimetry and TOPEX/Poseidon", *Ocean Surface Topography from Space,* 9th February 2002, http://sealevel.jpl.nasa.gov/education/workshop.html, 19th December 2003.

Vetterling, W. T., S. A. Teukolsky, W. H. Press and B. P. Flannery, Numerical Recipes, Example Book (C), Second Edition, Cambridge University Press, 1992.

Vinje, T., N. Nordlund and A. Kvambekk, Monitoring Ice Thickness in Fram Strait, *Journal of Geophysical Research,* Vol. 103, C5, pp 10,437-10,449, May 15, 1998.

Wadhams, P., Sea ice topography of the Arctic Ocean in the region70 W to 25 E, *Philos. Trans. R. Soc. Ser. A,* 302(1464), pp 45-85, 1981.

Wadhams, P., A. S. McLaren & R. Weintraub, Ice Thickness Distribution in Davis Strait in February From Submarine Sonar Data, *Journal of Geophysical Research,* Vol. 90, NO. C1, pp 1069-1077, January 20, 1985.

Wadhams, P., Evidence for thinning of the Arctic ice cover north of Greenland, *Nature,* Vol. 345, pp 795-797, 28 June, 1990.

Wadhams, P., N. R. Davis, J. C. Comiso, R. Kutz, J. Crawford, G. Jackson, W. Krabill, C. B. Sear, R. Swift and W. B. Tucker III, Concurrent remote sensing of Arctic sea ice from submarine and aircraft, *Int. J. Remote Sensing,* Vol. 12, No. 9, pp 1829-1840, 1991.

Wadhams, P., W. B. Tucker III, W. B. Krabill, R. N. Swift, J. C. Comiso and N. R. Davis, Relationship Between Sea Ice Freeboard and Draft in the Arctic Basin, and Implications for Ice Thickness Monitoring, *Journal of Geophysical Research,* Vol. 97, No. C12, pp 20,325-20,334, December 15, 1992.

Wadhams, P., Arctic sea ice extent and thickness, *In: The Arctic and Environmental Change,* Ed. P. Wadhams, J. A. Dowdeswell and A. N. Schofield, Gordon and Breach Publishers, 1996.

Wadhams, P., Ice Thickness in the Arctic Ocean: The Statistical Reliability of Experimental Data, *Journal of Geophysical Research,* 102, C13, 27,951-27,959, 15 December, 1997.

Wadhams, P., Ice in the Ocean, Gordon and Breach Science Publishers, 2000.

Wadhams, P., and N. R. Davis, Further evidence of ice thinning in the Arctic Ocean, *Geophysical Research Letters,* Vol. 27, 24, pp 3973-3975, December 15, 2000.

Warren, S. G., I. G. Rigor, N. Untersteiner, V. F. Radionov, N. N. Bryazgin, Y. I Aleksandrov and R. Colony, Snow Depth on Arctic Sea Ice, *Journal of Climate,* 12(6), pp 1814-1829, 1999.

Watson, R. T., *Climate Change 2001:Synthesis Report,* Contribution of working groups I,II and III to the Third Assessment Report of the Intergovernmental Panel on Climate Change, Cambridge University Press, 2001.

Weeks, W. F., Sea Ice, IN: Encyclopaedia of Ocean Sciences, Volume 5, Ed. J. H. Steele, Academic Press, 2001 (B) OJ 03 2001

Williams, D., Clementine Laser Image Detection and Ranging (LIDAR) System, *NSSDC Master Catalogue: Experiment,* 9 January 2002, http://nssdc.gsfc.nasa.gov/database/MasterCatalog?sc=1994-004A&ex=4, 19 March 2004.

Wingham, D., CryoSat Science and Mission Requirements, ESA/UCL, 21 September, 1999.

Wingham, D. J., R. Forsberg, S. Laxon, P. Lemke, H. Miller, K. Raney, S. Sandven, P. Vincent and H. Rebhan, CryoSat Calibration & Validation Concept, Centre for Polar Observation & Modelling, University College London, Doc. CS-PL-UCL-SY_004, 14 November 2001.

Wingham, D. J., L. Phalippou, C. Mavrocordatos and D. Wallis, The Mean Echo and Echo Cross Product From a Beamforming Interferometric Altimeter and Their Application to Elevation Measurement, *IEEE Transactions on Geoscience and Remote Sensing*, Vol. 42, No. 10, October 2004.

Wingham[2], D. J., C. R. Francis, S. Backer, C. Bouzinac, R. Cullen, P. de Chateau-Thierry, S. W. Laxon, U. Mallow, C. Mavrocordatos, L. Phalippou, G. Ratier, L. Rey, F. Rostan, P. Viau and D. Wallis, CryoSat: A Mission to Determine the Fluctuations in Earth's Land and Marine Ice Fields, *Advances in Space Research*, Submitted, 2004.

Winsor, P., Arctic Sea Ice Thickness Remained Constant During the 1990s, *Geophysical Research Letters*, Vol. 28, 6, pp 1039-1041, March 15, 2001.

Woods Hole Oceanographic Institution, Arctic map, *Woods Hole Oceanographic Institution*, http://www.whoi.edu/media/arctic_map.html, 2004

Zwally, H. J., B. Schutz, W. Abdalati, J. Abshire, C. Bentley, A. Brenner, J. Bufton, J. Dezio, D. Hancock, D. Harding, T. Herring, B. Minster, K. Quinn., S. Palm, J. Spinhirne and R. Thomas, ICESat's laser measurements of polar ice, atmosphere, ocean, and land, *Journal of Geodynamics*, 34, pp 405-455, 2002.

Appendix 1: Description of ATM QFIT Output Data

[S. Manizade, personal Communication]

The ATM data is distributed in the output format of the processing program, qfit, which combines airborne laser ranging data and aircraft attitude from the INS with positioning information from processed kinematic differential GPS trajectory. The output files are organised as 32-bit (4-byte) binary words, equivalent to a C or IDL long integer, which are scaled to retain the precision of the measurements. The qfit program is run on a Sun Sparc Workstation and therefore written in big-endian format.

The files are organised into fixed-length logical records. The beginning of the file contains a header of one or more records followed by a data segment, in which there is one record per laser shot.

The first word of the header (and the file) is a 32-bit binary integer giving the number of bytes in each logical record. The remainder of the header is generally a series of logical records containing the processing history of the file. In these logical records, the initial word contains a 32-bit binary integer with a value between 9000000 and –9000008. The remaining bytes in each header record are filled with a string of ASCII characters containing information on file processing history.

In the data segment of the file, the information contained in words one to nine of the output record pertains to the laser pulse, its footprint, and aircraft attitude. Words 10 to 13 pertain to the passive brightness signal, which is essentially a relative measure of radiance reflected from the earth's surface within the vicinity of the laser pulse. This data is not calibrated and should only be used qualitatively. Word 14 is the time. Either the 14 word format or a 10 word format, consisting of words one to nine and word 14, is used.

Word	Content
1	Relative Time (msec from start of file)
2	Laser Spot Latitude (degrees × 1,000,000)
3	Laser Spot Longitude (degrees × 1,000,000)
4	Elevation (mm)
5	Start Pulse Signal Strength (relative)
6	Reflected Laser Signal Strength (relative)
7	Scan Azimuth (degrees × 1,000)
8	Pitch (degrees × 1,000)
9	Roll (degrees × 1,000)
10	Passive Signal (relative)
11	Passive Footprint Latitude (degrees × 1,000,000)
12	Passive Footprint Longitude (degrees × 1,000,000)
13	Passive Footprint Synthesized Elevation (mm)
14	UTC Time packed (e.g.: 153320100 = 15h 33m 20s 100ms)

Appendix 2: Description of D2P data files

Parameter	Byte's	Format	Description
Valid Pulse	0:3	long int	1: valid, 0: invalid
Seconds	4:7	long int	Secs (×1e3)
Latitude	8:11	long int	Degrees (×1e6)
Longitude	12:15	long int	Degrees (× 1e6)
Altitude	16:19	long int	Metres (× 1e3)
Heading	20:23	long int	Degrees (× 1e3)
Pitch	24:27	long int	Degrees (× 1e3)
Roll	28:31	long int	Degrees (× 1e3)
Range	32:35	long int	Tracking range steps
Reference	36:39	long int	Tracking shift
Attenuation	40:43	long int	Receiver attenuation setting
Length	44:47	long int	Samples/Pulse
Doppler Bin Size	48:51	long int	Metres (× 1e3)
Data Array	51:51+8*length	(float *real part I*, float *imag part Q*)	Array of complex numbers. Magnitude: cross-channel power Phase: cross-channel phase

Format of D2P files [Raney & Leuschen, 2003]

Appendix 3: D2P data filters

Date	File number	Number of points	Points after filter 1	Points after filter 2	Points after filter 3	Points after filter 4	Percentage of points removed
20	8	23785	23725	23717	23717	23717	0.3%
20	9	23933	23887	23879	23879	23879	0.2%
20	10	12437	12435	12427	12416	12416	0.2%
20	11	25003	23946	23937	23937	22094	11.6%
20	12	28320	27996	27996	27996	23550	16.8%
20	13	30982	30936	30928	30906	30906	0.2%
20	14	25008	24781	24772	24772	24772	0.9%
20	15	28964	28666	28658	28658	28658	1%
20	16	27737	24605	24597	24597	24597	11.3%
20	17	739	537	529	529	529	28.4%
23	5	10967	10967	10958	10958	10958	0.1%
23	6	12277	12277	12268	12268	12268	0.1%
23	7	33397	33345	33336	33336	33336	0.1%
23	8	34552	32968	32959	32959	32959	4.6%
23	10	10131	0	0	0	0	100%
23	11	38698	0	0	0	0	100%
23	12	39373	37999	37999	37999	35470	9.9%
23	13	34555	34470	34461	34461	32746	5.2%
23	14	20626	15837	15828	15828	15828	23.3%
23	15	8894	0	0	0	0	100%
23	16	8268	0	0	0	0	100%
23	17	35726	13952	13952	13952	13952	60.9%
23	18	37386	35211	35182	35166	35166	5.9%
23	19	36209	22111	22111	22111	22111	38.9%
Total		587967				443350	24.6%

List of symbols

a	peak of D2P echo (UCL D2P re-tracker)
a	length of D2P antenna (along track)
$a(x)$	along track signal history
acf	auto-correlation function
A_σ	footprint area
A_a	antenna area
b	length of D2P antenna (across track)
b_f	vector between the **D2P_b** and **D2P_f**
b_fn	the projection of **b_f** onto the xy coordinate system
c	speed of light in air (3×10^8 ms^{-1})
cc	correlation coefficient
D2P	vector describing the location of the D2P antenna
D2P_b	vector between the D2P antenna and the antenna boresight
D2P_n	vector between the D2P antenna and the antenna nadir
D2P_f	vector the D2P antenna and the facet
dc	distance to the centre of the range window (m)
ds	distance to the start of the range window (m)
f	Doppler frequency
fc	radar frequency
f_i	ice freeboard
f_{IF}	intermediate frequency
f_s	snow freeboard
F_0	centre frequency
ΔF	bandwidth
$\Delta f'$	frequency shift
G	antenna gain
h	height
h_{GPS}	height above reference ellipsoid
h_i	ice thickness
h_{ILA}	ice level anomaly
h_{laser}	laser range

List of symbols (continued)

h_n	height of n^{th} scatterer
h_s	snow thickness
h_{SLA}	local sea level anomaly
Δh	deviation of sea surface from the geoid
I	real part of power in D2P data format
k	parameter of the re-tracking function
k_0	wave number ($2\pi/\lambda$)
len	pulse length (bins)
L	loss factor
m_v	volume fraction of liquid water
N	number of coherent pulses in a burst
prf	pulse repetition frequency
$P_I(t)$	average surface impulse response
$P_{FS}(t)$	flat surface impulse response
P_r	power received by a radar
Pr	polar response
P_{rad}	total radiated power
P_t	power transmitted by a radar
$P(t)$	transmitted power envelope (radar simulator)
$P(\delta_p)$	transmitted power at δ_p
$P(0+)$	power just beneath a surface
Q	imaginary part of power in D2P data format
Q_c	chirp sweep rate
$q(z)$	height probability density function
r_e, ϕ_e, λ_e	ellipsoidal coordinates describing the position the laser footprint (e) on the Earths surface
$\boldsymbol{r_e}$	vector describing the position of the laser footprint (e) in ellipsoidal coordinates
$\boldsymbol{r_g}$	vector describing the position of the GPS antenna (g) in ellipsoidal coordinates

List of symbols (continued)

$\boldsymbol{r}_{gl}$	vector describing the position of the laser altimeter with respect to the GPS antenna
$\boldsymbol{r}_{le}$	vector describing the location of the laser footprint with respect to the laser altimeter
ref	gives the location of the centre of the range window above the reference ellipsoid
R	range to target from radar
Re	Earth radius
RMS_{ATM}	root mean squared error associated with a single ATM survey
RMS_{COM}	root mean squared error of differences between two surveys
RMS_{D2P}	root mean squared error associated with a single D2P survey
ΔR	beam curvature
S_b	brine salinity
S_i	sea ice salinity
$S_r(t)$	radar point target response
t	time
t_0	position of peak of D2P echo
t_1	two way travel time between the radar and the surface (seconds)
t_b	position where 2nd re-track function takes over from 1st re-track function
t_d	time lag between transmitted chirp and received chirp (seconds)
t_r	round trip travel time (seconds)
Δt_d	error in the time lag t_d between transmitted and deramping chirp
$\tan\delta$	loss tangent
$\tan\delta_i$	loss tangent of pure ice
v	aircraft velocity
V_s	satellite orbital velocity
w_w	percentage of liquid water
x_0	D2P nadir
x_n	along track position of nth scatterer
Δx_{D2P}	D2P along track footprint (m)
Δx_P	digital photograph along track footprint (m)

List of symbols (continued)

Δy_{D2P}	D2P across track footprint (m)
Δy_P	digital photograph across track footprint (m)
α	scanner tilt angle (AMT)
β	rotation axis angle (AMT)
$\beta(\theta_l)$	function approximating the along track synthetic aperture processing
δ_p	penetration depth
$\delta r(f)$	extra range delay at n^{th} scatterer
ε	complex dielectric constant
ε'	real part (permittivity) of the complex dielectric constant
ε''	imaginary part (dielectric loss factor) of the complex dielectric constant
ε_b	complex dielectric constant of brine pockets
ε_b'	real part (permittivity) of the complex dielectric constant of brine
ε_b''	imaginary part (dielectric loss factor) of the complex dielectric of brine
ε_{ds}	complex dielectric constant of dry snow
ε_{ds}'	real part (permittivity) of the complex dielectric constant of dry snow
ε_{ds}''	imaginary part (dielectric loss factor) of the complex dielectric of dry snow
ε_{fi}	uncertainty in radar measured ice freeboard
ε_{fs}	uncertainty in laser measured snow freeboard
ε_{hs}	uncertainty in snow depth
ε_i	complex dielectric constant of pure ice
ε_i'	real part (permittivity) of the complex dielectric constant of pure ice
ε_i''	imaginary part (dielectric loss factor) of the complex dielectric of pure ice
ε_l	uncertainty in laser derived sea ice thickness
ε_r	uncertainty in radar derived sea ice thickness
ε_{si}	complex dielectric constant of sea ice
ε_{si}'	real part (permittivity) of the complex dielectric constant of sea ice
ε_{si}''	imaginary part (dielectric loss factor) of the complex dielectric of sea ice
$\varepsilon_{\rho i}$	uncertainty in sea ice density

List of symbols (continued)

$\varepsilon_{\rho s}$	uncertainty in snow density
$\varepsilon_{\rho w}$	uncertainty in sea water density
$\phi_{1,2}, \lambda_{1,2}$	centre line latitudes and longitudes for rotating the data sets
ϕ_p, λ_p	latitude and longitude of the transformation pole
ϕ_{pr}	polar response angle
κ_a	absorption loss
κ_e	extinction coefficient
κ_s	scattering loss
λ	wavelength
θ, ϕ	facet orientation angles
θ_l	look angle
θ_{pr}	angle between the normal to the facet and the D2P antenna
σ	width of Gaussian re-tracking function
σ^0	normalised scattering coefficient
σ_{bs}	backscattering cross section
σ_{diff}	diffuse measurement noise
σ_s	surface roughness
σ_{ATM}	error associated with a single ATM survey
σ_{COM}	standard deviation of differences between two surveys
σ_{D2P}	error associated with a single D2P survey
ρ_b	density of brine
ρ_i	density of pure ice
ρ_s	density of snow
ρ_w	density of sea water
τ	compressed pulse length
τ'	uncompressed pulse length
υ_b	brine volume fraction